

Thermo-hydraulic model of the two-phase flow in the brine circuit of a geothermal power plant

vorgelegt von
Diplom-Ingenieur
Henning Francke
aus Berlin

Fakultät III-Prozesswissenschaften
der Technischen Universität Berlin
zur Erlangung des akademischen Grades
Doktor der Ingenieurwissenschaften
- Dr.-Ing. -

genehmigte Dissertation

Promotionsausschuss:

Vorsitzender: Prof. Dr.-Ing. Felix Ziegler
Gutachter: Prof. Dr.-Ing. Matthias Kraume
Gutachter: Prof. Dr. Ernst Huenges
Gutachter: Prof. Dr.-Ing. Christoph Nytsch-Geusen

Wissenschaftliche Aussprache: 23. Januar 2014

Berlin 2014

D 83

Abstract:

Production rate, wellhead temperature and pressure are critical parameters of a geothermal well, which determine the technical and economic viability. Their prediction requires knowledge of brine properties and reservoir characteristics as well as a detailed thermal model of the well and surrounding formation. High salinity and gas content complicate the task.

This work presents a comprehensive numerical thermo-hydraulic model of the brine circuit of a geothermal plant. Implemented in DYMOLA/MODELICA, it has been parameterized and validated with data from the research site in Gross Schoenebeck, Germany. The properties of the complex brine are calculated with a compositional two-phase brine model that considers the specific gas and salt contents and determines the gas fraction with a flash calculation based on the individual gas solubilities. Different applications are demonstrated.

Key words:

Geothermal, well simulator, brine properties, two-phase, VLE, formation heat flow, coupled, MODELICA

Kurzfassung:

Förderrate, Kopftemperatur und Druck einer Geothermiebohrung sind die entscheidenden Größen für die technische Machbarkeit und die Wirtschaftlichkeit eines Geothermieprojektes. Ihre Vorhersage erfordert die Kenntnis der Eigenschaften von Thermalwasser und Reservoir sowie ein detailliertes Modell des Bohrlochs und des umgebenden Gesteins.

In dieser Arbeit wird ein umfassendes thermo-hydraulisches Computermodell des Thermalwasserkreislaufs einer Geothermie-Anlage vorgestellt. Es wurde parametrisiert und validiert anhand von Werten des Forschungsstandorts Groß Schönebeck. Die Berechnung der Fluideigenschaften erfolgt unter Berücksichtigung der Zusammensetzung und des ermittelten Flüssig-Dampf-Gleichgewichts. Verschiedene Anwendungen des in DYMOLA / MODELICA umgesetzten Modells werden vorgestellt.

Acknowledgements

This work was funded by the Federal Ministry of Education and Research of Germany (GeoEn II, Entwicklungsforschung im Bereich der Lagerstättenerkundung, der Bohr-, Reservoir- und Monitoring-Technologien, der Prozessmodellierung, der Material- und Korrosionsforschung und des Aufbaus geothermischer Anlagen, Grant 03G0767A) and the Federal Ministry for the Environment, Nature Conservation and Nuclear Safety (Qualification of geothermal technology - integration of subsurface and surface systems, Grant 0325217).

First, I wish to acknowledge the advice and constant support I received from my supervisor Prof. Dr.-Ing. Matthias Kraume and from the head of my section Prof. Dr. Ernst Huenges. Together with my third referee Prof. Dr.-Ing. Christoph Nytsch-Geusen they made an “express doctoral procedure” possible, for which I am very grateful. Special thanks go to my colleagues Dr.-Ing. Ali Saadat, Dr.-Ing. Thomas Reinsch, Stefan Kranz, Stephanie Frick, Matthis Thorade, Dr. Jan Hennings, Dr.-Ing. Guido Blöcher and Dr. Harald Milsch for unhesitant help, patient discussions, diligent corrections and, first and foremost, for being great people and fun to work with. This includes my colleague and travel mate Maren Brehme who provided me with geological insights and chocolate when I needed it most. I also owe my sincerest gratitude to Sandra Petersen for taking care of linguistic issues of this work.

Last but not least, I want to thank my brother and his family for always having an open door, a full fridge, a good word and a warm bed for me. Same goes for my parents, who have been supporting me already a little longer.

Table of contents:

Abstract:.....	i
Kurzfassung:.....	i
Acknowledgements	i
Table of contents:.....	ii
Nomenclature.....	v
Abbreviations	v
Indices.....	v
Symbols	v
1 Introduction	1
1.1 Geothermal power generation	1
1.2 General processes in the brine circuit.....	2
1.3 Multi-phase issues	3
1.4 Handling two-phase flow.....	4
1.5 Motivation	5
1.6 Objective / Method.....	6
2 State of the art.....	7
2.1 Two-phase pipe flow	7
2.2 Gas/oil wells	11
2.3 Wellbore models.....	11
2.4 Commercial two-phase flow / wellbore simulators	12
3 Fundamentals.....	14
3.1 Pipe flow – conservation laws.....	14
3.2 Phase transitions in the two-phase fluid.....	16
3.3 Heat flow	21
3.4 Reservoir productivity/injectivity.....	25
4 Gross Schoenebeck scenario	27
4.1 Formation.....	27
4.2 Medium properties.....	29
4.3 Reservoir parameters:	29
4.4 Well parameters	29
4.5 Production pump and injection pump	34
5 Model description.....	35
5.1 MODELICA / DYMOLA.....	37
5.2 Geofluid model.....	40

5.3	Reservoir model	52
5.4	Wellbore model	53
5.5	Formation model.....	59
5.6	Pump model.....	63
5.7	Heat exchanger model.....	64
5.8	Separator/degasser model	64
5.9	Model applicability (to other geothermal sites)	65
6	Model validation.....	66
6.1	Liquid phase density model validation	66
6.2	Liquid phase viscosity validation	67
6.3	Gas solubility model validation.....	68
6.4	Hydraulic validation (GrSk probe measurements 9/2011)	72
6.5	Thermal validation with analytical solution	75
6.6	Thermal validation of well model (GrSk circulation test 4/2012)	76
7	Model application.....	80
7.1	Brine properties compared to properties of water	80
7.2	Circulation test.....	81
7.3	Long term temperature prognosis.....	87
8	Sensitivity analysis – level of detail	90
9	Summary	96
10	Outlook	98
A	Conversions.....	I
A 1.	Molality \leftrightarrow mass fraction:	I
A 2.	Conversion between gas void fraction and gas mass fraction	I
A 3.	Gas volume/mass flow fraction \rightarrow Gas volume/mass fraction.....	I
A 4.	Bubble rise velocity \rightarrow Slip factor.....	II
A 5.	Specific heat capacity \rightarrow apparent molar heat capacity	II
B	Auxiliary calculations	IV
B 1.	Pipe flow – momentum balance	IV
B 2.	Raoult’s Law (ideal).....	V
B 3.	Boundary layer heat transfer calculation	V
B 4.	VLE calculation in flow with slip	VII
B 5.	Calculation of brine composition from measurements:	VIII
B 6.	Pump.....	X
B 7.	Calculation of the enthalpy of the liquid phase using solution heat	XII

B 8.	Surface fit for solution heat capacity ratios.....	XIII
C	Error estimations.....	XV
C 1.	Error in pressure calculation due to upstream scheme for velocity	XV
C 2.	Error in pressure calculation due to upstream scheme for density.....	XV
C 3.	Error in pressure calculation by neglecting kinetic head	XV
C 4.	Error in pressure calculation by neglecting slip in GrSk scenario.....	XVI
C 5.	Estimation of thermal error induced by neglecting slip in GrSk scenario.....	XVII
D	Numerics	XIX
D 1.	Finite difference formulation	XIX
D 2.	VLE Algorithm	XXI
D 3.	Axial pipe discretization.....	XXIII
D 4.	Radial Heat Flow.....	XXV
E	Programming environment.....	XXXI
E 1.	Modelling using MODELICA.....	XXXI
E 2.	Implementation Details.....	XXXI
E 3.	MATLAB Script - Heat wave propagation.....	XXXIV
F	List of figures	XXXV
G	List of tables	XXXVIII
H	References	XXXIX

Nomenclature

Abbreviations

ESP	production pump (Electrical Submersible Pump)
MSL	<i>Modelica Standard Library 3.2</i> (www.modelica.org)
PI	productivity index
TVD	true vertical depth
MD	measured depth
VLE	vapour-liquid equilibrium

Indices

' / ''	liquid / gaseous
1p, 2p	single-phase, two-phase
1/2	inflow / outflow
α, γ	component index
ann	open annulus
bh	bottomhole
cnv	convection
fw	fluid - wall
if	interface cement-formation
is	isentropic
mot	pump motor
wh	wellhead
pi	pump inlet
res	reservoir
s/g	salt / gas
∞	far-field, at radial outer formation model boundary

Symbols

A	area	[m ²]
a	thermal diffusivity	[m ² /s]
b	molality (amount of solute per mass of solvent)	[mol/kg]
C_p, c_p	heat capacity, specific heat capacity	[J/K], [J/(kg·K)]
$C_{p,\phi}$	apparent/partial molar heat capacity	[J/(K·mol)]
d	pipe diameter	[m]
f	friction factor	[-]

g	gravitational acceleration	[9.80665 m/s ²]
Gr	Grashof number	[-]
h	specific enthalpy	[J/(kg·K)]
H_{ϕ}^{α}	apparent/partial molar enthalpy	[J/mol]
htc	heat transfer coefficient	[W/(m ² K)]
k_{α}	Henry coefficient of gas α	[1/Pa]
M	molar mass	[kg/mol]
\dot{m}	mass flow rate	[kg/s]
m_{α}''	mass of component α in gas phase per kg fluid	[kg/kg _{fluid}]
n_{α}, \mathbf{n}'	amount of component α per kg fluid, as vector	[mol/ kg _{fluid}]
n'_{α}	amount of component α in liquid phase per kg fluid	[mol/kg _{fluid}]
	vector of n'_{α}	[mol/kg _{fluid}]
$n''_{\alpha}, \mathbf{n}''$	amount of component alpha in gas phase per kg fluid, as vector	[mol/kg _{fluid}]
$\tilde{n}''_{\alpha} = \frac{n''_{\alpha}}{n_{\alpha}}$	normalized amount of component α in gas phase	[-]
N_r	number of radial elements of the formation model	[-]
$N_{s/g}$	number of salts/gases in the brine	[-]
p	pressure	[Pa]
PI	well productivity index	[m ³ /(s·Pa)] ¹
Pr	Prandtl number	[-]
\dot{q}	heat flux density	[W/m ²]
\dot{Q}	heat flow rate	[W]
r	radius, measured horizontally from well centre	[m]
\bar{R}	universal gas constant	$\bar{R} = 8.314 \text{ J}/(\text{mol}\cdot\text{K})$
s	measured length of wellbore starting at inflow (> 0)	[m]
T	temperature	[K]
U	overall heat transfer coefficient / thermal transmittance	[W/(m ² K)]
\dot{V}	volume flow rate	[m ³ /s]

¹ in the equations basic units [m³/(s·Pa)] are used, values are given the common unit

[m³/(h·MPa)]

V_{ϕ}^{α}	apparent molar volume	[m ³ /mol]
w, w', w''	mean flow velocity, liquid mean flow velocity, gas mean flow velocity	[m/s]
W	washout	[-]
$x = m'/m$	mass fraction of gas phase	[-]
$\dot{x} = \dot{m}'/\dot{m}$	mass flow fraction of gas phase	[-]
X_{α}, \mathbf{X}	brine mass fraction of component α ($\sum X_{\alpha} = 1$), vector	[kg/kg]
$X'_{\alpha}, X''_{\alpha}$	mass fraction of component α in liquid/gas phase ($\sum X'_{\alpha} = 1$)	[kg/kg]
$y'_{\alpha}, y''_{\alpha}$	mole fraction of component α in liquid/gas phase	[-]
Z_{β}	number of ions per molecule of component β	[-]
z	true vertical depth (< 0)	[m]
α_{max}	radial element growth ratio	[-]
β	thermal expansion coefficient	[1/K]
$\delta_{\alpha\beta}$	Kronecker symbol, equals 1 if $\alpha = \beta$ else 0	
$\varepsilon = V''/V$	volume fraction of gas phase (gas void fraction)	
$\dot{\varepsilon} = \dot{V}''/\dot{V}$	volume flow fraction of gas phase	
η	dynamic viscosity	[Pa·s]
η_{is}, η_{mot}	efficiency of pump, pump motor	[-]
λ	thermal conductivity	[W/(m·K)]
ν	kinematic viscosity	[m ² /s]
ρ	density (in slip flow: homogenous fluid density)	[kg/m ³]
$\hat{\rho}$	static fluid density (in slip flow)	[kg/m ³]
σ	surface tension	
φ	wellbore inclination, angle to horizontal [-] ($\varphi = 90^{\circ}$ means normal flow upwards)	

1 Introduction

This chapter introduces the thematic background of this work. After a few words about geothermal power generation, the motivation, objective and method are presented.

1.1 Geothermal power generation

Geothermal energy, the heat of the earth's crust, is a non-fluctuating energy source with huge potential. The idea of tapping this source of abundant energy for power generation has a long tradition, at least in regions with exceptionally favourable geological conditions. In most regions the temperature of the earth crust increases with depth at an average rate of $30\text{ }^{\circ}\text{C}/1000\text{ m}$ (Press and Siever, 1995), but in some places, like the edges of tectonic plates or in formerly volcanically active areas, the temperature gradient reaches higher values (Loose, 2007).

For more than 100 years electricity has been produced in the geothermal power station in Larderello, Italy. But also other countries such as the USA, the Philippines, Indonesia, New Zealand and Iceland have gathered tremendous experience in the field of geothermal power production so that today the installed geothermal power capacity amounts to more than 11 GW (DiPippo, 2012).

In recent years, impending climate change and depletion of fossil fuels have spurred new research in geothermal energy, which aims at developing techniques to exploit also low-enthalpy geothermal reservoirs at larger depths (3 to 5 km) and with low temperatures (100 to 200 $^{\circ}\text{C}$). For that purpose the GFZ Research Centre for Geosciences established a research platform in Gross Schoenebeck (GrSk), located northeast of Berlin in the North-German Basin (Huenges, 2011).

The exploitation concept of the Gross Schoenebeck site, as depicted in Fig. 1, is typical for other low-enthalpy geothermal reservoirs. Two deep wells are drilled into the geothermal reservoir, one for production and one for reinjection. A closed (binary) power cycle with turbine, generator and heat exchangers, as well as a cooling system are set up on the surface for power generation. In Gross Schoenebeck, two wells access the Rotliegend formation in $\approx 4,300\text{ m}$ depth, reaching an aquifer that has a temperature of $145\text{ }^{\circ}\text{C}$ and is under a pressure of 455 bar.

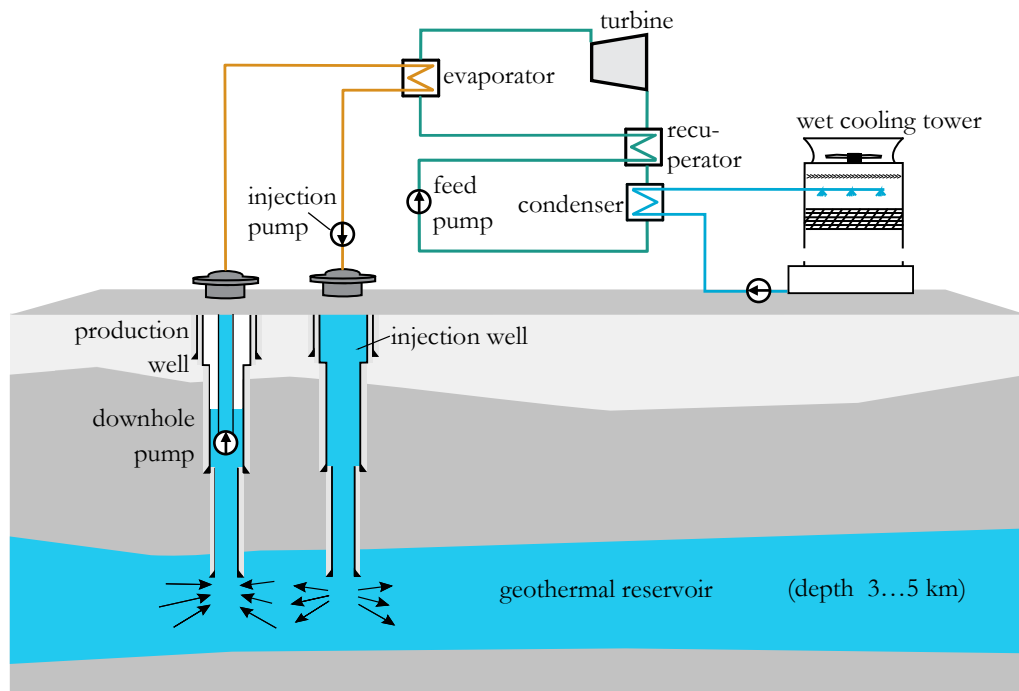


Fig. 1: Schematic view of a geothermal power plant including geofluid loop and cooling water loop (Frick et al., 2013)

Hot geofluid is pumped to the surface by an electrical submersible pump (ESP) installed in the production wellbore. Heat is extracted and the colder fluid is reinjected into the reservoir through the second well in order to maintain reservoir pressure. Both wells are drilled into the same aquifer, having a bottom distance of about 500 m. The distance is a compromise between being close enough for hydraulic interaction and having enough distance to avoid thermal breakthrough.

The extracted heat can be used directly or be transferred to a power cycle transforming the thermal energy to mechanical energy, which is eventually transformed to electrical energy by a generator. The waste heat from the power cycle is typically released into the environment by means of dry coolers or wet cooling towers.

A key aspect for the successful use of geothermal heat from deep aquifers is the reliable and efficient operation of the brine loop. This requires careful dimensioning of its components and knowledge of the geofluid properties. Geothermal fluids are complex mixtures consisting of salt solution and dissolved gases, which differ site-specifically. The properties of geothermal fluids hence depend on the reservoir characteristics, as well as on the temperature and pressure changes that occur during operation.

1.2 General processes in the brine circuit

The brine circuit, as depicted in Fig. 2, consists of the wells and the connecting components above ground. The relevant processes will be described in the following.

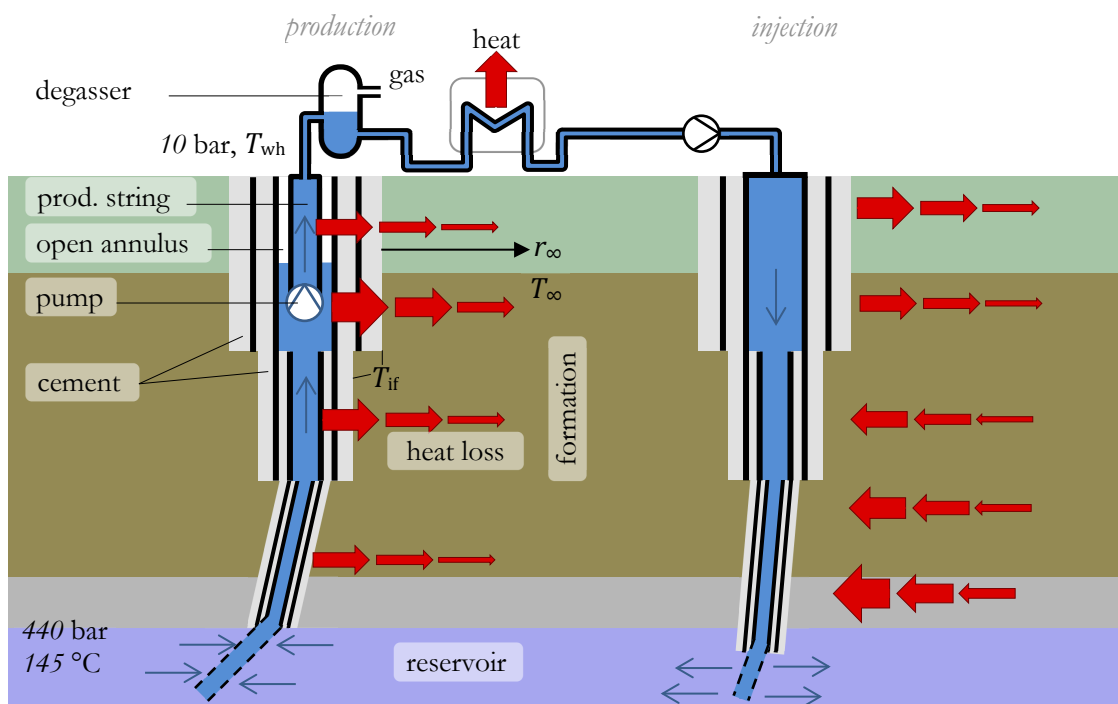


Fig. 2: Schematic view of the geothermal production site in Gross Schoenebeck with well, degasser and heat exchanger, arrows indicating fluid flow and heat flow, dashed box shows model boundary

The brine is produced through the wellbore, which is a conduit drilled through the formation vertically or more or less deviated. The well is completed by steel pipes cemented to the formation in telescope-like layout (Fig. 2).

Unless the well is artesian, i.e. aquifer pressure is sufficient to push the brine to the surface, a production pump has to be installed downhole. It is installed deep enough to guarantee that the pump is well below the liquid level during operation. That is because the liquid level sinks during production due to friction in the reservoir bringing down the bottomhole pressure (drawdown). Hence, production rate is determined by the pump, but limited by reservoir productivity. The pump is connected to the production string, a pipe with a smaller diameter centred within the casing and hanging from the top. The surrounding annulus

is connected to the well part below the pump, hence partly filled with liquid and therefore acts as a hydraulic buffer for pressure changes, for example, during production start-up. This annulus is sealed and pressurized at the wellhead. Although being closed on top, it is herein referred to as ‘open annulus’.

As mentioned above, the natural formation temperature decreases from reservoir to surface, creating a temperature difference between the formation and the hot fluid rising from the reservoir. This temperature gradient is the driving force for radial heat flow. Its magnitude depends on the thermal properties of the well completion and the formation. The properties strongly depend on the liquid level in the open annulus, because it makes the difference between heat transfer in liquid and heat transfer in gas. The radial heat flow can cause significant heat loss of the fluid on its way from the reservoir to the wellhead, so that the wellhead temperature T_{wh} may be considerably lower than the reservoir temperature. The heat flow gradually warms up the formation surrounding the well during production. This in turn reduces said temperature gradient, therefore lowers the heat loss and eventually increases T_{wh} . Depending on the production rate, this warming process may go on for days or years until T_{wh} is stationary.

Due to gravity and friction in the reservoir and in the wellbore, fluid pressure also decreases upwards, except for the pressure increase at the ESP. Due to the large vertical extension of the well, fluid pressure varies between reservoir pressure, which is approximately the hydrostatic pressure corresponding to the depth (a few hundred bar) and the system pressure above surface (a few bar). Friction pressure loss in the reservoir depends on the rock permeability, which can be increased by mechanic or chemical measures. The gravity effect depends on fluid density, which is largely affected by its temperature and composition.

There are geothermal reservoirs that virtually produce drinking water, and there are others where the brine is saturated with salts. The brine extracted from the deep aquifer in Gross Schoenebeck contains high amounts of dissolved salts (mostly NaCl, CaCl₂, KCl) and non-condensable gases (mostly N₂, CH₄, CO₂). Due to the high salinity the brine is hazardous to groundwater and would require costly disposal as special waste if it were not reinjected after heat extraction into the reservoir through the second well, which is the case in normal operation. Like production, injection requires good rock permeability and is subject to heat exchange with the formation.

If an injection pump is necessary, it can be installed on the surface contrary to the downhole production pump. This allows for easier access for installation and maintenance and requires a shorter cable for the power supply. The injection pump operates against the friction in the pipe and in the reservoir and, potentially, artesian pressure. The decrease of brine temperature by heat extraction has two opposite hydraulic effects: On the one hand, it increases density, which facilitates injection by augmenting static head. On the other hand the temperature decrease makes the brine more viscous, which increases friction in the reservoir.

In the injection well, opposed to the production well, heat flow may occur in both directions. Depending on the depth and fluid temperature, heat can flow from the brine to the formation or vice versa.

1.3 Multi-phase issues

Due to the large pressure decrease between aquifer and the above ground facility, degassing and evaporation may occur during production forming a gas phase. It may also occur locally and be reversed downstream due to local pressure minima, like at the pump inlet, in bends or components with nozzle effect. On the other hand, the temperature decrease in the production well and in the heat exchanger may trigger precipitation and form a solid phase. Degassing and precipitation form potentially three phases, which may have thermal, hydraulic and chemical implications.

Hydraulic consequences

The hydraulic effects involve the static head, the friction pressure loss and gas accumulation.

Static head is affected because precipitation and degassing change the effective fluid density. It is decreased by degassing because the gas phase has a significantly lower density than the brine, similar to the principle of an airlift pump. Precipitation has a weaker effect, because the density of precipitates does not differ as strongly from water density². Friction head is increased because the gas phase increases the volume flow rate and because phase slip³ causes inner friction. Due to buoyancy gas tends to accumulate in overhead regions, especially at low flow velocity. These stationary gas bubbles may obstruct the flow, create recirculation areas or otherwise change the flow in an undesirable way that leads to particle accumulation and increased scaling or corrosion, increased pressure drop or decreased heat transfer.

In the pumps, which are commonly centrifugal pumps, stationary bubbles on the vanes can cause the pump to stall. At lower gas fractions below the stalling threshold, the pump compresses the gas which consumes additional energy and deteriorates pump performance. At even lower gas fractions, below degassing pressure, the gas content may trigger cavitation, i.e. local bubble formation and collapse on the vanes, which can massively increase corrosion.

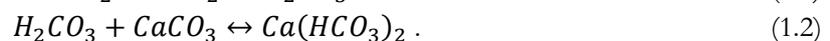
Thermal consequences

The additional compression work by the pump eventually heats up the fluid. Besides impairing the efficiency of the heat exchanger as described above, the gas phase formation by evaporation and degassing absorbs latent heat, thus reducing fluid temperature.

Chemical consequences

Degassing of CO₂ increases the pH, which can cause precipitation of solids.

Carbon dioxide dissolved in water forms carbonic acid, which dissolves minerals, for example limestone (calcium carbonate):



Reversing that process, degassing CO₂ from the brine will remove carbonic acid from the brine (eq. 1.1) and thus shift the limestone solution equilibrium (eq. 1.2). This triggers the precipitation of solids, commonly known as limescale, which can lead to scaling of the pipes and heat exchangers, clogging of filters or the reservoir at the injection well.

This is what also happens in a heated kettle, where degassing is caused by heating the water and not by pressure reduction as in the well. Opposed to that, the temperature decrease in the well can also cause precipitation because limestone solubility decreases with temperature.

1.4 Handling two-phase flow

Degassing can be limited by maintaining the pressure in the brine circuit above a certain level. In GrSk this is feasible for CO₂, because its solubility is high and content is low. However, preventing the degassing of nitrogen, the main component with low solubility, would require a very high wellhead

² Although the precipitates are heavier than water, precipitation of the main salts in GrSk also reduces density, because the apparent molar volumes of NaCl, KCl and CaCl₂ are smaller than their solid molar volumes (Mao and Duan, 2008).

³ Slip is the velocity difference between phases, here due to density difference and gravity.

pressure ($> 200 \text{ bar}^4$) and pipework, which is able to withstand that pressure. This, as well as the pump load required to maintain that wellhead pressure would be disproportionate.

If gas fraction in the pump is an issue, reaching the critical value can be avoided by installing the pump deeper in the well, where pressure is higher and gas fraction lower. Increasing the installation depth comes at the cost of longer power supply cables (higher ohmic losses) and is limited by well diameters, as the pump must be smaller than the casing diameter.

In GrSk the gas fraction is removed from the produced fluid before heat extraction in a degasser. This does not prevent further degassing of remaining dissolved gas, but it reduces problems in the downstream components like gas accumulation and additional compression work load for the injection pump.

Gas accumulation can be prevented by accordingly designing the pipework and heat exchanger, so that overhead bends, slow downward flow and diameter reductions (nozzle effect) are avoided. Generous filter dimensioning avoids big pressure drops which could trigger further degassing.

The extracted gas can be a mixture of gases, typically hydrocarbons, carbon dioxide, hydrogen sulphide and nitrogen. Carbon dioxide and methane have global warming potential. Hydrogen sulphide causes odour nuisance already in small concentrations, while nitrogen is unproblematic. The release of the extracted gas into the atmosphere may be restricted by emission limits and can impair the eco-balance of the plant. One alternative is reinjecting the gas together with the brine, which has the advantage of not affecting the chemical balance and avoiding unwanted fluid-rock-interactions. However, this causes additional pumping work unless the well's injectivity is high so that injection is possible without an injection pump.

Summing up, while degassing in the production well of a geothermal plant can be beneficial because of reduced pump effort, it may be disadvantageous because of increased friction, decreased pump efficiency, impaired heat exchange, scaling and evaporative heat loss.

1.5 Motivation

Predicting well flow parameters is of central interest for the use of geothermal energy, as these parameters are crucial for reliable plant operation and also for economic viability. Production rate and wellhead temperature are the critical parameters as they define the thermal output. So is the pressure profile in the production well, as it determines power consumption of the pump. Another important flow parameter is the gas fraction, because it can affect pump performance and may require additional or adapted installation, such as a degassing unit, special pumps or pressure maintenance to avoid degassing. Pressure and temperature in the injection well influence the injection pumping work load. Temperature in the brine circuit is of general relevance for temperature dependent processes like precipitation.

These key parameters of a geothermal power plant are of interest in the planning phase, when design decisions have to be made, in the construction phase, when the associated risks are to be insured, as well as in the production phase, when the operation is to be optimized.

Precise knowledge of the brine's density, heat capacity and viscosity is essential for thermal-hydraulic well calculations. With the hydrostatic head dominating the well hydraulics, precise density calculation is

⁴ Degassing pressure was calculated with the fluid model presented in 5.2 for $100 \text{ }^\circ\text{C}$ and the composition given in 4.2.

crucial because estimation errors cumulate over the whole length of the well. Besides density, other properties are relevant, namely viscosity, heat capacity or specific enthalpy and degassing pressure. Due to the potentially high salinity of the brine applying the (well available) properties of pure water may be a poor choice, because that would generate considerable errors (Francke and Thorade, 2010). Driesner (2007) developed a comprehensive model for the H₂O-NaCl system, but no equivalent models were available for the complex mixture of water with several salts and gases as found in the GrSk fluid.

1.6 Objective / Method

This work aims at developing a tool that provides information about the thermal hydraulics in a geothermal brine circuit, information that can help in making decisions in design or operation and in gaining a better understanding of the processes involved in the exploitation of geothermal energy.

Due the complex and coupled nature of the processes in the brine circuit, which have been described above, the prediction of most flow parameters requires a numerical model. Hence, the following chapters present the development, implementation, validation and application of a numerical model that is capable of predicting the transient thermal and hydraulic midterm/longterm well behaviour of the geothermal wells, whilst considering the influence of salinity and gas content.

Due attention is paid to a detailed heat loss calculation and a two-phase property model for the multi-salt multi-gas brine including the calculation of the vapour-liquid equilibrium.

The GrSk site was selected for parameterization of the model because of the abundance of available data. Well completion, geology and fluid chemistry were well documented and continue to be subject of research. Although midterm/longterm operational data could not be gathered to date on the expected scale, they nevertheless permit valuable validation. For hydraulic validation exceptional data from a short-term deep-well logging campaign with simultaneous distributed temperature measurement is available, while one week of continuous operation provided thermal data for comparison. The brine property model is validated independently with data from literature and measurements on site and in the lab.

The wellbore model is applied to the GrSk site for long-term prognosis. A study is conducted on the influence of the level of detail by applying various simplifications to the model and assessing the effect on the simulation result.

The following chapter 2 gives an overview over the current state of wellbore modelling. Chapter 3 introduces the physical fundamentals that are required for the numerical models of the geofluid and the brine circuit components which are developed in chapter 5 after specification of the GrSk scenario in chapter 4. The models of geofluid and wellbore are validated in chapter 6 before various applications are demonstrated in chapter 7. Chapter 8 examines which modelling details are relevant and which are dispensable. Chapter 9 and 10 summarize the work and present options for follow-up work.

2 State of the art

The processes in brine circuit which are of interest in this work are: vertical two-phase pipe flow, heat transfer at a flow boundary, heat transfer by free convection, heat conduction, gas (dis)solution, water evaporation. Separately these processes are generally well understood and described in literature. The combination in a complex system is, however, a challenge.

The need for the calculation and prediction of wellbore processes is not unique to geothermal production, but exists as well in related areas like CO₂ underground storage. By far most efforts that have been made in wellbore simulation are related to the production of hydrocarbons. However, not all of the developed methods can be applied to geothermal wells and are publicly accessible.

This chapter starts with an overview over established models for two-phase pipe flow. Then the particularities of gas/oil wells are explained before an overview over existing wellbore models is given.

2.1 Two-phase pipe flow

Multiphase flow occurs in various places and situations. Either beneficial or problematic, it is a common phenomenon in technical installations. As such it has been studied thoroughly by process engineers and fluid mechanics, theoretically as well as experimentally.

This work deals with two-phase flow formed by a liquid and a gas phase. A solid phase, potentially formed by precipitation and corrosion products, is not considered in this work, because its thermal and hydraulic influence is expected to be smaller than the consequences of the gas phase.

The flow in geothermal wells is essentially a vertical pipe flow, which is well described in literature for classic fluid mechanics. However, the applicability of the common hydraulic equations is limited because they assume that density and temperature are constant along the well, which they are not. As described in section 1.2, both quantities change due to heat loss and formation of a gas phase. The cumulative effect of errors in the density determination for pressure prediction suggests the importance of an accurate density correlation. That in turn requires knowledge of the fluid temperature. Fluid temperature depends on the heat flow to the formation, which therefore cannot be neglected when modelling geothermal wells (Hasan and Kabir, 2010).

Depending on the content of dissolved gasses and minerals and the in-situ pressure and temperature degassing and/or precipitation may occur. Consequentially a gas phase and/or a liquid phase may exist, affecting the flow thermally and hydraulically.

The special characteristics of two-phase pipe flow have been studied extensively. Depending on the flow parameters it forms different flow patterns ranging from bubbly flow with a continuous liquid phase, over slug flow with intermittent phases to annular flow with a continuous gas phase, to just name a few. More explanation and figures can be found in abundance in two-phase related literature, for example (e.g., Ishii and Hibiki, 2006). Several authors have investigated the flow patterns analytically and experimentally and attempted to chart threshold values for specific flow parameters, so that flow regimes can be predicted using those charts (Barnea et al., 1982; Hewitt and Roberts, 1969). However, these two-dimensional charts can only consider two independent flow parameters, which is not enough to characterize a two-phase flow, as some authors state that eight independent parameters are required to describe a two-phase flow (Kraume, 2003).

One essential parameter for two-phase is the volume fraction of the gas phase. It depends primarily on the pressure and can therefore not be assumed constant. As pressure in a geothermal well ranges from reservoir pressure (hundreds of bars) to wellhead pressure (several bars), the gas fraction may evolve from zero (completely dissolved) to significant by degassing, evaporation and decompression. The laws that can be used to describe those processes are explained below in 3.2.

According to Hasan (2010) in most geothermal wells prevails turbulent flow⁵. For low gas fractions and low flow velocities gravity dominates the well hydraulics, even on deviated sections, as long as they are not horizontal. Only for high flow velocities friction is influential.

Fig. 3 shows a schematic representation of a two-phase flow of a degassing/evaporating fluid flowing upward through an inclined pipe. It is used to introduce the quantities that are used later.

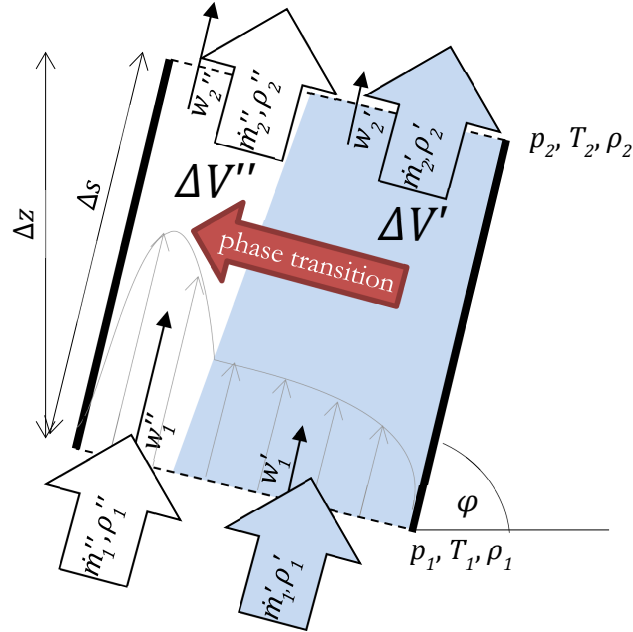


Fig. 3: Simplified (stratified) two-phase flow with slip upward in an inclined pipe

The two-phase mass flow \dot{m}_1 entering the pipe segment is composed of the liquid mass flow \dot{m}_1' and the gaseous mass flow \dot{m}_1'' . They are related to the corresponding volume flows \dot{V}_1' and \dot{V}_1'' via their respective average density. We define the gas mass flow fraction \dot{x} and gas volume flow fraction $\dot{\varepsilon}$:

$$\dot{x} = \frac{\dot{m}''}{\dot{m}} = \frac{\dot{m}''}{\dot{m}' + \dot{m}''} \quad (2.1)$$

$$\dot{\varepsilon} = \frac{\dot{V}''}{\dot{V}}. \quad (2.2)$$

Under stationary conditions mass conservation applies and the total mass flow rate \dot{m}_2 equals \dot{m}_1 . Its distribution among the phases \dot{m}_1' and \dot{m}_1'' can, however, change by evaporation or degassing, so that \dot{x} and $\dot{\varepsilon}$ also change. If no phase transition occurs, then $\dot{x}_1 = \dot{x}_2$ and $\dot{\varepsilon}_1 = \dot{\varepsilon}_2$.

Even though the two phases are usually not separated as cleanly as depicted in Fig. 3, they do occupy a certain fraction of the pipe volume ΔV or of the cross-section A . The liquid mass m' takes up the volume V' ; the gas mass m'' occupies the volume V'' . Division by the total fluid mass or the total volume yields the definition of the gas mass fraction x and gas volume fraction ε :

$$x = \frac{m''}{m} \quad (2.3)$$

⁵ The validity of this statement for GrSk is verified later in 4.4.4.

$$\varepsilon = \frac{V''}{V} = \frac{A''}{A} . \quad (2.4)$$

In one-dimensional pipe flow calculations, averaged values of field quantities (w , p , T) are used. Average phase velocities are assigned by dividing the volume flow rates by the cross section occupied by the respective phase A'/A'' :

$$w' = \frac{\dot{V}'}{A'} = \frac{\dot{V}'}{A(1-\varepsilon)} , \quad w'' = \frac{\dot{V}''}{A''} = \frac{\dot{V}''}{A\varepsilon} . \quad (2.5)$$

If both phase velocities are equal, then gas mass/volume fraction x/ε equals the gas mass/volume flow fraction $\dot{x}/\dot{\varepsilon}$.

2.1.1 Slip

The density of gas phase is significantly lower than the density of the liquid phase. The forces of friction and gravitation acting on the gas phase are therefore weaker. Assuming a homogenous pressure on the cross-section of the pipe, both phases are, however, subject to the same pressure gradient. This causes acceleration of the gas phase until the resulting interphase friction restores the static force balance. The velocity difference between the phases is called slip. In the vertical upward flow in a production well, slip is such that the gas phase has a higher velocity than the liquid phase.

Slip depends on the flow regime, i.e. how much the phases interact with each other and how large the interface area is. Generally slip increases with the gas volume fraction and the density difference of the phases. For example, in the continuous gas phase of annular flow it is higher than bubbly flow with small separate bubbles.

In a vertical upward flow slip increases static pressure head and adds inner friction pressure loss:

At constant gas volume flow rate the increased gas phase velocity reduces the cross section area and volume occupied by the gas. The liquid phase is, in turn, slower and takes up more space, which increases the weight of the fluid column and consequentially the static pressure head.

The gas velocity is determined by the force balance of buoyancy and friction between the phases. The movement against this inner friction dissipates mechanic energy.

Slip can be roughly estimated with simple correlations considering the ratio of phase densities, liquid viscosity and geometry (Ahmad, 1970) or more complex equations that consider gas fraction and flow regime (Ishii and Hibiki, 2006) (see C 4).

2.1.2 Friction pressure loss in two-phase pipe flow

The presence of a second phase with strongly differing properties greatly complicates pressure drop calculations, because the properties of each phase present must be taken into account. Furthermore, the interactions between the phases have to be considered.

Friction in a two-phase flow is higher than in single-phase flow with the same mass flow rate. When the gas phase forms in the production well, the effective density of the fluid decreases which increases the volume flow rate. Higher volume flow means higher mean velocity, higher wall gradient and higher wall shear stresses. Hence the additional gas flow increases the friction pressure drop.

Furthermore, the friction at the phase interface due to slip dissipates energy which results macroscopically in an additional pressure drop.

Various approaches with different complexity exist for the calculation of the friction pressure loss. A common approach is based on the single-phase pressure loss equation with the difference, that it uses effective two-phase values for fluid density ρ_m and velocity u_m . Furthermore it considers hydraulic diameter and the length of the pipe in question as well as a friction factor f , which depends on the Reynolds number, the flow state (laminar/turbulent) and wall roughness:

$$\Delta p_f = f \frac{\rho_m w_m^2}{2d_{hyd}} \Delta s. \quad (2.6)$$

Some correlations for the friction factor are purely empiric while more recent methods include detailed modelling of the two-phase flow phenomena. Some are only valid for only one flow regime or do not consider different flow regimes (Lockhart and Martinelli, 1949; Friedel, 1978). Others require prior prediction of the flow regime for the selection of the according equations (Ishii and Hibiki, 2006). An application of an advanced two-phase pressure drop calculation method on a geothermal well is presented by Antics (1995).

2.1.3 Existing models for two-phase flow

Direct numerical simulation of two-phase flows is possible with today's computers. It is used to study details like the behaviour of a few bubbles, such as their coalescence and break-up, or the flow in small geometries like bends and valves. For example Fuchs and Kather (2013) simulated the gas accumulation and its effect on component pressure drop in the piping of a geothermal plant. Two-phase CFD calculations may be advantageous for inexpensive parameter studies, but they are not suitable for the simulation of the long-term processes in a well of 4000 m including heat loss and phase transition, as these complex calculations are often slower than real-time by orders of magnitude in spite of the applied simplifications.

In many applications macroscopic flow parameters are more interesting than local values. For instance, the overall pressure drop of a pipe flow is relevant but not the shape and location of the phase interface. Therefore, simplifications are made, quantities are averaged over space and/or time and the fluctuations as well as fundamental equations, are replaced by (semi-)empirical correlations. Pipe flow has been studied extensively, hence a multitude of correlations for pressure drop and heat transfer is available.

Simplifications are obviously made according to specific characteristics of the studied flow situation, the quantities of interest and the expected phenomena. Frequent assumptions are: isothermal, incompressible fluid/liquid, constant gas fraction (no phase transition), constant bubble size, in pipe flow uniform pressure/temperature velocity over a cross-section, which reduces the problem to a one-dimensional flow.

One-dimensional two-phase modelling is usually done with one of the following approaches or with a variation of them: two-fluid models, drift-flux models or homogenous models (Ishii and Hibiki, 2006), (Sokolichin et al., 2004), (Kraume, 2003).

Two-fluid models are based on balances of energy, momentum and mass calculated separately for each phase and coupled by interaction terms that represent the exchange of momentum (inter-phase friction), optionally mass (phase transition) and energy between the two phases. This approach is rather straightforward, but the formulation of the coupling presents numerical difficulties. The dispersed phase is sometimes assumed to be present in bubbles/droplets of one or a few classes, with the respective uniform size (mass) and velocity (Sokolichin et al., 2004).

Drift-flux models treat the two-phase fluid as a mixture with an effective viscosity and an effective momentum density, including a relative velocity of the gas (slip). The constitutive equations are the balances of energy, momentum and mass for the mixture. Wall friction is determined from the effective viscosity, which is calculated by multiplying the liquid viscosity with a factor that considers the gas fraction (for small gas fractions it equals the liquid viscosity). Slip and, if considered, phase transition are introduced by empirical correlations that are functions of gas fraction and flow regime. The drift-flux model has fewer equations and is more approximate than the two-fluid model.

For bubble flows two fluid model and drift-flux model are mostly equivalent (Sokolichin et al., 2004).

In two-phase calculations two simplifying assumptions are quite common: Isothermal flow and constant gas fraction. Both assumptions do not apply for flow in a geothermal well, due to significant heat loss to

the formation (see 1.2) and large pressure differences between bottomhole and wellhead. Hence, energy balances and gas fraction have to be calculated.

The homogenous model, which is used in this work, is the most simplified representation of a two-phase flow. The homogenous model treats the flow like a single-phase flow with an effective/common density, enthalpy and velocity, thus neglecting slip. Hence, the closer the two-phase fluid is to a single-phase fluid, i.e. the smaller the differences of density and velocity of the phases are, the closer is the homogenous model to reality. That means it is applicable for flows where the phases are well dispersed in each other and therefore have a large interface surface and low slip, such as bubbly flow with small bubbles (Kraume, 2003).

2.2 Gas/oil wells

A scientific and economic field with many common problems to geothermal production is the production of oil and/or gas. The basic difference between the two fields lies in the products. While geothermal wells are drilled in order to extract heat with the actual brine being a mere by-product, in oil/gas wells the produced substance itself is the desired valuable resource. The high and ever rising oil price makes smaller lower flow rates as well as high investments of effort and energy acceptable. That implies that smaller wellbore diameters are sufficient and expensive techniques can be applied. One example of such a technique is the injection of water/steam or gas with the purpose of improving oil recovery.

Producing multi-phase flow is rather common in oil/gas production, because the oil reservoir contains also gas and water, which are either naturally present or have been injected. When steam is injected thermal losses to the formation become relevant and need to be estimated. However, the heat input to the formation is significantly lower than in geothermal wells due to the low flow rates and lower heat capacity. This may be a reason why the formation temperature is assumed constant by the commercial simulators listed below.

In calculations the complex fluid in gas/oil wells is either represented by compositional models or by the so-called black-oil approach. Compositional models treat the fluid as a mixture of individual components considering their respective properties. The black oil approach instead assumes a homogeneous two-phase fluid with common properties, the term 'black oil' hinting at a black box which disregards any component specific processes.

2.3 Wellbore models

The wellbore is the interface between reservoir, formation and power plant above ground. As such it is often strongly simplified and regarded as a constant boundary for the adjacent modeling domains, the reservoir and the power cycle. Nevertheless, advanced hydraulic and thermal wellbore models do exist. Their features and shortcomings will be sketched in the following paragraphs.

If geothermal wells can be operated at high flow-rates, in practice, usually no special interest is paid to the transient warm-up/cool-down phase described in section 1.2. The transient phase is considered just part of the start-up phase and virtually stationary conditions with a small overall temperature loss are expected to be reached very soon. In view of general exploration uncertainties the transient phase and the small residual temperature loss become insignificant, which brings the focus of geothermal wellbore simulations to hydraulics.

A common and obvious approximation for geothermal wells is the use of pure water property functions, which is not appropriate for highly saline brines and ignores the potential gas fraction. Two-phase models are limited to constant gas fractions or single substance flash calculations.

Pioneering work has been done by Ingersoll and Plass (1948) when they developed the analytical infinite line source model for heat pump systems and later the infinite cylindrical source based on the work of

Carslaw (1948)⁶. Ramey (1962) adopted the line source model for heat transmission in steam injecting wells. Willhite (1967) contributed with his work about wellbore heat transfer coefficients including free convection in the open annulus. Claesson and Eskilson (1988) integrated Carslaw's solution for point heat sources to obtain an equation for the finite line source. To date these analytical solutions are in use because their implementation is relatively easy and their solution is fast. However, they obviously have their limitations. They apply only to vertically uniform well layouts with constant parameters such as mass/heat flow or thermal properties of formation and brine. Furthermore, they are only valid after an initial phase when flow and heat transfer are quasistatic.

The increase of available computing power gave rise to the application of more detailed numerical models. Guðmundsdóttir (2012) gives a good overview of the history of geothermal wellbore models in the last millenium. Most wellbore models are limited to stationary hydraulic calculations, many considering two-phase flow using pressure drop correlations. As early as in 1980 the Lawrence Berkeley Laboratory presented the software WELBORE, a transient two-phase wellbore simulator that included formation heat loss and was coupled to a reservoir model (Miller, 1980). In 1991 they presented HOLA and its derivatives (Aunzo et al., 1991) that allowed for two-phase flow, multiple feed zones, CO₂ content and salinity. HOLA has been in use until recently (Bhat et al., 2005), (Elmi and Axelsson, 2009), (Ayala, 2010)

Later Hasan and Kabir developed a two-phase simulator for geothermal wells and compared calculation results to field data. Their model considers slip flow, flow regime and natural convection in the annulus. As in HOLA, heat loss to the formation is calculated using an analytical approach. (Hasan and Kabir, 1994), (Hasan and Kabir, 2010).

Several authors have studied the coupling of wellbore and reservoir (Bhat et al., 2005), (Guðmundsdóttir, 2012). Targeting oil/gas wells, coupled models are combined with multi-phase flow and compositional fluid models (Pourafshary et al., 2009) and allow stationary heat loss and branching wells (Livescu et al., 2010).

A wellbore model featuring a numeric solution of the formation heat flow was recently proposed by (Saeid et al., 2013). They present an integrated FEM⁷ model of a geothermal doublet, formation and reservoir, where two 1D wellbore models are embedded in a 2D model of formation and reservoir. One-phase brine density and viscosity are calculated temperature dependent with a simple exponential equation. Solution of their model is fast, so that a good performance can be expected also in a more realistic 3D model.

2.4 Commercial two-phase flow / wellbore simulators

Some wellbore models have evolved into commercial products that are advertised for professional use. They are based on steady-state hydraulic models, which basically calculate static head and friction pressure drop on the discretized well.

WELLSIM⁸ and SwelFlo⁹ are hydraulic geothermal wellbore simulator featuring two-phase flow with CO₂ content and multiple feedpoints. WELLSIM also supports NaCl brines.

⁶ This solution is used for validation and given in D 4.

⁷ Finite Element Method

⁸ <http://www.gradientgeodata.com/wellsim> [30 Nov 2013].

Various commercial solutions for simulations related to gas/oil production exist. As mentioned above, they have to consider water; hence they may also be applicable to geothermal wells.

OLGA¹⁰ is a multiphase flow simulator claiming to be ‘market standard’; its feature list does not mention any heat transfer modelling. Originating from the aerospace industry, SINDA/FLUINT¹¹ is capable of simulating transient two-phase flows with phase transition and heat transfer. It features a chemical reaction module that allows evaporation/condensation, gas solution and non-equilibrium states.

Specialized on simulation of well hydraulics are programs like TWBS¹² and the software packages offered by FEKETE¹³. TWBS features a compositional fluid model for mixed flow of oil, water, gas and steam, while in FEKETE’s FAST Piper oil and water are combined to form a pseudo liquid phase.

Last, not least, PipeSim¹⁴ is a widely used steady-state multiphase flow simulation that also includes heat transfer calculation and gives the user the choice between the black-oil approach and compositional models.

A lot of research and development has been done in the field of wellbore modelling. However, these models are usually developed for the application to specific sites. None of the wellbore/pipe models known to the author, academic or commercial, offers a compositional two-phase brine model and a rigorous transient formation heat flow model, both of which are expected to be essential to reproduce the processes in the GrSk site. This was the motivation for the development of a comprehensive wellbore model offering these features, which has been published previously (Francke et al., 2013). This thesis presents the model it with improvements, extension and further application.

⁹ <http://swelflo.com> [30 Nov 2013].

¹⁰ <http://software.slb.com/OLGA> [30 Nov 2013].

¹¹ <http://www.crtech.com/sinda.html> [30 Nov 2013].

¹² <http://www.petrostudies.com/twbs.htm> [30 Nov 2013].

¹³ <http://fekete.com> [30 Nov 2013].

¹⁴ <http://www.software.slb.com/products/foundation/pages/pipesim.aspx> [30 Nov 2013].

3 Fundamentals

Modelling a geothermal brine circuit touches various areas of process engineering, such as thermodynamics, chemistry, fluid mechanics, as well as geology. This chapter is dedicated to explaining some of the physics used in the brine circuit model described in detail in chapter 5, namely considerations about the two-phase pipe flow and the balance equations describing it (3.1), the vapour-liquid equilibrium in the two-phase fluid (3.2) and the heat flow (3.3).

The general processes during brine production have been described in section 1.2. Two phases of the flow in the well, namely the liquid brine as well as degassed and evaporated components in the gas phase, are considered in this work.

This work aims at reproducing mid-term (a few days) to long-term (plant operation time – a few decades) hydraulic and thermal behaviour of the geothermal brine circuit. Hence, dynamic hydraulic effects are not discussed and considered.

3.1 Pipe flow – conservation laws

The homogenous model is adopted to describe the two-phase flow in the wellbore. Assuming one-dimensional, quasistatic and homogenous two-phase flow, the flow through a pipe can be described with the following balances of mass, momentum and energy. The assumption of homogenous flow implies that a uniform velocity, pressure and enthalpy are assumed for both phases on a cross-section.

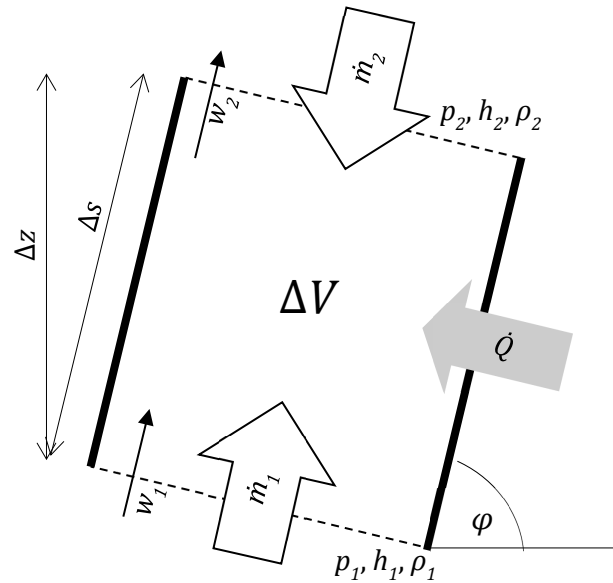


Fig. 4: balance volume (production well), homogenous flow

3.1.1 Homogenous model for two-phase flow

The effective density is the average of the densities of the two phases weighted by their volume fraction:

$$\rho = \frac{m}{V} = \frac{\rho' \cdot v' + \rho'' \cdot v''}{V} = \varepsilon \cdot \rho'' + (1 - \varepsilon) \cdot \rho' \quad (3.1)$$

Alternatively, density can be expressed directly as a function of the gas mass fraction:

$$\frac{1}{\rho} = v = (1 - x)v' + xv'' = \frac{1 - x}{\rho'} + \frac{x}{\rho''} \quad (3.2)$$

The friction pressure loss is usually calculated based on the pressure loss of the liquid phase, which is multiplied with the two-phase multiplier, taking into account the gas fraction.

The assumption of homogenous flow neglects the hydraulic and thermal effects of slip: Slip increases the static pressure head by reducing the cross section occupied by the gas flow and thus increasing the

weight of the fluid column. Besides, heat from the inner friction of the fluid (between the phases) increases the fluid enthalpy. Slip increases with gas volume fraction. So does the error induced by neglecting slip.

3.1.2 Mass balance

The stationary mass balance of pipe flow simply states that what enters ΔV on one end, leaves it on the other end:

$$0 = \dot{m}_1 + \dot{m}_2 \quad (3.3)$$

By convention, a mass flow entering the volume ΔV is positive, so that the mass flow at inlet 1 \dot{m}_1 equals \dot{m}_2 , the negative mass flow at outlet 2.

3.1.3 Energy balance

The total energy of the fluid in a well element is affected by the convective flow inward and outward, by conductive flow through the flow boundary (wall), by the heat that is generated by friction and by the change of elevation.

Based on the first law of thermodynamics for open systems (Baehr, 2003) and the mass balance eq. 3.3 the energy balance of a stationary pipe flow can be written as:

$$\dot{Q} + P = \dot{m} \left(h_2 - h_1 + g(z_2 - z_1) + \frac{w_2^2 - w_1^2}{2} \right) \quad (3.4)$$

No energy is transferred by performing mechanical work. Heat flow¹⁵ is only considered between the wall and the fluid. The change of elevation is determined by the length Δs and the inclination φ of the pipe element. At low speeds, as they can be expected in a well, the kinetic part is small compared to the other two. Hence, the energy balance is reduced to:

$$\frac{1}{\dot{m}} \int_{\partial V} \dot{q} dA = h_2 - h_1 + \Delta s g \sin \varphi . \quad (3.5)$$

The heat flow depends on the temperature difference between fluid and formation and the thermal properties of the boundary layer, the well completion and the formation. The details of heat flow calculation are explained later in the section 3.3.

Eq. 3.5 shows the balance of conductive and convective heat transfer. Without convection, conduction cannot be compensated and leads to non-stationary temperature change, i.e. for $\dot{m} = 0$ the stationary energy balance is not solvable. That is why idle wells cannot be described with this quasistatic equation. Zero-mass flow must be prevented or be treated with a different equation, which will be introduced in the model description in 5.4.2.

3.1.4 Momentum balance

The momentum balance for static pipe flow has been derived in B 1 as:

$$\frac{\partial p}{\partial s} = -\rho g \sin \varphi - f \frac{w^2 \rho}{2d} - \frac{\partial}{\partial s} \rho w^2 . \quad (3.6)$$

¹⁵ Convention for fluid energy balance: Positive heat flux flows from wall to fluid.

f is the friction factor as introduced in 2.1.2.

As eq. 3.6 shows, the pressure head is composed of the hydrostatic head, the friction head and the kinetic head. The latter is connected to the acceleration of the fluid. Acceleration occurs in stationary flow with constant pipe diameter when the volume flow rate increases because of a growing gas fraction. The effect of gravity on the flow depends on the density of the fluid in the pipe, which is reduced by the gas fraction ϵ .

3.2 Phase transitions in the two-phase fluid

The behaviour of two-phase flow depends on the volume fraction of the gas phase. As already stated before in 2.1, in a geothermal well with its large pressure range the volume fraction cannot be assumed to be constant and must hence be determined.

This section provides considerations about the conditions under which two phases can coexist, the processes that are involved and laws that can be used to determine the gas fraction.

3.2.1 Vapour-liquid equilibrium and two-phase state condition

The following considerations are limited to the equilibrium state and ideal gases. The assumption of a thermodynamic equilibrium between the liquid phase and the gas phase is appropriate for the flow in a geothermal well (Hasan and Kabir, 2010)

The gas phase forms from the liquid phase by degassing of the dissolved gases and evaporation of water. Vice versa, mass is transferred from the gas phase to the liquid phase by dissolution of gases and condensation of water (see Fig. 5).

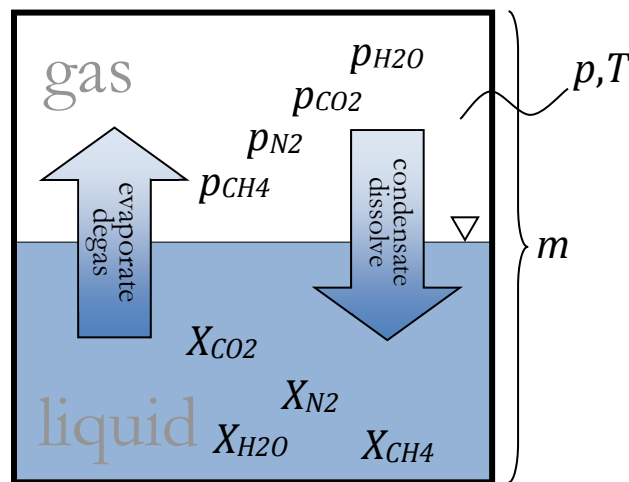


Fig. 5: Vapour-liquid equilibrium in a closed system for 3 gases + water

Thermodynamic equilibrium applied to a two-phase system means that both phases are in thermal, mechanical and chemical equilibrium. That implies that they have the same pressure, the same temperature and that mass transfer in both directions is equal. Evaporation and degassing depend on temperature and concentration of the species in the liquid phase, while condensation and dissolution depend on the partial pressures in the gas phase. Hence, the mass distribution between both phases depends on pressure, temperature and total composition of the fluid.

In equilibrium, the gas phase can only exist in a certain range of pressure and temperature: On one end of the range, if pressure is too high at a given temperature bubbles cannot form. On the other end, if pressure is too low or temperature is too high the water evaporates completely and there is no liquid phase.

Bubbles can only form if the pressure in the potential gas phase exceeds the sum of absolute pressure in the liquid plus the pressure generated by surface tension in the initial bubble (Baehr and Stephan, 2004). According to Dalton's law for ideal gases, the absolute pressure is the sum of the partial pressures of the gas mixture components. Hence, the pressure in the gas phase depends on the water vapour pressure and the degassing pressure of the dissolved gases. The degassing pressure is the partial pressure of a gas in equilibrium with its content in the liquid phase. Both, water vapour pressure and the degassing pressure, are influenced by the salinity of the liquid phase. The surface tension depends on the bubble radius. The presence of nucleation seeds increases the initial bubble size and hence reduces the initial surface tension. In a geothermal well, floating particles, such as precipitation products and fines from the reservoir as well as the rough, corroded wall surface act as nucleation seeds. Hence, in this work, bubble formation is assumed not to be delayed by surface tension and surface tension is not considered in the following determination of the vapour-liquid-equilibrium.

When the bubble grows, degassing and evaporation reduce the concentration of dissolved gas in the liquid, until mass transfer in both directions is in equilibrium. The associated water evaporation increases the salinity of the liquid phase. The kinetics of this degassing process is limited by the phase interface area that is available for gas exchange. Due to the large surface area created by gas bubbles no limitation is assumed and instantaneous vapour-liquid equilibrium is assumed instead.

3.2.2 Degrees of freedom

The thermodynamic state of a single-component medium is generally defined by two independent state variables, e.g., pressure and temperature. In the two-phase region, however, there is only one independent variable, as pressure equals the medium's saturation pressure which depends is determined by temperature. Having a second component in the medium adds two unknowns, one for the composition of every phase, but also one equation for the saturation pressure of the second component. Hence, the binary two-phase state has two degrees of freedom. Every additional component adds one degree of freedom.

This relation is expressed in Gibbs' phase rule. It provides the number of degrees of freedom F of a system in thermodynamic equilibrium with a given number of phases P and a given number of components C (Smith et al., 2001):

$$F = C - P + 2 . \quad (3.7)$$

Accordingly, a two-phase system in equilibrium has as many degrees of freedom as it has components:

$$F = C . \quad (3.8)$$

The two-phase state of a pure medium is hence defined by one variable, e.g., T . System pressure is the medium's saturation pressure which depends on the temperature. Every additional component adds one variable for its mass fraction in one phase. The composition of the other phase is connected via C component specific equations, which are usually based on the equilibrium of the chemical potential:

$$\mu'_\alpha = \mu''_\alpha . \quad (3.9)$$

Gibbs' phase rule applies to open systems and therefore makes no statement about the distribution of mass between the two phases. In a closed two-phase system in equilibrium this adds two or P additional variables, one for the mass in each phase. At the same time, the mass conservation in the closed system, evaluated component-wise, provides C new equations. Adding this to eq. 3.7 brings the number of degrees of freedom to 2, no matter how many components are in the system:

$$F = C - P + 2 + P - C = 2 . \quad (3.10)$$

This is Duhem's theorem, which states that for a closed system with known masses of prescribed species the equilibrium state is determined by two independent variables, irrespective of the number of phases and components (Smith et al., 2001).

3.2.3 Choice of state variables

State variables are thermodynamic quantities such as pressure p , temperature T , density ρ , specific enthalpy h , specific entropy s or specific internal energy u .

If a thermodynamic state is defined by F independent state variables, other variables can be calculated using equations of state or property functions. If the available property functions require other state variables as arguments than the ones already known, these have to be calculated first.

In idealized processes usually one state variable is constant. For example, an isothermal compression where pressures are known is best described by p and T with $T = \text{const}$. Hence, depending on the application, the described processes and the available property functions, some combinations of state variables are more convenient than others.

T and ρ is the combination that is used by the property functions, which derive all properties from one fundamental equation, the Helmholtz energy equation of state. It is used for example in REFPROP (Lemmon et al., 2010), a software package that calculates a multitude of thermodynamic properties for various pure substances and mixtures. States given with variables other than T and ρ usually have to be calculated by iteration. Water is an exception: The IAPWS-IF97 steam tables (Wagner et al., 2000) define ancillary equations that allow the calculation for many combinations of state variables without iteration.

The brine circuit model uses one medium: the geofluid, a mixture medium based on water. Its special property functions such as gas solubility or the salinity influence on density, viscosity and enthalpy are only available for p and T .

Furthermore, p and T is an obvious choice of state variables, because both variables can be measured and they are more descriptive than ρ , h , s or u . However, p and T cannot be used to specify the state for one-component fluids in the two-phase region, as they are not independent there, but two independent variables are required according to Duhem's theorem.

The combination of p and h is more convenient for process calculations, because energy transfer and pressure change can be expressed directly in terms of enthalpy change and pressure change. Also, p and h define two-phase states unequivocally (Baehr, 1998). Therefore, p and h are used here in the brine-circuit model for passing thermodynamic states from one component to the next¹⁶ and also within the wellbore model. Property functions based on p, T are used. T is determined by inverting $h(p, T)$.

3.2.4 Raoult's Law (ideal)

Raoult's law for vapour-liquid-equilibria (derived in B 2) describes the relation between molar fraction y_α' of a species α in the liquid phase, its saturation pressure p_α and its molar fraction y_α'' in the gas phase:

$$y_\alpha' p_\alpha(T) = y_\alpha'' p. \quad (3.11)$$

¹⁶ using the fluid ports defined in *Modelica.Fluid.Interfaces.FluidPort* in the MSL 3.2.

The right side is commonly referred to as the partial pressure of the gas. The left side is called herein degassing pressure. The degassing pressure of a gas in solution at a given concentration and temperature is its partial pressure in the gas phase in equilibrium, i.e. the partial pressure needed to maintain that concentration. The term describes the tendency of the gas to leave the liquid phase.

Raoult's law assumes ideal gas behaviour, which limits its applicability to low/moderate pressures. In an ideal solution eq. 3.11 is valid for all species independent from the concentration of the other species. However, assuming an ideal solution implies that the concerned components are chemically similar. The presence of saturation pressure implies that the law is only applicable in sub-critical conditions (Smith et al., 2001).

3.2.5 Modified Raoult's Law (non-ideal)

In order to account for non-ideal behaviour of gas phase and mixture due to high pressures or chemical reactive constituents, two coefficients are introduced in eq. 3.11, the activity coefficient γ and the fugacity coefficient ϕ :

$$\gamma(p, T, X') y'_\alpha p_\alpha(T) = \phi(p, T, X'') y''_\alpha p . \quad (3.12)$$

This is the fundamental equation for the calculation of the vapour-liquid equilibrium, which will be explained in detail later in the model description (5.2.2).

3.2.6 Water vapour pressure in a saline solution

Water vapour pressure is reduced by salt content. Raoult's law states that the vapour pressure of a component in an ideal solution is proportional to its liquid mole fraction. Dissolved salts split up into anions and cations, which are counted separately for the mole fraction. Hence, the water vapour pressure reduced by salt content is calculated as follows:

$$p_{H_2O}^{sat}(T, X') = y'_{H_2O} p_{H_2O}^{sat,0}(T) = \frac{n_{H_2O}}{\sum Z_\alpha n_\alpha} p_{H_2O}^{sat,0}(T). \quad (3.13)$$

Z_α is the number of ions per molecule of component α . For example, applied to a solution of NaCl, KCl and CaCl₂ eq. 3.13 becomes:

$$p_{H_2O}^{sat} = p_{H_2O}^{sat,0}(T) \frac{X_{H_2O}}{M_{H_2O}} / \left(\frac{X_{H_2O}}{M_{H_2O}} + 2 \frac{X_{NaCl}}{M_{NaCl}} + 2 \frac{X_{KCl}}{M_{KCl}} + 3 \frac{X_{CaCl_2}}{M_{CaCl_2}} \right). \quad (3.14)$$

3.2.7 Henry's law

Replacing saturation pressure in eq. 3.11 by the Henry coefficient \tilde{k} (dimension of pressure) yields a formulation of Henry's law, which is a simplified model of gas dissolution:

$$y'_\alpha \tilde{k}_\alpha = y''_\alpha p . \quad (3.15)$$

In analogy to Raoult's law, Henry's law links partial pressure of a gas in the gas phase to the concentration of the dissolved gas in the liquid phase. It is valid for partial pressures low enough to assume ideal gas (below 0.1 MPa). It also assumes ideal mixture and low solubility (Naumann, 2000). There is no limitation regarding the critical pressure / temperature of the gas.

A more common form, with the linear factor k representing the solubility instead of the volatility \tilde{k} is:

$$c_{\alpha} = k_{\alpha} \gamma_{\alpha}'' p, \quad (3.16)$$

with c_i denoting the gas concentration in the liquid phase in mol per litre water and k commonly given in mol/(l·atm)¹⁷.

A modified version of Henry's law accounts for non-ideal behaviour by multiplying with the fugacity coefficient ϕ :

$$c_{\alpha} = \phi k_{\alpha} \gamma_{\alpha}'' p \quad (3.17)$$

If temperature dependence of k_{α} is not neglected it can be expressed by

$$k_{\alpha}(T) = k_{\alpha}(T_{\text{ref}}) \cdot \exp\left(C(T^{-1} - T_{\text{ref}}^{-1})\right). \quad (3.18)$$

Values for $k_{\alpha}(T_{\text{ref}})$ and C can be found in the literature (Sander, 1999).

Further modified equations for the Henry coefficient consider the pressure dependence, which extends their validity to higher pressures.

3.2.8 Gas solubility

Gas solubility is the quantity of gas dissolved in a certain volume of solvent in equilibrium. In the literature it is given as molar concentration (mol per litre), as molality (mol per kilogram solvent), in norm litre of gas dissolved per kg solvent or in mass fractions. Solubility depends on the composition of the solute and the solvent, temperature and pressure.

Following Le Chatelier's principle, gas solubility increases with pressure. Generally, it decreases with increasing temperature until it reaches a minimum and increases again. Dissolved salts reduce the solubility by reducing the amount of water available for gas solution. Carbon dioxide dissolves much better in water than methane and nitrogen, which has the lowest solubility out of those three gases (Naumann, 2000). Salinity can, however, invert that behaviour as can be seen in Fig. 6 for nitrogen in a 4-molar NaCl solution according to (Mao and Duan, 2006).

¹⁷ Standard atmosphere, 1 atm = 101325 Pa. (deprecated pressure unit)

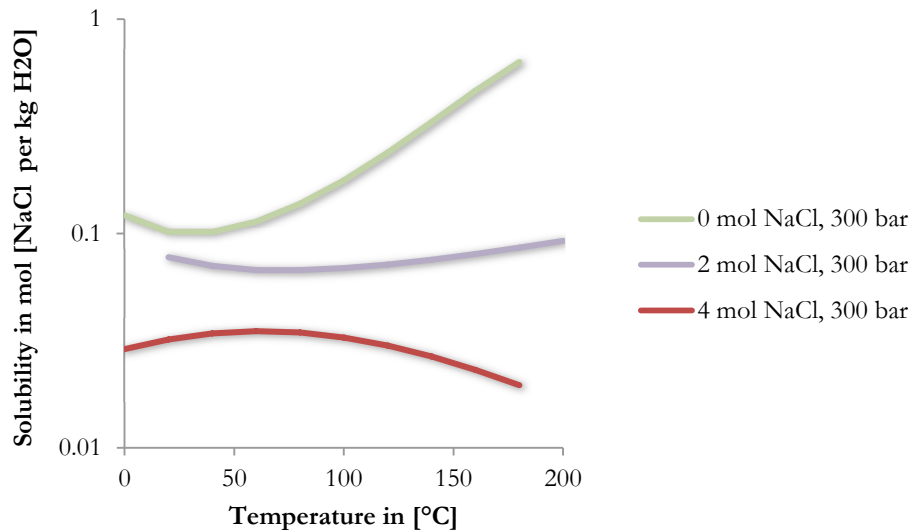


Fig. 6: Nitrogen solubility in different NaCl solutions as provided by Mao and Duan (2006)

As described above, Henry coefficients, constant or temperature dependent, are often used to describe gas solubility as a linear function of pressure. The research group around Zhenhao Duan has provided alternative equations for gas solubilities in aqueous chloride solutions (CO_2 : Duan et al., 2006; N_2 : Mao and Duan, 2006; CH_4 : Duan and Mao, 2006). They will be used to determine the vapour-liquid equilibrium (VLE) in the two-phase flow. The VLE calculation will be explained in detail later in 5.2.2.

3.3 Heat flow

Rigorous heat-transfer computation with non-constant value for heat transfer coefficient along with proper pressure drop estimation is essential for modelling geothermal wells (Hasan and Kabir, 2010).

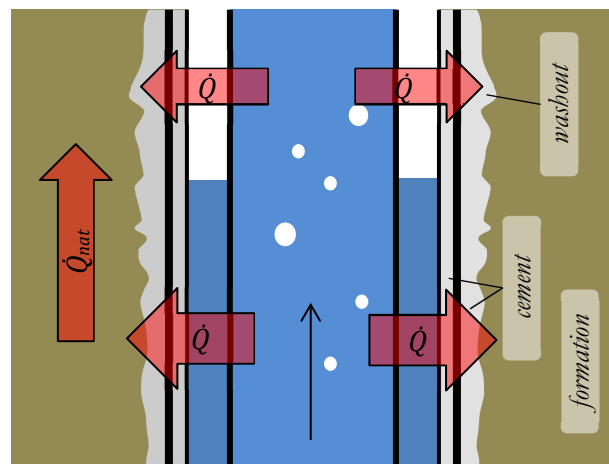


Fig. 7: well heat flow (above pump) superposes natural heat flow

As described in 1.2, in the production well, hot brine moves upward where the formation is colder than the fluid. Due to temperature difference heat flows from the flowing fluid to the wall of the inner pipe, through the pipe wall, then to and through the surrounding cement layer or the open annulus, to and through the surrounding layers of steel and cement (if present) and finally to and within the formation (see Fig. 7). The volume between the outer layer of steel and formation is increased by washout, which is explained in 5.4.7. Above the production pump the configuration is a little different. There the pipe is surrounded by a layer of liquid or gas. This annulus fluid can move freely so that additional heat transfer by free convection must be taken into account.

This heat loss of the fluid on its way from the reservoir to the wellhead directly affects the key parameter wellhead temperature.

After the heat extraction above ground the fluid in the upper part of the injection well is usually still warmer than the surrounding formation. Hence, it is cooled down further until it eventually reaches a depth where the formation temperature surpasses fluid temperature. Below that depth the heat flow is reversed and the fluid is warmed up.

This artificial heat flow between well and formation superposes the natural heat flow that results from the vertical temperature gradient. Conductive heat flow is described using Fourier's law by

$$\rho c \frac{\partial T}{\partial t} = -\nabla \cdot \dot{q} = \nabla \cdot \lambda \nabla T , \quad (3.19)$$

where ρ , c , λ are the density, heat capacity and thermal conductivity of the medium, \dot{q} is the heat flux and ∇ is the Nabla operator used for gradient and divergence (Baehr and Stephan, 2004). Unless the heat flow is stationary, i.e. eq. 3.35 equals zero, temperature changes. The natural heat flow is usually stationary and the vertical component of the artificial heat flow is expected to be very small compared to the radial component. Both assumptions will be verified for the simulated case later in 7.2.4. Hence, in the following considerations only radial heat flow is considered. Furthermore, considering the well radially symmetric and the formation horizontally homogenous reduces the three-dimensional heat conduction to a one-dimensional problem.

The radial heat flow changes the temperature of the well bore parts as well as of the formation. Due to their different heat capacities this happens in different time scales (Ramey, 1962). While the well completion quickly reaches steady state, the formation in the proximity of the production well is warmed up gradually over the years of production. Theoretically, in a radially infinite formation thermal steady state is never reached, as the temperature front continues to propagate. Hence, in this work heat flow within the well completion is modelled as steady-state, whereas the thermal formation model must be transient to reproduce the long-term behaviour.

The flow in the wellbore is usually considered as vertical pipe flow, which makes it a one-dimensional problem. Another common simplification for formation heat flow calculation is the assumption of radial symmetry, of the geometry as well as of the heat flow. This reduces the three-dimensional formation to a two-dimensional domain. If furthermore vertical heat flow in the formation is neglected, the formation heat flow can be described by a series of one-dimensional heat flow equations.

Hence, after these simplifications the wellbore heat flow problem presents itself as a combination of two phenomena: static heat flow in multi-layered cylinders, including the fluid-wall transition and the open annulus, as well as transient one-dimensional heat flow on a radially symmetric, horizontal domain. The equations that describe these phenomena are given below.

3.3.1 Heat transfer from fluid to wall

The heat flux \dot{q} ¹⁸ from fluid to the pipe wall is proportional to the temperature difference between fluid and wall:

$$\dot{q} = -htc_{fw}(T_{wall} - T_{fluid}) \quad (3.20)$$

¹⁸ Convention for heat flow in well completion: positive heat flux flows radially outward.

The proportionality factor htc_{fw} is called heat transfer coefficient and it describes the heat transfer properties of the boundary layer. It depends on the fluid properties and the state of the flow, i.e. if it is laminar or turbulent and if it is hydrodynamically and thermally developed. In turbulent flow more heat is transported than in laminar flow due to the lateral movement of the particles. The flow is considered hydrodynamically developed after a given length of the flow path s . Turbulent flow is fully developed after $s = (10 \dots 60) \cdot d_{hyd}$ (Baehr and Stephan, 2004). This being rather short compared to the length of the well section, fully developed flow can be assumed if the applied equation does not include the developing flow anyway.

The heat transfer from fluid to wall is commonly expressed with the dimensionless Nusselt number, defined as (Gnielinski, 2010):

$$Nu = \frac{htc_{fw} \cdot d_{hyd}}{\lambda} \quad (3.21)$$

Nusselt number correlations can be found in the literature for various flow configurations.

3.3.2 Static cylindrical heat transfer

Steady state radial heat conduction in the thin wall of a long cylinder with constant thermal conductivity λ can be calculated as (Çengel, 2002):

$$\dot{Q} = -2\pi\Delta s \frac{\lambda}{\ln(R/r)} (T(R) - T(r)) \quad (3.22)$$

with Δs being length of cylinder and r, R being the inner, outer radius of cylinder, $T(r), T(R)$ are the temperatures inside, outside the cylinder. Positive heat flow is directed outward.

Division by a lateral surface at a reference radius and, in analogy to eq. 3.20, introducing the thermal transmittance U gives an expression for the heat flux on the reference surface:

$$\dot{q}_{ref} = \frac{\dot{Q}}{2\pi\Delta s r_{ref}} = \frac{-\lambda}{\ln(R/r) \cdot r_{ref}} \Delta T = -U^{ref} \cdot \Delta T \quad (3.23)$$

Δs is the length of the cylinder, A_{ref} is the inner lateral surface. U^{ref} is the cylindrical heat transfer coefficient with respect to the reference surface A_{ref} at the radius r_{ref} .

3.3.3 Heat transfer in multi-layered cylinders

If two of the cylinders are arranged concentrically, the steady heat flow is the same in both cylinders. The temperature difference over both shells is the sum of the respective temperature differences (eq. 3.23):

$$\Delta T_{tot} = \Delta T_1 + \Delta T_2 = \frac{-\dot{Q}}{U_1 \cdot A_1} + \frac{-\dot{Q}}{U_2 \cdot A_2} = \frac{-\dot{Q}}{U_{tot}^{ref} \cdot A_{ref}} = \frac{-\dot{q}_{ref}}{U_{tot}^{ref}} \quad (3.24)$$

In analogy to a single cylinder, the total temperature difference can be calculated by dividing the heat flow density on a reference surface by a combined heat transfer coefficient (with respect to that surface). The latter describes the thermal properties of the combination of the two cylinders.

Eq. 3.24 shows that steady state heat conduction in a cylinder composed of several layers with different (constant) thermal properties can be treated as thermal resistances in series, by analogy to electrical resistors, the thermal resistance being the reciprocal product of area and heat transfer coefficient (Çengel, 2002: 149):

$$\dot{q}_{ref} = -U_{tot}^{ref} \cdot \Delta T = -\left(\sum \frac{1}{U_j^{ref}}\right)^{-1} \cdot \Delta T \quad (3.25)$$

The total thermal resistance $\psi_{tot}^{ref^{-1}}$ is then calculated as:

$$\frac{1}{U_{\text{tot}}^{\text{ref}}} = \sum \frac{1}{U_j^{\text{ref}}} = \sum \frac{\ln(r_{j+1}/r_j) r_{\text{ref}}}{\lambda_j} . \quad (3.26)$$

Small thermal resistances have little effect on the overall heat transfer. Hence, very large heat transfer coefficients contribute only little to the sum by reciprocal addition, thus having little effect.

3.3.4 Heat flow in washout

The borehole diameters d_{if} are actually larger than the indicated drill diameters d_{drill} due to washout, irregular cavities washed out by the circulating drilling fluid or formed by falling loose rock (depicted in Fig. 13). The washout increases the volume of the annulus between casing and formation, which is later filled by cement. In other words, rock is replaced by cement with different thermal properties (compare rock properties in Table 1 with cement properties in 4.4.1), which can significantly change the heat flow between well and formation (see 8).

The washout is calculated from calliper measurements that have been conducted in the borehole after drilling. They are essential for the estimation of the amount of cement that will be necessary to fill the borehole around the casing. The washout is usually specified as the relative volume difference¹⁹ between the actual borehole volume V_{cal} and the drilled volume V_{drill} :

$$W = \frac{V_{\text{cal}} - V_{\text{drill}}}{V_{\text{drill}}} = \frac{\overline{d_{\text{cal}}^2} - d_{\text{drill}}^2}{d_{\text{drill}}^2} - 1 . \quad (3.27)$$

3.3.5 Heat flow in open annulus

The open annulus is the annular volume surrounding the production string (see Fig. 2). Pressure at the pump inlet fills it to a certain level with brine. The volume above that level is filled with pressurized nitrogen mixed with degassed brine gas. Heat transfer through the open annulus around the production string is strongly influenced by the level of the annulus liquid, because heat conduction is much higher in liquid brine than in gas. Furthermore, heat transfer in fluids can be substantially increased by free convection and radiation.

Heat is transported in the open annulus radially by radiation and free convection from the outer surface of the production string to the inner surface of the casing through the annulus fluid. The convection is driven by the density gradient due to the temperature gradient (Willhite, 1967). Willhite also mentions heat transport by conduction, but according to Çengel (2002: 30) in a moving fluid conduction is included in convection. Hence, herein it is not considered separately.

$$\dot{q}_{\text{ann}} = \dot{q}_{\text{rad}} + \dot{q}_{\text{cnv}} = -(h_{\text{tcrad}} + h_{\text{tccnv}})(T(R) - T(r)) . \quad (3.28)$$

Radiation

The heat flow by radiation can be estimated using the Stefan–Boltzmann law (Çengel, 2002):

$$\dot{Q}_{\text{rad}} = -\sigma \Delta s 2\pi r \varepsilon (T(R)^4 - T(r)^4) . \quad (3.29)$$

¹⁹ The relative increase of annulus volume, i.e. of cement volume, W_{ann} is greater and may become considerably greater than the increase of borehole volume W :

$$W_{\text{ann}} = \frac{(V_{\text{cal}} - V_{\text{cas}}) - (V_{\text{drill}} - V_{\text{cas}})}{V_{\text{drill}} - V_{\text{cas}}} = \frac{\overline{d_{\text{cal}}^2} - d_{\text{drill}}^2}{d_{\text{drill}}^2 - d_{\text{cas}}^2} = \frac{W}{1 - \frac{V_{\text{cas}}}{V_{\text{drill}}}}$$

where the Stefan-Boltzmann constant is $\sigma = 5.67 \cdot 10^{-8} \text{ W}/(\text{m}^2 \cdot \text{K}^4)$, r is the radius of the inner surface and emissivity ε is assumed to be equal for both surfaces.

Written with the radiative heat transfer coefficient $htc_{\text{rad}}^{\text{ref}}$ similar to Willhite (1967) the radial heat flux is (with respect to the reference surface at the radius r_{ref}):

$$\dot{q}_{\text{rad}}^{\text{ref}} = \sigma \varepsilon \frac{r}{r_{\text{ref}}} (T_o^2 + T_i^2)(T_o + T_i) \cdot (T_o - T_i) = htc_{\text{rad}}^{\text{ref}}(T_o - T_i) . \quad (3.30)$$

Free convection

The heat transfer by free convection can be estimated with an equation given by Willhite (1967). Adapted to temperatures in Kelvin instead of Fahrenheit it is:

$$\frac{\lambda_{\text{cnv}}}{\lambda} = 0.0596(GrPr)^{0.333} Pr^{0.074} , \quad (3.31)$$

λ is the thermal conductivity of the annular fluid, while λ_{cnv} is the effective one, increased by convection. The Grashof number and the Prandtl number are defined as:

$$Gr = (R_o - R_i)^3 g \beta |T_i - T_o| / \nu^2 \quad \text{and} \quad (3.32)$$

$$Pr = \frac{c_p \eta}{\lambda} , \quad (3.33)$$

where $R_{i/o}$ and $T_{i/o}$ are the inner/outer radius and inner/outer temperature of the annulus and ρ , η and c_p are the density, dynamic viscosity and specific heat capacity of the fluid.

β is the isobaric thermal expansion coefficient, defined as:

$$\beta = \frac{1}{v} \left. \frac{\partial v}{\partial T} \right|_p . \quad (3.34)$$

The resulting heat transfer coefficient of the annulus is calculated with eq. 3.22 using λ_{cnv} .

3.3.6 Transient cylindrical heat transfer

Heat transfer in the formation surrounding the wellbore is not assumed to be stationary. Hence eq. 3.23 cannot be applied. One-dimensional transient radial heat conduction without heat generation is described by a partial differential equation (Çengel, 2002: 71):

$$\rho c \frac{\partial T}{\partial t} = \frac{1}{r} \frac{\partial}{\partial r} \left(\lambda r \frac{\partial T}{\partial r} \right) . \quad (3.35)$$

An analytical solution is known for constant boundary conditions (Çengel, 2002).

3.4 Reservoir productivity/injectivity

The reservoir is generally a porous layer of rock, possibly with fractures or fault zones. If the fluid filled porous cavities are hydraulically connected the rock is permeable and fluid can be produced from the reservoir. Due to friction in the porous rock the fluid flow to a producing well creates a pressure gradient. The resulting pressure difference between far-field reservoir (p_{∞}) and well bottom (p_{bh}) is called drawdown.

The idealized relation between pressure gradient and volume flow rate \dot{V} through a cross-section A for radial flow in a homogenous porous medium is described by Darcy's law. Darcy's law assumes laminar flow. Consequentially, as in laminar pipe flow, the relation between pressure drop and velocity is linear:

$$\frac{\dot{V}}{A} = - \frac{K}{\eta} \frac{dp}{dx} . \quad (3.36)$$

K is the rock permeability and has the dimension of area; η is the fluid's dynamic viscosity.

Applying Darcy's law to the radial flow to a well yields an equally linear relation of the drawdown ($p_\infty - p_{bh}$) and the volume flow rate \dot{V} (DiPippo, 2012).

$$\dot{V} = PI(p_\infty - p_{bh}) \cdot \quad (3.37)$$

Fluid viscosity, rock permeability and the assumed geometry of the reservoir and the well have been combined in the productivity index PI . It indicates how much drawdown is caused by a given production rate \dot{V} and, consequentially, how much additional pump load is caused by the friction in the reservoir at a given production rate.

Instead of calculating the PI with Darcy's law for ideal reservoirs, it is usually determined from well tests, which are conducted in order to characterize the reservoir-well performance. During a well test fluid is produced while production rate and pressure in the well are measured at bottomhole or another constant location in the well. In order to obtain the PI , the production rate is divided by the difference between the static pressure (no production) and the steady-state flowing pressure.

The same theory and method can be applied to an injection well to obtain the analogous injectivity index II .

This chapter has discussed the details of the thermo-hydraulic processes in the geothermal brine circuit. The well hydraulics, the phase equilibrium as well as the heat transfer from the fluid through the layers of the well completion to the formation have been described with equations. Based on them a numerical model will be devised in chapter 5 after presenting the application scenario Gross Schoenebeck in chapter 4.

4 Gross Schoenebeck scenario

Although the brine circuit model presented in this work is designed largely universal, it was developed around and parameterized for one geothermal site, for which ample constructive and experimental data is available. This work focuses on the research platform for the development of geothermal technologies in Gross Schoenebeck, northeast of Berlin (Huenges, 2011), hereafter referred to as GrSk.

GrSk features two wells drilled about 4,400 m down to the Rotliegend formation, GrSk3 and GrSk4. From this aquifer low temperature (≈ 145 °C), highly saline brine is produced, by means of an electrical submersible pump that is installed in GrSk4. The wells are connected above ground by pipes²⁰ via a degassing unit, filters and an injection pump.

This chapter lists the site parameters that are relevant for the modelling of the brine circuit.

4.1 Formation

4.1.1 Stratigraphy – Thermal parameters of formation

Thermal parameters, depths and thicknesses of the formation layers used in the wellbore model are listed in Table 1.

Table 1: Stratigraphy of GrSk site - thermal parameters. Layer definition (Ollinger et al., 2010) and thermal conductivity λ under normal temperature, pressure and saturated conditions (Norden et al., 2008). Thermal capacity c_p by (Norden et al., 2012) and density (Norden et al., 2008)

bottom of layer [m TVD ²¹]			λ_{20} [W/(m·K)]	c_p [J/(kg·K)]	ρ [kg/m ³]
-43	L01	Silts and mudstones	1.8	1029	2100
-170	L02	Sand- and siltstones, with calcareous sandstones in the upper part	2	1000	2300
-1990	L03	Siltstones, marls and sandstones	2.2	902	2540
-2500	L04	Evaporites (mainly halite)	4.5	1060	2160
-3875	L05	Evaporites, mainly anhydrite and carbonates	4.5	746	2600
-3945	L06	Siltstones/mudstones/fine sandstones	2.6	746	2600
-4030	L07	Sandstones	3.5	838	2600
-4092.5	L08	Sandstones	3.5	838	2600
-4155	L09	Sandstones	4	838	2600
-4200	L10	Conglomerates and sandstones	3.8	838	2600
-4300	L11	Andesites	2.3	981	2650

²⁰ The piping above ground has not been parameterized because it was not necessary for the simulations that were conducted.

²¹ true vertical depth - vertical distance to surface, opposed to measured depth (MD) along the well

The thermal conductivity is corrected for temperature dependence (see 5.5.3).

4.1.2 Formation temperature profile

In the context of sample taking in March 2012, shortly before the circulation test that will be subject in section 6.4, the temperature of the fluid in the well has been measured top-down (Henniges, 2012). In the weeks before the samples were taken there had been no production. Hence the fluid is assumed to have been at thermal equilibrium with the formation and the measured temperature profile is understood as the far-field formation temperature profile.

Due to technical reasons the temperature could not be measured over the whole depth, so that the profile is incomplete (red line in Fig. 8). Furthermore, in gas (above the liquid level at $z = -230$ m) the measurement is strongly delayed, hence is more influenced by the surface temperature than by the in-situ formation temperature. Therefore, the measured profile has been completed with data from an older measurement, adding an offset in order to meet the measured profile and reach 145 °C at the reservoir depth (see Fig. 8). The thus created temperature profile was used in the model as far-field formation temperature. For comparison and later use in chapter 8, the figure also shows a linear profile, starting at 8 °C (assumed annual average) and ending likewise at 145 °C.

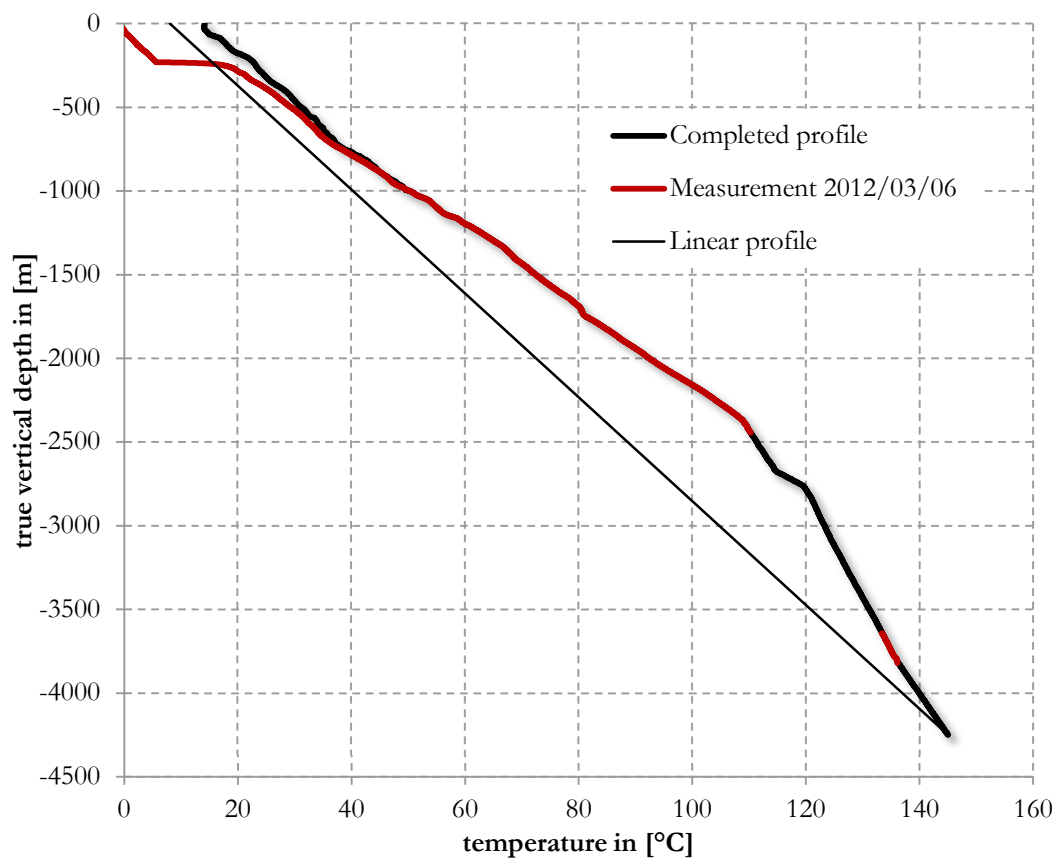


Fig. 8: Formation temperature profile: measurement, completed and linear

4.2 Medium properties

The brine that can be produced from the Rotliegend aquifer is highly saline. It contains around 265 grams²² of dissolved salt per litre, meaning it is nearly saturated with respect to CaCl₂ and NaCl, which together constitute 98% of the salt content (Regenspurg et al., 2010).

Analyses of deep-well fluid samples showed a varying content of dissolved gas that corresponds to a gas-liquid volume ratio of about 1:1 at 1 atm, 0 °C. The dissolved gas is mainly nitrogen ($\approx 80\%$), methane ($\approx 15\%$) and carbon dioxide ($\approx 4.7\%$) (Wiersberg et al., 2004, Huenges and Seibt, 2004). The gas content is also close to saturation, so that (additional) free gas in the reservoir cannot be ruled out, especially during production.

The detailed medium composition in mass fractions as used in the model is given in Table 2.

Table 2: GrSk Brine composition 2/2012 – calculated in B 5

Component	NaCl	KCl	CaCl ₂	CO ₂	N ₂	CH ₄
Mass fractions [g per kg fluid]	83.8	2.53	122.7	0.072	0.690	0.061

Brine salinity does not only strongly influence density, heat capacity and viscosity but also the gas solubility: Gas solubility is decreased to 40 % of the solubility of pure water (Wiersberg et al., 2004). Calculation results of the comparison pure water to brine given in 7.1 confirm that value for CO₂ and show an even stronger reduction for N₂ and CH₄. Carbon dioxide behaves differently and dissolves better in water/brine than nitrogen or methane because additional to physical solution it reacts and forms a weak acid.

4.3 Reservoir parameters:

The tapped geothermal reservoir is at a depth of 4100...4300 m. Brine enters the wellbore from volcanic rock at bottomhole and from two frac zones in the sandstone above through perforated liners.

Measurements indicate a reservoir temperature of 145 °C (Henninges et al., 2012) and the static reservoir pressure (pressure without production) is assumed to be 44 MPa (Blöcher, 2008).

The productivity index PI is assumed to be transient and derived from measured pressures (in 6.5) or to be stationary at 15 m³/(h·MPa) (in 7.2.5). The injectivity index is assumed to be 4 m³/(h·MPa) (in 7.2.5).

4.4 Well parameters

The layouts of the production well GrSk 4/05 and of the injection well GrSk 3/05 are depicted in Fig. 9. More details are given in Table 3 and Table 4. All data was provided by the drilling documentation.

The well consists of sections with different diameters. The annulus between casing and formation (borehole diameter) is filled with cement. The diameters decrease section-wise with depth. The respective depths are displayed in true vertical depth and measured depth (along the borehole). The production string connects the pump to the wellhead. It is enclosed by the open annulus, which is filled with brine or gas, depending on the hydraulic conditions in the well.

²² Average seawater salinity: 35 g/L, Dead Sea salinity: 24 % at $\rho = 1240$ g/L \rightarrow 298 g/L (wikipedia.org, 2013)

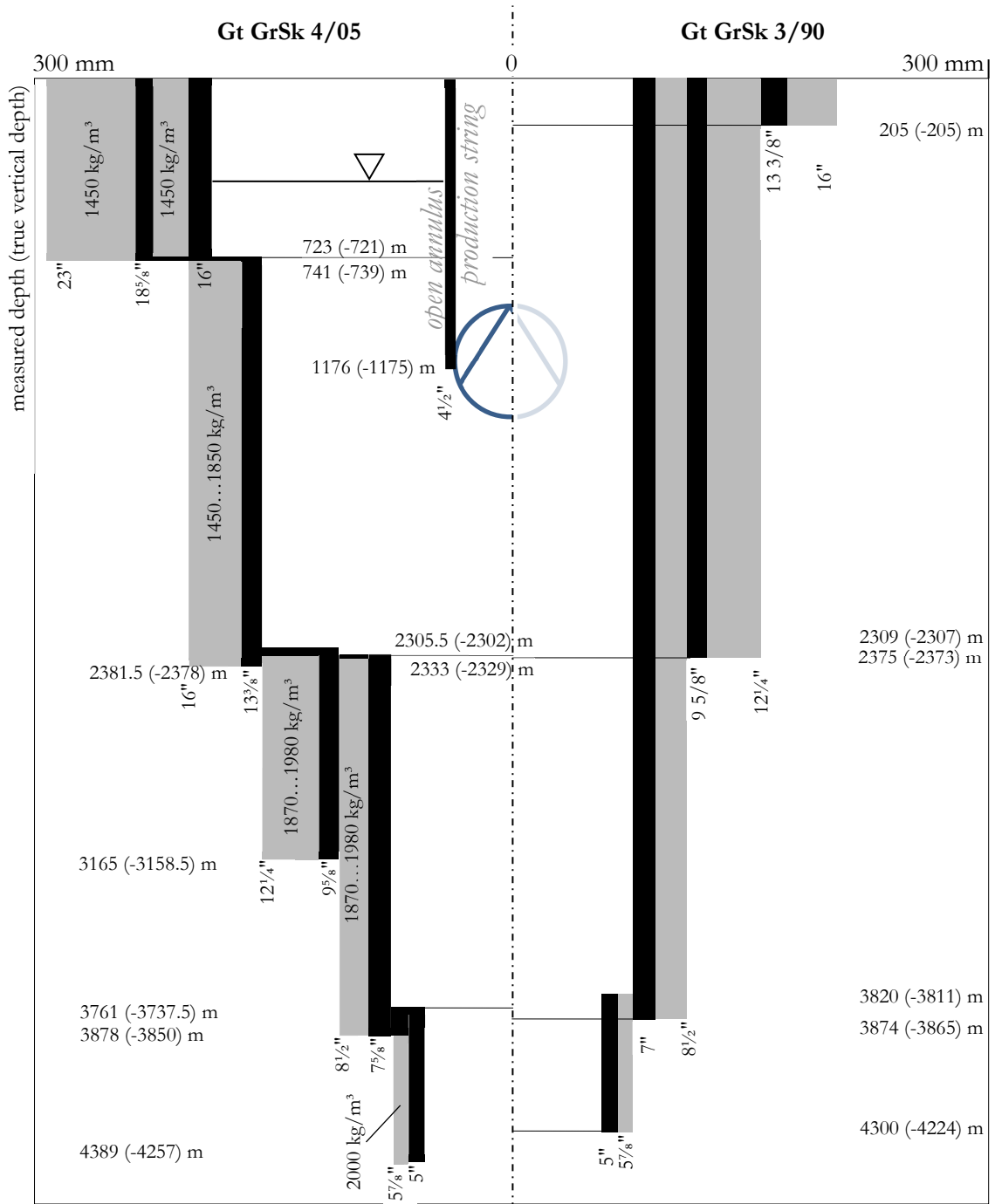


Fig. 9: Wellbore schema for a) production wellbore and b) injection wellbore in Gross Schoenebeck. The indicated diameters are outer diameters of casing/liner/tubing or drilled diameter.

4.4.1 Well completion materials

The well casing, liner and tubing are assumed to be carbon steel with a constant thermal conductivity of 50 W/(m·K) (Dubbel, 2001). The thermal conductivities of carbon steel vary over a broad range, but its influence on the heat flow in the well completion is marginal, as it is much higher than the one of cement and formation, which results in a small contribution in eq. 3.25.

The cement properties are different for each well section. The densities of the cement used in GrSk are documented (indicated in Fig. 9) and have been used to estimate the thermal conductivities using the density-conductivity relation presented in 5.4.8.

The thermal resistances of the interfaces between steel, cement and formation cannot be quantified and are therefore neglected, i.e. perfect contact is assumed.

4.4.2 Production well (GrSk 4/05)

Table 3 lists the geometry parameters of the production well completion used in the model. The pump is installed at $z = -1174$ m (position of the inlet). The volume without annulus is calculated from the geometry as 131 m^3 ; the open annulus has a volume of 105 m^3 .

Calliper logs from this well below $z = -721$ m are available with a resolution of 1 m. Borehole washout (see 3.3.4) has been calculated from these logs and is displayed in Fig. 10, along with total and segment-wise average values. For the part above $z = -721$ m washout was calculated from cementation data.

The washout reaches values of more than 400 % and its overall average amounts to $W = 38$ %. The well has been cemented with approximately 333 m^3 of cement.

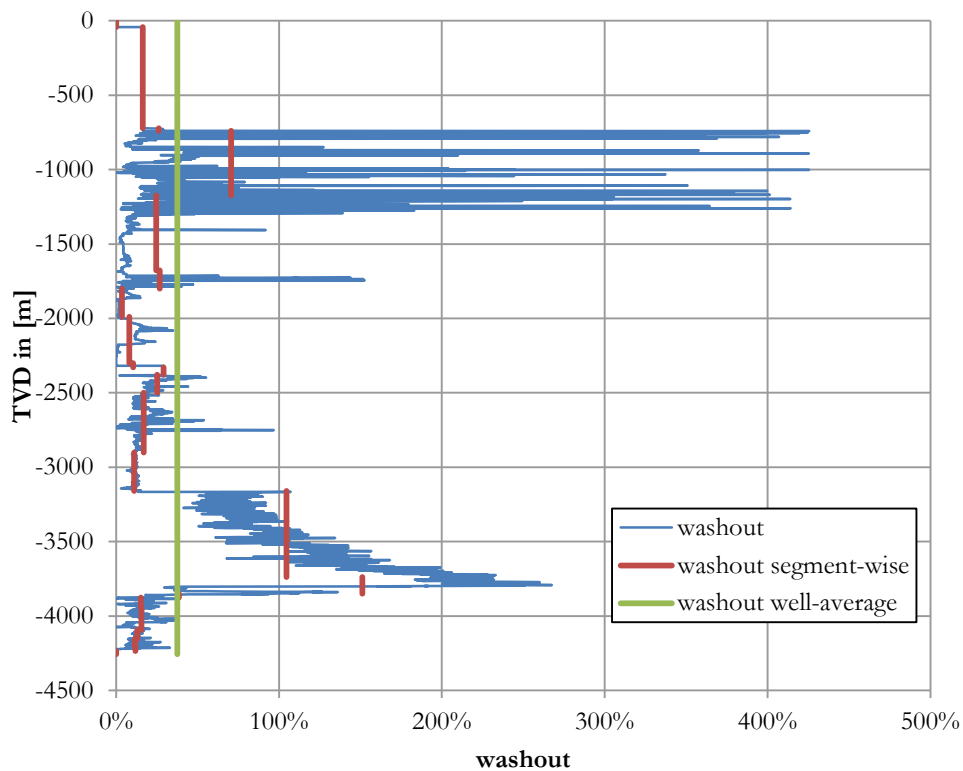


Fig. 10: Washout (relative borehole volume increase) in production well plotted vs. true vertical depth. Profile from calliper measurements (blue), average values per well-segment (red) and overall well average (green).

Table 3: Well geometry GrSk4 (production well). Depths are given for the lower end of the respective well section. Ollinger layer specifies the assigned lithology as defined in Table 1. Cementation density is given for inner and outer cement layers.

	depth		inclination nation layer	Ollinger layer	diameters in mm						cementation		
	MD s / m	TVD z / m			completion	inner pipe		middle pipe		outer pipe		borehole outer ø	therm. cond. λ / [W/(m·K)]
1	43	-43	90.0 °	L01	4.5" in 16" in 18 ⁵ / ₈ " in 23"	100.5	114.3	377.19	406.4	450.98	473.08	584.2	0.61/-
1b	170	-170	86.1 °	L02	4.5" in 16" in 18 ⁵ / ₈ " in 23"	101.5	114.3	378.19	406.4	451.98	473.08	584.2	0.61/1.02
1c	723	-721.4	86.1 °	L03	4.5" in 16" in 18 ⁵ / ₈ " in 23"	102.5	114.3	379.19	406.4	452.98	473.08	584.2	0.61/1.02
2	741	-739.4	90.0 °	L03	4.5" in 13 ³ / ₈ " in 18 ⁵ / ₈ " in 23"	100.5	114.3	313.61	339.73	450.98	473.08	584.2	0.61/1.13
3	1177	-1174.6	87.9 °	L03	4.5" in 13 ³ / ₈ " in 16"	100.5	114.3	313.61	339.73			406.4	0.61
4	1680	-1677.6	87.4 °	L03	13 ³ / ₈ " in 16"	313.61	339.73					406.4	0.72
5	1803	-1800.4	86.7 °	L03	13 ⁵ / ₈ " in 16"	314.33	346.08					406.4	0.72
6	1993	-1990	86.8 °	L03	13 ³ / ₈ " in 16"	313.61	339.73					406.4	0.72
6b	2306	-2301.85	86.0 °	L04	13 ³ / ₈ " in 16"	314.61	339.73					406.4	0.72
7	2333	-2329.3	86.7 °	L04	9 ⁵ / ₈ " in 13 ³ / ₈ " in 16"	216.79	244.48	313.61	339.73			406.4	1.53/0.72
8	2382	-2377.7	86.3 °	L04	7" in 9 ⁵ / ₈ " in 13 ³ / ₈ " in 16"	152.5	177.8	216.79	244.48	314.61	339.73	406.4	1.39/1.53/0.72
9	2504	-2500	86.7 °	L04	7" in 9 ⁵ / ₈ " in 12 1/4"	152.5	177.8	216.79	244.48			311.15	1.39/1.53
9b	2907	-2901.93	85.8 °	L05	7" in 9 ⁵ / ₈ " in 12 1/4"	153.5	177.8	217.79	244.48			311.15	1.39/1.53
10	3165	-3158.5	84.0 °	L05	7 ⁵ / ₈ " in 9 ⁵ / ₈ " in 12 1/4"	151.46	193.68	216.79	244.48			311.15	1.39/1.53
11	3761	-3737.5	76.3 °	L05	7 ⁵ / ₈ " in 8 1/2"	151.46	193.68					215.9	1.39
12	3878	-3850.34	74.7 °	L05	5" in 7 ⁵ / ₈ " in 8 1/2"	108.61	127	153.46	193.68			215.9	1.24/1.39
13	3903	-3875	76.4 °	L05	5"	108.61	127					149.23	1.24
13b	3976	-3945	73.7 °	L06	5" in 5 ⁷ / ₈ "	108.61	127					149.23	1.24
13c	4146	-4092.5	60.3 °	L07+L08	5" in 5 ⁷ / ₈ "	108.61	127					149.23	1.24
13d	4235	-4155	44.8 °	L09	5" in 5 ⁷ / ₈ "	108.61	127					149.23	1.24
13e	4302	-4200	41.9 °	L10	5" in 5 ⁷ / ₈ "	108.61	127					149.23	1.24
13f	4355	-4234.28	41.0 °	L11	5" in 5 ⁷ / ₈ "	108.61	127					149.23	1.24
14	4389	-4257.05	41.3 °	L11	5" perforated in 5 ⁷ / ₈ "	111.98	127					149.23	1.24

4.4.3 Injection well (GrSk 3/90)

Table 4 lists the geometry parameters of the injection well completion as used in the model. The total inner volume of the well can be calculated as 76.6 m³

Table 4: Well geometry GrSk3 (injection well). Depths are given for the lower end of the respective well section. Ollinger layer specifies the assigned lithology as defined in Table 1

	MD s / m	Depth TVD z / m	inclination	Ollinger layer	completion	diameters in mm						
						inner pipe inner ø	inner pipe outer ø	middle pipe inner ø	middle pipe outer ø	outer pipe inner ø	outer pipe outer ø	borehole outer ø
1	43	-43.0	90.0 °	L01	7" in 9 ⁵ / ₈ " in 13 ³ / ₈ " in 16"	154.78	177.8	217	244.48	315.32	339.73	406.4
1b	170	-170.0	90.0 °	L02	7" in 9 ⁵ / ₈ " in 13 ³ / ₈ " in 16"	154.78	177.8	217	244.48	315.32	339.73	406.4
1c	205	-205.0	90.0 °	L03	7" in 9 ⁵ / ₈ " in 13 ³ / ₈ " in 16"	154.78	177.8	217	244.48	315.32	339.73	406.4
2	1991	-1990.0	88.1 °	L03	7" in 9 ⁵ / ₈ " in 16"	154.78	177.8	217	244.48			406.4
2b	2309	-2307.4	86.3 °	L04	7" in 9 ⁵ / ₈ " in 16"	154.78	177.8	217	244.48			406.4
3	2375	-2373.1	84.9 °	L04	7" in 9 ⁵ / ₈ " in 16"	154.78	177.8	217	244.48			406.4
4	2502	-2500.0	85.5 °	L04	7" in 8 ¹ / ₂ "	154.78	177.8					215.9
4b	3820	-3811.3	84.4 °	L05	7" in 8 ¹ / ₂ "	154.78	177.8					215.9
5	3874	-3865.1	84.9 °	L05	5" in 7" in 8 ¹ / ₂ "	112	127	154.78	177.8			215.9
6	3954	-3945.0	84.8 °	L06	5" in 5 ⁷ / ₈ "	112	127					149.23
6b	4102	-4092.5	85.4 °	L07+L08	5" in 5 ⁷ / ₈ "	112	127					149.23
6c	4165	-4155.0	85.5 °	L09	5" in 5 ⁷ / ₈ "	112	127					149.23
6d	4210	-4200.0	85.5 °	L10	5" in 5 ⁷ / ₈ "	112	127					149.23
6e	4300	-4289.7	83.2 °	L11	5" in 5 ⁷ / ₈ "	112	127					149.23

4.4.4 Reynolds number

The lowest Reynolds number in the GrSk wells occurs in the well sections with the largest diameter (13^{3/8}"). Assuming as 'worst case' pure water (dynamic viscosity $\nu = 10^{-6} \text{ m}^2/\text{s}$ at 20 °C) flowing at $\dot{V} = 10 \text{ m}^3/\text{h}$ (cf. to nominal pump operating range below in section 4.5) in a pipe with a diameter of $d = 314 \text{ mm}$ (largest flow diameter in production well) it is $Re_{\min} = 11264$.

$$Re = \frac{\dot{V}4d}{\pi d^2 \nu} = 11264 \quad (4.1)$$

Hence the Reynolds number can be assumed to be always well above the threshold for turbulent flow of 10^4 , which is in accordance with Hasan and Kabir (2010) who state that in most geothermal wells turbulent flow prevails.

4.5 Production pump and injection pump

The production pump is installed at a true vertical depth of $z = -1175 \text{ m}$ (see Fig. 9). This depth marks the position of the pump inlet. The actual length of the pump is 60 m.

The installed pump is a Centrilift 44-675 HC12500. The same model is used as injection pump. It is installed above ground.

According to the data sheet its efficiency reaches 70...77 % within the operating range of 50...88 m^3/h .

The efficiency of the electric motor is assumed to be $\eta_{\text{mot}} = 90 \%$, a typical value for electric motors.

5 Model description

The purpose of this brine circuit model is to simulate the mid-term and long-term hydraulic and thermal behaviour of a low-enthalpy geothermal brine circuit similar to the one described in chapter 4. The full model, as illustrated in Fig. 11, is composed of sub-models of the two wells, the geofluid, the reservoir, the formation, the production pump, the degasification unit, the heat exchanger and an injection pump. The sub-models can be freely combined and arranged in order to adapt the model to site specific configurations and/or limit the modelling to the area of interest.

This work focuses on the processes in the wellbore. The reservoir and the components between the wellheads are represented by basic models. The heat exchanger can be replaced by a more complex model as developed by (Thorade, 2014) or by a model of a power plant assembled from available libraries such as ThermoCycle (Quoilin et al., 2013). Although only linear flow configurations without branches have been implemented and tested, hydraulic junctions are possible²³, so that modelling of multiple confluence horizons, multiple wells or parallel heat use is conceivable.

Model boundaries are the bottoms of the wells with inflow/outflow from/to the reservoir, the heat exchanger with heat flow and the cylindrical outer boundary of the formation around the wellbore. The model allows for quasistatic simulation of well behaviour under varying thermal conditions. Idle wells without mass flow cannot be simulated (see 3.1.3).

The heat flow model is divided in two parts, the steady-state well completion²⁴ (5.4.5) and the transient formation (5.5). Both models are coupled via heat flux and temperature at their interface (cement to formation). Following the considerations made in the beginning of chapter 3 the following assumptions were made for the heat flow model:

- Heat flows only radially. Well and formation are radially symmetric (see 3.3).
- Heat flow in the well completion is static (see 3.3).
- Heat flows in open annulus by free convection and radiation (see 3.3.5).
- Thermal material properties of the well completion are constant and homogenous per radial layer and vertical section.
- The formation material is homogenous for each well section, i.e. density and specific heat capacity are constant, and the temperature-dependent thermal conductivity is described by the same equation.

The model is composed of exchangeable sub-models for the components, so that easy switching between different implementations is possible. For example, implemented are the well section model with/without open annulus, the pump with/without control and the static/transient formation model. Equally exchangeable are the sub-models for the brine properties, pipe friction and fluid-wall heat transfer and formation temperature. The thermal properties of the formation layer are configured via predefined records representing lithological layers, which define density, thermal conductivity and specific heat capacity. The structure of the well section model including the formation heat flow model is depicted in Fig. 59 in the appendix.

²³ Supported by the connectors in Modelica.Fluid (MSL).

²⁴ Well completion is the entirety of pipes and cement installed in the borehole.

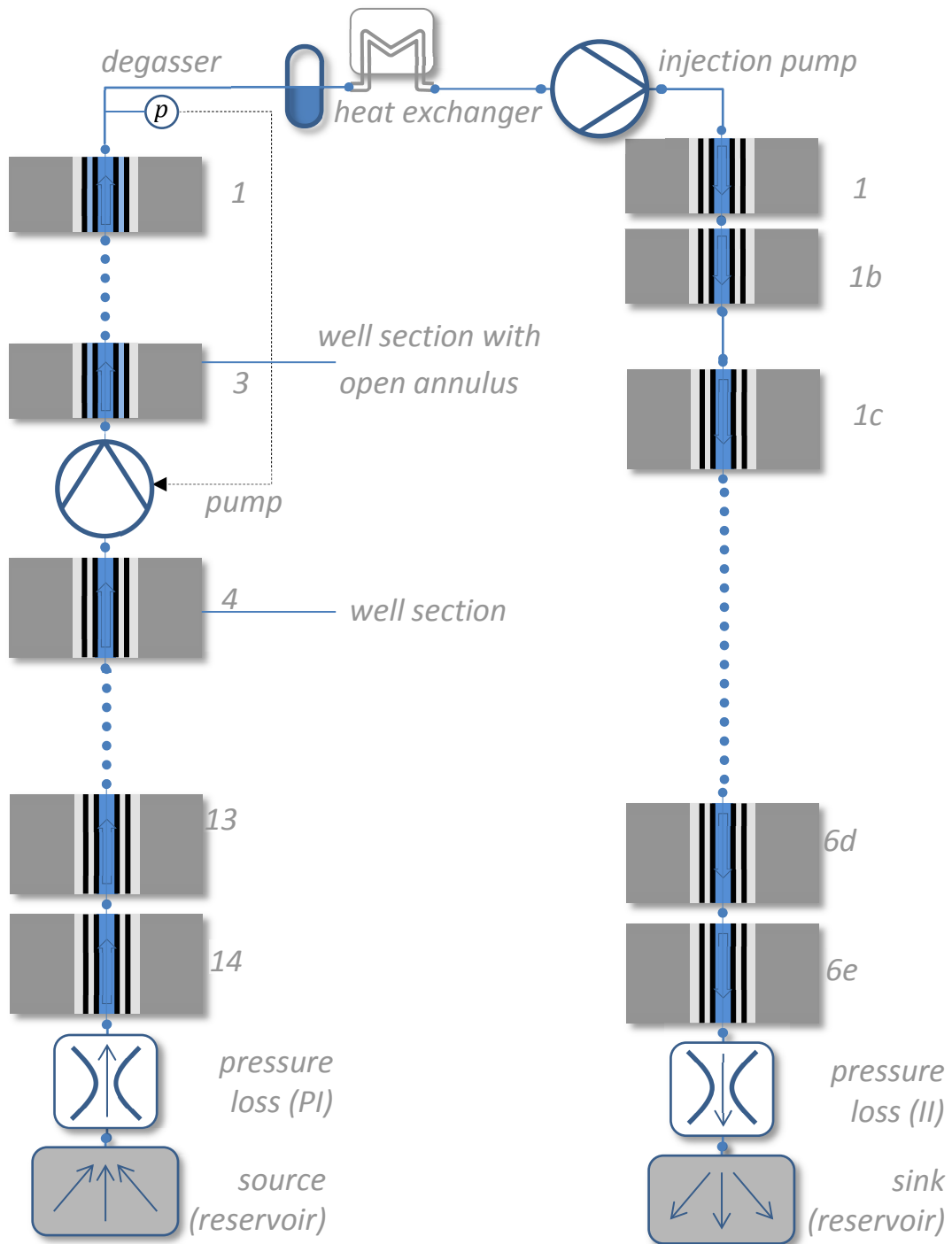


Fig. 11: Graphical representation of the model of GrSk brine circuit

The sub-models that contribute most to the model's complexity are the fluid model and the well section model. The fluid model provides fluid properties for a given thermodynamic state. It is used in the component models.

In addition to the disciplines listed in the beginning of chapter 3, the model implementation in a computer program touches other wide areas as it requires programming and numerical techniques. The brine circuit model has been implemented in MODELICA using MSL²⁵ 3.2 (Elmqvist et al., 2003) and DYMOLA 2013 (Dassault Systèmes AB, 2013). That is why this chapter opens with some remarks about MODELICA and DYMOLA (5.1), before describing the sub-models for the geofluid (5.2), the reservoir (5.3), the wellbore (5.4), the formation (5.5), the pump (5.6), the heat exchanger (5.7) and the separator/degasser (5.8). The chapter is concluded by listing the limitations of the model's applicability (to other geothermal sites (5.9)).

5.1 MODELICA / DYMOLA

Different solutions were conceivable for the implementation of the brine circuit model.

Using MS Excel with VBA²⁶ would have the advantage of familiarity and high availability of the software. It is, however, rather inadequate for the solution of transient problems.

Within the range between writing the complete model "from the scratch" in C, MATLAB, etc. and highly specialized commercial well simulators, MODELICA / DYMOLA is a compromise between flexibility and availability of ready-to-use models. The choice is further motivated below.

Also on an intermediate level are products like SIMULINK²⁷ or EES²⁸ as they likewise feature an ODE solver for transient problems. Based on the author's experience (Francke, 2008) with EES it was considered unsuitable for more complex tasks. SIMULINK differs from MODELICA in the fundamental approach. It is signal based, i.e. it uses causal blocks/components, while MODELICA is generally acausal. Acausal models contain the physical relations that describe the respective system, without specifying input and output or cause and effect. These models are more versatile because they allow for simple inversion of the problem, just by specifying other variables. Causal blocks, on the other hand, cover only the forward case, i.e. the inverse, if needed, must be formulated explicitly. Besides these structural advantages models implemented in DYMOLA are reported to run more stable and faster than when implemented in SIMULINK (Richert et al., 2003).

5.1.1 What is it?

MODELICA is an object oriented language for complex (nested) transient models of physical systems. DYMOLA is a commercial simulation environment for MODELICA including editor, compiler, solver and postprocessor.

MODELICA is the product of an ongoing development, driven by the open, independent MODELICA Association²⁹. They also continuously develop the MODELICA Standard Library (MSL) which provides, among others, mathematical functions, file input/output, material properties (water, ideal gases, air) as well as components and connectors for hydraulical, mechanical, thermal and electrical systems including controllers.

²⁵ Modelica Standard Library

²⁶ Visual Basic for Applications, scripting language for MS Office programs

²⁷ <http://www.mathworks.de/products/simulink> [30 Nov 2013]

²⁸ <http://www.fchart.com/ees> [30 Nov 2013]

²⁹ <https://www.modelica.org> [30 Nov 2013]

A model in MODELICA is acausal, i.e. a system of algebraic and ordinary differential equations in arbitrary order. To be solvable, it must contain the same number of equations and variables. A model can make use of functions. A function is a set of instructions that is processed sequentially in the given order, like in conventional programming.

The solution of the algebraic equations is handled by performing analytic operations (flattening, replacing, simplifying), thus reducing the order of the system of equations as far as possible. A system of ordinary equations that can be solved completely analytically will be referred to herein as ‘explicit’ else ‘implicit’. An implicit system is solved numerically by an iterative algorithm.

The solved algebraic system is then passed to the solver for systems of ordinary differential equations, which then repeats the algebraic solution in every time-step.

5.1.2 Why MODELICA?

This model was developed within a work group dealing with reservoir technologies, where the decision had been made to deploy MODELICA for the modelling of power plants.

MODELICA offers the following advantages:

The user is free to write the complete model in one block, however, adopting the philosophy of object-oriented programming imposes a hierarchical and modular structure that facilitates code readability, reuse, exchangeability, debugging and maintenance. If the model structure follows an obvious logic such as splitting up the domain in spatial segments and/or physics, the resulting code is, to some degree, self-documenting. Furthermore, the structure can be used for graphical model representation that allows the easy assembly of components by Drag & Drop and configuration of the components by dialogs that are generated for each component from its parameters.

MODELICA permits the specification of units for variables/parameters. If supported by the compiler, that allows for unit based checking for errors in either the physical model or the implementation.

Being not a highly specialized application but instead a versatile modelling language, MODELICA has a considerable and growing number of users, which has the associated benefits like exchange of information, experience and solutions via online forums and conferences.

Also growing is the choice of available simulation environments, both commercial and free³⁰. Hence, choosing MODELICA does not mean committing to a single commercial product or open-source project with potentially discontinued development in the future.

As a last point, coupling of the brine circuit model with a power plant model via an advanced heat exchanger model was envisaged. As both models were planned to be implemented in MODELICA and coupling is comparably simple between MODELICA models, the choice of MODELICA for the brine circuit seemed advisable.

5.1.3 Why DYMOLA?

Free open-source simulation environments exist, but at the beginning of this work they did not fully support the MSL, especially the implementation of the library Modelica.Media was missing. The commercial environment DYMOLA was already sophisticated and performed well.

³⁰ <https://www.modelica.org/tools> [30 Nov 2013]

In order to run a model, DYMOLA translates the MODELICA code into C code, which is then compiled into a binary executable. This allows the use of highly advanced and optimized compilers³¹.

DYMOLA user interface allows text-based coding as well as graphical arrangement of components. Components are added by Drag & Drop and connected by drawing lines using the mouse. This creates a clear representation of the model structure, where the component's parameters can be configured via automatically generated dialog boxes.

Quick evaluation of simulation results is possible with the integrated plotting tools. Data export to MATLAB is almost seamless as DYMOLA stores results in mat-files, the DYMOLA data format. Data import (e.g., temperature profiles, transient boundary conditions) is possible via text files. Running multiple simulations can be controlled via a script within DYMOLA or from MATLAB by a script.

5.1.4 Model inversion and iterative solution

As mentioned above, in MODELICA models are defined by equations that represent the physical relations of the model variables to each other without specifying which variables will be known and which will have to be calculated. The solver then takes care of rearranging the equations according to the input variables and solving the resulting equations systems. These models are more versatile because they allow for simple inversion of the model, just by specifying other input variables.

For algebraic equations the solver may try to symbolically solve the equation system, ideally generating a new stable forward equation system. If, however, the equation set contains explicit functions whose input variables are unknown, then these functions have to be inverted numerically, with negative consequences for calculation speed, stability and necessary start and limit values. In order to avoid numerical inversion, the MODELICA standard allows for the definition of inverse functions, which the solver can switch to alternatively.

The solution with a generic iterative algorithm is problematic, not only because it takes longer than calculating only forward equations, but also because it may run into value ranges for which one or more of the equations are not defined. Equations/functions may be undefined because one of the variables is out of the generally allowed range (e.g., negative absolute pressure/temperature in [K]), the specifically allowed range (e.g. $T < 0^\circ\text{C}$ in water property functions), because discontinuities occur (e.g., at the phase transition) or for mathematical reasons (e.g., square root / logarithm of a negative number). Workarounds can be applied that limit values to the allowed range. These cumbersome workarounds, however, make the code hard to read and are error-prone. They may also require additional calculations if the allowed range is not constant, for example when pressure is to be limited to be above saturation pressure to ensure liquid state.

That is why the issue of implicit equations is repeatedly brought up in this chapter. Implicit equations were avoided when possible in the implementation of model. Nevertheless, the acausal approach is advantageous when applying the formation heat flow equations (5.5.6), which could be implemented in their discretized form directly, because no problematic property functions are involved.

In several cases iterative solutions cannot be avoided. That is the case in the VLE calculation, in the calculation of the fluid temperature $T(p,h)$ and in the inversion of the gas solubilities. These iterative solutions could be handled by DYMOLA if the problems were isolated, but the solver fails to do so for the

³¹ Under Windows commonly Microsoft Visual C++ (Express) is used

complete model. In order to gain more control about the iterative solutions, they were implemented in dedicated functions. This allowed stable solutions and tuning of the algorithms specific to the problem.

5.2 Geofluid model

The implementation of geofluid property model is based on the Modelica.Media Library which is part of the MSL. For more implementation details see E 2.3.

The geofluid is modelled as a mixture of water, multiple salts and multiple non-condensable gases, potentially having two phases, liquid and gas. In analogy to the compositional model in gas/oil modelling mentioned in chapter 2, the individual content of the components is considered.

Density and enthalpy of the fluid are calculated from single phase properties and phase mass fractions. Viscosity and thermal conductivity are approximated by the values for liquid water. Phase equilibrium and transition are reproduced with gas solubility functions and water vapour pressure. Property functions for aqueous chloride solutions are applied.

For a given p-T-state the fluid model first determines the gas mass fraction x and then the other state variables (h, ρ) by calculating them separately for both phases and combining them according to x in order to obtain the effective homogenous values. If enthalpy is known instead of temperature, the p-T-state is found by iteration (see 5.2.5).

According to brine the composition the geofluid model is parameterized for the three main salts (NaCl, CaCl₂, KCl) and the three main gases (N₂, CH₄, CO₂), but by design it is not limited to these substances or to this number of constituents. The geofluid model can be applied to other substances if the required property functions³² are available. The number of gases is limited by the convergence of the VLE algorithm (5.2.2.3), which also relies on solubilities being sufficiently different in order to produce a consistent unequivocal solution.

5.2.1 Fluid model assumptions

The following modelling assumptions have been made about the geofluid:

The fluid is a mixture of water, N_s salts and N_g non-condensable gases; its composition is given by vector of mass fractions \mathbf{X} ³³. There are one or two phases: always liquid and, if the two-phase condition is fulfilled, gas. The gas phase is an ideal mixture of water vapour and gases.

Salts are completely dissolved in and limited to the liquid phase, i.e. they do not precipitate or evaporate. Water and gases are exchanged between the liquid and the gas phase by degassing/dissolution or evaporation/condensation, taking into account mass and energy conservation. Both phases are assumed to be in thermodynamic equilibrium, i.e. they have the same pressure and temperature. The vapour-liquid equilibrium is instantly reached.

In the GrSk scenario the fluid model considers the $N_g = 3$ main gases: carbon dioxide, nitrogen and methane. They can be considered as non-condensable under the conditions that occur in the brine

³² salts: apparent molar volume/enthalpy, viscosity; gases: solubility considering salinity

³³ In order to be compliant with the standard of Modelica.Fluid connector mass fractions are used to specify the complete fluid composition, i.e. salts and gases, although the common unit for gas content is molality (mol of gas per kg solvent)

circuit³⁴. The gas dissolved in the GrSk brine is mainly composed of these three gases. (see 4.2). Nitrogen is the main constituent and has the lowest solubility; it can therefore be expected to dominate the degassing process. Methane is the second main constituent and relevant due to its global warming potential and flammability. Carbon dioxide is interesting because of precipitation issues and its global warming potential.

Gases dissolve in liquid according to their respective solubility, which depends on temperature and salt content, but not on the content of other gases. Evaporation and condensation of water are determined by its saturation pressure, which depends on temperature and the salt content according to Raoult's law. In two-phase state degassing pressures equal the respective partial pressures (see 3.2.4).

Boundary surface enthalpies (surface tension), gas solution enthalpies and dilution enthalpies are neglected. Evaporation enthalpy is considered.

Dalton's law is applied to combine the solubilities and find the equilibrium with 4 degrees of freedom.

5.2.2 Calculation of vapour-liquid equilibrium

A closed system is considered. It contains the fluid mass m , which is composed of water, salts and gases in a given composition \mathbf{X} . The system temperature is T and the pressure is p . If the two-phase state condition is fulfilled (see 5.2.2.1), the VLE establishes and the masses of the gases and water are distributed between both phases, so that the gas mass fraction is x .

For a known fluid composition \mathbf{X} , in two-phase state the system is determined by two thermodynamic variables (e.g., p, T) (acc. to Duhem's theorem) and, with the salts being restricted to the liquid phase, has N_g+1 degrees of freedom (acc. to Gibbs' phase rule, see 3.2.2). The single-phase state is also specified by two variables.

Hence, if gas solubilities are known and the assumptions stated above are made, phase equilibrium and thus mass distribution of the gases and water between the two phases can be determined for a given pair p and T , by solving an equation system with N_g+1 degrees of freedom. The algorithm used for that is described below.

5.2.2.1 Two-phase state condition

As explained in 3.2.1, the two-phase equilibrium is only possible if pressure is below a certain level. Whether pressure is sufficiently low for two-phase state, is checked before launching the VLE algorithm as follows. One-phase liquid is assumed (gases are completely dissolved in liquid) and the corresponding degassing pressures and water vapour pressure are calculated. Only if the sum of the water vapour pressure and the degassing pressures in the liquid exceeds total pressure, water can evaporate and the fluid can degas so that a gas phase develops. Otherwise the fluid is in single phase state and the VLE calculation is not necessary.

The other limiting case, complete evaporation, is not covered by the model. However, this cannot be checked beforehand, as a water vapour pressure greater than the absolute pressure does not necessarily

³⁴ The critical temperatures of CO₂, CH₄ and N₂ are 31°C, -82.5°C and -146.85°C. The critical pressures are 73.8 bar, 45.9 bar and 33.83 bar.

lead to complete evaporation. Concentration increase by evaporation may reduce vapour pressure far enough to make equilibrium possible. Hence, the VLE algorithm is started and if it does not succeed in finding a solution, an error occurs when the concentration limits of saturation functions are reached.

5.2.2.2 Equations

As stated above, the system is determined with two thermodynamic variables and has N_g+1 degrees of freedom. Pressure and temperature are selected to set the state (see 3.2.3 for rationale), whereas the mass distribution between the phases will be described by \tilde{n}_α'' , the mole fractions of the components being in the gas phase. \tilde{n}_α'' is defined as the quotient of mole number of one component in gas phase n_α'' divided by total moles number of that component n_α :

$$\tilde{n}_\alpha'' = \frac{n_\alpha''}{n_\alpha} \quad (5.1)$$

This normalization avoids big differences in the order of magnitude of the variables of the mass distribution, which may otherwise lead to numerical errors.

Gas mass fraction

The VLE state is described by \tilde{n}_α'' , but actually the interesting macroscopic quantities are gas mass/volume fraction and composition of both phases, which allow the calculation of the properties for both phases and eventually for the two-phase fluid. Here the mass fraction is used to avoid the dependence on the thermodynamic state that the volume is subject to. The gas mass fraction is defined as the quotient of mass in gas phase and total mass in an arbitrary volume:

$$x = \frac{\text{mass of (gases + water vapour)}}{\text{total mass}} = \frac{\sum_{\alpha=1}^{N_g+1} m_\alpha''}{m} \quad (5.2)$$

Expressing that with the variables \tilde{n}_α'' and setting $m = 1$ kg yields:

$$x = \sum_{\beta=1}^{N_g+1} \tilde{n}_\beta'' n_\beta M_\beta \quad (5.3)$$

Pressure balance

The fundamental equation for the VLE is the pressure balance of saturation pressure and partial pressure from eq. 3.12:

$$p_\alpha^{\text{sat}}(p, T, X') = y_\alpha'' p \quad , \quad \alpha = 1 \dots N_g + 1 \quad (5.4)$$

In equilibrium eq. 5.4 must be fulfilled for each component (gas/water) for a given gas mass distribution, while respecting the mass balances for each component.

While the fugacity in eq. 3.12 has been set to 1, assuming an ideal mixture of ideal gases, the left side is replaced by a function for the water vapour pressure or the degassing pressure p_α^{sat} , respectively. Water vapour pressure is calculated using Raoult's law. Degassing pressures are calculated with correlations, which reproduce the non-ideal solution behaviour (at high pressures) of single gases. Both calculations will be explained in the next paragraphs.

Water vapour pressure

According to Raoult's law applied to an aqueous solution of chlorides (eq. 3.13), the water vapour pressure is reduced by the molar fraction of water in the liquid:

$$p_{H_2O}^{\text{sat}}(\tilde{n}'', T) = y_{H_2O}' p_{H_2O}^{\text{sat},0}(T) \quad (5.5)$$

where the molar fraction is calculated from the normalized mole numbers in the gas phase:

$$y_{H_2O}' = \frac{n_{H_2O}'}{\sum_{\beta=1}^{N_g+1} n_\beta' Z_\beta} = \frac{n_{H_2O} \tilde{n}_{H_2O}'}{\sum_{\beta=1}^{N_g+1} \tilde{n}_\beta' n_\beta Z_\beta} \quad (5.6)$$

Z_β is the number of ions per molecule of component β (1 for water and gases, 2 for NaCl). Dissolved salt molecules are split up in anions and cations and have to be accounted for separately.

Degassing pressures

The degassing pressures are calculated by numerically inverting the solubility correlations listed in 5.2.2.4. The degassing pressures depend on temperature and liquid composition, i.e. the content of salts and the respective gas.

$$X'_\alpha = X'_\alpha(T, p_\alpha^{sat}) \xrightarrow{\text{numerical inversion}} p_\alpha^{sat} = p_\alpha^{sat}(T, X') = X'_\alpha/k_\alpha(T, X') \quad (5.7)$$

k_α is the Henry coefficient (see 3.2.7) of the respective gas, here in Pa⁻¹. They will be used later in the gradient calculation (5.2.2.3). The gas concentration in the liquid phase is calculated from the mole fractions as:

$$X'_\alpha = \frac{n'_\alpha M_\alpha}{1-x} = \frac{(n_\alpha - n''_\alpha) M_\alpha}{1 - \sum n'_\beta M_\beta} = \frac{(1 - \tilde{n}''_\alpha) n_\alpha M_\alpha}{1 - \sum \tilde{n}''_\beta n_\beta M_\beta} . \quad (5.8)$$

Mass balance

When a mole of gas/water moves to the gas phase by degassing/evaporation, it obviously disappears from the liquid phase, as its total amount in the fluid n_α does not change. This is expressed by the mass balance for each component:

$$n'_\alpha + n''_\alpha = n_\alpha . \quad (5.9)$$

n'_α is the amount of substance α in the liquid, n''_α idem in the gas phase.

Phase composition

The salt concentration in liquid phase can then be calculated from the normalized gas mole numbers (see eq. 5.1) as

$$X'_\alpha = \frac{X_\alpha}{1-x} = \frac{X_\alpha}{1 - \sum \tilde{n}''_\beta n_\beta M_\beta} , \alpha = 1 \dots N_s . \quad (5.10)$$

The gas concentration in the gas phase consequently is

$$X''_\alpha = \frac{X_\alpha - X'_\alpha(1-x)}{x} , \alpha = 1 \dots N_g . \quad (5.11)$$

Partial pressure

The partial pressures sum up to the given absolute pressure

$$p = \sum_{N_g+1} p_\alpha . \quad (5.12)$$

They are related to the molar numbers of the gas phase by Dalton's law:

$$p_\alpha = p n''_\alpha / \sum_{N_g+1} n''_\gamma = p \tilde{n}''_\alpha n_\alpha / \sum_{N_g+1} \tilde{n}''_\gamma n_\gamma . \quad (5.13)$$

5.2.2.3 Algorithm

The VLE equation system given above in 5.2.2.2 is implicit. The solution with a generic iterative algorithm is problematic as explained in 5.1.4. Nevertheless, the MODELICA compiler/solver DYMOLA is generally capable of solving the VLE equation system as long as it is isolated and appropriate start values are set. However, while the start values can be specified appropriately in DYMOLA, the subsequent iterations cannot be influenced directly, so that the algorithm may try to use variables in undefined ranges. The solver tries to handle occurring errors by altering values and may succeed, depending on the simulation parameters.

However, in a more complex model with multiple instances of the VLE problem, one big equation system is generated, which the solver will attempt to solve simultaneously. Because this frequently fails and because relying on the solver's error-handling capability is not a very robust and efficient approach, the 'wheel had to be reinvented' and the VLE algorithm was implemented as a function to enforce the isolation of the problem.

The VLE equations are written in matrix form and then solved using the multidimensional Newton's method.

The algorithm's task is to find the combination of normalized gas mole numbers $\tilde{n}''_{\alpha} = n''_{\alpha}/n_{\alpha}$ that fulfils eq. 5.4 for all $\alpha = \{1 \dots N_{gas}+1\}$:

$$f_{\alpha}(\tilde{n}'') = p_{\alpha}(\tilde{n}'') - p_{\alpha}^{sat}(\tilde{n}'') \stackrel{!}{=} 0 \quad (5.14)$$

According to Newton's method \tilde{n}'' can be found by iteratively solving the following linear equation system after choosing a start vector $\tilde{n}''[0]$ and stopping when $|\mathbf{f}|$ falls below a given tolerance.

$$\nabla f \Delta \tilde{n}''[j] + \mathbf{f}(\tilde{n}''[j]) = 0 \quad (5.15)$$

$\Delta \tilde{n}''[k]$ is the correction vector and used to determine the concentration for the next iteration:

$$\tilde{n}''[j+1] = \tilde{n}''[j] + \Delta \tilde{n}''[j] \quad (5.16)$$

The start vector is set to $\tilde{n}''[0] = \{0.5, \dots, 0.5\}$, i.e. all gases and water are equally distributed between both phases. Based on numerical tests (see D 2.2) the stop criterion was set to $\max|\Delta \tilde{n}''[k]| \leq 10^{-3}$. The start vector has virtually no influence on the solution if the stop criterion is set low enough (for details see D 2.1). The algorithm typically needs 7 iterations until the stop criterion is fulfilled.

Gradient calculation

The gradient or the Jacobi matrix of the pressure difference function \mathbf{f} with respect to the normalized mole numbers in the gas phase \tilde{n}''_{α} is calculated as follows.

$$\frac{\partial}{\partial \tilde{n}''_{\gamma}} f_{\alpha} = \frac{\partial}{\partial \tilde{n}''_{\gamma}} p_{\alpha} - \frac{\partial}{\partial \tilde{n}''_{\gamma}} p_{\alpha}^{sat} \quad (5.17)$$

Using the following derivatives of the mole numbers

$$\frac{\partial}{\partial \tilde{n}''_{\kappa}} \tilde{n}''_{\alpha} = \delta_{\alpha\kappa} = \begin{cases} 1 & \text{if } \alpha = \kappa \\ 0 & \text{else} \end{cases}, \quad \frac{\partial}{\partial \tilde{n}''_{\kappa}} \sum \tilde{n}''_{\beta} n_{\beta} = n_{\kappa} \quad (5.18)$$

$$\frac{\partial n''_{\alpha}}{\partial \tilde{n}''_{\gamma}} = \delta_{\alpha\gamma} n_{\alpha}, \quad \frac{\partial n'_{\alpha}}{\partial \tilde{n}''_{\gamma}} = -\delta_{\alpha\gamma} n_{\alpha} \quad (5.19)$$

the derivative of the partial pressure (eq. 5.13) can be written as

$$\frac{\partial}{\partial \tilde{n}''_{\gamma}} p_{\alpha}(\tilde{n}'') = p \frac{\delta_{\alpha\gamma} n_{\gamma} \sum \tilde{n}''_{\beta} n_{\beta} - \tilde{n}''_{\alpha} n_{\alpha} n_{\gamma}}{(\sum \tilde{n}''_{\beta} n_{\beta})^2} = p \frac{n_{\gamma} (\delta_{\alpha\gamma} \sum \tilde{n}''_{\beta} n_{\beta} - \tilde{n}''_{\alpha} n_{\alpha})}{(\sum \tilde{n}''_{\beta} n_{\beta})^2} \quad (5.20)$$

Linearizing the saturation pressures according to Henry's law the derivatives of the degassing pressures (eq. 5.7) are expressed with the Henry constants k_{α} as

$$\frac{\partial}{\partial \tilde{n}''_{\gamma}} p_{\alpha}^{sat} = \frac{\partial}{\partial x'_{\gamma}} p_{\alpha}^{sat} \frac{\partial x'_{\gamma}}{\partial \tilde{n}''_{\alpha}} \approx \frac{\partial x'_{\gamma}}{\partial \tilde{n}''_{\alpha}} \cdot \begin{cases} k_{\alpha}(p, T, X')^{-1} & \text{if } \alpha = \gamma \\ 0 & \text{else} \end{cases} \quad (5.21)$$

The required derivative of the gas mass fraction (eq. 5.8) in the liquid phase is, using eq. 5.3:

$$\frac{\partial x'_{\alpha}}{\partial \tilde{n}''_{\gamma}} = n_{\alpha} M_{\alpha} \frac{-\delta_{\alpha\gamma} (1 - \sum \tilde{n}''_{\beta} n_{\beta} M_{\beta}) - (1 - \tilde{n}''_{\alpha}) \cdot (-n_{\gamma} M_{\gamma})}{(1 - \sum \tilde{n}''_{\beta} n_{\beta} M_{\beta})^2} = n_{\alpha} M_{\alpha} \frac{\delta_{\alpha\gamma} (x-1) + (1 - \tilde{n}''_{\alpha}) n_{\gamma} M_{\gamma}}{(1-x)^2} \quad (5.22)$$

The derivative of the water vapour pressure (eq. 5.5) can be calculated by

$$\begin{aligned}
\frac{\partial}{\partial \tilde{n}'_\gamma} p_{\text{H}_2\text{O}}^{\text{sat}} &= p_{\text{H}_2\text{O},0}^{\text{sat}}(T) \cdot n_{\text{H}_2\text{O}} \frac{-\delta_{\gamma\text{H}_2\text{O}} \sum \tilde{n}'_\beta n_\beta Z_\beta - \tilde{n}'_{\text{H}_2\text{O}} \cdot (-n_\gamma)}{(\sum \tilde{n}'_\beta n_\beta Z_\beta)^2} \\
&= p_{\text{H}_2\text{O},0}^{\text{sat}}(T) \cdot n_{\text{H}_2\text{O}} \frac{-\sum \tilde{n}'_\beta n_\beta Z_\beta + n'_{\text{H}_2\text{O}}}{(\sum \tilde{n}'_\beta n_\beta Z_\beta)^2}.
\end{aligned} \tag{5.23}$$

Simplified Newton's method

The non-diagonal elements of the Jacobi matrix (eq. 5.17) account for the interaction of the gases, i.e. the influence of the phase mass distribution of one gas on the equilibrium of the other gases. That is why Newton's method is expected to handle coupled systems quite well, given a good start value. Applied to the present problem, however, the algorithm does not converge for certain pressure values, even if tolerance is reduced and iteration progress is dampened.

Using only the gradient's diagonal elements leads to a stable algorithm, which needs fewer iterations. This is also computationally less demanding, because no equation system has to be solved, as eq. 5.15 can be solved for the correction vector by simple division:

$$\Delta \tilde{n}''_\alpha = \frac{-f_\alpha(\tilde{n}'')}{\partial f_\alpha / \partial \tilde{n}''_\alpha}. \tag{5.24}$$

5.2.2.4 Gas solubility

Solubility of the three gases is calculated using empiric models based on measurements of NaCl solutions. These measurements are extrapolated to solutions of other salts (Na^+ , K^+ , Mg^{2+} , Ca^{2+} , Cl^- and SO_4^{2-}) by considering their corresponding NaCl contents using a simple approach based on the ion valence. In all three models the fugacity coefficient of the gas in the gas phase is calculated as the fugacity of the pure gas, because the water content in the vapour phase is expected to be low. Furthermore, the water vapour pressure of the mixture is assumed to be pure water saturation pressure. The errors caused by that assumption are, however, to some extent considered by the parameterization.

The solubility functions contain several auxiliary functions that have been parameterized for p and T . For the application in the multi-gas system the absolute pressure p is replaced as function argument by $p_\alpha + p_{\text{H}_2\text{O}}$, the sum of the respective partial pressure and the water vapour pressure.

The three solubility correlations listed below calculate gas solubility in moles per kg of solvent (water) for a given (partial) pressure, temperature and salt contents of the liquid. They have been developed for single gases dissolving in brine. By using them for mixtures of gases, ideal solution and ideal gas is assumed, thus interactions of the gases are neglected.

Carbon dioxide solubility

A solubility function for carbon dioxide in an aqueous solution containing Na^+ , K^+ , Ca^{2+} , Mg^{2+} , Cl^- and SO_4^{2-} is given by (Duan et al., 2006). It is valid for $T = 273 \dots 533$ K, $p = 1 \dots 2000$ bar and a total salt molality of $b = 0 \dots 4.5$ mol/kg.

Nitrogen solubility

A solubility function for nitrogen in an aqueous solution of sodium chloride is given by (Mao and Duan, 2006). It is valid for $T = 273 \dots 400$ K, $p = 1 \dots 600$ bar and $b = 0 \dots 6$ mol/kg.

Methane solubility

A solubility function for methane in an aqueous solution of sodium chloride is given by (Duan and Mao, 2006). It is valid for $T = 273 \dots 523$ K, $p = 1 \dots 2000$ bar and $b = 0 \dots 6$ mol/kg.

5.2.3 Density of the geofluid

Using eq. 3.2, the density of the two phase fluid is calculated from the specific volumes of both phases weighted with their mass fraction, that has been determined with the VLE algorithm (5.2.2):

$$\rho = \left(\frac{1-x}{\rho'} + \frac{x}{\rho''} \right)^{-1} \quad (5.25)$$

Density of the liquid phase is calculated by combining the densities of solutions of single salts, while gas phase density is calculated using the ideal gas law.

This approach ignores the potential effect of the interaction of solutes.

The influence of dissolved gases on the liquid density is neglected, because the mass of dissolved gas in saturation is very small under the pressures that occur in this model.

5.2.3.1 Density of gas phase

For the density calculation the gas phase is assumed to be an ideal mixture of ideal gases. Hence, the ideal gas law is used with the specific gas constant of the gas phase R_s'' , which is the average of the specific gas constants of gas and water, mass weighted according to the actual composition and calculated from the universal gas constant \bar{R} :

$$R_s'' = \sum X_\alpha'' \frac{\bar{R}}{M_\alpha} \quad (5.26)$$

$$\rho'' = \frac{p}{T \cdot R_s''} \quad (5.27)$$

The ideal gas law is valid for low pressures and high temperatures, but pressure reaches considerable levels at greater depth of the well. There, however, the influence of the gas phase, if present, on the fluid density is negligible, because due to said high pressure the gas phase occupies little or no volume.

The validity of the ideal gas assumption can be estimated with the compressibility factor Z , a gas property quantifying non-ideal behaviour (Baehr, 2003):

$$Z = \frac{pM}{\rho \bar{R} T} \quad (5.28)$$

It can be calculated directly for gas mixtures with REFPROP (Lemmon et al., 2010). Fig. 12 displays Z for an exemplary mixture of three gases over the p - T range present in the GrSk scenario. Contrary to the initial statement about the validity of the ideal gas law, it shows better accordance at lower temperatures. Anyway, the arbitrary error threshold of 1 % is only trespassed for $p > 50$ bar, where a gas fraction of less than 1:50³⁵ can be expected.

³⁵ gas-liquid ratio of 1:1 at 1 bar (see 4.2) applied to 50 bar for ideal gas and further reduced by gas dissolution.

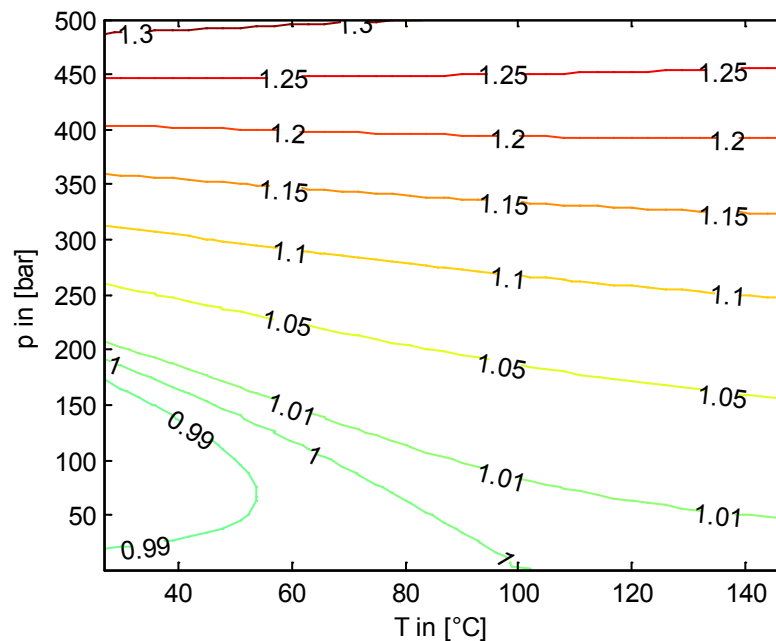


Fig. 12: Gas compressibility factor of test mixture of $N_2/CH_4/CO_2$ with 80/15/5 Vol. %

5.2.3.2 Density of binary aqueous chloride solutions

Density equations for different binary aqueous chloride solutions are provided by Mao and Duan (2008). Here only NaCl, KCl, and $CaCl_2$ are considered, because those are the constituents with the highest percentages in the GrSk fluid (see 4.2). The validity ranges are for NaCl: (273 K...573 K, 0.1 MPa...100 MPa and 0...6.0 mol/kg), for KCl: (273 K...543 K, 0.1 MPa...50 MPa and 0...4.5 mol/kg) and for $CaCl_2$: (273 K... 523 K, 0.1 MPa...60 MPa and 0...6.0 mol/kg).

The density of pure water used in this approach is provided by the IAPWS/IF97 steam tables (Wagner et al., 2000), which is included in the MSL 3.2. Pure water density is calculated for the given pressure and temperature. Pressure is limited to be above saturation pressure, so that density can also be calculated for the small pressure range between the saturation pressures of pure water and the reduced saturation pressure of the aqueous solution.

A comprehensive equation of state for sodium chloride solution has been developed for applications involving seawater by Driesner (2007). It provides density, specific enthalpy and isobaric heat capacity for the variables pressure, temperature and NaCl mole fraction. It is valid from 0 to 1000 °C, 1 to 5000 bar and over the full range of NaCl mole fraction from 0 to 1.

Densities calculated with both models have been found to be consistent (Francke and Thorade, 2010).

5.2.3.3 Density of liquid phase / Mixing rule

For a given brine composition the densities of the chloride solutions are calculated and then combined by applying a mixing rule:

In the density function for binary chloride solutions by Mao and Duan (2008) (see 5.2.3.2) the final equation converts the apparent molar volume V_{ϕ}^{α} to solution density ρ . It is extended for the use with multiple salts into a mixing rule also proposed by Laliberté and Cooper (2004). The respective apparent molar volumes V_{ϕ}^{α} calculated for the respective salt content are combined to yield the density of the multi-salt solution:

$$\rho'(p, T, X') = \left(\frac{X'_{\text{H}_2\text{O}}}{\rho_{\text{H}_2\text{O}}(p, T)} + \sum_{N_s} X'_\alpha \frac{V_\Phi^\alpha(p, T, X'_\alpha)}{M_\alpha} \right)^{-1}. \quad (5.29)$$

The liquid density model has been successfully validated against measurements of the ternary solutions NaCl+CaCl₂ and KCl+CaCl₂ (see 6.1.1), as well as against online measurements of the GrSk fluid (see 6.1.2).

5.2.3.4 Isobaric thermal expansion coefficient

The isobaric thermal expansion coefficient appears in the equation for convective heat transfer in the open annulus (see 3.3.5). It is defined as

$$\beta = \frac{1}{V} \frac{\partial V}{\partial T} \Big|_p = - \frac{1}{\rho} \frac{\partial \rho}{\partial T} \Big|_p. \quad (5.30)$$

For the liquid phase this derivative is determined numerically.

For an ideal gas β can be directly calculated from the temperature and the equation is simplified to

$$\beta = \frac{1}{T}. \quad (5.31)$$

5.2.4 Enthalpy of the geofluid

The total specific enthalpy of the geofluid is calculated by combining the specific enthalpies of gas phase and liquid phase according to their mass fractions:

$$h = (1 - x)h'(p, T, X') + x \cdot h''(p, T, X'') \quad (5.32)$$

Enthalpies of boundary surface, gas solution and dilution are not considered.

5.2.4.1 Enthalpy of the gas phase

Enthalpy of the gas phase is modelled as the enthalpy of an ideal mixture of ideal gases, i.e. it is calculated as the mass weighted average of the individual gas enthalpies including water.

$$h'' = \sum_{\alpha=1}^{N_g} h''_\alpha X''_\alpha. \quad (5.33)$$

The individual gas enthalpies are calculated using ideal gas functions in the MSL³⁶. The documentation regarding this refers to a NASA report (McBride et al., 2002).

5.2.4.2 Enthalpy of chloride solutions

The specific enthalpy of a sodium chloride solution can be calculated using the aforementioned equation by Driesner (2007).

For other chlorides, let alone multi-salt solutions, such a correlation is not available. Depending on the available data, brine enthalpy can be composed via temperature dependent solution heat (see B 7) or via temperature dependent heat capacity. The latter approach is used in the present model and explained here.

³⁶ Modelica.Media.IdealGases.SingleGases

5.2.4.3 Calculation of the enthalpy of the liquid phase using apparent molar enthalpy

The apparent or partial molar enthalpy is a convenient quantity for the calculation of the specific enthalpy of a mixture with variable composition, as it directly quantifies the influence of the molality of one component on the enthalpy of the mixture. Smith et al. (2001) defined it as:

$$H_{\phi}^{\alpha} = \frac{\partial H_{\text{brine}}}{\partial n_{\alpha}} = \frac{\Delta(mh_{\text{brine}})}{n_{\text{salt}}} \quad (\text{Unit: J/mol}). \quad (5.34)$$

H_{brine} is the total enthalpy and n_{α} is the mole number of the respective component.

Assuming constant partial molar enthalpies with respect to n_{α} , the enthalpy of an aqueous solution is consequently expressed as:

$$H_{\text{brine}}(p, T, n_{\alpha}) = H_{\text{H}_2\text{O}}(p, T) + \sum H_{\phi}^{\alpha} n_{\alpha} \quad (5.35)$$

Division by mass of the solution provides the specific enthalpy:

$$\begin{aligned} h_{\text{brine}}(p, T, b_{\alpha}) &= h_{\text{H}_2\text{O}}(p, T) \frac{m_{\text{H}_2\text{O}}}{m} + \sum H_{\phi}^{\alpha} \frac{n_{\alpha}}{m_{\text{H}_2\text{O}}} \frac{m_{\text{H}_2\text{O}}}{m} \\ &= X'_{\text{H}_2\text{O}} \left(h_{\text{H}_2\text{O}}(p, T) + \sum_{N_s} H_{\phi}^{\alpha} b_{\alpha} \right). \end{aligned} \quad (5.36)$$

This approach (like the alternative in B 7) neglects any mutual influence of the chlorides. Both approaches are based on the enthalpy of pure water, but they ignore the increase of evaporation temperature due to salinity. That is why a small range between the evaporation temperatures of pure water and brine is not covered by the model. In that range pure water would evaporate, whereas the salinity prevents evaporation of the brine.

This approach also allows the implementation of the equation by Driesner (2007) for NaCl solutions as the basic enthalpy h_{Dr} instead of the pure water enthalpy $h_{\text{H}_2\text{O}}$:

$$h_{\text{brine}}(p, T, \mathbf{b}) = \frac{(1 + b_{\text{NaCl}} M_{\text{NaCl}}) h_{\text{Dr}}(p, T, b_{\text{NaCl}}) + \sum_{N_s-1} b_{\alpha} H_{\phi}^{\alpha}(p, T, n_{\alpha})}{1 + \sum_{N_s} b_{\alpha} M_{\alpha}} \quad (5.37)$$

Alternatively expressed with mass fractions:

$$h_{\text{brine}}(p, T, \mathbf{b}) = (X'_{\text{H}_2\text{O}} + X'_{\text{NaCl}}) h_{\text{Dr}} \left(p, T, \frac{X_{\text{NaCl}}}{X_{\text{H}_2\text{O}} + X_{\text{NaCl}}} \right) + X'_{\text{H}_2\text{O}} \sum_{N_s-1} H_{\phi}^{\alpha} b_{\alpha} \quad (5.38)$$

The enthalpy of water used by the enthalpy model by Driesner is calculated using the IAPWS97 formulation (Wagner et al., 2000) provided by the MSL.

Unfortunately, data for the partial molar enthalpy of other salts is not available. However, apparent molar heat capacity data can be found and used instead.

5.2.4.4 Apparent molar heat capacity

By analogy to eq. 5.34 the apparent molar heat capacity is defined as change of absolute heat capacity of an arbitrary amount of solution caused by the addition of salt:

$$C_{p,\phi}^{\alpha} := \frac{\Delta C_{p,\text{brine}}}{n_{\text{salt}}} = \frac{\Delta(m c_{p,\text{brine}})}{n_{\text{salt}}} \quad (\text{Unit: J/(K}\cdot\text{mol)}). \quad (5.39)$$

Consequently, by analogy to eq. 5.36, the specific heat capacity of the brine can be expressed with the specific enthalpy of water and the apparent molar heat capacities of the respective salts (assumed to be constant with respect to b_{α}):

$$c_p = X'_{\text{H}_2\text{O}} \left(c_p^{\text{H}_2\text{O}} + \sum C_{p,\phi}^{\alpha} b_{\alpha} \right) \quad (5.40)$$

Using the symmetry of mixed equations it can be converted to the specific molar enthalpy by integration:

$$C_{p,\phi}^{\alpha} = m \left. \frac{\partial}{\partial n_{\alpha}} \frac{\partial h}{\partial T_{\alpha}} \right|_p = \left. \frac{\partial^2 m h}{\partial T \partial n_{\alpha}} \right|_p = \frac{\partial H_{\phi}^{\alpha}}{\partial T} , \quad (5.41)$$

$$H_{\phi}^{\alpha}(T) = H_{\phi}^{\alpha}(T_0) + \int_{T_0}^T C_{p,\phi}^{\alpha} dT . \quad (5.42)$$

The integration constant $\bar{H}_i(T_0)$ contains the solution and dilution heat. It may be set to an arbitrary value if the enthalpy function is used to calculate enthalpy differences due to temperature change without concentration change, because then the $\bar{H}_i(T_0)$ will cancel out. Otherwise it can be taken from literature (Sanahuja and Gómez-Estévez, 1986; Sinke et al., 1985).

The apparent molar heat capacities of aqueous CaCl_2 and KCl solutions are calculated from a function fitted to the values given in White et al. (1987a) and White et al. (1987b):

$$C_{p,\phi}^{\alpha} = (b_{\alpha}^{a_1} + a_2)(a_3 - a_4(a_5 - T)^{-1}) , \quad (5.43)$$

The fitting parameters for eq. 5.43 and 5.44 are given in Table 5. Integration of the fitting function (eq. 5.42) provides the apparent molar heat capacities required for eq. 5.35:

$$H_{\phi}^{\alpha}(T) = H_{\phi}^{\alpha}(T_0) + ((b_{\alpha}^{a_1} + a_2) \left(a_3(T - T_0) - a_4 \ln \left(\frac{a_5 - T}{a_5 - T_0} \right) \right)) , \quad (5.44)$$

Table 5: Validity ranges and fitting parameters for apparent molar heat capacity (eq. 5.43) and apparent molar enthalpy (eq. 5.44)

	KCl	CaCl₂
$T_{\min} / [\text{K}]$	325	306.8
$T_{\max} / [\text{K}]$	600	602.7
$p_{\min} / [\text{bar}]$	164	21.2
$p_{\max} / [\text{bar}]$	178.8	178.2
$b_{\min} / [\text{mol/kg}]$	0.1005	0.1011
$b_{\max} / [\text{mol/kg}]$	3.0073	3.0284
a_1	0.09818	-0.001977
a_2	-1.244	-0.9958
a_3	-327.9	1373
a_4	-1.31e+05	6.736e+06
a_5	628.8	628
R^2	0.9759	0.9957

5.2.4.5 Heat capacity

Expressing eq. 5.40 based on specific heat capacity of a sodium chloride solution instead of pure water by analogy to eq. 5.38 gives

$$c_p = (X'_{\text{H}_2\text{O}} + X'_{\text{NaCl}}) c_{p,\text{Driesner}} \left(p, T, \frac{X_{\text{NaCl}}}{X_{\text{H}_2\text{O}} + X_{\text{NaCl}}} \right) + X'_{\text{H}_2\text{O}} \sum C_{p,\phi}^\alpha b_\alpha . \quad (5.45)$$

The resulting heat capacity of the GrSk fluid is given in 7.1.

5.2.5 Temperature

In several places in the brine circuit model the temperature T has to be calculated from pressure and specify enthalpy, because they are used to define the thermodynamic state, but property functions require p and T (see 3.2.3). In that case $T(p, h, X)$ is calculated by numerical inversion of the function of specific enthalpy (5.2.4). The employed MODELICA compiler DYMOLA is capable of this inversion, but it may fail at discontinuities, as they occur at the threshold between single-phase and two-phase state. Additionally, as in the case of the VLE calculation, even if the inversion is successful in an isolated test case, that does not mean it will also work for the complete model. Therefore, the inverse function (see E 2.1) $T(p, h, X)$ is assigned to the enthalpy function. It is called when p and h are given and it determines T by using an bisection algorithm (see D 2.3 for details).

5.2.6 Thermal conductivity

The thermal conductivity λ of the brine is used in the calculation of the heat transfer in the boundary layer and in the open annulus.

λ is calculated using the water model of the MSL 3.2. Neglecting the salinity has little impact here because salinity dependence is weak for λ compared to c_p (Yusufova et al., 1975).

For the gas in the open annulus λ is calculated by the simple air media model³⁷ of the MSL.

5.2.7 Viscosity

The viscosities of the liquid phase and the gas phase are calculated and used separately, so no effective two-phase viscosity³⁸ is needed.

5.2.7.1 Liquid viscosity

The viscosity of the liquid phase is assembled from the viscosities of the binary solutions of NaCl, KCl (Mao and Duan, 2009) and CaCl₂ (Zhang et al., 1997). They calculate a relative viscosity $\tilde{\eta}$, the viscosity ratio of solution and pure water:

$$\eta_\alpha = \eta_{\text{H}_2\text{O}} \cdot \tilde{\eta}_\alpha(p, T, b'_\alpha) . \quad (5.46)$$

Instead of the proposed linear mixing rule weighted by molalities a logarithmic mixing rule weighted by molar or mass fraction γ is applied:

$$\ln \eta' = \gamma_\alpha \sum_{N_s} \ln \eta_\alpha \left(p, T, \frac{b'_\alpha}{\gamma_\alpha} \right) . \quad (5.47)$$

³⁷ `Modelica.Media.Air.SimpleAir`

³⁸ Mixing rules exist (Kraume, 2003), but they can only be approximate, because two-phase viscosity depends not only on the medium property gas volume fraction, but also on flow properties like flow regime and bubble distribution.

γ can be either the molar fraction or the mass fraction of the respective of the binary salt solution with respect to all salts:

$$\gamma_{\alpha} = \frac{b'_{\alpha}}{\sum_{N_s} b'_{\beta}} \quad \text{or} \quad \gamma_{\alpha} = \frac{X'_{\alpha}}{\sum_{N_s} X'_{\beta}}. \quad (5.48)$$

That mixing rule, weighted by molar fraction, has been proposed by Arrhenius for binary mixtures. It showed good results for that application (Viswanath et al., 2006). Here the mixing rule has been extended to solutions of more than two salts, in analogy to the mixing rules for density (5.2.3.3) and enthalpy (5.2.4.3). As the validation of the viscosity function for binary mixtures in 6.2 shows, the molar weighted mixture rule reproduces measured data slightly better than the mass weighted one. It is therefore used in the model.

The mixing rule 5.49 can be written explicitly for η' as:

$$\eta' = \eta_{\text{H}_2\text{O}} \prod_{N_s} \left(\tilde{\eta}_{\alpha} \left(p, T, \frac{b'_{\alpha}}{\gamma_{\alpha}} \right) \right)^{\gamma_{\alpha}}. \quad (5.49)$$

The mixture viscosity is hence calculated from the viscosities of binary solutions that are mixed in a ratio that results in the given mixture composition. This assumption does not unambiguously specify the composition of the binary solutions b'_{α} , as the water fraction of the mixture can be freely distributed among the binary solutions. In the presented viscosity model the water mass is divided between the binary solutions according to the amount of the respective salt represented by φ , so that in the case of molar weight all binary solutions have the same molality $b = \sum_{N_s} b'_{\beta}$.

The viscosity of pure water $\eta_{\text{H}_2\text{O}}$ for this approach is provided by the MSL. The liquid molality b'_i in the argument of the binary viscosity function η_i is converted from the respective liquid mass fraction X'_i (see A 1).

5.2.7.2 Gas viscosity

Viscosity of the gas phase is provided by the moist air media model of the MSL (Casas et al., 2005).

5.3 Reservoir model

The reservoir is represented in the model by a mass flow source/sink and a flow resistor. The latter is connected to the end of the lowest well section. That means the distributed inflow from several horizons is represented by one point at bottomhole.

The source usually has a predefined (constant or time dependent) temperature or specific enthalpy, pressure and mass flow with constant composition.

Following eq. 3.37, the resistor creates a pressure proportional to the volumetric flow rate. The bottomhole pressure is assumed to be a linear function of the extracted/injected volume flow rate. It is parameterized by the productivity/injectivity index.

$$p_{bh}^P = p_{Res} - \frac{\dot{V}}{PI} \quad (5.50)$$

$$p_{bh}^I = p_{Res} + \frac{\dot{V}}{II} \quad (5.51)$$

The unit of the resistivity (= productivity/injectivity) index is $\text{m}^3/(\text{h} \cdot \text{MPa})$, i.e. volume flow rate per pressure drop.

Reservoir depletion can be considered by decreasing the reservoir pressure.

Resistivity can be set in the resistor component as a constant or not at all. In the latter case it should result from the downstream pressure or be set outside of the model, as a potentially time-dependent function.

5.4 Wellbore model

The wellbore model aims at calculating pressure loss and temperature loss of the fluid in the well. The well is considered radially symmetric, with a constant geometry that is not affected by temperature (heat strain) or pressure (ballooning).

As explained in section 1.3, the effect of the gas fraction on the pressure in the wellbore is two-fold. It reduces the weight of the fluid in the well and it increases the friction pressure drop. Because the influence of friction is expected to be minor compared to the effects of gravitation and heat loss, this model focuses on the calculation of liquid density, gas fraction and heat flow while not considering slip explicitly. Hence the homogenous two-phase model (see 3.1.1) with variable gas fraction is used for the wellbore.

Paglianti et al. (1995) state that ‘assuming homogenous flow without slip between the phases gives rise to serious errors’. However, their study deals with high gas contents: up to 7 % wt. compared to approximately 0.1 %³⁹ in the GrSk scenario. In the GrSk scenario, due to the high pressure in the bigger part of the well, gas volume fraction is expected to remain small so that bubbly flow with low slip occurs and the error by neglecting slip is limited. The effect of slip in the GrSk scenario on the homogenous density and on the static head has been estimated to be not insignificant at the wellhead ($\approx 5.3\%$) but small ($\approx 1.6\%$) on the pump load (see C 4), while the effect on wellhead temperature is not visible (see C 5). The slip effect on friction is included in the two-phase friction model applied here (see 5.4.4).

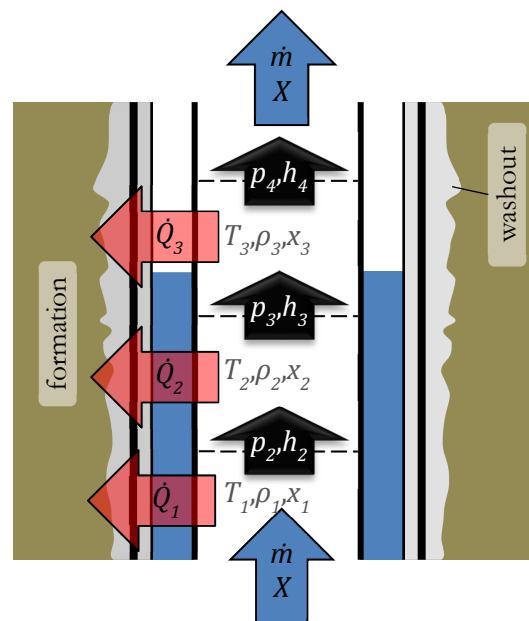


Fig. 13: Thermo-hydraulic wellbore model (one section)

³⁹ Corresponds to a gas volume fraction of 50 % at standard conditions (see also section 4.2).

The flow is modelled as being non-isothermal, one-dimensional, quasistatic and homogenous, but with potentially two phases formed by phase transition. That means, a uniform velocity (no slip), pressure and enthalpy are assumed for both phases over a cross-section.

The hydraulic problem of a vertical flow can only be solved analytically for constant density or a density with analytically simple pressure dependence. Given the complex temperature dependent density function (5.2.3), which requires coupling with the thermal part, a numerical approach is imperative. Therefore, every well section is sub-divided in elements (5.4.1). Pressures/temperatures along the well and at the wellhead pressure are calculated by subtracting the pressure/temperature drop along the well from the bottomhole pressure by applying the balance equations of mass, energy and momentum given in chapter 3.1 on each element.

The wellbore is divided in sections (see Fig. 11), so that each section has homogenous geometrical parameters such as length, diameter and inclination as well as homogenous thermal parameters of the connected formation (Resulting in 23+14 sections in the GrSk case). The wellbore model is coupled with the formation model via the interface temperature T_{if} and heat flux \dot{q}_{if} , both varying with depth.

For the heat flow calculation within the well the well sections are assigned constant thermal parameters, namely diameters and thermal conductivities of several layers of steel, cement and gas or liquid in the annulus. Heat flow within the well completion is also modelled as quasistatic, while heat flow in the formation is modelled as transient, as will be explained in chapter 5.4.5 and 5.5.1, respectively. The discretization of the formation is described in 5.5.6.

5.4.1 Axial discretization

Every wellbore section is divided into elements. All pipe elements of one well-section have the same length. A good value for the approximate element length has been found to be 25 m (see D 3). The error conditions postulated in C 1, C 2, C 3 are monitored during simulation.

5.4.2 Balance equations

In order to avoid an implicit equation system, a finite difference forward-space/upstream scheme is applied. That means, all variables (p , T , ρ , X) are assumed to be constant over an element and to have the inflow values of the respective section (= outflow values of the previous section). Velocity and temperature profiles are assumed to be fully developed, i.e. position within the pipe is irrelevant for friction and heat flow calculations.

The balances are calculated on each discretization element sequentially, usually in flow direction. Inflow values are known and outflow values are calculated and passed on to the next element.

The balance equations from chapter 3.1 are:

Mass balance:

$$\dot{m}_{i+1} = -\dot{m}_i \quad (5.52)$$

Momentum balance:

An explicit discretized version of the momentum balance is obtained by neglecting the kinetic gradient and applying an upstream scheme, i.e. setting the average density and velocity to their upstream values ($u_m = u_1$ and $\rho_m = \rho_1$):

$$p_{i+1} = p_i - g\rho_i \sin \varphi \Delta s - f \frac{w_i^2 \rho_i}{2d} \Delta s \quad (5.53)$$

The errors in the pressure calculation made by these three assumptions are estimated in C 1, C 2 and C 3 and the following error conditions eq. C.87 and C.90 have been derived:

$$\left| \frac{\rho_{i+1}}{\rho_i} - 1 \right| \stackrel{!}{<} 2e_{\max}$$

and

$$\frac{\rho_{i+1}}{\rho_i} - 1 \stackrel{!}{<} \frac{A^2 g \sin \varphi \rho^2 \Delta s}{\dot{m}^2} e_{\max}.$$

They limit the density change and the element length for a given maximum error e_{\max} in pressure calculation.

Energy balance:

The energy equation without the kinetic contribution is explicit in axial direction, but forms an implicit equation system in radial direction with the formation heat transfer equations:

$$h_{i+1} = h_i + \frac{\dot{q}_i \pi d \Delta s}{\dot{m}} - g \sin \varphi \Delta s \quad (\dot{m} > 0) \quad (5.54)$$

In the case of zero mass flow thermal equilibrium between fluid and well completion is assumed. Hence the fluid temperature is set to the interface temperature, which is calculated by the formation model:

$$T_2 = T_{if,1} \quad (\dot{m} = 0). \quad (5.55)$$

The equations are implemented in a MODELICA model (not in a function); therefore, inputs and outputs as well as the order of solution are not predefined. So instead of defining the fluid state at the inflow of the well (bottomhole in production well), it could easily be set at the outflow (wellhead in production well). However, this would make the equation system implicit and require iterative solution, which is not unlikely to fail for reasons described in 5.1.4.

5.4.3 Kinetic contribution

The density change due to evaporation or degassing causes acceleration of the fluid. This creates an additional pressure drop which also affects enthalpy. For low gas fractions and velocities these effects are very small and therefore usually neglected in the model. The kinetic contributions in the balances of energy and momentum can, however, be activated, which will make the equations explicit (for explanation and consequences see 5.1):

Momentum balance (eq.B.37) with kinetic head:

$$p_2 = p_1 - g \rho_1 \sin \varphi \Delta s - f \frac{w_1^2 \rho_1}{2d} \Delta s - (\rho_2 w_2^2 - \rho_1 w_1^2). \quad (5.56)$$

Energy balance (eq. 3.5) with optional kinetic part:

$$h_2 = h_1 + \frac{\dot{q}_i \pi d \Delta s}{\dot{m}} - g \sin \varphi \Delta s - \frac{w_2^2 - w_1^2}{2}. \quad (5.57)$$

If the kinetic head is neglected, the error conditions C.84 and C.93 are monitored.

5.4.4 Friction

Several friction models have been implemented and can be selected: The single-phase equation for turbulent flow by Prandtl (1925), a simple two-phase equation by Dukler et al. (1964), the two-phase equation by Chisholm and the more complex equation by Friedel (1978), both recommended in the VDI heat atlas (Wellenhofer and Muschelknautz, 2010). None of the equations requires identification of flow regimes. The first and the last one are reproduced here. The equation by Friedel has been used in the simulations.

Friedel (1978) adopted the approach by Lockhart and Martinelli (1949) by first calculating a two-phase multiplier Φ_L^2 , which is then multiplied with a single-phase pressure drop or here the friction factor f (see 2.1.2):

$$f_{2p} = \Phi_L^2 \cdot f_{1p} . \quad (5.58)$$

The single phase friction factor f_{1p} is calculated for liquid turbulent flow with the equation by Prandtl & Kármán using the liquid superficial velocity w_s' (i.e. assuming the total mass flow to be liquid and to cover the whole cross-section of the pipe):

$$f_{1p} = \frac{0.309}{\log\left(\frac{Re'}{7}\right)^2}, \quad (5.59)$$

where

$$Re'' = w_s'' \frac{d_{\text{hyd}} \rho''}{\eta''} = \frac{\dot{m}'' \cdot 4 d_{\text{hyd}}}{\pi d_{\text{hyd}}^2 \eta''}. \quad (5.60)$$

The liquid viscosity as well as the gas viscosity (used in the next equation) is provided by the geofluid model (see 5.2.6).

The two-phase multiplier is determined by:

$$\Phi_L^2 = (1 - \dot{x})^2 + \dot{x}^2 \frac{\zeta'' \rho'}{\zeta' \rho''} + \frac{2.3667 \dot{x} (1 - \dot{x})^{0.24} \left(\frac{\rho'}{\rho''}\right)^{0.8} \left(\frac{\eta''}{\eta'}\right)^{0.22} \left(1 - \frac{\eta''}{\eta'}\right)^{0.89}}{Fr'^{0.047} We'^{0.033}}. \quad (5.61)$$

The Froude number⁴⁰ and the Weber number are also calculated with the superficial liquid velocity:

$$Fr' = \frac{w_s'^2}{g d_{\text{hyd}}} = \frac{16 \cdot \dot{m}^2}{g \rho'^2 \pi^2 d_{\text{hyd}}^5}, \quad (5.62)$$

$$We' = \frac{w_s'^2 \rho' d_{\text{hyd}}}{\sigma} = \frac{16 \cdot \dot{m}^2}{\rho' \pi^2 d_{\text{hyd}}^3 \sigma}. \quad (5.63)$$

The surface tension is provided by the water property model of the MSL (Wagner et al., 2000).

The friction factors of liquid ζ' and gas ζ'' are calculated from their respective Reynolds numbers Re' and Re'' :

$$\zeta'' = \begin{cases} \frac{64}{Re''} & \text{if } Re'' \leq 1055 \\ \left(0.86859 \cdot \log\left(\frac{Re''}{1.964 \cdot \log Re'' - 3.825}\right)\right)^{-2} & \text{else} \end{cases}. \quad (5.64)$$

Based on measurements, this friction equation includes slip effects.

⁴⁰ This is the definition of Fr used in fluid mechanics. The alternative definition is its square root.

5.4.5 Heat flow to and within well completion

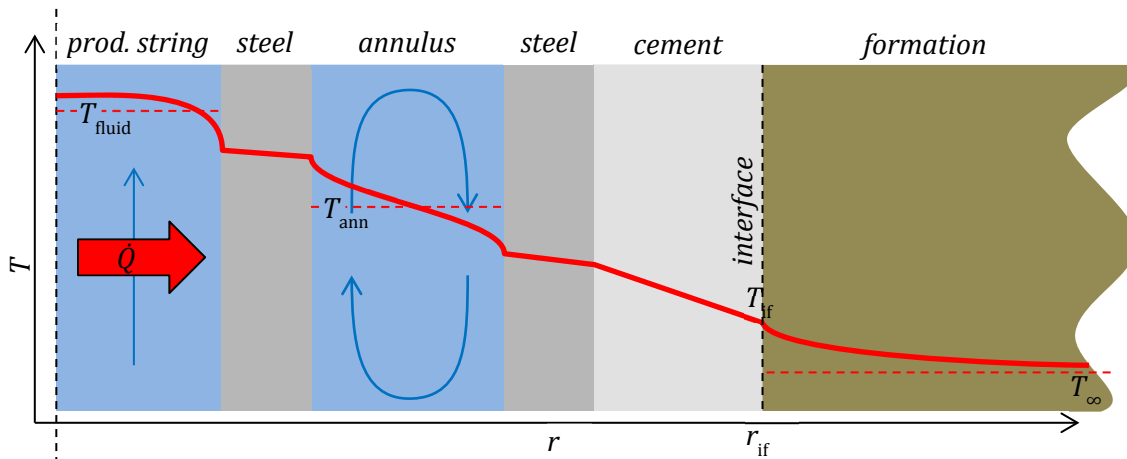


Fig. 14: Heat flow in the well completion (with open annulus)

Heat flow in the well completion is determined by the thermal interaction of the flow boundary layer, the concentric layers of the well completion (pipe walls, cement, open annulus) and the formation. According to eq. 3.22 and 3.20 heat flow depends on the thermal conductivities of the conducting materials, the heat transfer coefficient of the boundary layer and the temperature gradient between fluid and formation.

Heat flow in the wellbore is described by steady-state equations with transient boundary conditions, whereas in the formation transient heat conduction equations are applied. The well completion is represented by radial-symmetric isotropic multi-layered cylinders. The cylinders have constant thermal conductivity λ except for the open annulus, where free convection is considered and λ is calculated from geometry and fluid properties.

Heat flow between fluid and formation is calculated from the heat transfer coefficient of the flow boundary layer htc_{fw} , the thermal transmittances U_j of the well components (tubing, cement, open annulus) and the difference between the temperatures of the fluid T_{fluid} and the interface cement-formation T_{if} . Within each well section thermal properties are axially constant, but individual for each of the concentric layers.

With the coefficient for the fluid-wall heat transfer $htc_{fw}^{r_1}$ (referring to the hydraulic pipe diameter $2 \cdot r_1$) according to eq. 3.25 the heat flux through the interface \dot{q}_{if} is calculated with:

$$\dot{q}_{if} = -\frac{1}{r_{if}} \left(\frac{1}{htc_{fw}^{r_1} r_1} + \sum \frac{\ln(r_{j+1}/r_j)}{\lambda_j} \right)^{-1} \cdot (T_{if} - T_{fluid}), \quad (5.65)$$

with r_j being the inner diameters of the respective layers (tubing, cement, open annulus).

Heat flow is positive when the fluid is warmed up. T_{if} is the temperature of the interface between outer (anchor) cement layer and formation. T_{if} is calculated by the formation model or alternatively directly specified by a temperature profile $T(z)$.

5.4.6 Heat transfer flow from fluid to wall

Several boundary layer heat transfer models have been implemented and can be selected:

- The approximate solution by Stephan for laminar flow as given in Dubbel (2001) (appendix B 3.1).
- The simple equation by McAdams/Pertukhov for turbulent flow as given in Dubbel (2001) (appendix B 3.2).

The equations recommended by the VDI-Heat Atlas (Gnielinski, 2010):

- A simplified equation for estimation purposes (see appendix B 3.3).
- An equation for both laminar and fully developed turbulent flow, including the transition (appendix B 3.5).

Each sub-model returns a Nusselt number, which is converted to a heat transfer coefficient using its definition (eq. 3.21), which is then inserted in eq. 5.65.

Slightly different from the definition (see B 3), the material properties are calculated for flow temperature instead of the mean temperature of flow and wall, in order to avoid an implicit equation. The effective two-phase values are used, except for the viscosity where only the liquid phase value is used.

5.4.7 Washout

In the model the washout is either specified as an average value per well section or read for each element from a caliper log. The washout value is converted to the actual borehole diameter or radius of the well-formation interface by inverting eq. 3.27:

$$d_{if} = d_{\text{drill}} \sqrt{W + 1} \quad (5.66)$$

The increased interface diameter affects the heat flow calculation in both the well-completion (eq. 5.65) and in the formation (eq. 5.78 and 5.86).

5.4.8 Thermal conductivities in well completion

The thermal conductivities of the well completion, consisting of steel and cement, are assumed to be constant. In order to represent an imperfect heat transfer at the interfaces between steel, cement and formation, their thermal resistances can be represented by additional layers of water or air.

The cement properties are different for each well section. Density is the dominant parameter for thermal conductivity of cement. The cement density can be adapted to the specific requirements in the respective section by adding different materials (Nelson, 1986). If it is known, the thermal conductivity of the cement can be estimated from its density via the ρ - λ -relation given in a chart by Nelson (1986). The curve can be described by the following polynome:

$$\frac{\lambda(\rho)}{1 \text{ Wm}^{-1}\text{K}^{-1}} = 4.12 \cdot 10^{-7} \left(\frac{\rho}{1 \text{ kg m}^{-3}} \right)^2 - 2.83 \cdot 10^{-4} \frac{\rho}{1 \text{ kg m}^{-3}} + 0.306 \quad (5.67)$$

5.4.9 Heat flow in open annulus

As explained in section 3.3.5 heat flow in the open annulus depends on the liquid level. Hence, it has to be determined before the heat flow can be calculated. The liquid level depends on the pressure at the pump inlet and the density of the annulus fluid. Assuming a gas density of zero, the liquid level is found where annulus fluid pressure p^{ann} equals top annulus pressure $p_{\text{top}}^{\text{ann}}$. p^{ann} is calculated from the pump inlet pressure p_{pi} by integrating static pressure head at in-situ temperature upwards from the pump:

$$p_{i+1}^{\text{ann}} = \max \left(p_{\text{top}}^{\text{ann}}, p_{\text{pi}} - \sum_{i=1}^j \rho(p_i^{\text{ann}}, T_i^{\text{ann}}) g (z_{i+1} - z_i) \right) \quad (5.68)$$

When the depth of the liquid level is known, the heat flow in the open annulus is calculated with the equation for radiation and free convection as described in 3.3.4.

The liquid/gas properties needed there and for the hydraulic calculation above are calculated for in-situ conditions with the geofluid model. The in-situ conditions are defined by pressure, temperature and composition in the annulus:

Annulus pressure p^{ann} is provided by eq. 5.68. Annulus temperature is taken from the heat flow calculation as the linear average between the temperatures at the inner and the outer wall of the annulus:

$$T_i^{\text{ann}} = T_i + \dot{q}_i \left(\frac{1}{U_{i,1}} + \frac{0.5}{htc_{i,2}} \right). \quad (5.69)$$

The heat transfer coefficient of the annulus $htc_{i,2}$ depends again on the effective thermal conductivity λ_c of the annulus. This makes the annulus heat transfer model implicit in radial direction. This does not pose a problem, since the equations describing transient formation heat flow are implicit anyway.⁴¹

The annulus liquid has the same composition as the brine at the pump inlet, but without gas content, as it is assumed to have degassed. Therefore, the time consuming VLE calculation can be skipped here. It would otherwise slow down the computation significantly, considering the repeated calls due to iterative solution of the implicit heat transfer model.

The annulus above the liquid level is filled by the gas which has degassed from the liquid. Therefore, the annulus gas is assumed to have the composition of the gas phase at the pump inlet.

5.5 Formation model

The formation is represented by a vertical array of transient 1D-models of conductive radial heat flow, as vertical heat flow is not considered (see 7.2.4 for justification). The vertical discretization is the same as in the wellbore model. Temperature is vertically constant over an element. Vertical discretization is the same as in the wellbore model.

The thermal properties of the formation are described by density ρ , specific heat capacity c_p and thermal conductivity λ . They are horizontally constant and vertically constant per well section, considering the detailed lithology. λ may, however, be a function of temperature.

The formation model is coupled with the wellbore model via the interface temperature T_{if} and heat flux \dot{q}_{if} , both varying with depth.

The formation model can be switched from transient to static or off (predefined interface temperature profile).

5.5.1 Transient model

The transient formation model solves eq. 3.35 for a constant temperature at the outer boundary (Dirichlet), the far-field formation temperature T_∞ .

$$T(r_\infty) = T_\infty. \quad (5.70)$$

T_∞ is either taken from a given temperature profile (read from file) or defined by a surface temperature (temperature at $z = 0$) and the geothermal gradient Γ :

$$T(r_\infty, z) = T_{z0} + \Gamma \cdot z. \quad (5.71)$$

The inner boundary condition is the heat flux \dot{q}_{if} at the interface cement-formation (Neumann condition):

⁴¹ However, if the open annulus model is used in the injection well with opposed flow direction, a large implicit system of equations is created, comprising the whole annulus in axial direction. The reason is: in the injection well sequential calculation starts at the wellhead while the heat flow in the open annulus depends on the pressure at the bottom of the annulus, which in turn is the outcome of the sequential calculation down the well. The solution of such a model is very slow. Predefining the annulus liquid level to a constant value avoids the axially implicit system.

$$-\dot{q}_{\text{if}} = \lambda \left. \frac{\partial T}{\partial r} \right|_{r_0}. \quad (5.72)$$

\dot{q}_{if} is not constant, because it depends on the temperature drop between the fluid and the cement-formation interface. \dot{q}_{if} is returned from the wellbore model for the interface temperature T_{if} , which is calculated by the formation model and passed to the wellbore model.

Because analytical solutions for the transient radial heat flow are only available for simple cases (see 2.3), the formation is discretized and thus the problem is converted to a system of coupled ordinary equations. MODELICA is designed for the solution of systems of ODEs⁴² and allows for the use of time derivatives, so temporal discretization is handled by the MODELICA solver.

The heat flow equation is radially discretized using the Finite Volume Method (5.5.6), which is more suitable than the Finite Differences Method (for comparison see 5.5.5).

5.5.2 Static formation heat transfer

For testing purposes the formation heat transfer model can be switched to a stationary mode. It then uses the analytical solution eq. 3.22. It was used to assess the discretization error in D 4.1.

For a constant thermal conductivity the interface temperature is then calculated as:

$$T_{\text{if}} = T_{\infty} + \frac{\dot{q}_{\text{if}}}{\psi^{\text{for}}} = T_{\infty} + \dot{q}_{\text{if}} \frac{\ln(r_{\infty}/r_{\text{if}}) \cdot r_{\text{if}}}{\lambda} \quad (5.73)$$

If thermal conductivity is temperature dependent or if temperatures within the formation are of interest, the formation is discretized and eq. 5.73 is applied per element.

The static solution corresponds to the transient solution after an infinitely long time, where heat flow at the interface and the outer boundary are in balance. Note that the choice of r_{∞} does influence the solution.

5.5.3 Thermal conductivity of the rock

The thermal conductivity changes with pressure and temperature. Pressure influence is relatively small compared to temperature dependence (Schön, 2004) and is therefore neglected. Temperature influence is taken into account with the temperature correction according to (Somerton, 1992):

$$\lambda(T) = \lambda_{20} - 10^{-3}(T - 293)(\lambda_{20} - 1.38)(\lambda_{20}(1.8 \cdot 10^{-3}T)^{-0.25\lambda_{20}} + 1.28)\lambda_{20}^{-0.64}. \quad (5.74)$$

It has been developed for sandstones. In the GrSk model it is therefore used for all geological layers except L04 and L05 (see Table 1).

5.5.4 Radial discretization

The semi-infinite domain of the formation is discretized with finite cell sizes and with a finite radius r_{∞} of the outer boundary. Badly chosen cell size and an insufficient r_{∞} can affect the transient solution. Coarse cells may add numerical diffusion (examined in D 4.1).

For a given radial element size the number of elements and hence computational cost increases with the increase of r_{∞} . Therefore, r_{∞} should be set as low as possible. On the other hand r_{∞} has to be large enough to guarantee the no-heat-flow condition at the outer boundary within simulation time, i.e. the

⁴² ordinary differential equations

'heat front' does not reach the outer boundary. A non-zero heat flow at the outer boundary will not change the temperature at r_∞ because it is fixed by the boundary condition. This eventually affects the heat flow at the inner boundary \hat{q}_{if} . Therefore, the heat flow at the outer boundary is monitored during calculation and when it exceeds a certain tolerance level, an error is thrown.

r_∞ must be larger than the propagation range of the heat flow, which depends on the heat flux from the well, the thermal parameters of the formation and simulation time. For the typical values of a geothermal well the heat front propagates with a velocity in the order of meters per days at the beginning. Propagation range of the heat flow and the velocity of the heat front have been estimated in D 4.2 and D 4.1.

When trying to minimize the number of radial elements while having a fine mesh near the well, radially exponentially increasing elements are an obvious choice. The radii of the elements grow from the interface radius r_i to the outer radius r_∞ following this rule:

$$r_j = r_{if} \exp\left(\frac{\ln r_\infty - \ln r_{if}}{n_r} j\right) \quad j = \{0, 1, 2, \dots, N_r\} \quad . \quad (5.75)$$

Consequentially, the number of elements N_r is calculated for a given inner and outer radius from a maximum radius growth ratio $a_{\max} = r_{j+1}/r_j$:

$$N_r = \text{ceil}\left(\frac{\ln r_\infty - \ln r_{if}}{\ln a_{\max}}\right) \quad . \quad (5.76)$$

The resulting ratio a between two neighbouring elements is generally not exactly a_{\max} , because N_r is required to be an integer. Rounding up (ceil) guarantees that $a \leq a_{\max}$. If a_{\max} is set below 1.4, the maximum discretization error with this FVM formulation is below 1 %, as the comparison with the analytic solution in D 4.1 shows.

5.5.5 Finite Volume Method vs. Finite Difference Method

The use of a finite difference scheme is the obvious way to discretize a partial differential equation. Applying it to a non-equidistant mesh on a radially symmetric domain is, however, not the standard case that can easily be found in literature. Although eventually not used in the model it has been done and is described in D 1. The FDM is limited in the element growth ratio absolutely (D 1.4), but it requires a rather low ratio anyway (D 4.1). It also requires a virtual mesh point outside the domain in order to implement a Neumann boundary condition with an error in the same order of magnitude as the finite differences.

The advantages of the FDM can be seen in the derivation shown below: The second derivative disappears and the first derivative can be written as central difference quotient with only two points. The FDM allows for an unproblematic handling of a non-equidistant grid and a non-constant conductivity, because the thermal conductivity does not have to be differentiated. The central difference quotient gives a lower order of error than an asymmetric one. The most important advantage is, however, the drastically reduced error on the same mesh, as shown in D 4.1. This reduces the number of radial elements for a given maximum error and therefore the computational load.

5.5.6 Finite volume formulation on non-equidistant grid:

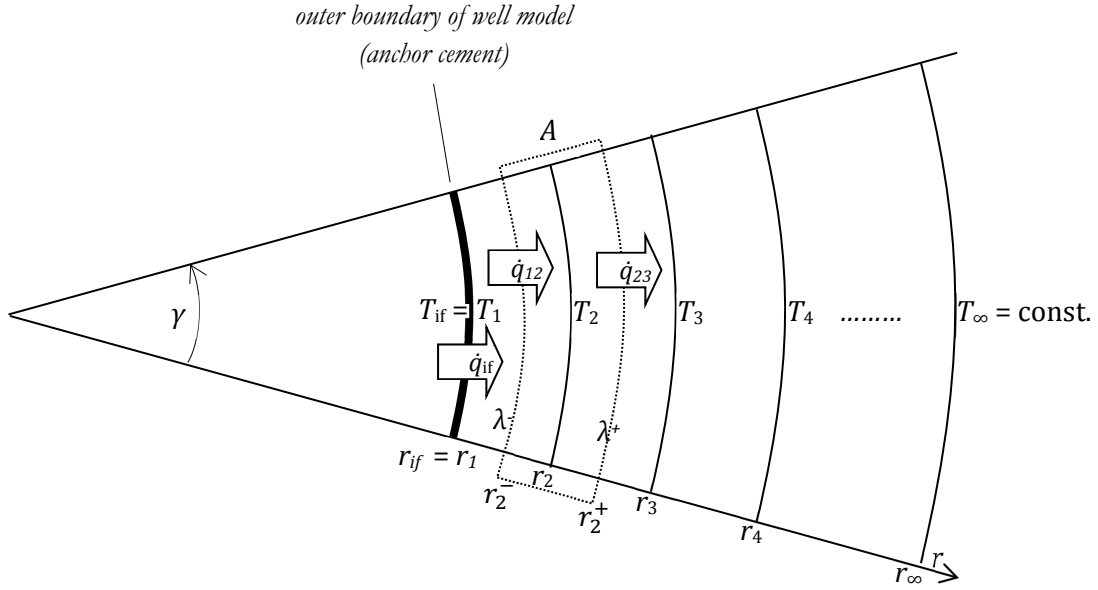


Fig. 15: Radial symmetric discretization of formation for Finite Volume Method

The transient one-dimensional heat equation (eq. 3.35) is integrated over the cell area A with $\gamma = 2\pi$.

$$\begin{aligned} \rho c_p \frac{\partial T}{\partial t} &= \frac{1}{r} \frac{\partial}{\partial r} \left(\lambda(T) r \frac{\partial T}{\partial r} \right) \\ \rho c_p \int_A \frac{\partial T}{\partial t} dA &= \int_0^{2\pi} \int_{\Delta r} \frac{1}{r} \frac{\partial}{\partial r} \left(\lambda(T) r \frac{\partial T}{\partial r} \right) dr r d\varphi \\ \rho c_p \frac{\partial}{\partial t} \int_A T dA &= 2\pi \int_{\Delta r} \frac{\partial}{\partial r} \left(\lambda(T) r \frac{\partial T}{\partial r} \right) dr. \end{aligned} \quad (5.77)$$

Mean temperature on A is T_i

$$\rho c_p A \frac{\partial}{\partial t} T_i = 2\pi \left(\lambda(T) r \frac{\partial T}{\partial r} \right) \Big|_{r_-}^{r_+} \quad (5.78)$$

With $A = \pi(r^{+2} - r^{-2})$:

$$\rho c_p \pi (r^{+2} - r^{-2}) \frac{\partial}{\partial t} T_i = 2\pi \left(\lambda^+ r^+ \left(\frac{\partial T}{\partial r} \right)_{r^+} - \lambda^- r^- \left(\frac{\partial T}{\partial r} \right)_{r^-} \right) \quad (5.79)$$

$$\rho c_p \pi (r^{+2} - r^{-2}) \frac{\partial}{\partial t} T_i = 2\pi \left(\lambda(T(r^+)) r^+ \left(\frac{\partial T}{\partial r} \right)_{r^+} - \lambda(T(r^-)) r^- \left(\frac{\partial T}{\partial r} \right)_{r^-} \right) \quad (5.80)$$

Assuming a linear temperature profile in the cell and placing its boundaries in the middle between the r_i :

$$\begin{aligned} \rho c_p \frac{\partial}{\partial t} T_i &= 2 \frac{\lambda \left(\frac{T_i + T_{i+1}}{2} \right) \frac{r_i + r_{i+1}}{2} \frac{T_{i+1} - T_i}{r_{i+1} - r_i} - \lambda \left(\frac{T_{i-1} + T_i}{2} \right) \frac{r_{i-1} + r_i}{2} \frac{T_i - T_{i-1}}{r_i - r_{i-1}}}{\left(\frac{r_i + r_{i+1}}{2} \right)^2 - \left(\frac{r_{i-1} + r_i}{2} \right)^2} \\ &= 8 \frac{\left(\dots \right)}{r_i^2 + 2r_i r_{i+1} + r_{i+1}^2 - (r_{i-1}^2 + 2r_i r_{i-1} + r_i^2)} \\ &= 8 \frac{\left(\dots \right)}{2r_i(r_{i+1} - r_{i-1}) + r_{i+1}^2 - r_{i-1}^2}. \end{aligned} \quad (5.81)$$

With constant thermal conductivity:

$$\rho c_p \frac{\partial}{\partial t} T_i = 4\lambda \frac{\frac{r_i + r_{i+1}}{r_{i+1} - r_i} (T_{i+1} - T_i) - \frac{r_{i-1} + r_i}{r_i - r_{i-1}} (T_i - T_{i-1})}{(2r_i + r_{i+1} + r_{i-1})(r_{i+1} - r_{i-1})}. \quad (5.82)$$

With $\lambda^+ = \lambda(T(r^+)) = \lambda(T^+) = \lambda\left(\frac{T_i + T_{i+1}}{2}\right)$:

$$\rho c_p \frac{\partial}{\partial t} T_i = 4 \frac{\lambda\left(\frac{T_i + T_{i+1}}{2}\right) \frac{r_i + r_{i+1}}{r_{i+1} - r_i} (T_{i+1} - T_i) - \lambda\left(\frac{T_{i-1} + T_i}{2}\right) \frac{r_{i-1} + r_i}{r_i - r_{i-1}} (T_i - T_{i-1})}{(2r_i + r_{i+1} + r_{i-1})(r_{i+1} - r_{i-1})}. \quad (5.83)$$

This system of ordinary differential equations can be solved if T_i and T_∞ are set by the boundary conditions. T_∞ is the far-field temperature (Dirichlet), whereas T_1 is determined using the Neumann boundary condition $\dot{q}(r_1) = \dot{q}_{if}$:

$$-\dot{q}(r^-) = \lambda(r^-) \left. \frac{\partial T}{\partial r} \right|_{r^-} \approx \frac{\lambda_1 + \lambda_2}{2} \frac{T_2 - T_1}{r_2 - r_1} \quad (5.84)$$

$$\dot{q}_{if} 2\pi r_1 = \dot{q}(r^-) 2\pi r^- \xrightarrow{\text{yields}} \dot{q}_{if} = \dot{q}(r^-) \frac{r_1 + r_2}{2r_1} \quad (5.85)$$

$$\dot{q}_{if} = -\lambda\left(\frac{T_1 + T_2}{2}\right) \frac{T_2 - T_1}{r_2 - r_1} \frac{r_1 + r_2}{2r_1} = \xrightarrow{\text{yields}} T_1 = \frac{\dot{q}_{if}}{\lambda\left(\frac{T_1 + T_2}{2}\right)} \frac{2(r_2 - r_1)r_1}{r_1 + r_2} + T_2. \quad (5.86)$$

5.6 Pump model

The pump is modelled as non-isentropic, but adiabatic. It has no physical height or length. The equations are as follows:

Mass conservation:

$$\dot{m}_1 + \dot{m}_2 = 0 \quad (5.87)$$

$$X_1 = X_2 \quad (5.88)$$

Momentum balance:

Δp_{ESP} , the pressure difference created by the pump is specified directly, by setting the outlet pressure p_2 or by using the controlled pump head (see below 5.6.1). If it is not specified, it will be calculated from the downstream conditions, creating an implicit equation system with the implications mentioned before (see 5.1.4).

$$p_2 - p_1 = \Delta p_{\text{ESP}} \quad (5.89)$$

Energy conservation:

In the isentropic case, assuming constant density, the enthalpy difference between inflow 1 and outflow 2 is, as derived in B 6.1:

$$h_{2,s} - h_1 = \frac{p_2 - p_1}{\rho_1}. \quad (5.90)$$

In the non-isentropic stationary case, the enthalpy difference is increased by losses that heat up the fluid. They are represented by the efficiencies η_{is} and η_{mot} :

$$h_2 - h_1 = \frac{p_2 - p_1}{\rho_1 \eta_{is} \eta_{\text{mot}}}. \quad (5.91)$$

The isentropic pump efficiency η_{is} specifies the friction losses in the pump. It is defined as the ratio of isentropic and non-isentropic enthalpy difference:

$$\eta_{is} = \frac{h_1 - h_{2,is}}{h_1 - h_2} \quad (\text{see B 6.3 or Baehr (2003)}). \quad (5.92)$$

η_{is} can be set as a constant value or calculated based on the production rate using an equation fitted to the pump characteristics.

The motor efficiency η_{mot} accounts for fluid warming caused by dissipation in the electric motor of the pump. It is defined as the ratio of the delivered rotational power and the electric power consumption:

$$\eta_{\text{mot}} = \frac{P_{\text{shaft}}}{P_{\text{el}}} \quad (5.93)$$

As by design the pumped fluid acts as pump engine coolant, it is assumed to absorb the dissipated energy completely. The heating effect caused by losses in the pump and the cable are estimated in B 6.5.

5.6.1 Controlled pump head

Instead of defining outlet pressure or pressure head directly, the pump model can be switched to control mode, meaning that the pressure head is adjusted so that the input on an extra connector attains a specified value, the setpoint value. In that way a desired downstream pressure determines the pump head without creating an implicit equation system (see 5.1.4). For example, in the brine circuit model that extra connector delivers a pressure value from a pressure gauge at the wellhead. Thus, $p_{\text{wh,set}}$, the setpoint well head pressure can be specified in the pump.

Instead of a classic PID-controller a simple I(ntegration)-controller was implemented using this equation:

$$p_{\text{head}} = p_{\text{head}}^0 + \frac{1}{\tau} \int_0^t (WHP_{\text{set}} - WHP(\tilde{t})) d\tilde{t} \quad (5.94)$$

Proportional control was omitted, because it would make the equation system implicit, as it depends on the current input value. Differential control is not used because it tends to generate high control values and thus brings p_{head} out of its allowed range. Consequently, the controller performance is rather poor, but sufficient for this application as long as no sudden pressure changes occur and the start value for the pressure head is set to a reasonable initial value.

5.7 Heat exchanger model

The heat exchanger is represented by a very simple model. It contains only the brine stream; pressure loss and heat extraction are predefined. Either the heat flow or the outlet temperature is defined directly or the latter is set via the boundary conditions. Pressure drop is set as a parameter. The implemented equations are as follows:

Mass conservation:

$$\dot{m}_1 + \dot{m}_2 = 0 \quad (5.95)$$

$$X_1 = X_2 \quad (5.96)$$

Energy conservation

$$\dot{m}_1(h_2(p_2, T_2) - h_1) = \dot{Q}_{HX} \quad (5.97)$$

Momentum balance

$$p_1 - p_2 = \Delta p_{HX} \quad (5.98)$$

5.8 Separator/degasser model

The degasser only transports the liquid part of the mass flow and generates a constant pressure loss. The separated gas is blown off. Hence, the degasser is the only component that does not fulfil mass conservation between inflow and outflow on the brine circuit. The implemented equations are as follows:

Mass conservation:

$$\dot{m}_2 = (1 - x_1)\dot{m}_1 \quad (5.99)$$

$$X_2 = X_1' \quad (5.100)$$

Energy conservation

$$h_2 = h'_1 \quad (5.101)$$

Momentum balance

$$p_1 - p_2 = \Delta p_{\text{sep}} \cdot \quad (5.102)$$

5.9 Model applicability (to other geothermal sites)

The model presented in this chapter was developed to represent the GrSk scenario. Nevertheless, emphasis was put on flexibility and versatility during implementation. If certain prerequisites are met, the model can also be adapted and applied to other locations by rearranging the components, changing parameters and/or adding further correlations for geometry and chemistry.

This work aimed at reproducing mid-term and long-term behaviour; hence the model is not suitable for simulating the short-term hydraulics during abrupt changes of the production rate, such as startup.

The simulation results can only be as good as the parameterization of the model. Hence site parameters (washout, cement density, stratigraphy, fluid composition) must be available to an extent and with a precision according to the desired precision of result. The consequences of incomplete parameterization and simplifying assumptions are investigated later in 8.

The presented model is applicable to reproduce geothermal sites that fulfil the following requirements:

- p , T in brine circuit are within validity range of property functions.
- The formation is radially homogenous and isotropic.
- The formation heat flow induced by the well is mainly conductive.
- The geofluid is mainly brine, i.e. an aqueous solution of salts and gases. Other constituents are physically irrelevant.
- Brine contains gas or stays completely liquid, but no flashing occurs (complete evaporation) (no oil), solid phase only in irrelevant amounts, no flash in well
- Brine contains NaCl, KCl, CaCl₂ or other salts for which correlations are available for: the apparent molar enthalpy, apparent molar volume, viscosity, influence on gas solubility.
- Brine contains CO₂, N₂, CH₄ or other gases for which correlations are available for solubility in brine.
- Slip between gas and liquid phase is low (for error estimation see C 4).

6 Model validation

This chapter presents the validation of the geofluid property model and the wellbore model presented in chapter 5 against values from literature (ternary solutions), from the laboratory (ternary solutions) and from field-tests (GrSk fluid). Lab measurements were conducted under atmospheric pressure and field data was gathered at the wellhead at up to 10 bar, with temperature not exceeding 90 °C. Hence, the range of available viscosity and density data does not include reservoir conditions. For pressure this is less of a problem as pressure sensitivity of density and especially of viscosity is low.

The wellbore model has been validated thermally with data from a circulation test of 7 days. The data could not be used for the hydraulic validation, because down-hole pressure was not measured during that test. The hydraulic validation was performed with data from another, shorter (3 h) measurement campaign, which in turn was not long enough for thermal validation.

6.1 Liquid phase density model validation

6.1.1 Comparison with data from the literature

Zhang, Chen and Han (1997) provide measured densities of aqueous solutions of sodium chloride + calcium chloride and potassium chloride + calcium chloride for different compositions and over ‘the entire concentration range’ at 25 °C. They have been compared to values calculated with the density model described in 5.2.3. The relative differences between the density model and the measured values are shown in Fig. 16. Except for three outliers the error is always positive and shows a consistent positive trend with increasing salinity. Salinity cannot increase further as the maximum is close to saturation. Hence, at 25 °C the calculation error does not exceed 1 % for any of the mixing ratios listed in the article.

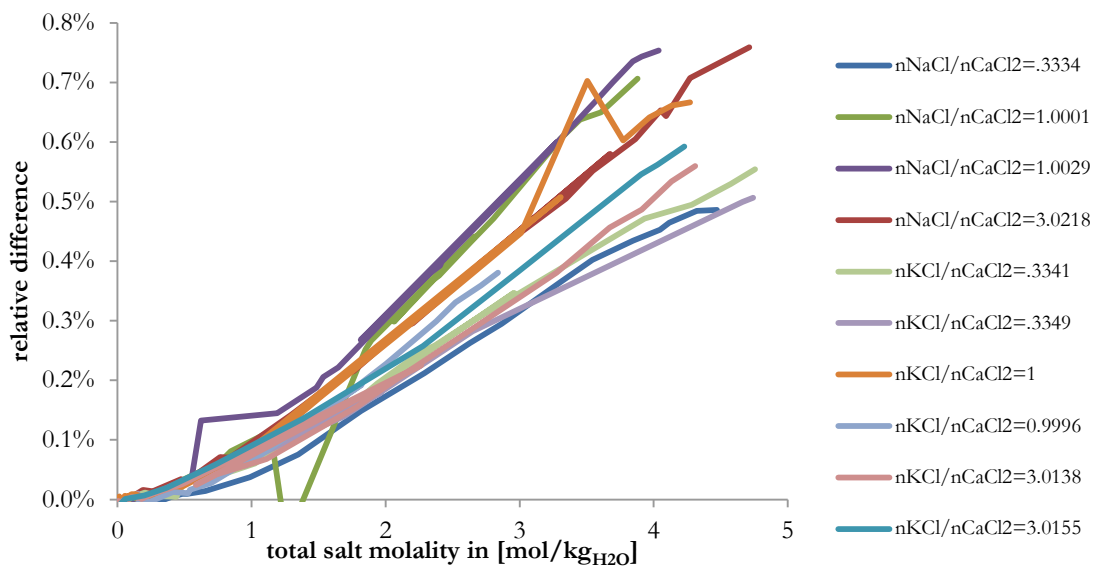


Fig. 16: Comparison of calculated densities with measured data (discrete values are shown with continuous lines)

6.1.2 Comparison with field measurements of the GrSk fluid

During the circulation test described in 6.4 density of the GrSk fluid has been measured online using a fluid-chemical monitoring device (Milsch et al., 2013), along with pressure and temperature. The employed density meter has a precision of 0.1 kg/m³ (PAAR, 2008). The composition of fluid samples taken during that test has been analysed and published by Feldbusch et al. (2013). It is given in Table 11.

The very long time-series of pressure and temperature were condensed by averaging values with similar p-T values⁴³ and outliers (possibly two-phase occurrence) were removed. The p-T range of the condensed data can be seen in Fig. 17. The p-T data was then fed into the geofluid model (see 5.2.3) along with a composition averaged from the measurements. The density calculated with the model was compared to the measured one. The relative difference of calculated and averaged measured density is displayed in Fig. 17. It was calculated as

$$\Delta\rho = \frac{\rho_{calc} - \rho_{meas}}{\rho_{calc}} \quad (6.1)$$

Calculated values match the measured ones reasonably well, as the relative difference is in the range of -0.6...1.4 % with an average of 0.5 %. The difference shows a systematic behaviour, having negative gradient with respect to pressure, which increases with temperature.

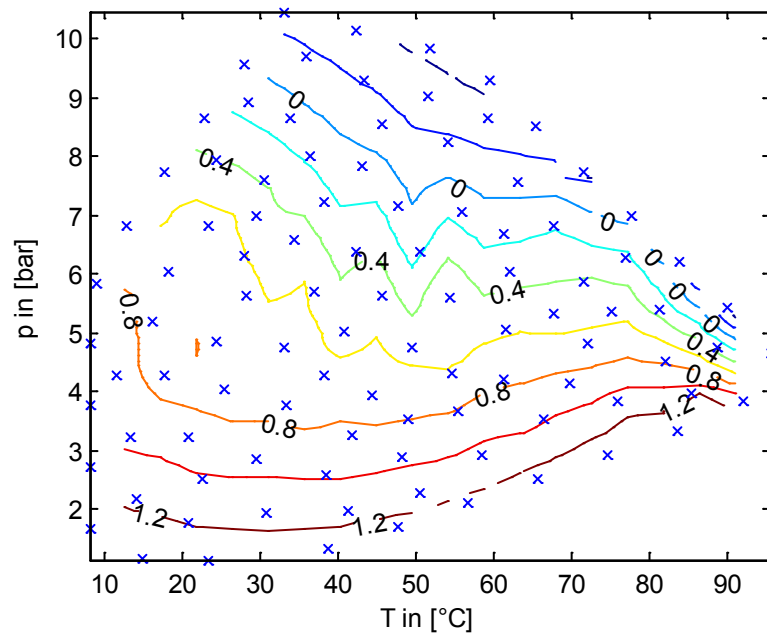


Fig. 17: Measured data (crosses) and difference of calculated to measured density in [%]

6.2 Liquid phase viscosity validation

Viscosities of binary and ternary solutions of sodium chloride and calcium have been measured in the laboratory with varying composition and temperature (Hoffert and Milsch, 2013a). Measurements were conducted for a salinity up to saturation concentration at $p = 1$ bar, $T = 20 \dots 80$ °C using an ANTON PAAR AMVn viscometer with a stated precision of 0.5 %. 504 of the measured points were within the validity range of the equations described in 5.2.7. Viscosity for these points was calculated and compared with the measurements.

The average difference between measured viscosities and their calculated counterparts was calculated as:

$$\Delta\eta = \frac{|\eta_{calc} - \eta_{meas}|}{\eta_{meas}} \quad (6.2)$$

⁴³ A least square fit was performed on a plane in the p-T-Q space and its mesh points were used.

2 sets of viscosity functions and 2 mixture rules, so together 4 different viscosity models were used and compared to each other. Viscosity was calculated in 4 different ways, either with the correlation by Zhang et al. (1997) for all three salts or with a combination of the correlations by (Zhang et al., 1997) for CaCl_2 and by (Mao and Duan, 2009) for NaCl , KCl . The mixture rule from eq. 5.49 was either weighted with weight fraction or molar fraction.

Table 6 shows good accordance between measured and calculated values for all models with a slight advantage for the molar weighted mixture of Mao and Zhang viscosities.

Table 6: Viscosity model validation results

viscosity models	average relative difference	
	mass weighted	molar weighted
Mao/Zhang	6.01%	5.43%
Zhang	6.52%	6.25%

This accordance is sufficient, especially given the minor importance of friction compared to hydrostatic pressure head.

6.3 Gas solubility model validation

Harting, May and Schütze (1981) compiled results of measurements on nitrogen-methane mixtures dissolved in sodium chloride solutions to provide correlations and a collection of tables covering pressures from 25 atm⁴⁴ to 600 atm and temperatures between 25 °C and 150 °C. Each of their table lists gas phase composition and solubility for a varying ratio of dissolved gases. Water vapour is neglected so that fractions of N_2 and CH_4 in the gas phase add up to 100 %. This has to be considered when comparing with values from other sources, because high temperature and low pressure lead to a significant gas volume fraction of water. For example, at 150 °C and 30 bar, the water saturation pressure is 4.8 bar, being 15.8 % of the total pressure.

Solubilities and gas phase compositions for pure water at 25 °C (Fig. 18), for 1-molar NaCl -solution at 150°C (Fig. 20), for 5-molar NaCl -solution at 25 °C (Fig. 19) and 150 °C (Fig. 21), all at 25 atm were compared to values calculated with the geofluid model. The same was done for pure water (Fig. 22) and 5-molar NaCl -solution (Fig. 23) at 150 °C and 450 atm. For 150 °C the total pressure in the model was increased by the neglected water vapour pressure (to the value indicated in the figure captions), so that the difference $p-p_{H_2O}$ equals the pressure given in the respective table.

⁴⁴ Standard atmosphere, 1 atm = 101325 Pa. atm is a deprecated pressure unit, but it is used in this validation, because conversion to bar would result in lengthy numbers.

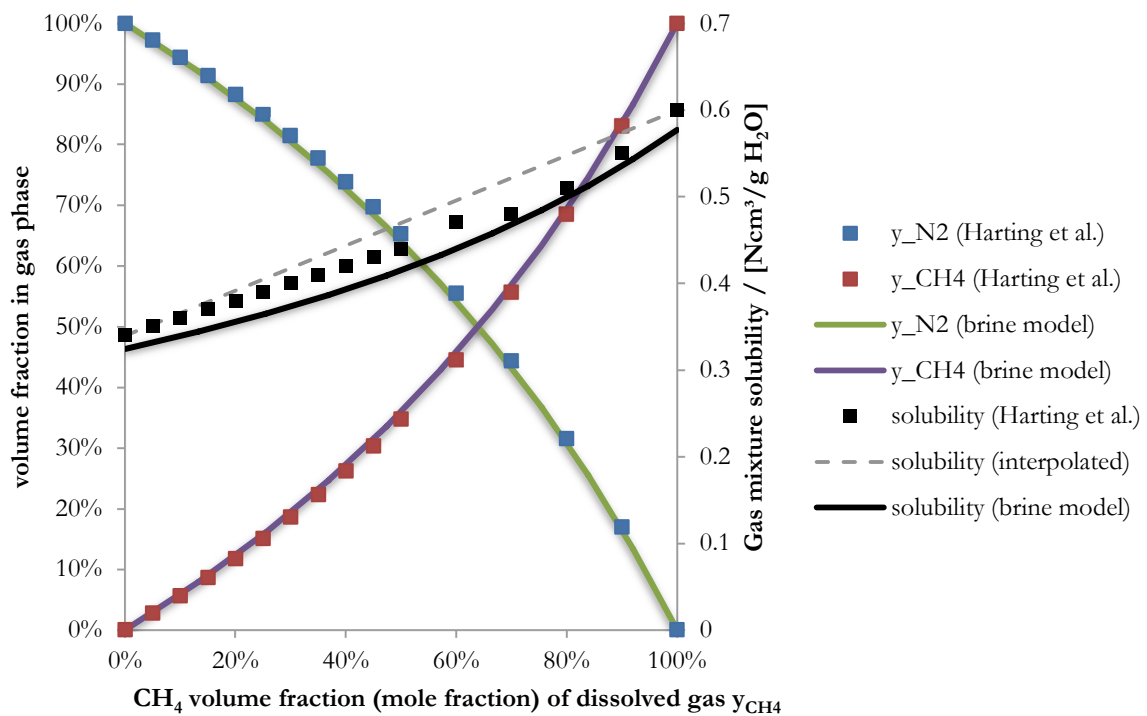


Fig. 18: gas phase composition as a function of composition of dissolved gas in oversaturated water at 25 atm, 25 °C

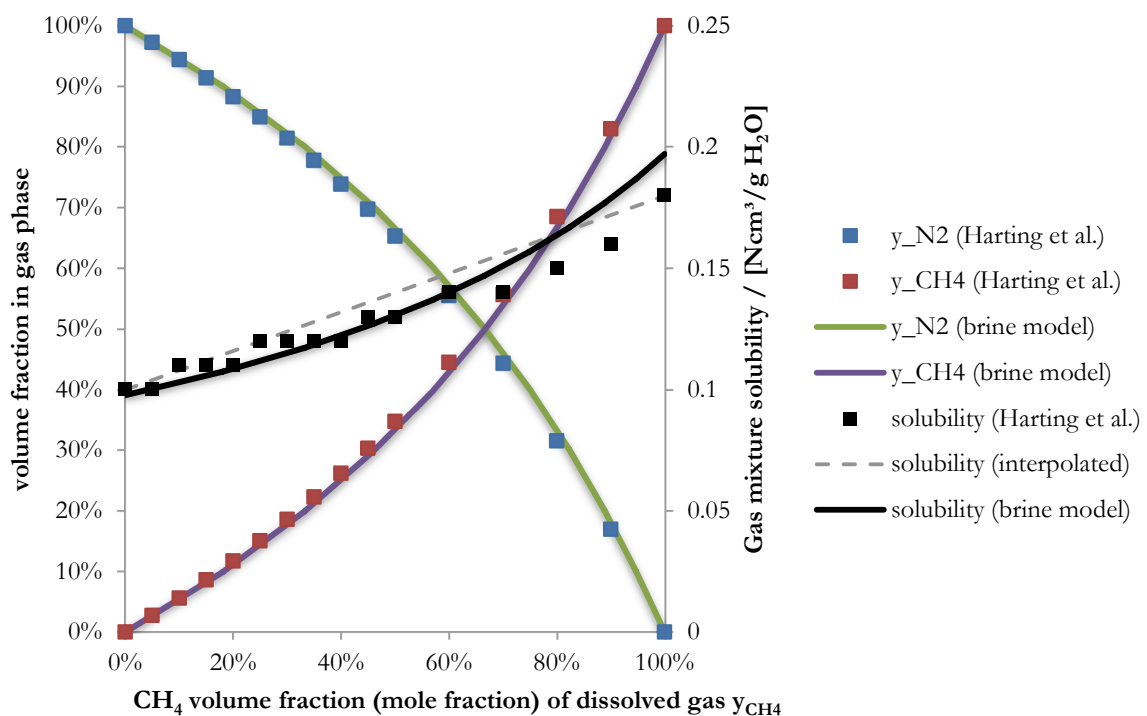


Fig. 19: gas phase composition as a function of composition of dissolved gas in oversaturated 5-molar NaCl-solution at 25 °C, 25 atm

Volume fractions match rather good at both temperatures for low salinities and low pressures, whereas the volume of total dissolved gas is predicted lower (2...7 % at 25°C (Fig. 18), 0...11 % at 150 °C (Fig. 20)) by the model. Best matching solubility prediction is for pure methane at 150 °C (Fig. 20).

At high salinity the geofluid model overestimates nitrogen solubility and underestimates methane solubility (Fig. 19, Fig. 21, Fig. 23). The same happens at high pressures in pure water (Fig. 22) so that at reservoir conditions values differ considerably (-20 % N₂, +45 % CH₄). At reservoir conditions solubility is almost

linear in respect to CH₄ fraction in the data given by (Harting et al., 1981), while the model shows a curve (Fig. 23).

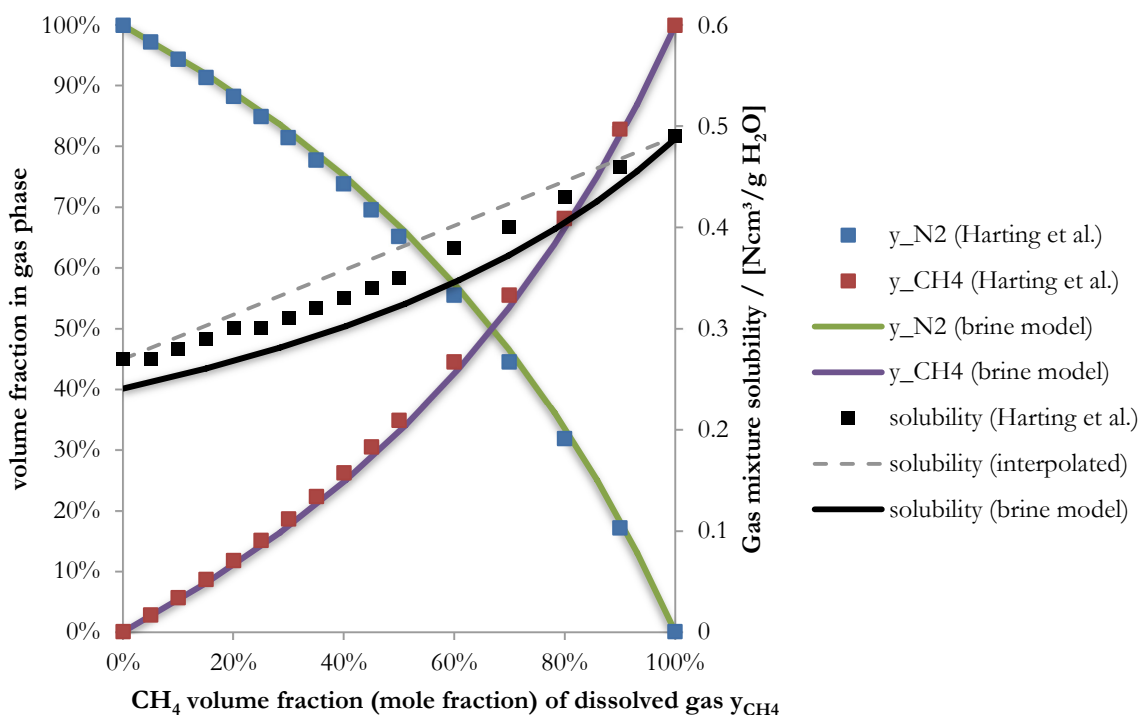


Fig. 20: gas phase composition as a function of composition of dissolved gas in oversaturated 1-molar NaCl-solution at 150 °C, 25 atm (Harting) compared to 29.9 bar (geofluid model)

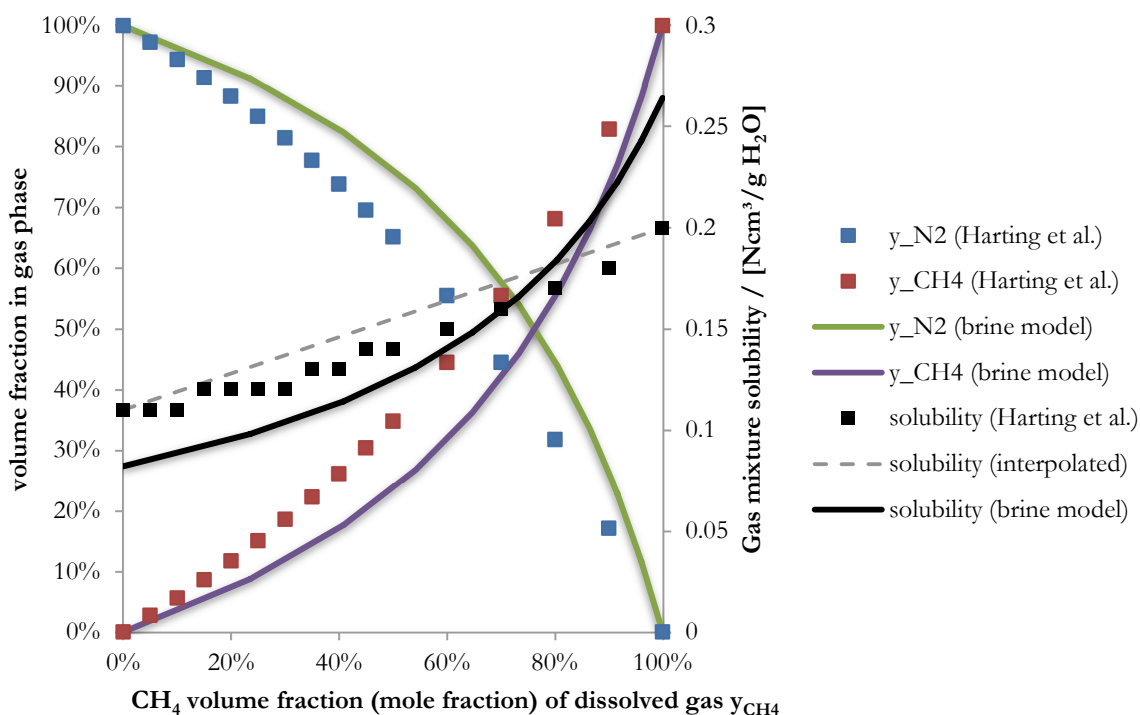


Fig. 21: gas phase composition as a function of composition of dissolved gas in oversaturated 5-molar NaCl-solution at 150 °C, 25 atm (Harting) compared to 29.4 bar (geofluid model)

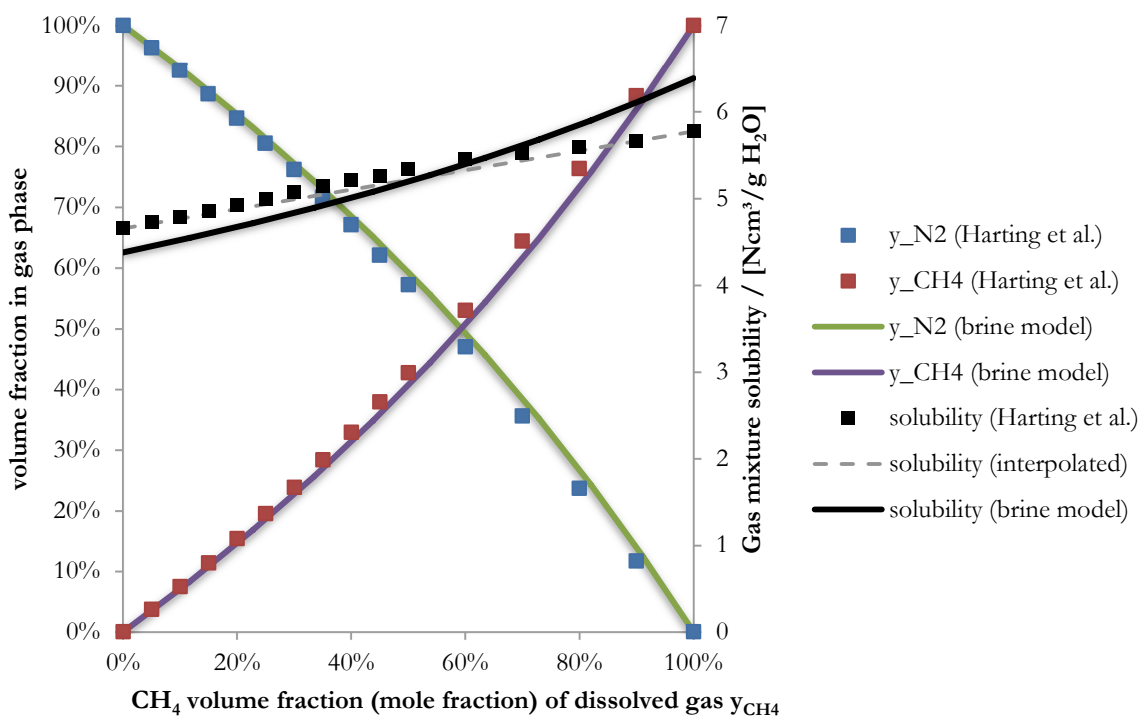


Fig. 22: gas phase composition as a function of composition of dissolved gas in oversaturated pure water at 150 °C, 450 atm (Harting) compared to 461 bar (geofluid model)

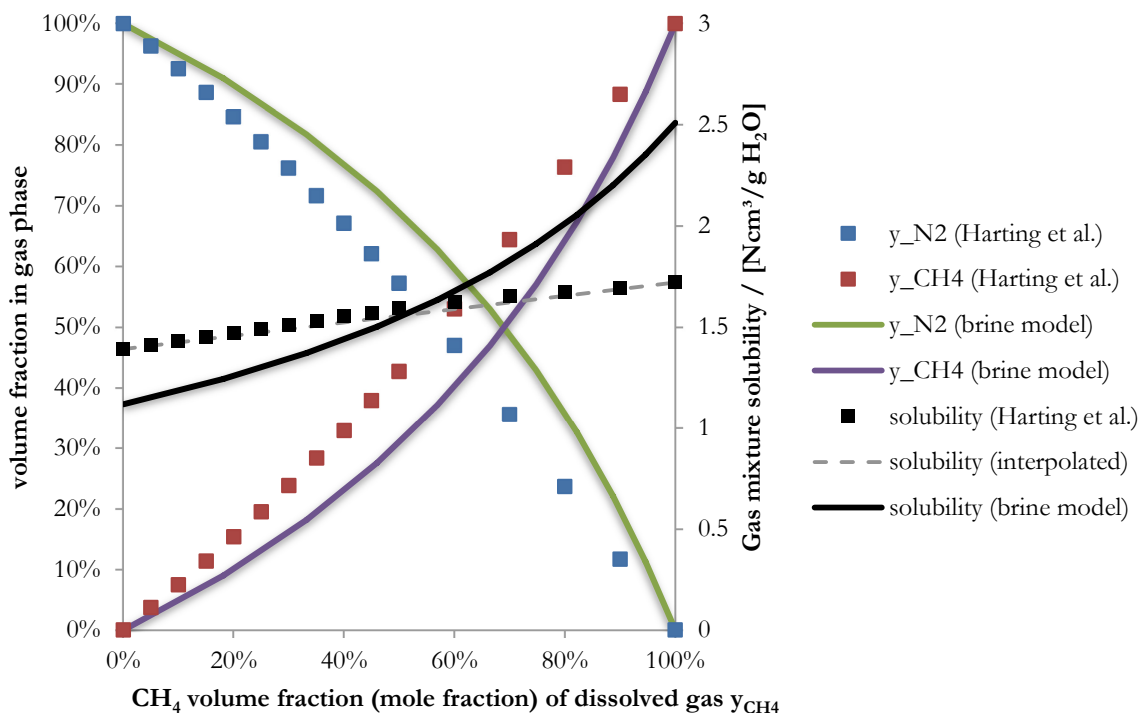


Fig. 23: gas phase composition as a function of composition of dissolved gas in oversaturated 5-molar NaCl-solution at 150°C, 450 atm (Harting) compared to 460 bar (geofluid model)

6.4 Hydraulic validation (GrSk probe measurements 9/2011)

6.4.1 Experiment setup

On 9 September 2011 a probe, a p-T-spinner, was lowered into the GrSk production well. The production string is equipped with a Y-Tool, a fork which allows bypassing the production pump. The bypass can be sealed and unsealed remotely so that wellbore measurements are possible even when the ESP is operating (Schlumberger, 2008). The probe was hanging on a hybrid cable, which contains electric wires to feed the sensors, as well as a DTS cable, so that distributed temperature measurements could be conducted simultaneously with probe measurements of pressure, temperature and flow rate (Henninges et al., 2012).

While lowering the probe into the well a continuous p-T-log was recorded. Later the pump was started while the probe measured pressure and temperature for about 2 h at 4350 m (MD). Due to technical problems, the DTS measurement stopped after about 6300 s near the end of the first measurement. An offset of pressure sensor of 2.2 m and a cable elongation of estimated 1.4 m was considered.

Parallel to the probe and DTS measurements, pressure and temperature near the pump inlet at $s = 1202.5$ were measured by permanently installed sensors and recorded by the permanent data acquisition system.

The volume flow extracted from the reservoir has been estimated based on the production rate measured at the wellhead and the liquid level in the open annulus. The level was calculated from the measured pressure at the pump inlet and an average density of 1170 kg/m^3 ⁴⁵. Within 3 hours of production approximately 80 m^3 of brine were produced from the reservoir, which is less than the borehole volume below the pump (120 m^3). Hence the assumption of a thermally quasistatic flow is not fulfilled and this data cannot be used for thermal validation. Hydraulic validation, however, is possible because the transient temperature profile of the fluid in the well is known.

The brine has been sampled during production at the surface within 2 weeks before and 1 week after, but not during this test. Its composition was determined as given in Table 7.

Table 7: GrSk Brine composition in 9/2011 - Analysis by VKTA, uncertainty 10 %

Component	NaCl	KCl	CaCl ₂	CO ₂	N ₂	CH ₄
Mass fractions [g per kg fluid] (used for calculation)	83	5.4	111.7	0.181	0.744	0.066

6.4.2 Density profile

Using the brine property model with p and T from the log, the brine density profile was calculated (black line in Fig. 24). Prior to the log measurement the well had been shut-in for about 21 h. Hence, the fluid was assumed to be degassed, so that the free gas is expected to have largely left the fluid column by rising as bubbles. Another density profile could be obtained from the pressure gradient of the same log (green line) by solving eq. 5.53 without friction for the density:

$$\rho = \frac{\Delta p}{\Delta z \cdot g} = \frac{\Delta p}{\sin \varphi \Delta s \cdot g}. \quad (6.3)$$

⁴⁵ unpublished Internal Technical Report 5/2013, by Dr.-Ing. Guido Blöcher, GFZ Potsdam

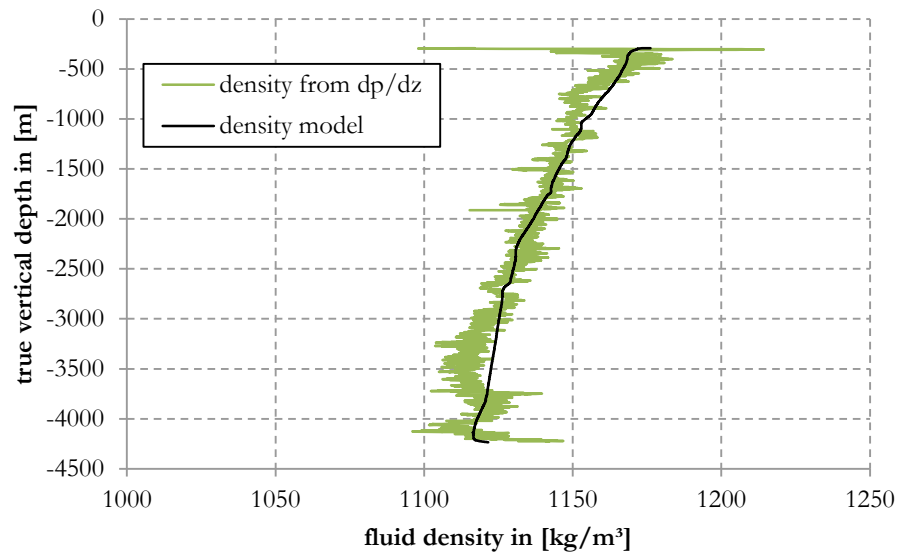


Fig. 24: Density profile calculated from pressure gradient and from p-T profile using geofluid model

Both profiles match very well, although density differs up to 10 kg/m^3 in two zones at 500...1100 m and 2900...3700. Nevertheless the average offset is $\overline{\rho_{\text{model}} - \rho_{\text{grad}}} = 0.8 \text{ kg/m}^3$, well within the specified uncertainty of the composition analysis. This validates once more the brine density model and confirms the assumed salinity for this test (Table 7). Hence, this brine composition was used for the following simulation.

6.4.3 Model setup

For this simulation, the wellbore model was adapted to the measurement setup: The wellbore was ‘cut’ at the measurement depth and connected to the flow source without the flow resistor (cf. Fig. 11). Measured pressure and temperature from the probe sensors as well as the calculated volume flow rate were fed as timelines into the source. The fluid temperature in the well was not calculated, but rather set directly using the transient profile provided by the DTS measurement (4350 m). Hence, the thermal formation model was deactivated and the wellbore model was thus reduced to its hydraulic part.

6.4.4 Simulation results

The modified wellbore model was used to calculate pressure at the pump inlet, which was then compared to the recorded pressure. The duration of the measurements and the determined differences are shown in Table 8.

Table 8: Probe measurements: Location, time, duration, mass flow rate from the reservoir, difference of measured and calculated pump inlet pressures, friction pressure loss and fitted variation of gas mass content.

	MD	TVD	begin	duration	mass flow	mean calc. error	Δp_{dyn}	fitted gas content
	[m]	[m]		[s]	[kg/s]	[bar]	[bar]	
a)	4353.6	-4233.7	12:04	6376	0...11	-0.3	0...0.7	-
b)	4353.6	-4233.7	13:50	100	10	-1.0	0.6	+60 %

Fig. 25 shows the detailed results for the first measurement at $s = 4300 \text{ m}$. Calculated and measured pressure match very well, having a difference between -1 and $+0.5 \text{ bar}$ with an average of -0.36 bar (i.e. calculated pressure is mostly below measured pressure). If that is put into relation to the total pressure difference of around 330 bar , the mean error is below 0.3% with an average around 0.1% .

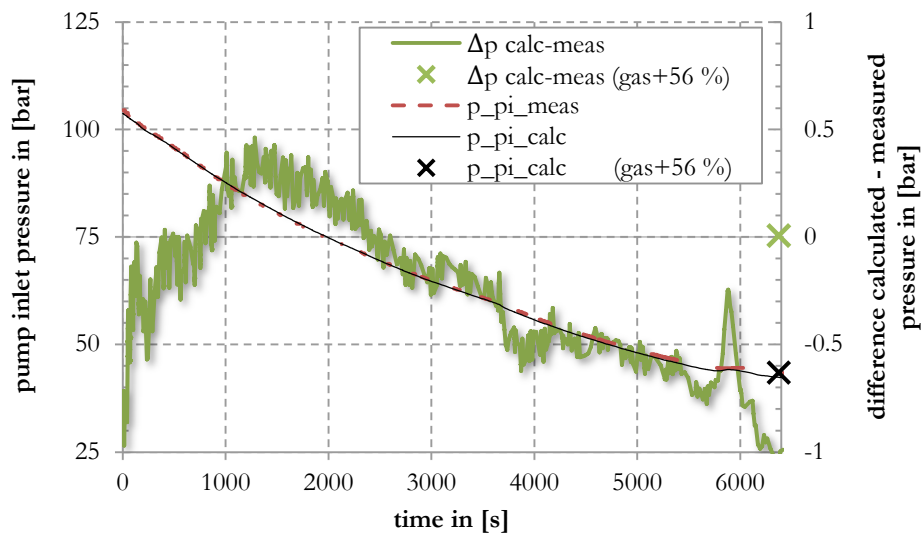


Fig. 25: Comparison of measured ($p_{pi,meas}$) and calculated ($p_{pi,calc}$) pump inlet pressure during probe measurement at $s = 4350$ m, X's mark absolute value and difference of calculation for last moment of measurement with fitted gas content

The calculation error has been plotted separately on the second axis to show its systematic trend. Starting negative, it reaches a positive maximum at $t = 1100$ s and then decreases until the end of the test. Assuming constant salt contents, the decreasing trend could be qualitatively explained with the error in the friction loss calculation or a varying gas content of the brine, superposed by an offset due to the density error. As mass flow increases, so does the friction pressure loss and its potential error.

On the other hand, the gas content is supposedly not constant as assumed in the simulation, so that pump inlet pressure increases with the gas fraction in the well: Initially the fluid is in equilibrium, i.e. without free gas, i.e. gas content is overestimated in the simulation, hence fluid density is underestimated which eventually leads to the positive pressure calculation error ($t < 2500$ s). During production the fluid column is lifted and fresh brine from the reservoir with higher gas content enters the well. Additionally, pressure in the well is reduced because the open annulus is drained by the pump. The fluid is decompressed, hence not in equilibrium anymore and degasses, thus reducing density and hydrostatic head and eventually increasing the pump inlet pressure. This trend should continue until the wellbore volume below the pump has been replaced. Unfortunately, measurements did not last long enough to verify this. Slip of the gas phase in turn reduces static fluid density, which counteracts the described trend.

Plotting mass flow rate, friction pressure loss and calculation error in one diagram (Fig. 26) clearly shows a correlation. Mass flow rate and friction are obviously connected. The error follows a similar trend, but is superposed by another positive contribution that peaks at $t \approx 2000$ s (maximum difference between green and blue line).

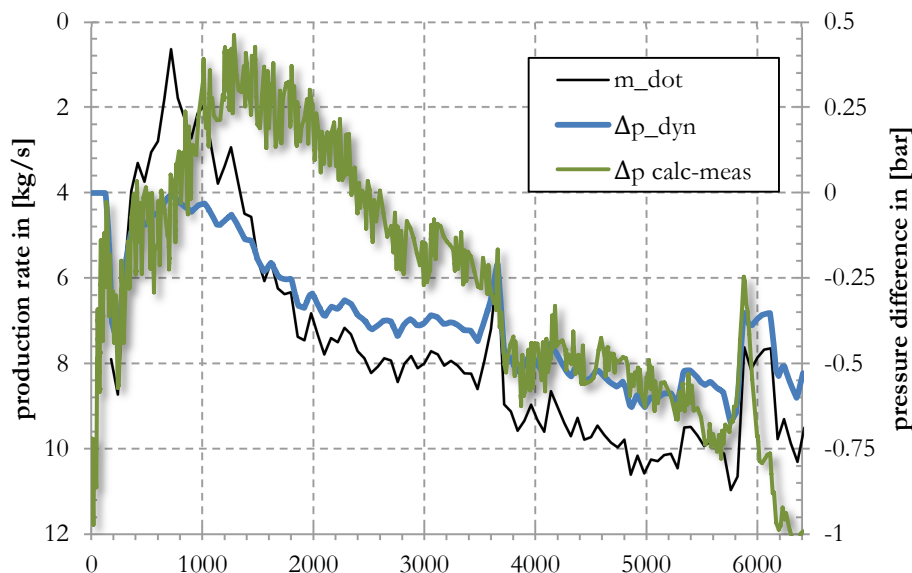


Fig. 26: Production rate (inversed), friction pressure loss (Δp_{dyn}) and calculation error ($\Delta p_{\text{calc-meas}}$) during probe measurement at $s = 4350$ m

Near the end of the simulation the calculated friction pressure drop reaches the level of the calculation error. Hence, the friction model cannot be validated unless the reason for the systematic error is identified, quantified and subtracted.

If the calculation error is to be attributed to the slowly increasing gas fraction, the real gas content can be estimated by increasing the gas content until the calculation pressure matches the measured one. This has been done for the last point in time (black and green X in Fig. 25) and yields an increase of the total gas mass fraction of 56 %. However, this value represents the effective average over the wellbore between probe and pump; it underestimates the actual gas content of the inflowing fluid. A more precise and transient quantification of the varying gas content would require a flow model with convective transport and slip.

Up to date the gas content could only be roughly determined from fluid sampling and indirect measurements and maybe subject to cumulative effects, so a temporary increase of this magnitude cannot be ruled out.

Given the detailed temperature profile, the measured pump inlet pressure can be reproduced with an average error around 0.1 %. However, the hydraulics in the wellbore is dominated by the gravitational pressure loss, which is based on the (already validated) fluid density. Friction pressure loss only becomes significant at production rates higher than reached during this test. Therefore, the validity of the friction calculation cannot be assessed. The small remaining systematic error is possibly caused by variations in the gas fraction due to decompression and exchange of degassed fluid by fresh brine from the reservoir.

6.5 Thermal validation with analytical solution

Despite their limitations (see 2.3) analytical solutions for wellbore heat flow are helpful for quick estimations and verification of the numerical solution, as will be done here. After having validated the transient formation heat flow model separately (see D 4.3), the wellbore model including the formation model described in 5.4 and 5.5 is applied to a simplified scenario and the calculated temperatures are compared to an analytical solution.

The wellbore model is validated with the analytical solution for the transient wellbore heat transmission proposed by Ramey (1962). It is based on the assumption of a line source and is therefore not valid close to the well and for short times. It was applied to a simple test case and compared to the results from the wellbore model described before. In the test case 10 kg/s of pure water is produced from a depth of 1000 m at 100 °C through the sandstone formation (L07 from Table 1) with a temperature gradient of

3 K/100 m and a surface temperature of 8 °C. Pipe friction and gravitation have been deactivated in the model to eliminate pressure influence on the specific heat capacity, which is constant in the analytical solution.

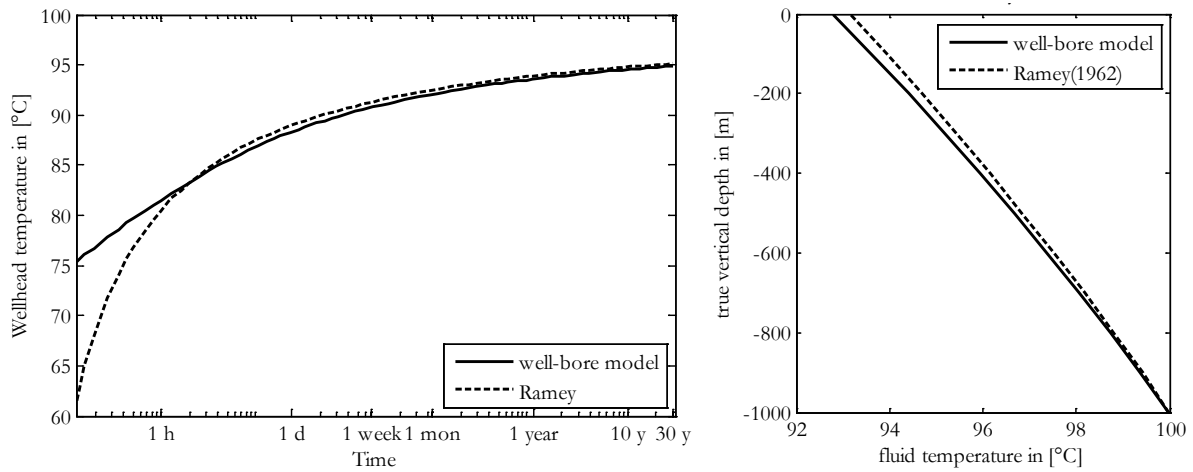


Fig. 27: Comparison of simulated wellhead temperature with analytical solution (Ramey, 1962):
a) Wellhead temperature over 30 years. b) Fluid temperature profile after 90 days. (Francke et al., 2013)

Fig. 27a and Fig. 27b show the calculated well head temperature and a temperature profile for the analytical and the numerical model. Accordance after 1 day is very good, the difference after 30 years amounts to 0.2 K.

6.6 Thermal validation of well model (GrSk circulation test 4/2012)

From 18 until 24 April 2012 production at the GrSk site was maintained for 163 h. Being the longest continuous circulation test, it was selected for thermal validation of the wellbore model.

6.6.1 Recorded data

Among the quantities that were measured and recorded during the operation time, the following ones were selected for model input and comparison with values calculated by the model:

- Temperatures, measured at production pump inlet (T_{pi}) and at the wellhead (T_{wh}), were compared to calculated data.
- The volume flow rate \dot{V} , shown in Fig. 28 has been measured after the degasser. It was converted to mass flow with the in-situ liquid density (calculated for the measured pressure and temperature at the wellhead). This mass flow was used as source mass flow in the model. The annulus volume was produced after 5.1 h, the total well volume was produced after 10.4 h.
- Measured wellhead pressure p_{wh} varied between 8 and 11 bar for $t < 50$ h and was then stationary at 9.1 ± 0.1 bar. The total average of $p_{wh} = 9.175$ bar was used as constant target value for the pump control.
- The pressure in the open annulus at wellhead was averaged to 4.52 bar and used as top annulus pressure in the model, where it determines the liquid level in the open annulus.
- Pressure at production pump inlet has been measured and was used to calculate the varying reservoir pressure using eq. 6.4:

$$p_{res}(t) = p_{in}^{ESP}(t) + \bar{\rho}(t)g(z_{ESP} - z_{res}) \quad (6.4)$$

The average density $\bar{\rho}$ below the pump was determined by calculating the liquid phase density for the measured values of pressure and temperature at the pump inlet.

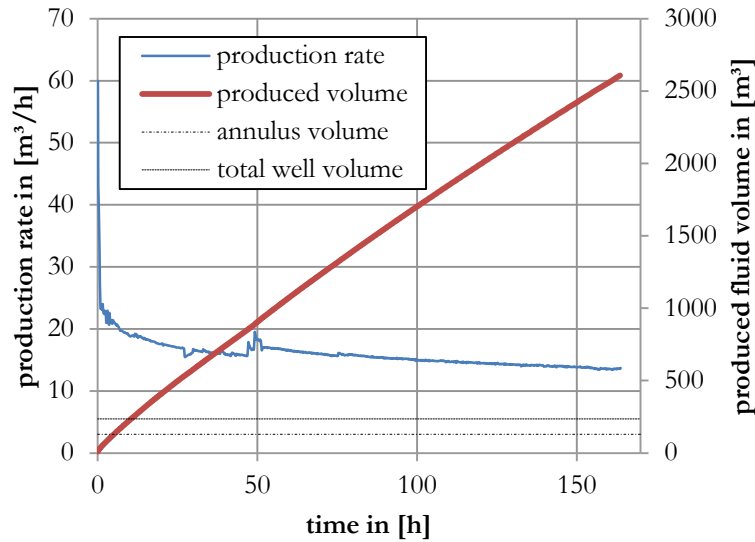


Fig. 28: Production rate \dot{V} and produced fluid volume after degasser

6.6.2 Simulation parameters

The simulation time starts at $t = 1$ h and ends at $t = 164$ h. Time stepping is dynamic and chosen by the solver. The integration tolerance is set to 10^{-5} . It had to be set lower than the default value, because otherwise small peaks in the production rate curve are skipped and missed due to large time steps. Only measured data with $t > 1$ h has been used in order to exclude the very high production rate in the beginning which is mostly produced from the open annulus and does not affect the lower part of the well.

The radial discretization of the formation uses a maximum growth rate of 1.4 (see D 4.1) and a radial extension of $r_\infty = 8$ m. The constant boundary temperature is applied at r_∞ , which is beyond the range of thermal influence of the well within 1 week, as the simulation confirms. The formation temperature (initial and far-field) is based on a measured temperature log (shown as T_∞ in Fig. 8). Seasonal influence is not considered, because it reaches only a few metres into the ground (Scheffer et al., 2009).

The model was parameterized according to the values listed in chapter 4, with the following exceptions:

The flow resistor component is deactivated by setting the productivity index PI to a high value, because the hydraulic behavior of the reservoir is already represented by the reservoir pressure, which was calculated with eq. 6.4.

The transient values of reservoir pressure and the mass flow rate are read from a file containing the measured and converted values.

$p_{wh,set}$, the setpoint value of the well head pressure in the controlled production pump, was set to 9.175 bar, the average of the measured p_{wh} . During the pump test the pump was operated below its nominal operation range, where the efficiency given in the pump documentation does not apply. Extrapolation to lower production rates would be speculation. Hence, the efficiency was instead set to the minimum value within the operation range of $\eta_{is} = 70\%$ ⁴⁶.

⁴⁶ The efficiency during the pump test was later determined from measured electrical data as $\eta_{is} = 56.3\%$ (see B 6.4).

With the indicated discretization parameters the well has 172 vertical elements while the formation is discretized with 10...14 radial elements. Translation of the model with these parameters results in a system of around 38'000 variables. Running the simulation takes roughly 5 h on a 2.8 GHz CPU using one core.

6.6.3 Simulation results – Temperatures

The comparison of measured and calculated T_{wh} and T_{pi} is shown in Fig. 29.

At the beginning of the circulation test the fluid column in the well and the formation are approximately in thermal equilibrium. When the pump starts to produce, the initial fluid column is lifted past measurement points and temperatures quickly rise. Only after the bore-hole volume has been produced completely the assumption of quasistatic flow is justified. According to the recorded production rate (Fig. 28) the wellbore volume including the open annulus of about 235.5 m³ has been produced after 10.4 h. During these 10.4 h, in the model, the formation has been warmed up by ‘fresh’ brine from the reservoir flowing with a high volume flow rate, giving the simulation a ‘head start’ over reality. After production of roughly 1...2 more wellbore volumes the T_{pi}/T_{wh} curves converge.

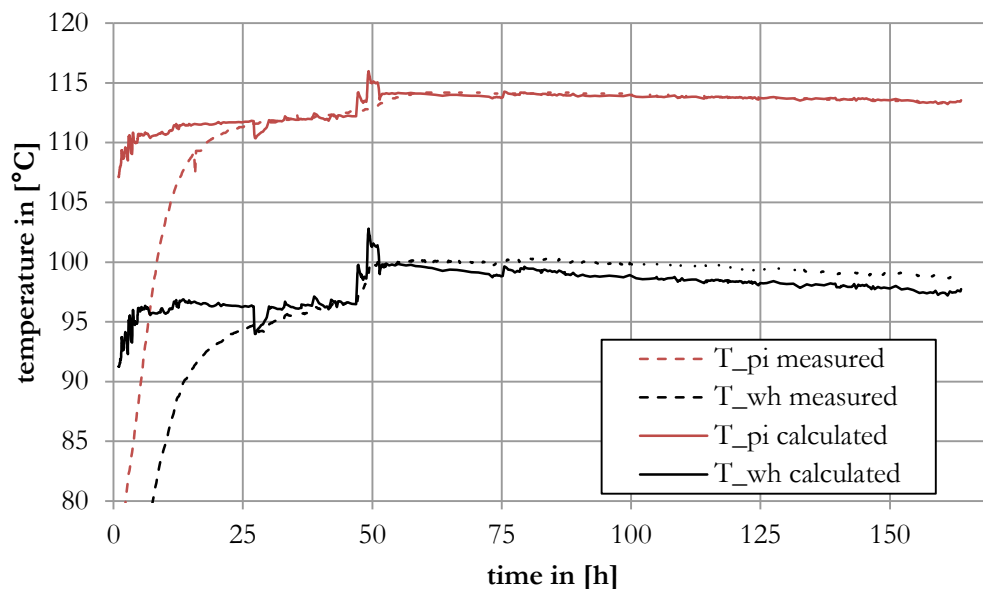


Fig. 29: Pump inlet temperature (T_{pi}) and wellhead temperature T_{wh} , comparison of measured and calculated values during 7 days pump test

Later at $t = 50$ h, where the peak in production rate causes a temperature step, the peak is much more pronounced in the simulated data than in the measurements. Dampening of temperature fluctuations by heat storage in well completion and in the fluid is presumably responsible for smoothing out the measured temperature curves. This dynamic effect is not reproduced by the quasistatic wellbore model.

After the peak at $t > 50$ h the measured temperatures decrease slowly due to the decreasing production rate. When mass flow has fallen low enough, heat transport into the formation exceeds heat flow from fluid to the interface and the interface temperature and consequentially fluid temperature fall.

After the start-up phase the curves match well, especially in the more stationary phase. For $t > 60$ h the average temperature difference amounts to 0.1 K at the pump (T_{pi}) and 1.1 K at the wellhead (T_{wh}), with calculated temperatures being lower than the measured ones. The calculated T_{pi} is very close to the measured value while T_{wh} shows a small difference. T_{wh} is a result of the processes in the pump and in the production string. In particular, it depends on the efficiencies of pump and motor, which have been estimated to be $\eta_{is} = 0.7$ and $\eta_{mot} = 0.9$ (see 4.5). They can, however, be expected to have been lower during the circulation test, as the pump was operating outside the nominal values. Effectively, the

efficiency determined from measured electrical currents during the pump test is $\eta_{is} = 56.3 \%$ (see B 6.4). And indeed, decreasing the pump efficiency in the model to this value brings the calculated wellhead temperature very close to the level of the measured temperatures (see the sensitivity analysis in 8). The good accordance should, however, not be overrated, as one has to keep in mind that this validation is specific for one site and one short operational scenario. The uncertainties of the parameters and the measured values have not been studied here, but the fact that errors can cumulate over the whole length of the well gives reason to expect a bigger difference.

Differences between calculation and measurement were expected due to parameter uncertainties and neglected phenomena, for example:

- the fact that the formation has not been undisturbed before the pump test, as assumed for the far-field formation temperature,
- imperfect contact of interfaces steel-cement and cement-formation,
- scaling or corrosion on the pipes,
- deviations from the radial symmetry of the wellbore geometry, such as a off-centred production string,
- reduced radiation in the annulus by non-ideal emissivity (temperatures are more consistent at $\epsilon = 0.75$ - see 8),
- thermal parameters and inhomogeneity / anisotropy of the cementation and the formation.⁴⁷

The thermo-hydraulic wellbore model proved to be capable of reproducing the transient temperature development during the seven days pump test with a surprisingly small error. This was obtained with a rather high level of detail, because preliminary calculations with simpler models revealed the need for refinement (see sensitivity analysis 8). The rather simple radially symmetric conductive thermal model of the formation appears sufficient.

⁴⁷ For example, during cementation, the injected cement partly mixes with the liquid instead of completely displacing it. The liquid intrusion affects the thermal parameters.

7 Model application

This chapter presents some selected applications of the geofluid model and the wellbore model.

In 7.1 brine properties, determined with the geofluid model, are compared to those of pure water for exemplary p-T-conditions in order to confirm the need for a sophisticated property model instead of applying pure water properties in the GrSk scenario. 7.2 presents additional results, that have been extracted from the simulation of the circulation test (6.4), such as profiles of temperature, density and gas fraction in the wellbore as well as formation heat flow data. In 7.3 the wellbore model is used to make a long-term prognosis of the wellhead temperature and analyse the exergy losses. Finally, in 7.2.5 the wellbore model is applied to the injection well to predict bottomhole temperature and injection pressure.

7.1 Brine properties compared to properties of water

Properties of pure water and brine with the composition as given in 4.2 have been calculated for standard conditions and the reservoir conditions. The values listed in Table 9 illustrate the strong influence of the salinity. The effect using pure water properties on the wellbore calculation is examined in chapter 8.

Table 9: Brine properties compared to water properties for selected states

model	pure water IAPWS97 (Wagner et al., 2000)	GrSk brine without gas media model (see 5.1)	GrSk brine with gas
gas volume fraction			
20 °C, 1.01325 bar	0	0	46 %
145 °C, 455 bar	0	0	0
density			
20 °C, 1.01325 bar	998.2 kg/m ³	1180.5 kg/m ³ ^a	637.9 kg/m ³ ^b
145 °C, 455 bar	944.7 kg/m ³	1123.6 kg/m ³ ^a	1124.7 kg/m ³
specific heat capacity			
1.01325 bar	4.184 kJ/(kg·K)	3.296 kJ/(kg·K) ^c	3.291 kJ/(kg·K)
145 °C, 455 bar	4.176 kJ/(kg·K)	3.224 kJ/(kg·K) ^c	3.221 kJ/(kg·K)
dynamic viscosity (liquid)			
20 °C, 1.01325 bar	1001.6 μPa·s	1882 μPa·s ^d	1494 μPa·s
145 °C, 455 bar	200.5 μPa·s	382 μPa·s ^d	383 μPa·s
bubble point pressure			
20 °C	0.023 bar	0.020 bar ^e	227 bar ^f
145 °C	4.16 bar	3.64 bar ^e	237 bar ^f
solubility			
	<i>Henry coefficient in Pa⁻¹ (as in eq. 5.7)</i>		
CO ₂ 20 °C	168·10 ⁻¹⁰		61.3·10 ⁻¹⁰ g
CO ₂ 145 °C	40.8·10 ⁻¹⁰		16.3·10 ⁻¹⁰ g
N ₂ 20 °C	1.93·10 ⁻¹⁰		0.435·10 ⁻¹⁰ g
N ₂ 145 °C	1.57·10 ⁻¹⁰		0.357·10 ⁻¹⁰ g
CH ₄ 20 °C	2.45·10 ⁻¹⁰		0.541·10 ⁻¹⁰ g
CH ₄ 145 °C	1.64·10 ⁻¹⁰		0.626·10 ⁻¹⁰ g

Table 9 shows that the geofluid model reproduces:

- the considerable density increase by salinity (+18/19 %).
- the density decrease by degassing and evaporation.
- the heat capacity decrease by salinity (salt replaces water mass; salt has lower heat capacity than water) (-21/23 %).
- the viscosity increase by salinity (+88/91 %).
- the reduction of the bubble point pressure by salinity.
- the increase of bubble point pressure by the dissolved gases.
- the solubility decrease due to salinity to 22...40 %

7.2 Circulation test

In section 6.6 the simulation of the circulation test was described and the calculated fluid temperatures at pump inlet and wellhead were used for validation. In this section other calculated values from the same simulation are presented. The last subsection 7.2.5 describes the simulation and results of the injection during the test.

7.2.1 Temperature profile

Fig. 30 displays the calculated temperatures of the fluid, the annulus, the well-formation interface and the formation boundary as well as the heat flux per length unit along the well. It shows the location and the amount of the fluid's heat loss to the formation. It also exhibits the cooling effect of the open annulus where it is filled with liquid and the insulation effect above the liquid level.

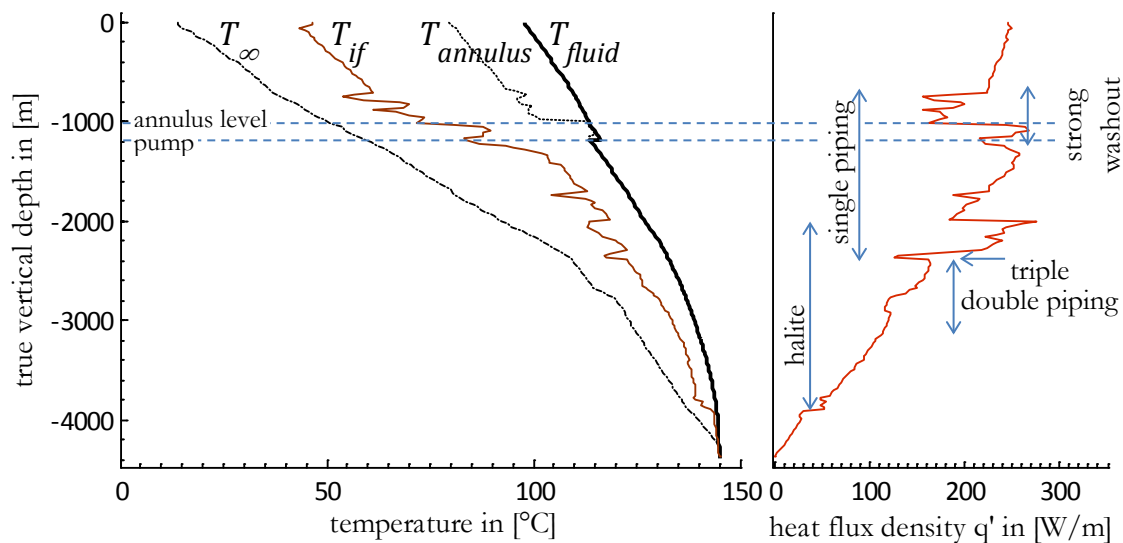


Fig. 30: Simulated temperature profiles of fluid (T_{fluid}), interface well-formation (T_{if}), annulus (T_{annulus}) and far-field formation (T_{∞}) as well as profile of heat flux density at the end of the pump test

Heat flow increases generally with the growing temperature difference between fluid (T_{fluid}) and formation (T_{∞}), but varies with wellbore layout, washout and lithology. The liquid level in the annulus is superposed by the effect of the strong washout but still visible by the distinct drop of heat flow and interface temperature T_{if} at $z = -1008$ m. Comparison with the well layout (Fig. 9a) and stratigraphy (Table 1) reveals that between -2302 m and -1990 m heat flow is increased by single piping in a halite layer (with high thermal conductivity). Between the single and the double piping there is a short zone with triple piping, which causes the heat flow to drop at $z = -2329 \dots -2378$ m. The lower boundary of the halite layer is visible in the heat flow, albeit less distinct than the upper boundary due to weaker heat flow.

7.2.2 Degassing

Identifying the location of degassing is interesting with regards to the pump performance, which can be decreased by a high gas fraction. A gas fraction profile, as shown in Fig. 31, may help in choosing the installation depth of a pump. For chemical considerations and understanding of deep fluid sampling results the degassing behaviour of the individual gases is of interest.

According to the calculation for the circulation test, at the GrSk site fluid pressure falls below the degassing pressure of 262 bar (at 131 °C) initially at 3068 m (TVD). This is the degassing depth, where the first gas bubble occurs. Fluid temperature increases during the test, which increases degassing pressure so that the degassing depth sinks, eventually reaching 3359 m.

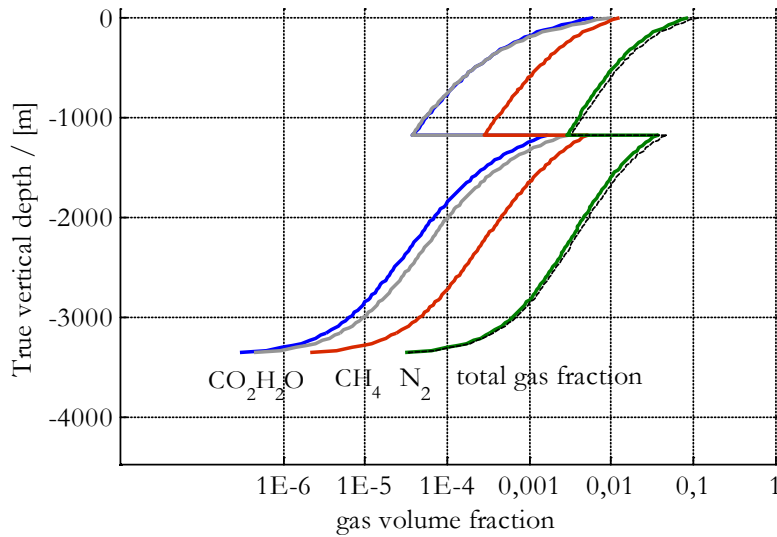


Fig. 31: Simulated profiles of gas volume fractions of total gas phase, N₂, CO₂, CH₄ and water vapour at the end of the pump test

Fig. 31 shows the gas volume fraction of the single gases of the gas phase ϵ_α . ϵ_α is the product of gas volume fraction and partial pressure, so that the ϵ_α add up to the total gas volume fraction ϵ .

$$\epsilon_\alpha = \epsilon \cdot y''_\alpha, \quad \sum_{N_G+1} \epsilon_\alpha = \epsilon \tag{7.1}$$

The total gas volume fraction reaches a maximum of 11.5 % at the wellhead where the minimum pressure is reached. Nitrogen dominates the gas phase. The pressure increase at the pump causes re-dissolution of gases and re-condensation of water. Note that CO₂ below the pump has a lower partial pressure (or void fraction) than water, but a higher one above. The pressure increase at the pump does not restore the conditions from a depth of approx. 2300 m, where pressure is the same as at the pump outlet, because of the different temperature dependence of the CO₂ degassing pressure and the water vapour pressure.

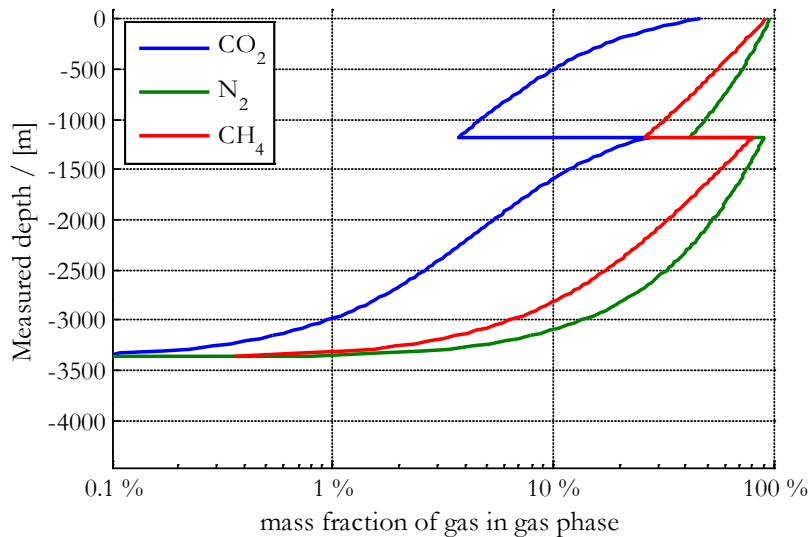


Fig. 32: Simulated profiles of mass percentage of gas in gas phase (at 100 % gas is fully degassed) for N₂, CO₂, CH₄ at the end of the pump test

If individual degassing depths are to be determined, a threshold has to be selected, because degassing start for all gases at the same depth. The reason is that in the VLE model, as soon as a gas phase has formed, all gases are present in the gas phase, even if only to a very little extent. Fig. 32 shows how much gas has degassed at a given depth relative to the respective gas content expressed as the fraction $X''_\alpha x / X_\alpha$.

If the degassing threshold is set to the arbitrary value of 1 %, the degassing depths are read off as: N₂ at -3352 m, CH₄ at -3317 m and CO₂ at -2986 m.

7.2.3 Density

The density of the fluid in the wellbore, production string and in the annulus is shown in black in Fig. 33. The green line (left) and the blue line (right) indicate the density of the gas phase and of the liquid phase, respectively.

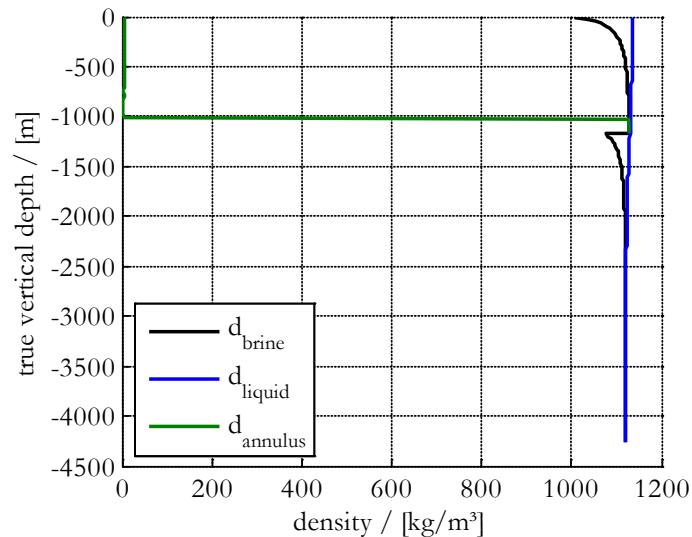


Fig. 33: Density profile in wellbore and open annulus at the end of the circulation test

In analogy to the gas fraction graph in Fig. 31, degassing reduces the density before the pump and recommences after redissolution in the pump. Liquid density increases upward, because the effect of the decreasing temperature (Fig. 30) prevails over the pressure effect.

7.2.4 Formation heat flow

As described in 5.5, the thermal model of the formation consists of stacked radially symmetric discs that are subject to transient radial heat flow. Hence, the model calculates radial but not vertical heat flow. This section is dedicated to studying the radial heat flow and to estimate the neglected vertical heat flow.

Fig. 34a and b show the temperature and radial heat flux in the formation at the end of the circulation test (described in chapter 6.4) as calculated by the model. The vertical heat flux that would result from the temperature field is shown in Fig. 34c. It is calculated using Fourier's Law:

$$\dot{q}_z(r, z) = -\lambda(z, T) \frac{\partial T(r, z)}{\partial z}. \quad (7.2)$$

Fig. 34d shows the vertical component of the 'artificial heat flux', i.e. the vertical heat flux induced by the alteration of the temperature field due to the radial heat flow from the well. The artificial heat flux is calculated by subtracting the vertical heat flux from the initial state. The temperature data has been mapped to a regular mesh in order to calculate the vertical gradients⁴⁸.

⁴⁸ The temperature data $T(r, z)$ is calculated by the model on a structured irregular mesh and is extracted as a matrix. While z is constant on every line and r_∞ is constant in the last column, r varies within a column because r_∞ depends

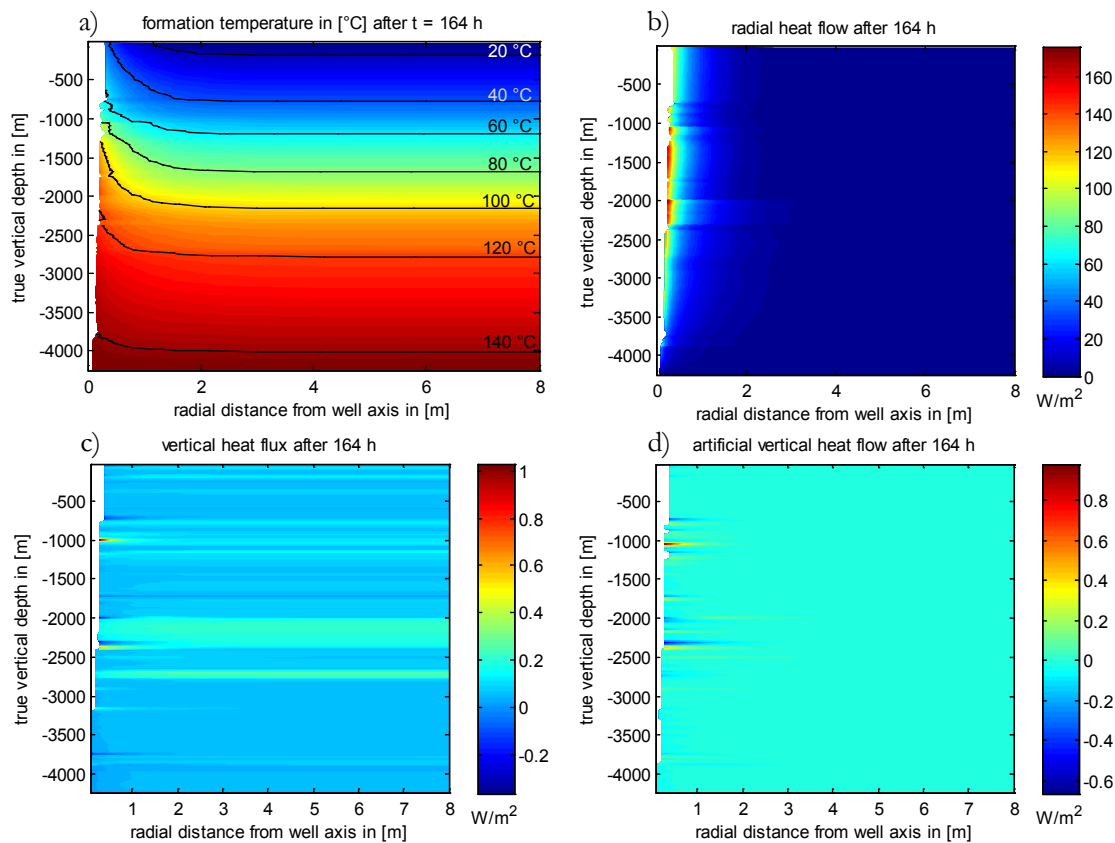


Fig. 34: (a) Temperature, (b) radial heat flow, (c) potential vertical heat flow and (d) artificial contribution in formation at end of pump test. The values have been calculated with a radially refined mesh (growth ratio of 1.1)

The radial heat flow caused by the temperature gradient between fluid and formation has changed the temperature field by warming up the vicinity of the well. The radial heat flux (Fig. 34b) has a limited influence range of about 2 m as it decreases radially. A sudden drop at $z \approx 1000$ m clearly marks the liquid level in the open annulus. The heat flow is reduced above the liquid level (cf. Fig. 30), which is also visible in Fig. 34a where one of the isotherms is not parallel to the others.

The temperature increase around the well affects the vertical temperature gradient, because it is not uniform along the well. As stated above, vertical heat flow is not calculated by the model. However, the natural temperature profile, applied to the formation as initial and boundary condition (outer/right boundary in Fig. 34a), implies a gradient and hence a stationary vertical natural heat flux. The stationary energy balance requires it to be vertically constant. If the transient vertical heat flow equation were to be solved for this natural heat flux, it would converge to a temperature profile according to the thermal conductivities set in the model. In Fig. 34c the outer/right boundary is still unaffected by the heat flux from the well, so it shows the natural heat flow generated by the temperature profile and the thermal conductivities given in 4.1.1. The fact that it is not constant indicates a discrepancy between the temperature profile and the parameterized lithology. This means that either the formation is not in thermal equilibrium and/or the lithology differs from the model parameters.

on the local washout. Mapping was done by the MATLAB function `TriScatteredInterp` which uses Delaunay triangulation.

Fig. 34d also shows a limited range of influence, a maximum of the heat flux at the depth of the liquid level in the annulus and a minimum at the transitions between well segments, where well completion, changes abruptly. Therefore, the absolute values of these extrema depend on the vertical discretization and the following comparison is, strictly speaking, only valid for the applied discretization.

In order to estimate the importance of the neglected vertical heat flux, the induced additional vertical heat flux is compared to the radial one: The value range ($0.4 \dots 0.8 \text{ W/m}^2$) is small compared to the range of radial heat fluxes ($0 \dots 120 \text{ W/m}^2$) and the values are highest close to the well in both directions. If the vertical element size ($\approx 20 \text{ m}$) was drastically reduced to the size of the innermost radial elements ($\approx 1 \text{ cm}$), the maximum heat fluxes would increase correspondingly, as they derive from vertical discontinuities. Their spatial extension would, however, be equally reduced, so that no increased influence on the flow in the wellbore is expected. Also, in reality, vertical heat flow is expected to ‘smear out’ such discontinuities, similar to a coarser vertical discretization.

Therefore, comparing radial and vertical heat flux confirms that the vertical heat transport is negligible compared to the radial one, as assumed in the thermal formation model (5.5).

The same conclusion is reached when the penetration depth calculated in D 4.2 is set into relation with the vertical element size. The linear penetration depth after 1 week was determined as 2.1 m. This is in accordance with the range of influence seen in Fig. 34b,d. It is well below the element size of about 20 m and therefore cannot have a significant impact on the simulation.

7.2.5 Injection

For the simulation of the injection well the wellbore model is set up with the parameters listed in 4.3 and 4.4. It is completed by the source (above ground), the injection pump and the reservoir including flow resistor, as depicted in Fig. 11 downstream of the heat exchanger. The injected fluid is completely degassed. The injection pump is, like the production pump, controlled and is configured such that the pressure after the flow resistor reaches the reservoir pressure of $p_{\text{res}} = 440 \text{ bar}$.

The injection during the circulation test is simulated by using measured volume flow rate and injection wellhead temperature as input for the source component.

Fig. 35 shows the calculated development of bottomhole pressure during the circulation test. The sudden changes at $t = 50 \text{ h}$ is caused by the peak of the production rate (cf. Fig. 28).

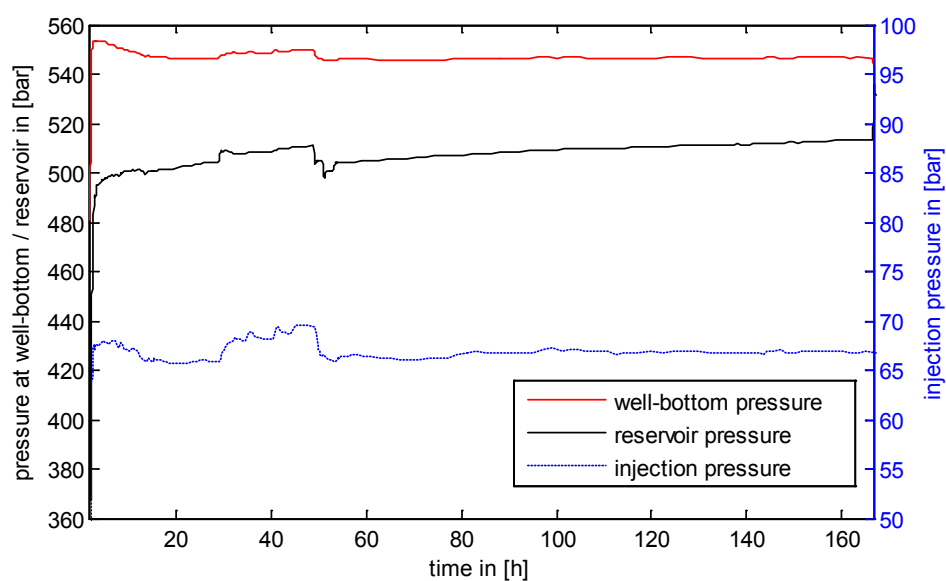


Fig. 35: Calculated pressure at wellhead (right p-axis), bottomhole and reservoir of injection well (both left p-axis) during circulation test

The black solid line represents the far-field pressure in the reservoir, which is supposed to be constant. It is, however beyond 440 bar, because the controlled injection pump head cannot become negative and injection pressure is rather high. The difference to the red line is the back pressure generated by viscosity in the reservoir. Due to the decreasing flow rate, reservoir pressure still rises for $t > 80$ h although bottomhole pressure is constant.

Fig. 36 shows the calculated development of bottomhole temperature during the circulation test.

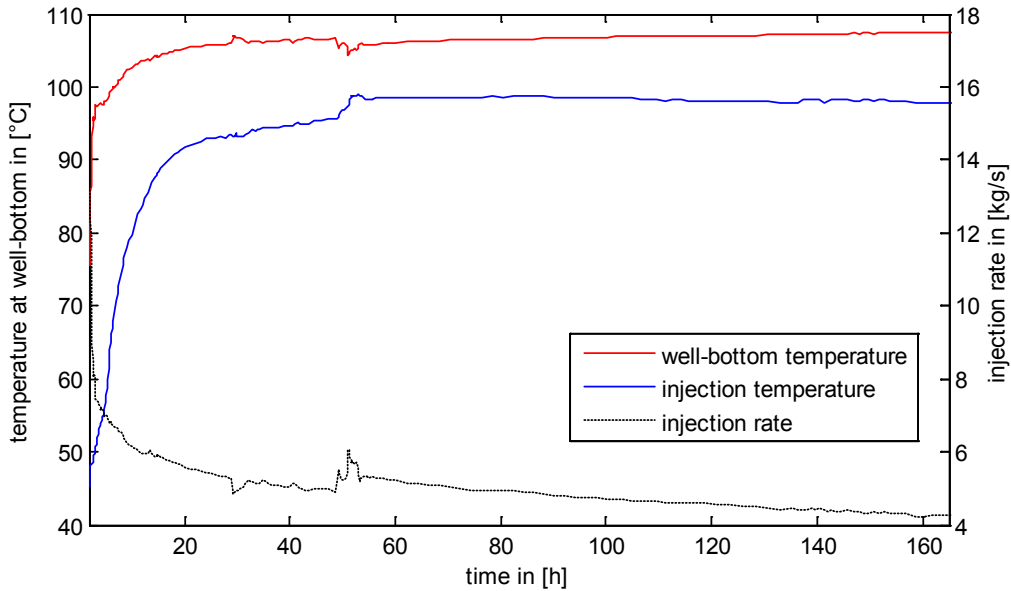


Fig. 36: Calculated temperature at wellhead and bottom of injection well, injection rate during circulation test

The bottomhole temperature curve follows the production wellhead temperature with a positive offset. That means, that the fluid reaches the reservoir warmer than it was at the wellhead, the opposite of what happens in the production well. Consequentially, the behaviour near the peak of production rate at $t \approx 51$ h is reversed. The temperature offset increases towards the end of the test because of the decreasing injection rate.

Two main differences to the production well are: Firstly, the absence of gas in the injection well, due to separation in the degasser. Secondly, temperature profile is not monotonous (shown in Fig. 37 for the end of the test), because here the flow direction is reversed with respect to the temperature gradient.

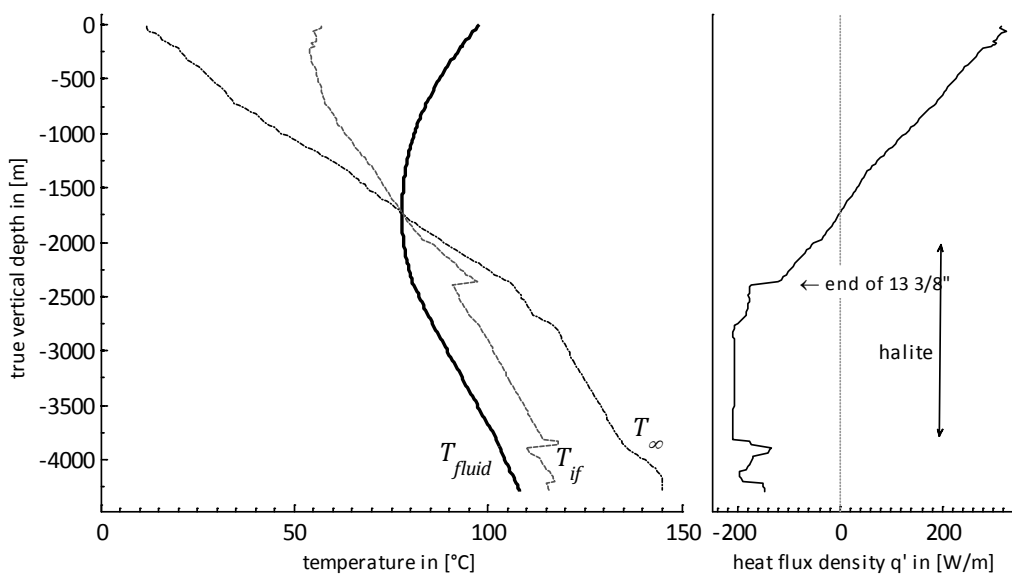


Fig. 37: Profiles of temperature and heat flux of the injection well at the end of the circulation test

Because injection temperature is warmer than the formation near the surface, in the upper part the fluid is cooled further down until it reaches a minimum of 77.9 °C at $z = -1714$ m. There temperatures of fluid, interface and formation coincide and the heat flow changes sign. Below the minimum the fluid is warmed up again by the warmer formation so that it finally reaches the reservoir warmer than at the wellhead.

The temperature profile is similar when heat is injected with a lower temperature at the beginning of the test or when heat is extracted at the surface. In that case the minimum temperature is lower and reached earlier. This minimum temperature is noteworthy, because it might be a limiting factor for design or operation as mineral saturation may occur at decreased temperature causing precipitation of minerals, potentially clogging the reservoir.

Fig. 38 illustrates the resulting formation temperature. While the formation is heated up in the upper part, recognizable by the isotherms bend upwards, temperature is unchanged near the fluid temperature minimum and cooled down in the lower part.

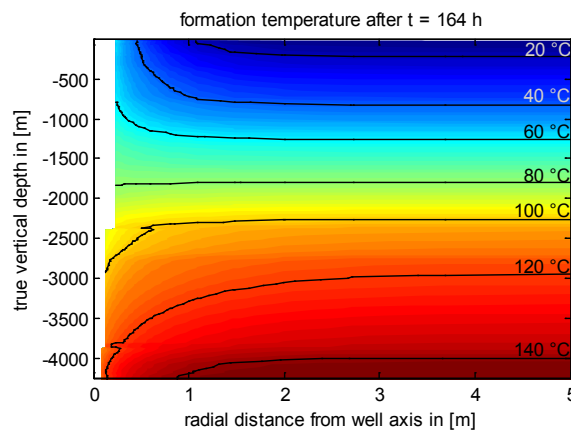


Fig. 38: Formation temperature in the vicinity of the injection well at the end of the circulation test

7.3 Long term temperature prognosis

Setting the simulation time to 30 years, the production rate constant to $\dot{V} = 25/50/75/100$ m³/h and assuming constant reservoir conditions with a productivity index of $PI = 15$ m³h⁻¹/MPa⁴⁹ yields the T_{wh} prognosis given in Fig. 39. T_{wh} does not reach a stationary level because the formation continues to absorb heat, albeit at a decreasing rate. While at 100 m³/h T_{wh} is within 5 K of the reservoir temperature within 30 years of operation, it does not get closer than 15 K at 25 m³/h.

The calculations show, that, with regard to the thermal output⁵⁰, a higher production rate is desirable not only because of the larger mass flow itself, but also because of the higher achievable T_{wh} . T_{wh} increases with mass flow because a higher mass flow is cooled less by the upper formation, as it flows faster and remains shorter in the well. It also brings more heat to the formation, thus warming it up faster and consequentially shortening the initial warm-up phase. This reduces the temperature range of T_{wh} in the operation time and shortens the heat consumer's operation time at off-design temperature.

⁴⁹ These were the projected parameters for GrSk.

⁵⁰ thermal output with respect to a reference temperature: $P_{th} = \dot{m} \cdot (h(T_{wh}) - h(T_{ref}))$

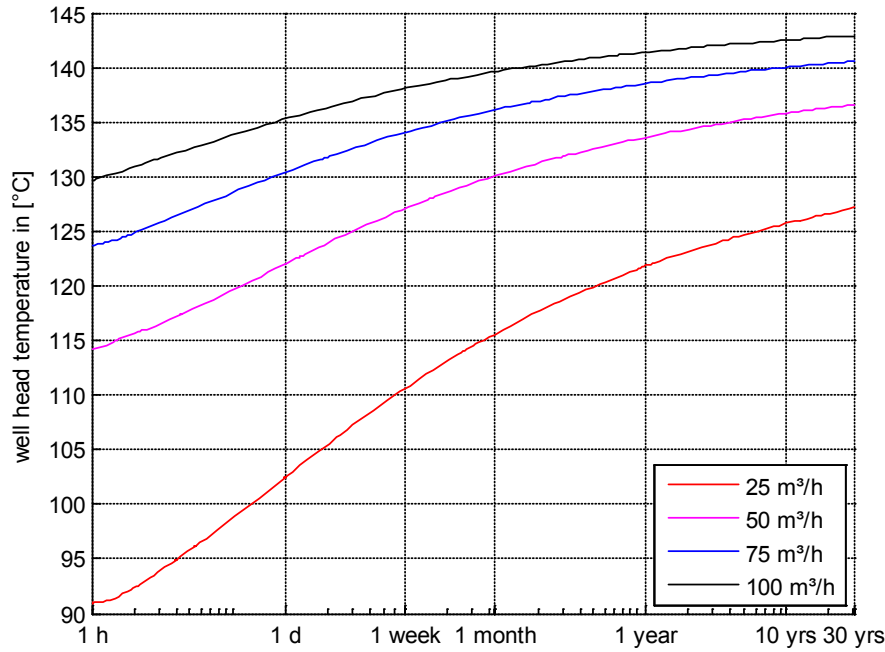


Fig. 39: Prognosis of wellhead temperature for 30 years for different volume flow rates

This T_{wh} prognosis can be used to select the design temperature according to the (limited) production rate and the expected operation time and to estimate the duration of the warm-up phase.

However, the assumption of constant reservoir parameters is disputable. Blöcher et al. (2010) showed that in GrSk at a constant production rate of 75 m³/h, thermal breakthrough can be expected after 3.6 years. A simulation with variable reservoir parameters provided by the reservoir model by Blöcher et al. (2010) would consider the thermal breakthrough, but it would in turn neglect the change of bottom hole injection temperature due to heat exchange with the formation. Hence, a more credible longterm prognosis for GrSk requires a coupled simulation of reservoir and complete brine circuit, which will be subject of future work.

Exergy analysis

The exergy flow is understood as the thermal power that would be released by bringing the fluid to a reference/ambient state p_0, T_0 . Following Baehr (2003, p.169) and neglecting kinetic and gravitational potential energy the exergy flow can be written as:

$$\frac{\dot{E}}{\dot{m}} = ((h - h_0) - T_0(s - s_0)) = (h - h_0) - T_0 \int_{s_0}^s d\tilde{s} . \quad (7.3)$$

Using the fundamental equation of state

$$ds = \frac{1}{T} dh - \frac{v}{T} dp \quad (7.4)$$

the entropy can be replaced:

$$\frac{\dot{E}}{\dot{m}} = h - h_0 - T_0 \left(\int_{s_0}^s \frac{1}{T} dh - \int_{p_0}^p \frac{v}{T} dp \right) = h - h_0 - T_0 \left(\int_{T_0}^T \frac{1}{T} c_p(T) dT - \int_{p_0}^p \frac{v}{T} dp \right) . \quad (7.5)$$

Finally, if the exergy contribution by pressure change is neglected and the specific heat capacity c_p is assumed constant, the exergy flow can be written in terms of p , T and c_p :

$$\dot{E} = \dot{m} \left(h - h_0 - T_0 c_p \ln \frac{T}{T_0} \right) = \dot{m} c_p \left(T - T_0 - T_0 \ln \frac{T}{T_0} \right) . \quad (7.6)$$

This equation is used to show the relative exergy loss by heat flow to the formation by dividing the exergy flow at bottomhole by the one at wellhead as:

$$\frac{\dot{E}_{wh}}{\dot{E}_{res}} = \frac{T_{wh} - T_0 \left(1 + \ln \frac{T_{wh}}{T_0}\right)}{T_{res} - T_0 \left(1 + \ln \frac{T_{res}}{T_0}\right)}. \quad (7.7)$$

The reference temperature is by convention $T_0 = 20 \text{ }^\circ\text{C}$.

Fig. 40 shows the exergy ratio that has been calculated for the temperatures from the long-term prognosis presented above.

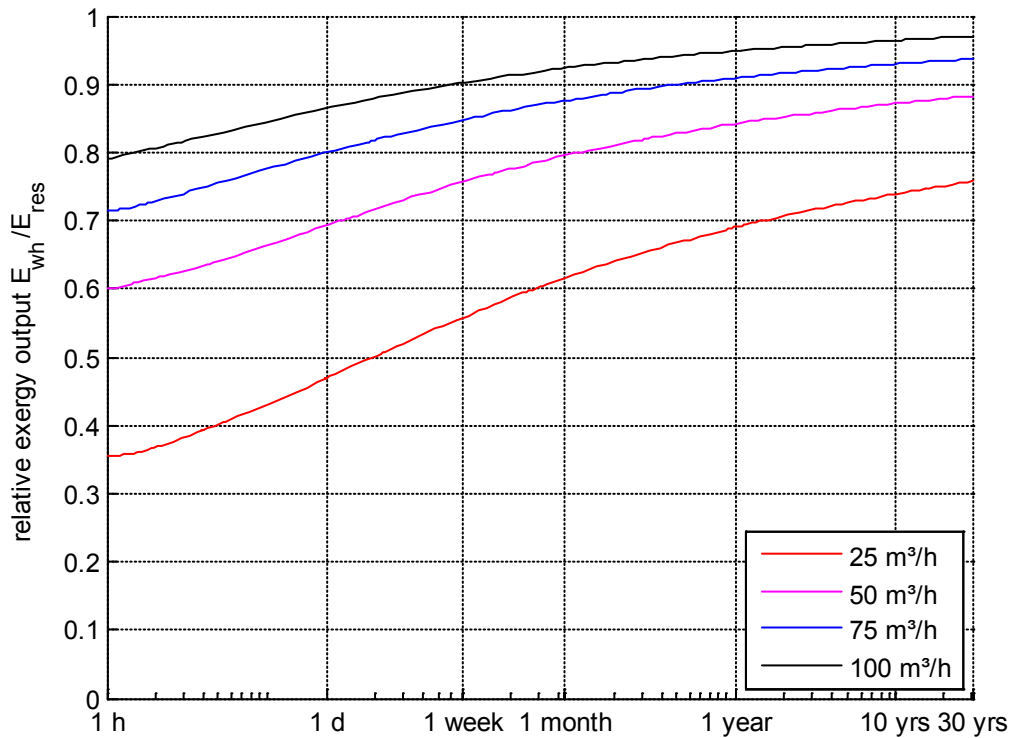


Fig. 40: Relative exergy output (ratio of exergy flows at wellhead and from reservoir) for different production rates

The exergy flow ratio plot appears similar to the temperature plot in Fig. 39, but as eq. 7.7 suggests, it is not a scaled and offset version of the temperature.

The area between a curve and $\beta = 1$ is the respective exergy loss to the formation. The graph shows that for the GrSk scenario with a low flow rate even after a long production time about 25 % of the exergy flow extracted from the reservoir is lost to the formation.

8 Sensitivity analysis – level of detail

The wellbore model described in chapter 5 has a high level of detail. The information needed for its parameterization may not be available for other, possibly not yet existing sites. In order to get an idea of the importance of single model features, they have been deactivated or simplified before repeating the calculation for the circulation test (described in 6.4) and comparing the results to the one from the full model. The effects on the temperatures (at the pump inlet and at the wellhead) are listed in Table 10. It gives the differences between calculated and measured temperature ($\Delta T = T_{\text{meas}} - T_{\text{calc}}$), averaged between 60 h after the beginning and the end of the circulation test. The respective cell background colour indicates the value on a scale from blue to red, thus highlighting the largest differences.

Table 10: Sensitivity on simulated temperatures on removal of model features, the average has been calculated between 24 h after the beginning and the end of the circulation test

Simplifications		ΔT_{pi}	ΔT_{wh}
	Reference scenario	-0.1	-1.1
brine	no gas content	-0.1	-1.1
	no salt content	5.1	1.3
	all salt as NaCl ($X_{\text{NaCl}} = 0.21$)	1.3	0.02
pipe flow	no thermal boundary layer	-0.35	-1.3
	no friction pressure loss	-0.1	-1.1
completion	no washout	-1.7	-3.3
	washout averaged over segments	-0.02	-0.9
	washout averaged over well	1.2	0.1
	cement density averaged over whole well, weighted by length	-0.4	-1.3
	cement density averaged over whole well, weighted by volume	-0.5	-1.3
annulus	No radiation in annulus ($\epsilon = 0$)	-0.1	3.7
	low emissivity ($\epsilon = 75\%$)	-0.1	-0.1
	no free convection in annulus	-0.1	3.4
	no heat flow through annulus gas	-0.1	14.4
	simpleAir from MSL instead of BrineGas	-0.1	-0.9
	constant annulus liquid level at $z = -1008$ m	-0.1	-1.1
formation	thermal formation parameters averaged over well	-1.4	-3.6
	linear formation temperature profile gradient	-13.2	-12.7
	coarse formation mesh (growth ratio $a_{\text{max}} = 2$)	-0.5	-1.5
	fine formation mesh (growth ratio $a_{\text{max}} = 1.1$)	-0.03	-1.0
pump	ideal pump ($\eta_{\text{is}} = 1$)	-0.1	-2.3
	pump efficiency from measured electrical data ($\eta_{\text{is}} = 56.3\%$)	0.07	-0.02

The figures given in this section are obviously site specific. Therefore, the conclusions drawn from them may be valid only for the present parameterization and simulation time. If a simplification shows little or no influence on the simulation result here, it may be different in another setting. If simplifications are combined in a certain manner, errors may cancel each other out, so that the respective model simplification has no influence. Also, average values may be close to effective values, so that averaging does not change the result. On the other hand, if the removal of a certain feature proves to have a big influence in the present setting, then one can generalize that this feature is potentially influential and must

not be neglected without further investigation. This being said, the figures will be given a closer look and explained in detail:

Temperature profile

The biggest error is induced by replacing the ‘real’ temperature profile by a linear profile between 8 °C and 145 °C on the surface, so that the far-field formation temperature is defined by

$$T_{\infty}(z) = \frac{145 \text{ °C} - 8 \text{ °C}}{4257 \text{ m}} \cdot z \quad (8.1)$$

For comparison with the ‘real’ profile the linear profile is displayed in Fig. 8.

If the linear temperature profile is assumed, T_{pi} and T_{wh} would be underestimated by around 13 °C, which corresponds to the difference between both temperature profiles of up to 20 °C. This underestimation would be slightly reduced if both profiles had the same surface temperature.

Salt / Gas content

Neglecting the salt content has the opposite, yet smaller effect on the calculated temperatures. T_{pi}/T_{wh} are 5.2/2.3 K higher than in the full model. That is due to the fact that pure water has a greater mass specific heat capacity than brine (see 7.1), while heat transmittance in the flow boundary is unaffected by salinity (in the model). This means that the temperature of pure water changes less *when* subjected to the same heat flow as brine. In the well heat flow is only initially the same for both media. The higher temperature of pure water further up the well causes a higher heat flow, mitigating the temperature difference.

Cumulating over the length of the well, the difference between pure water calculation and base scenario should grow with the distance from the reservoir. It is, however, larger at the surface than at the wellhead. A look at the annulus hydraulics quickly explains the contradiction: Having a lower density (see 7.1), the water column sinks to $z = -408 \text{ m}$, whereas the liquid level in the base scenario with brine falls to $z = -980 \text{ m}$. Between those two depths, the annulus heat flow through water is higher than in gas, which reduces the gap between both scenarios. Another phenomenon that qualitatively explains the higher T_{wh} is the higher gas solubility in pure water. Higher solubility means less degassing and less heat absorbing evaporation.

Replacing all dissolved salts by sodium chloride has a similar, albeit weaker effect, as calcium chloride has a lower heat capacity and a greater density than sodium chloride.

Setting the gas content to zero has no effect on the calculated temperatures, but it drastically reduces calculation time to less than 10 % of the base scenario. Apparently the in this case unnecessary VLE calculation accounts for most of the computation time.

Pipe flow

In order to assess the influence of the flow boundary layer on the heat flow, the heat transfer coefficient of the boundary layer is removed (or set to a very high value) in eq. 5.65. Calculation with the thus modified model yields slightly lower temperatures (-0.27/-0.25 K), because the boundary layer constitutes an additional resistivity for the heat flow. Hence, without it the heat flow is higher and temperatures are lower. The effect is small because the heat transfer coefficient of the flow boundary layer is 2-3 orders of magnitude higher than the overall HTC of the well completion and reciprocal addition in eq. 5.65 only changes the overall HTC by a few per cent.

Neglecting pipe friction has virtually no impact on T_{wh} or T_{pi} . At the low flow rates occurring in the circulation test the overall friction pressure loss in the well adds up to less than 1 bar. The potential thermal effect of pressure change is a shift of the vapour-liquid equilibrium, which implies a change of the energy-absorbing evaporation of water. As wellhead pressure is kept constant, this shift does, however, mostly occur close to the pump, where the gas fraction is small.

Cementation / Washout

Ignoring the washout lowers the T_{pi}/T_{wh} by 1.6/2.3 K. With the cement's thermal conductivity being lower than the one of the formation (Table 3 vs. Table 1), the washout has an insulating effect. Hence, omitting it increases heat flow and lowers fluid temperatures.

Taking the washout into account as averaged over the whole well increases both temperatures. Averaging the washout generally does not average the heat flow, as the influence of the washout is non-linear (logarithm in eq. 5.65) and 'weighted' with the formation's temperature and thermal parameters. A look at the washout profile and its average in Fig. 10 suggests that in the GrSk scenario the extended zone of low washout with high thermal conductivity (Zechstein) at $z = -1300...-3150$ m is not balanced (in terms of heat flow) by zones of high washout at $z = -700...-1300$ m and $z = -3170...-3800$ m as both have low thermal conductivities (Sandstone) and one of them is deep where the driving temperature difference is small.

Using a similar argumentation based on the skewed distribution of washout and thermal conductivity one can explain the much smaller yet positive temperatures effect of averaging the washout per well-segment (as defined in Table 3). The same holds for the cement density averaged over the whole well: The zones of high density and hence high thermal conductivity in the lower part of the well have a smaller effect on the heat flow than the low-density low-conductivity upper part of the well (see Fig. 9).

Formation

Averaging the thermal formation properties weighted by the thickness of the respective geological layer increases the calculated T_{pi} but decreases T_{wh} . In analogy to the previous explanation, this can be ascribed to the dominant Zechstein layer whose thermal conductivity is underestimated by the average value; vice versa for the sandstone layers above the pump.

The radial discretization of the formation is governed by the maximum radius growth ratio a_{max} (see 5.5.4). In the base calculation it is set to $a_{max} = 1.4$, which was determined in D 4.1 for an arbitrary maximum error of 1 %. This error adds up over the length over the well so that a refined formation mesh with $a_{max} = 1.1$ returns slightly increased temperatures. Although the radial mesh of the formation has up to 50 instead of 14 elements in the base calculation, the calculation takes only 30 % longer. A coarser mesh with up to 7 radial elements returns lower temperatures (both -0.4 K), but does not reduce calculation time.

Open annulus

Changes made in the model concerning the open annulus obviously do not affect T_{pi} , the temperature below the annulus, but have a large impact on the wellhead temperature.

A calculation without radiation in the annulus ($\epsilon = 0$), shows the strong contribution of the radiation to the heat loss as it increases T_{wh} by 4.7 K. By reducing the emissivity to $\epsilon = 0.75$ T_{wh} can be brought close to the measured value.

Deactivating the free convection in the open annulus - heat is transported only by conduction and radiation – equally reduces annulus heat flow and thus T_{wh} by almost as much (4.5 K) as neglecting radiation.

Replacing the annulus gas model with the simpleAir⁵¹ from the MSL has little influence. It increases T_{wh} by 0.2 K, because simpleAir contains no water and has therefore a lower heat capacity than the moisture saturated annulus gas.

Neglecting heat flow above the liquid level altogether has the greatest effect of all listed simplifications. Without any heat flow in the gas filled annulus the fluid stops losing heat at the liquid level and reaches the wellhead with T_{wh} increased by 15.5 K compared to the reference calculation.

Locking the annulus liquid level at $z = -1008$ m, the final value from the reference calculation, does not affect the average temperature for $t > 60$ h (Fig. 41a). Contrary to what one might expect the lower liquid level in the initial phase results in a slightly lower T_{wh} than in the reference calculation with dynamic liquid level (Fig. 41b). There the initially high mass flow with a high (but rapidly sinking) liquid level quickly heats up the formation close to the well above the final annulus level. This again reduces the temperature gradient between fluid and formation and leads to lower heat flow after the liquid level has fallen below the monitored depth (Fig. 42a,b). That is why, supported by the peak of production rate, temperatures with constant and dynamic level are the same after the liquid level has fallen to the final depth after $t = 50$ h.

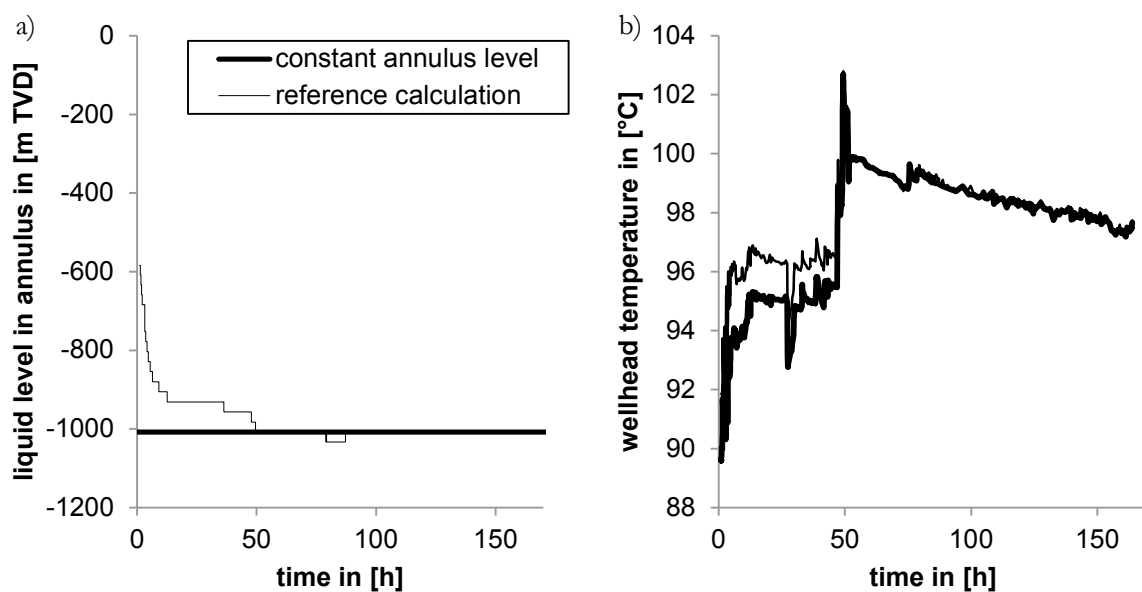


Fig. 41: a) Annulus liquid level and b) Wellhead temperature for constant and dynamic liquid level in annulus

⁵¹ Modelica.Media.Air.SimpleAir - ideal gas with constant c_p and λ representing air

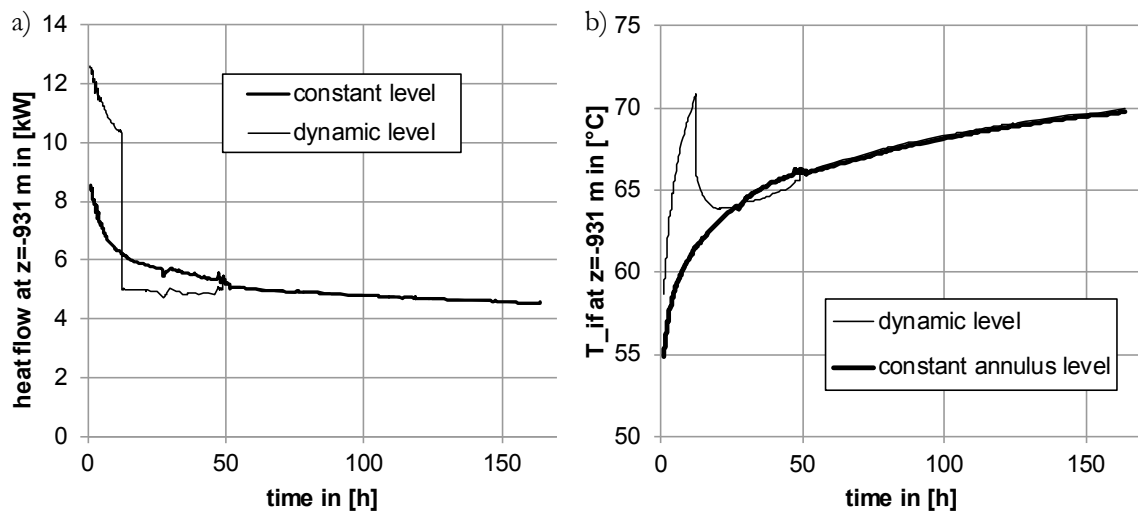


Fig. 42: a) Heat flow and b) Temperature at interface well-formation for constant and dynamic liquid level in annulus

Pump/motor efficiency

Pump and motor efficiency have the same effect as they appear as a product in eq. 5.91. The pump efficiency in the reference calculation is set to $\eta_{is} = 0.7$, the minimum efficiency within the operation range. The pump has, however, been operating outside of the operation range, so the efficiency can be expected to be lower. The calculation with $\eta_{is} = \eta_{mot} = 1$ shows the effect of neglecting the losses with a T_{wh} decrease of 1.2 K. A calculation with $\eta_{is} = 56.3\%$, as determined from measured electrical data (see B 6.4), brings T_{wh} very close to the measured value (Fig. 43). The two calculated temperatures differ less than 0.1 K from the measured values.

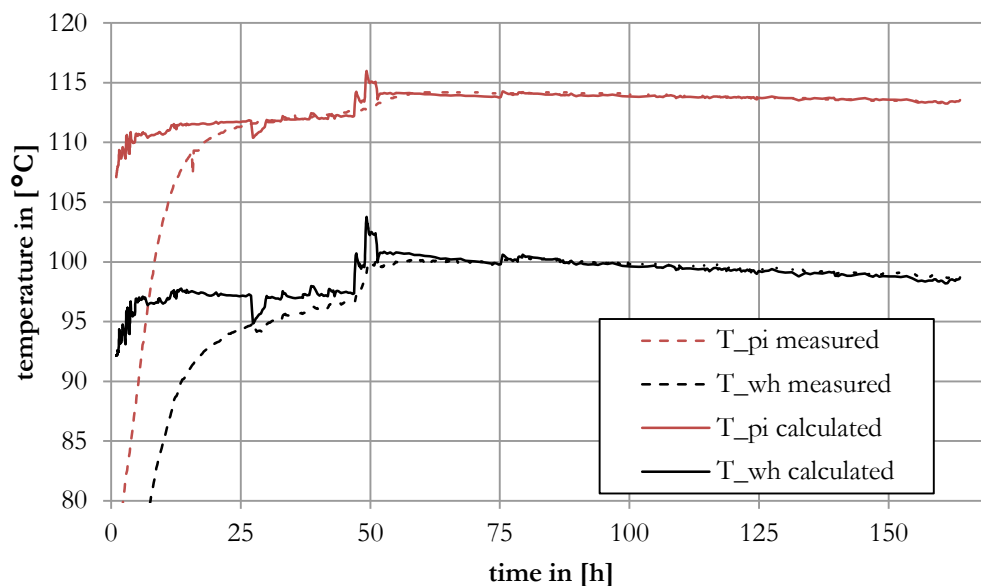


Fig. 43. Pump inlet temperature (T_{pi}) and wellhead temperature T_{wh} , comparison of measured and calculated values during 7 days pump test. Pump efficiency set to 56.3 %, as calculated from electrical measurements.

Summary

The biggest errors are introduced by neglecting heat flow in the annulus gas, the specific temperature profile, the salt content, the radiation or the convection in the annulus and the washout. This identifies the information that is indispensable for precise results for similar scenarios. On the other hand, the washout

as a profile (segment-wise average is sufficient), the friction calculation and the two-phase brine model with VLE calculation seem dispensable, at least for the temperatures in this scenario.

The model could be calibrated to return the measured T_{wh} by neglecting gas fluid content, reducing the annulus emissivity or the pump efficiency within plausible limits. Solely changing the latter is not only plausible, but also backed up by measured data. Pump efficiency varies, however, with the pump load. Hence it should be calculated based on the pump characteristics.

9 Summary

A comprehensive, yet flexible thermo-hydraulic model of a geothermal brine circuit with potential two-phase flow has been presented, implemented and validated on the basis of field data from the GFZ's research site in Gross Schoenebeck. Several model applications have been demonstrated and sensitivity on model depth has been investigated.

The model is capable of making mid-term (few days) to long-term (plant operation time ≈ 30 years) prediction of flow parameters that are essential in the design and dimensioning of the components of the brine circuit, such as the production pump, heat exchanger and the potentially connected power cycle. The model can also be deployed for preparation and follow-up of field experiments, optimization of operation or prediction of plant performance.

In contrast to existing models this work combines a compositional two-phase brine model with rigorous calculation of the formation heat flow. The presented model is applicable to deviated wells with non-flashing flow⁵² and highly saline geofluids with significant gas contents. The brine model is capable of reproducing phase transition by degassing/dissolution and evaporation/condensation. The vapour-liquid equilibrium is determined in a flash calculation that considers three gases and water. Then density, enthalpy and viscosity of the multi-gas multi-salt geofluid are calculated for both phases from the respective composition. The reservoir is characterized via a constant or transient productivity/injectivity index. Two-phase flow is represented by a quasistatic one-dimensional homogenous flow model. Heat loss to the formation is considered by a transient 2D FVM⁵³ formation model, which includes the detailed well completion and borehole washout, the processes in the open annulus as well as a detailed stratigraphy with temperature dependent thermal formation parameters.

The model was implemented in the modelling language MODELICA using the sophisticated development environment DYMOLA. MODELICA's object-oriented principle results in modular self-documenting models with graphical representation and configuration dialogues. As a result, the present brine circuit model can be easily configured and adapted to other geothermal sites via DYMOLA's graphical user interface using intuitive Drag & Drop and dialog boxes.

This approach proved fit for dealing with the model's complexity and its transient nature, although some considerable difficulties had to be overcome. Application to continuous problems with one or more dimensions like the formation heat flow equation is laborious, because discretization of the differential equation has to be implemented by the user. Also, the limited possibility to impose constraints on the solver made the manual implementation of equation solvers for the VLE calculation and function inversion necessary.

Due to the good data availability a very detailed model parameterization was possible without any calibration. After calculating the pump efficiency from logged electrical data, thermal validation with measured temperatures from one week of continuous operation showed a remarkable accordance ($\Delta T = 0.1$ K) after an initial phase of two days. The decrease of the wellhead temperature in spite of continued production is reproduced. Due to the lack of operational measurement data with elevated production rate, hydraulic validation was only possible for the static head, but not for the frictional

⁵² Single-phase gas flow is not covered by the model.

⁵³ Finite Volume Method

pressure head. The flow rates during the measurement were so low that the calculated friction pressure drop was in the range of the mean simulation error of 0.36 bar, being 0.3 % of the total pressure drop.

The application of the model to the GrSk site demonstrated that heat flow to the formation is relevant beyond a short start-up phase. While in the given scenario at a production rate of 100 m³/h the wellhead temperature T_{wh} gets within 5 K of the reservoir temperature in 30 years of operation, it does not get closer than 15 K if production rate is only 25 m³/h. This means that power plant design has to consider the reduced wellhead temperatures instead of just assuming that the brine is produced with reservoir temperature. This finding also underlines that determination and/or improvement of reservoir productivity is vital in geothermal projects. A higher production rate is desirable not only because of the larger mass flow itself, but also because of the higher achievable temperature T_{wh} . This relevance of transient heat flow puts sites similar to GrSk apart from both high flow rate geothermal wells, where stationary temperatures are reached within a negligibly short start-up phase and low flow rate oil wells where heat flow is so small that formation temperature can be considered constant.

Subsequent analysis of the sensitivity on selective model simplifications (for the GrSk site) confirmed that detailed modelling and precise parameterization are necessary for good accordance with measurements. Particularly relevant are the heat flow modelling in the open annulus, precise knowledge of the formation temperature profile and brine salinity as well as the importance of considering the washout volume and cement quality. Considering two-phase flow is relevant for the hydraulics, but can be omitted for thermal calculations.

10 Outlook

Future work should include further validation and could involve further refinement, extension and, of course, application of the model.

Validation of the wellbore model has been conducted with a small set of data, so that the good accordance may be partly coincidental. Hence, validation with data from longer experiments with higher flow rates and higher temperature or even with data from other sites is advisable. Alternatively other proven wellbore simulators could provide validation data.

Parameter studies can be conducted to determine the model sensitivity on individual parameters and to identify optimization possibilities. For example, the effect of imperfect contact between the layers of the well completion could be evaluated. A proof-of-concept optimization of the production string diameter has been conducted with the wellbore model. It could be applied to a real scenario.

The implemented component specific correlations and the mixture rules for density, viscosity and heat capacity can be updated with new research results, once they become available. For example, Hoffert and Milsch (2013b) currently work on mixture rules for density and viscosity of chloride solutions. If the brine property model is to be applied to fluids from other sites the different fluid chemistry may require an extension in order to include other components than the presently implemented chlorides (NaCl, KCl, CaCl₂) and gases (N₂, CO₂, CH₄).

Geofluid inflow to the well from the reservoir has been simplified to happen at one depth in the model of the GrSk site. Including confluence from several horizons with different temperatures and different productivities could help in understanding their hydraulic interaction and the origin of the produced geofluid. Branched hydraulic systems are supported by MODELICA's stream connectors, so this should be possible with the presented model.

Accordance with measured values for low production rates or short-term behaviour, i.e., quickly changing production rate, can possibly be improved by including the heat storage in the well completion. The next step would be implementing a non-steady-state thermal flow model that considers storage and convective transport of heat in the fluid. This would, however, bring the flow calculation problem numerically to level of non-stationary CFD⁵⁴. Implementation in MODELICA would be difficult, resource intensive and error-prone, so that the use of existing CFD code or software should be considered following the approach by Saeid et al. (2013).

Pump efficiency can be calculated for the actual operation point from the pump characteristics. This feature has been implemented. It was, however, not used in this work, because the given pump characteristics are only valid within nominal operation range, which was not reached in the validation scenarios. The validity range could be extended with measured electric data. Applying the variable efficiency instead of assuming a constant value could reduce the error in predictive calculations. Furthermore, production rate and pump head would be connected via the pump speed as a new operational parameter. Thus, if wellhead pressure was to be kept constant, the production rate would be realistically controlled via the pump speed and simulation with impossible operation points could be avoided.

⁵⁴ Computational Fluid Dynamics

More detailed two-phase flow modelling considering slip and different flow regimes is state of the art in other wellbore simulators. Hydraulic validation showed that the homogenous flow model is sufficient for the given scenario. However, more advanced models are probably necessary when simulating flows with higher void fractions as they occur in other sites (e.g., in Bruchsal, Germany (Fuchs and Kather, 2013) or Romania (Antics, 1995)).

PHREEQC⁵⁵ is freely available software for geochemical calculations with the option to be integrated as a library into other programs. After evaluating its ability to reproduce the geofluid properties, it could be used to further validate or replace the geofluid model described here. Either integrated or separately as post-processing, PHREEQC could be used to predict precipitation, which is a key issue in geothermal plant operation. PHREEQC can also reproduce reaction kinetics. It could be used to evaluate the time-scale of gas solution, dissolution and precipitation and assess its significance in the well flow.

The model has been implemented in the commercial software DYMOLA. Alternative (free) simulation environments are available. They should be evaluated regarding their capability of running the brine circuit model with a few adaptations.

Stability and functionality rather than efficiency were the guideline during model implementation. Hence a significant reduction of computing time is deemed possible by tweaking simulation parameters, removing redundant calculations (see E 2.1), providing analytic differentials (see E 2.2), tabularizing or caching property values, moving property functions to external code or by parallelization for multi-core CPUs. These strategies should be evaluated regarding their potential benefit and feasibility.

The modelling domains adjacent to the brine circuit, reservoir and power plant interact with the brine circuit. They are represented by constant or time-dependent boundary conditions in the presented model. If they were replaced by variables that are exchanged with models of the reservoir/power plant, feedback effects (e.g., thermal breakthrough) could be studied in order to predict the life cycle behaviour (Blöcher et al., 2010). Coupling of a brine circuit model including heat exchanger, injection pump and injection well with existing complex models of reservoir including fractures and faults (Blöcher et al., 2010) and power plant has been implemented as proof-of-concept and is subject of a current project at GFZ.

⁵⁵ http://wwwbrr.cr.usgs.gov/projects/GWC_coupled/phreeqc [30 Nov 2013]

A Conversions

A 1. Molality ↔ mass fraction:

Molality is the number of moles of solute per volume of solvent.

Molality → mass fraction:

$$X_i = \frac{b_i \cdot M_i}{1 + \sum b_i \cdot M_i} \quad (\text{A.1})$$

Mass fraction is the ratio of mass of solute and the total mass of the solution.

mass fraction → Molality:

$$b_i = \frac{X_i}{M_i \cdot X_{H_2O}} \quad (\text{A.2})$$

A 2. Conversion between gas void fraction and gas mass fraction

Gas mass fraction → gas volume fraction (using eq. 3.2):

$$\varepsilon = \frac{V''}{V} = \frac{m''}{\rho''} \cdot \frac{\rho}{m} = x \cdot \frac{\rho}{\rho''} = \frac{x}{\rho''} \left(\frac{1-x}{\rho'} + \frac{x}{\rho''} \right)^{-1} = \left(\frac{1-x}{\rho'} \frac{\rho''}{x} + 1 \right)^{-1} \quad (\text{A.3})$$

Gas volume fraction → gas mass fraction:

$$x = \varepsilon \cdot \frac{\rho''}{\rho} = \frac{\varepsilon \rho''}{\varepsilon \rho'' + (1-\varepsilon) \rho'} = \left(1 + \frac{(1-\varepsilon) \rho'}{\varepsilon \rho''} \right)^{-1} \quad (\text{A.4})$$

A 3. Gas volume/mass flow fraction → Gas volume/mass fraction

Gas volume flow fraction $\dot{\varepsilon}$ is defined as the ratio of gas volume flow V'' and total volume flow V .

$$\varepsilon \rightarrow \dot{\varepsilon}: \quad \dot{\varepsilon} = \frac{\dot{V}''}{\dot{V}} = \frac{\varepsilon A w''}{\dot{V}' + \dot{V}''} = \frac{\varepsilon A S w'}{((1-\varepsilon) w' + \varepsilon w'') A} = \frac{\varepsilon S}{(1-\varepsilon) + \varepsilon S} = \frac{\varepsilon}{\frac{1-\varepsilon}{S} + \varepsilon} = \left(\frac{1-\varepsilon}{S} + 1 \right)^{-1} \quad (\text{A.5})$$

Cancellation of ε or $\dot{\varepsilon}$ in the last step of this and the following equations requires $\varepsilon \neq 0$ or $\dot{\varepsilon} \neq 0$.

Inverting eq. A.5 gives:

$$\dot{\varepsilon} \rightarrow \varepsilon: \quad \varepsilon = \frac{\dot{\varepsilon}}{S - S\dot{\varepsilon} + \dot{\varepsilon}} = \left(\frac{S}{\dot{\varepsilon}} - S + 1 \right)^{-1} \quad (\text{A.6})$$

Gas volume flow fraction $\dot{\varepsilon}$ is related to the gas mass flow fraction \dot{x} like gas volume fraction to gas mass fraction (by analogy to eq. A.4):

$$\dot{\varepsilon} \rightarrow \dot{x}: \quad \dot{x} = \dot{\varepsilon} \cdot \frac{\rho''}{\rho} \quad (\text{A.7})$$

Inserting eq. A.6 in eq. A.4 gives the mass fraction as a function of gas volume flow fraction $\dot{\varepsilon}$:

$$\dot{\varepsilon} \rightarrow x: \quad x = \frac{\dot{\varepsilon}}{S - S\dot{\varepsilon} + \dot{\varepsilon}} \frac{\rho''}{\rho} = \left(\frac{S}{\dot{\varepsilon}} - S + 1 \right)^{-1} \frac{\rho''}{\rho} \quad (\text{A.8})$$

eq. A.5 in eq. A.7:

$$\varepsilon \rightarrow \dot{x}: \quad \dot{x} = \frac{\rho''}{\rho} \frac{\varepsilon}{\frac{1-\varepsilon}{S} + \varepsilon} = \frac{\rho''}{\rho} \frac{1}{\frac{1-\varepsilon}{S} + 1} \quad (\text{A.9})$$

A 4. Bubble rise velocity → Slip factor

$$S = \frac{w''}{w'} = \frac{w'+w_B}{w'} = 1 + \frac{w_B}{w'} \quad (\text{A.10})$$

Simple approximate solution when assuming $w' = w$: (very little difference to full solution)

$$S = \frac{w''}{w} = \frac{w+w_B}{w} = 1 + \frac{w_B}{w} = 1 + \frac{w_B A}{\dot{V}} \quad (\text{A.11})$$

The exact solution:

$$\dot{V} = (1 - \varepsilon)w'A + \varepsilon w''A = (1 - \varepsilon + \varepsilon S)w'A \Leftrightarrow w' = \frac{\dot{V}}{A(1 + \varepsilon(S-1))} \quad (\text{A.12})$$

A.12 in A.10:

$$S = 1 + \frac{w_B}{\dot{V}} A (1 + \varepsilon(S-1)) \quad (\text{A.13})$$

A.6 in A.13 (assuming $\dot{\varepsilon} \neq 0$):

$$S = 1 + \frac{w_B}{\dot{V}} A \left(1 + \frac{S-1}{\frac{\dot{\varepsilon}}{S-1}} \right) \quad (\text{A.14})$$

$$\frac{S-1}{\frac{w_B A}{\dot{V}}} - 1 = \frac{S-1}{\frac{\dot{\varepsilon}}{S-1}} \quad (\text{A.15})$$

$$\left(\frac{S-1}{\frac{w_B A}{\dot{V}}} - 1 \right) \left(\frac{\dot{\varepsilon}}{S-1} \right) = S-1 \quad (\text{A.16})$$

$$\frac{S-1}{\frac{w_B A}{\dot{V}}} S \left(\frac{1}{\dot{\varepsilon}} - 1 \right) + \frac{S-1}{\frac{w_B A}{\dot{V}}} + S \left(1 - \frac{1}{\dot{\varepsilon}} \right) - 1 = S-1 \quad (\text{A.17})$$

$$S(S-1) \frac{\left(\frac{1}{\dot{\varepsilon}}-1\right)\dot{V}}{w_B A} + S \left(\frac{\dot{V}}{w_B A} + 1 - \frac{1}{\dot{\varepsilon}} - 1 \right) - \frac{\dot{V}}{w_B A} = 0 \quad (\text{A.18})$$

$$S^2 \frac{\left(\frac{1}{\dot{\varepsilon}}-1\right)\dot{V}}{w_B A} + S \left(-\frac{\left(\frac{1}{\dot{\varepsilon}}-1\right)\dot{V}}{w_B A} + \frac{\dot{V}}{w_B A} - \frac{1}{\dot{\varepsilon}} \right) - \frac{\dot{V}}{w_B A} = 0 \quad (\text{A.19})$$

$$S^2 \frac{\left(\frac{1}{\dot{\varepsilon}}-1\right)\dot{V}}{w_B A} + S \left(\frac{\left(2-\frac{1}{\dot{\varepsilon}}\right)\dot{V}}{w_B A} - \frac{1}{\dot{\varepsilon}} \right) - \frac{\dot{V}}{w_B A} = 0 \quad (\text{A.20})$$

$$S^2 + \left(\frac{\left(2-\frac{1}{\dot{\varepsilon}}\right)\dot{V}}{w_B A} - \frac{1}{\dot{\varepsilon}} \right) \frac{w_B A}{\left(\frac{1}{\dot{\varepsilon}}-1\right)\dot{V}} S - \frac{1}{\frac{1}{\dot{\varepsilon}}-1} = 0 \quad (\text{A.21})$$

$$S^2 + \left(2 - \frac{1}{\dot{\varepsilon}} - \frac{w_B A}{\dot{\varepsilon}\dot{V}} \right) \frac{1}{\frac{1}{\dot{\varepsilon}}-1} S - \frac{1}{\frac{1}{\dot{\varepsilon}}-1} = 0 \quad (\text{A.22})$$

$$S_{1,2} = -\frac{1}{2} \left(2 - \frac{1}{\dot{\varepsilon}} - \frac{w_B A}{\dot{\varepsilon}\dot{V}} \right) \frac{1}{\frac{1}{\dot{\varepsilon}}-1} \pm \sqrt{\left(\frac{1}{2} \left(2 - \frac{1}{\dot{\varepsilon}} - \frac{w_B A}{\dot{\varepsilon}\dot{V}} \right) \frac{1}{\frac{1}{\dot{\varepsilon}}-1} \right)^2 + \frac{1}{\frac{1}{\dot{\varepsilon}}-1}} \quad (\text{A.23})$$

$$S_{1,2} = \left(-1 + \frac{1}{2\dot{\varepsilon}} + \frac{w_B A}{2\dot{\varepsilon}\dot{V}} \right) \frac{1}{\frac{1}{\dot{\varepsilon}}-1} \pm \sqrt{\left(\left(1 - \frac{1}{2\dot{\varepsilon}} - \frac{w_B A}{2\dot{\varepsilon}\dot{V}} \right) \frac{1}{\frac{1}{\dot{\varepsilon}}-1} \right)^2 + \frac{1}{\frac{1}{\dot{\varepsilon}}-1}} \quad (\text{A.24})$$

A 5. Specific heat capacity → apparent molar heat capacity

Starting from eq. 5.40 for a single salt solution:

$$c_p = X_{H_2O} (c_p^{H_2O} + \bar{C}_p b) \quad (b \text{ is salt molality}) \quad (\text{A.25})$$

$$\frac{c_p}{c_p^{\text{H}_2\text{O}}} = \left(1 + \frac{\bar{C}_p b}{c_p^{\text{H}_2\text{O}}}\right) X_{\text{H}_2\text{O}} \Leftrightarrow \left(\frac{c_p}{X_{\text{H}_2\text{O}}} - c_p^{\text{H}_2\text{O}}\right) \frac{1}{b} = \bar{C}_p \quad (\text{A.26})$$

With

$$X_{\text{H}_2\text{O}} = \frac{m_{\text{H}_2\text{O}}}{m_{\text{H}_2\text{O}} + m_{\text{salt}}} = \frac{1}{1 + bM_{\text{salt}}} \quad (\text{A.27})$$

it becomes

$$\bar{C}_p = (c_p(1 + bM) - c_p^{\text{H}_2\text{O}}) \frac{1}{b} \quad (\text{A.28})$$

$$\bar{C}_p = \left((1 + bM) \left[\frac{c_p}{c_p^{\text{H}_2\text{O}}} \right] - 1 \right) \frac{c_p^{\text{H}_2\text{O}}}{b} . \quad (\text{A.29})$$

$$\bar{C}_p = \left((b + M) \left[\frac{c_p}{c_p^{\text{H}_2\text{O}}} \right] - \frac{1}{b} \right) c_p^{\text{H}_2\text{O}} . \quad (\text{A.30})$$

B Auxiliary calculations

B 1. Pipe flow – momentum balance

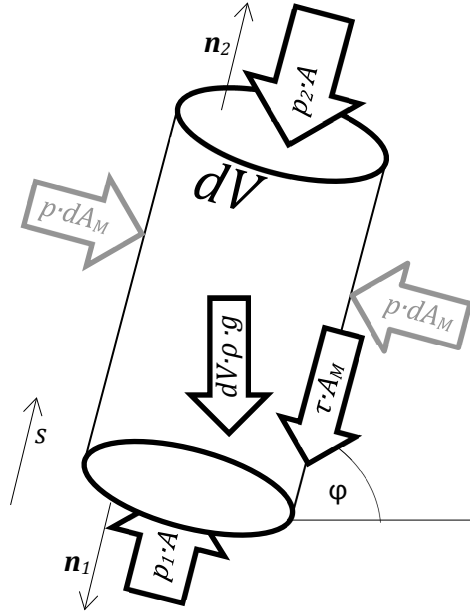


Fig. 44: Force equilibrium in static pipe flow

The momentum balance for a static open system can be written as (Müller, 2001):

$$\int_{\mathcal{V}} \frac{\partial \rho w_j}{\partial t} dV + \int_{\partial \mathcal{V}} (\rho w_j w_i + t_{ij}) n_i dA = \int_{\mathcal{V}} \rho f_j dV. \quad (\text{B.31})$$

Application to a steady flow in a pipe section of the length Δs with constant cross section area A , diameter d und inclination angle φ gives in flow direction:

$$\int_{\mathcal{V}} \rho w^2 dA + \int_{\partial \mathcal{V}} (-p \delta_{ij} + \tau_{ij}) n_i dA = - \int_{\mathcal{V}} \rho g \sin \varphi dV \quad (\text{B.32})$$

The effects of pressure on the lateral surface cancel each other out. Shear stress is applied only to the lateral surface.

$$\int_{\partial \mathcal{V}} -p \delta_{ij} n_i dA = -g \sin \varphi \int_{\mathcal{V}} \rho dV - \int_{\partial \mathcal{V}} \tau_{ij} n_i dA - \int_{\partial \mathcal{V}} \rho w^2 dA \quad (\text{B.33})$$

$$\int_{A_2} p dA - \int_{A_1} p dA = -g \sin \varphi \int_{\mathcal{V}} \rho dV - \int_M \tau dA - \left(\int_{A_2} \rho w^2 dA - \int_{A_1} \rho w^2 dA \right) \quad (\text{B.34})$$

The three terms on the right side are referred to as hydrostatic, friction and kinetic head. The friction head can be expressed by introducing a dimensionless friction factor f , a mean density ρ_m and a mean velocity u_m . Pressure, density and velocity are assumed to be constant over a cross section. The density within the pipe section is assumed to be ρ_m .

$$(p_2 - p_1)A = -g \sin \varphi \rho_m A \Delta s - f \frac{w_m^2 \rho_m}{2d} A \Delta s - A(\rho_1 w_2^2 - \rho_2 w_1^2) \quad (\text{B.35})$$

Division by $A \cdot \Delta s$ and decreasing Δs to ds leads to the local form of the momentum balance of stationary pipe flow:

$$\frac{\partial p}{\partial s} = -\rho g \sin \varphi - f \frac{w^2 \rho}{2d} - \frac{\partial}{\partial s} \rho w^2 \quad (\text{B.36})$$

Assuming a constant gradient (in flow direction) of velocity and density by setting $u_m = (u_1 + u_2)/2$ and $\rho_m = (\rho_1 + \rho_2)/2$ gives the discretized form:

$$p_2 = p_1 - \frac{1}{2} g (\rho_1 + \rho_2) \sin \varphi \Delta s - f \frac{(w_1 + w_2)^2 (\rho_1 + \rho_2)}{16d} \Delta s - (\rho_2 w_2^2 - \rho_1 w_1^2) \quad (\text{B.37})$$

Apparently p_2 depends on the density and the velocity of fluid leaving the pipe section, which in turn depend on p_2 , which makes the equation implicit.

B 2. Raoult's Law (ideal)

By analogy to (Müller, 2001) chapter 7.5 we state that in a phase equilibrium Gibbs energy is minimized and therefore start from the equality of chemical potential between phases:

$$\mu_\alpha'(p, T, y_\alpha') = \mu_\alpha''(p, T, y_\alpha'') \quad (\text{B.38})$$

y_α' and y_α'' denote the mole fractions of the component α in the liquid phase and in the gas phase, respectively. Then we assume that both liquid and gas phase are ideal mixtures:

$$g_\alpha'(T, p) + \frac{R}{M_\alpha} T \ln y_\alpha' = g_\alpha''(T, p) + \frac{R}{M_\alpha} T \ln y_\alpha'' \quad (\text{B.39})$$

Furthermore, we assume incompressibility of the liquid phase (so that g is linear in p) and that the gas phase consists of ideal gases:

$$g_\alpha'(T, p_\alpha(T)) + v_\alpha'(p - p_\alpha(T)) + \frac{R}{M_\alpha} T \ln y_\alpha' = g_\alpha''(T, p_\alpha(T)) + \frac{R}{M_\alpha} T \ln \frac{p}{p_\alpha(T)} + \frac{R}{M_\alpha} T \ln y_\alpha'' \quad (\text{B.40})$$

The free enthalpies have been rewritten in such a way that they refer to the saturation pressure of the pure constituent $p(T)$. Assuming that specific volume of the liquid is negligible compared to the one of gas phase and using the relation

$$g_\alpha'(T, p_\alpha(T)) = g_\alpha''(T, p_\alpha(T)) \quad (\text{B.41})$$

one obtains Raoult's law for vapour-liquid-equilibria:

$$y_\alpha' p_\alpha(T) = y_\alpha'' p \quad (\text{B.42})$$

B 3. Boundary layer heat transfer calculation

The following equations use the Reynolds number and the Prandtl number which are defined as:

$$Re = \frac{w d_{\text{hyd}} \rho}{\eta} \quad (\text{B.43})$$

$$Pr = \frac{c_p \eta}{\lambda} \quad (\text{B.44})$$

With the mean flow velocity w , the pipe diameter d_{hyd} , the fluid density ρ , the dynamic viscosity η , the specific heat capacity c_p and the thermal conductivity λ .

The material properties are to be calculated for the average between flow temperature and the wall temperature.

B 3.1 Nusselt number for laminar flow

For the fully developed laminar pipe flow with a parabolic velocity profile the Nusselt number can be calculated analytically with an infinite series (Dubbel, 2001). Due to its bad convergence a more convenient approximate solution is recommended, the equation by Stephan:

$$Nu = \begin{cases} \frac{Nu_0}{\tanh(2.43 \cdot Re^{1/6} \cdot X^{1/6})} & \text{for } \frac{l}{d_{\text{hyd}} Re} < 5.75e - 2, \\ Nu_0 & \text{else} \end{cases}, \quad (\text{B.45})$$

where $X = \frac{l}{d_{\text{hyd}} Re Pr}$ and

$$Nu_0 = \frac{3.657}{\tanh\left(2.264 \cdot X^{\frac{1}{3}} + 1.7 \cdot X^{\frac{2}{3}}\right)} + \frac{0.0499}{X} \tanh X, \quad (\text{B.46})$$

B 3.2 Nusselt number for fully developed turbulent flow by McAdams

The equation for fully developed turbulent flow by McAdams is valid for $10^4 \leq Re \leq 10^5$, $l/d \geq 60$ and $0.5 < Pr < 100$:

$$Nu = 0.024 \cdot Re^{0.8} \cdot Pr^{1/3}, \quad (\text{B.47})$$

B 3.3 Nusselt number for fully turbulent flow (estimation)

An equation for estimations of the Nusselt number of turbulent pipe flows is given by the VDI Heat Atlas (Gnielinski, 2010) as:

$$Nu = Pr^{0.4} \left(1 + \left(\frac{d_{\text{hyd}}}{l}\right)^{\frac{2}{3}}\right) \cdot \begin{cases} 0.0214(Re^{0.8} - 100) & \text{for } Pr < 1.5 \\ 0.012(Re^{0.87} - 280) & \text{else} \end{cases}, \quad (\text{B.48})$$

Its validity is limited to $0.5 \leq Pr \leq 500$.

B 3.4 Nusselt number for fully turbulent flow by Gnielinski

The equation by Gnielinski is given in Dubbel (2001) and VDI-Heat Atlas (2010) as:

$$Nu = \begin{cases} \frac{Re Pr^{\frac{\zeta}{8}}}{1 + 12.7 \sqrt{\frac{\zeta}{8}} (Pr^{\frac{2}{3}} - 1)} \left(1 + \left(\frac{d_{\text{hyd}}}{l}\right)^{\frac{2}{3}}\right) & \text{for } \frac{l}{d_{\text{hyd}}} < 60, \\ 0.024 \cdot Re^{0.8} \cdot Pr^{1/3} & \text{else} \end{cases}, \quad (\text{B.49})$$

where $\zeta = (0.78 \log Re - 1.5)^{-2}$.

It is valid for developing and developed flow with $10^4 \leq Re \leq 10^5$, $0.1 \leq Pr \leq 1000$, $d_{\text{hyd}}/l \leq 1$.

B 3.5 Nusselt number for laminar and turbulent flow (VDI)

Gnielinski (1995) proposed to calculate the Nusselt number for the heat transfer in the transition between laminar and turbulent flow ($2300 \leq Re \leq 10^4$) by linear interpolation between the Nusselt numbers for laminar and turbulent flow:

$$Nu = (1 - \gamma) Nu_{m,L,2300} + \gamma Nu_{m,T,10^4}. \quad (\text{B.50})$$

The weighting factor γ represents the state of the flow between laminar and turbulent flow:

$$\gamma = \min\left(1, \frac{Re - 2300}{10^4 - 2300}\right), \text{ where } 0 \leq \gamma \leq 1 \text{ and} \quad (\text{B.51})$$

$$Re = \frac{w d_{\text{hyd}} \rho}{\eta} \text{ with the average velocity } w = \dot{V}/A. \quad (\text{B.52})$$

By limiting it to 1 eq. B.51 has been adapted to include the fully turbulent range.

The Nusselt number for laminar flow ($Re = 2300$) and constant wall temperature⁵⁶ is:

$$Nu_{m,L,2300} = \left(49.371 + (Nu_{m,\theta,2,2300} - .7)^3 + Nu_{m,\theta,3,2300}^3 \right)^{\frac{1}{3}}, \text{ where} \quad (\text{B.53})$$

$$Nu_{m,\theta,2,2300} = 1.615 \cdot \sqrt[3]{2300 \cdot Pr \frac{d_{\text{hyd}}}{l}} \quad \text{and} \quad (\text{B.54})$$

$$Nu_{m,\theta,3,2300} = \left(\frac{2}{1 + 22 \cdot Pr} \right)^{\frac{1}{6}} \sqrt[3]{2300 \cdot Pr \frac{d_{\text{hyd}}}{l}}. \quad (\text{B.55})$$

The Nusselt number for fully turbulent flow ($Re = 10^4$) is the equation by Gnielinski (eq. B.49) with ζ plugged in:

$$Nu_{m,T,10^4} = \frac{(0.0308/8)10^4 Pr}{1 + 12.7\sqrt{(0.0308/8)} \left(Pr^{\frac{2}{3}} - 1 \right)} \left(1 + \left(\frac{d_{\text{hyd}}}{l} \right)^{\frac{2}{3}} \right). \quad (\text{B.56})$$

$$Pr = \frac{\eta c_p}{\lambda}. \quad (\text{B.57})$$

The equation is valid for developing and fully developed single-phase flow with $2300 \leq Re \leq 10^4$, $0.6 \leq Pr \leq 1000$

and $d_{\text{hyd}}/l \leq 1$.

B 4. VLE calculation in flow with slip

We consider the thought experiment depicted in Fig. 45: The fluid mass $\Delta m = \Delta m_1'' + \Delta m_1'$ is in thermodynamic equilibrium in container 1 at pressure p_1 and Temperature T_1 . Both valves are opened for the time Δt and the fluid is pumped completely at constant pressure through the pipe into the second container, where a different equilibrium is established. The mass flow $\dot{m} = \Delta m / \Delta t$ leaving container 1 is composed of gas flow $\dot{m}_1'' = \Delta m_1'' / \Delta t$ and liquid flow $\dot{m}_1' = \Delta m_1' / \Delta t$. The two mass flows may have different velocities u'' and u' .

⁵⁶ The alternative equation is valid for constant heat flux. Both equations are appropriate for the quasistatic modeling, as they are recalculated in every time step before wall temperature or heat flux has changed significantly.

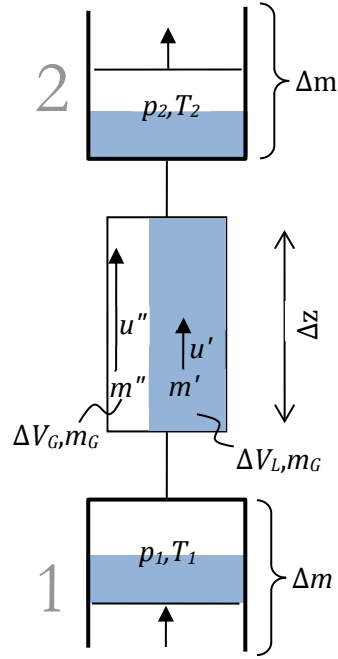


Fig. 45: Thought experiment to make VLE solution use for slip flow plausible

$$x(p, T, X) = \frac{\Delta m_1''}{\Delta m_1} = \frac{\Delta m_1''/\Delta t}{\Delta m_1/\Delta t} \Rightarrow \frac{dm_1''/dt}{dm_1/dt} = \frac{\dot{m}''}{\dot{m}} = \dot{x}(p, T, \dot{X}) \quad (\text{B.58})$$

Reducing Δm and Δt to dm and dt in eq. B.58 while still assuming thermodynamic equilibrium, shows that the gas mass flow fraction is also the ratio of (initial) phase masses in container 1 m''/m . Thermodynamic equilibrium implies constant pressure and temperature on a cross section. So, the VLE algorithm for static closed system can be used to calculate the phase equilibrium in slip flow.

The in-situ volume fraction of the gas phase ε obviously depends on gas flow fraction $\dot{\varepsilon}$ determined above and phase densities, but also on the slip (see A 3):

$$\varepsilon = \dot{x} \frac{\dot{m}}{\rho'' w'' A} = \left(\frac{\rho'' w''}{\rho' w'} \frac{1-\dot{x}}{\dot{x}} + 1 \right)^{-1} \quad (\text{B.59})$$

Gas mass fraction and mean density are calculated from this ε using eq. A.4 and eq. 3.1.

B 5. Calculation of brine composition from measurements:

The GrSk brine has been sampled and analysed for salinity and gas content (see also 6.1.2). The values have to be converted to the total composition in mass fraction for use in the brine property model (5.1).

The ion composition has been analysed and published by Feldbusch et al. (2013). The gas content and composition is published in the technical report STR04/16 (Huenges and Seibt, 2004). The values of the three main cations and the three main gases are listed in Table 11.

The salt content is specified by the mass of ions per litre. The gas content is given as the volume fractions of the gas phase. The total gas content is given as the volume ratio of gas and liquid phase: 84.75 % (average of all measurements).

The gas content has been determined with the following procedure described in (Wiersberg et al., 2004):

A sample container (autoclave) is lowered into the well. The fluid is sampled and kept under in-situ pressure. It is then transferred into an evacuated vessel of known volume, which is kept under standard conditions⁵⁷ and submerged in an ultrasonic bath to accelerate degassing. The gas composition is determined by means of a gas mass spectrometer.

The measured gas content and composition specifies the gas phase at standard conditions. The gas that remains in solution can be determined via the gas solubility functions (5.2.2.4).

Table 11: Brine composition Gross Schoenebeck

Ion	Na⁺	K⁺	Ca⁺⁺			
Molarity / [mmol/l] (measured)	1691.4	40.0	1303.4			
Component	NaCl	KCl	CaCl₂	CO₂	N₂	CH₄
Volume fraction in gas phase (measured)				3.8 %	82.9 %	12.8 %
g per kg liquid – gas phase	0	0	0	0.050	0.686	0.061
g per kg liquid – liquid phase	83.9	2.53	122.8	0.023	0.0036	0.0007
g per kg fluid - total	83.8	2.53	122.7	0.072	0.690	0.061

1st row: measured ion content. 2nd row: averaged measured values for volume fraction of gas phase. 3rd row: composition of gas phase. 4th row: composition of liquid phase. Last row: total brine composition (mass fractions).

Liquid phase density: 1079 kg/m³ (fluid model). CO₂/N₂/CH₄/gas phase density: 1.81/1.15/0.66/1.10 kg/m³.

The gas volume fractions have been converted to masses of free gas per kg liquid, using the total gas fraction and gas densities (see 5.2.3) of the respective gas and the brine under standard conditions (third row of Table 11).

The ion masses from the fluid analysis mentioned in 6.1.2 have been combined according to their valence to obtain the concentration of the chlorides NaCl, KCl and CaCl (fourth row in Table 11).

Assuming equilibrium during the measurement, the solubility functions (5.2.2.4) have been used to calculate gas concentrations in liquid phase from the given gas volume fractions. Adding them to the gas masses in the gas phase (derived from ratio gas-liquid and the volume fractions) yields the total composition of the fluid (last row in Table 11).

Most of the gas is degassed for N₂ and CH₄, but due to the higher solubility a considerable fraction of CO₂ remains in solution even under low pressure.

⁵⁷ STP: 0 °C, 1.01325 Pa

B 6. Pump

B 6.1 Isentropic Pump

The pump is idealized as an adiabatic reversible (isentropic) process, i.e. no heat transfer, no friction loss. The change of specific enthalpy is then approximated by linear extrapolation of the gradient at inflow conditions:

$$\Delta h_{\text{is}} = \int_{p_1}^{p_1+\Delta p} \left. \frac{\partial h}{\partial p} \right|_s dp \approx \left. \frac{\partial h(p_1, T_1)}{\partial p} \right|_s \Delta p. \quad (\text{B.60})$$

The isentropic derivative can be found in the Bridgman tables (Bridgman, 1914):

$$\left. \frac{\partial h}{\partial p} \right|_s = \frac{1}{\rho}. \quad (\text{B.61})$$

Hence, if the density change is negligible ($\Delta \rho \ll \rho$), as it is the case in a single-phase flow, the enthalpy change in the pump can be calculated explicitly as:

$$\Delta h = \frac{\Delta p}{\rho_1}. \quad (\text{B.62})$$

B 6.2 Estimation of temperature increase in pump

The pressure increase in the ESP increases the fluid temperature by isentropic compression and by dissipation in the pump and the motor:

$$\Delta T_{\text{ESP}} = \Delta T_{\text{is}} + \Delta T_{\text{loss}}. \quad (\text{B.63})$$

The first is estimated here, the latter in B 6.5.

The temperature increase by isentropic pressure increase is approximated by linear extrapolation of the gradient at inflow conditions:

$$\Delta T_{\text{is}} = \int_{p_1}^{p_1+\Delta p} \left. \frac{\partial T}{\partial p} \right|_s dp \approx \left. \frac{\partial T(p_1, T_1)}{\partial p} \right|_s \Delta p. \quad (\text{B.64})$$

The isentropic derivative can be found in the Bridgman tables (Bridgman, 1914):

$$\left. \frac{\partial T}{\partial p} \right|_s = \left. \frac{\partial v}{\partial T} \right|_p \frac{T}{c_p} = \frac{\beta T}{\rho c_p}. \quad (\text{B.65})$$

β is the isobaric thermal expansion coefficient, also used in eq. 3.34:

The temperature increase is independent from the mass flow:

$$\Delta T_{\text{isentrop}} = \frac{\beta T}{\rho c_p} \Delta p. \quad (\text{B.66})$$

Evaluation for a pump head of 1000 m, a density of $\rho = 1000 \text{ kg/m}^3$, a specific heat capacity of $c_p = 3300 \text{ kJ/(kg}\cdot\text{K)}$ (see 5.2.4.5) and a thermal expansion coefficient of $\beta = 5 \cdot 10^{-4} \text{ J/(kg}\cdot\text{K)}$ ⁵⁸ returns a temperature increase of the fluid by isentropic pressure increase of 0.55 K.

B 6.3 Isentropic efficiency

The energy balance for static open systems (Müller, 2001) can be written as follows, when the fluid is assumed to flow through two homogenous surfaces (denoted 1 and 2) and when radiation, gravity and kinetic energy are neglected:

$$P + \dot{Q} = \dot{m}(h_2 - h_1), \quad (\text{B.67})$$

where P is– mechanical work into the system, \dot{Q} is heat flow into the system, \dot{m} is mass flow through boundaries and h_1, h_2 are the specific enthalpies on the homogeneous boundaries.

In the isentropic case the heat flow is by definition zero:

$$P_{\text{is}} = \dot{m}(h_1 - h_{2,\text{is}}). \quad (\text{B.68})$$

The ratio of enthalpy differences of isentropic and non-isentropic case is called isentropic efficiency:

$$\eta_{\text{is}} = \frac{P_{\text{is}}}{P + \dot{Q}} = \frac{h_1 - h_{2,\text{is}}}{h_1 - h_2} = \frac{P_{\text{hydr}}}{P_{\text{el}}} \quad (\text{B.69})$$

It can be used to specify the losses in a pump, as it accounts for dissipation during the conversion of rotational power from the pump shaft to actual hydraulic pump power. Under stationary conditions the dissipated energy is absorbed by the pumped fluid.

In the case of the ESP used in GrSk the isentropic efficiency also equals the ratio of hydraulic power and electric power fed to the pump:

$$\eta_{\text{is}} = \frac{P_{\text{is}}}{P_{\text{shaft}} + \dot{Q}_{\text{loss,mot}}} = \frac{P_{\text{hydr}}}{P_{\text{el}}} \quad (\text{B.70})$$

P_{is} is the power needed for the adiabatic pressure increase, the desired hydraulic power of the pump. The electric power of pump motor P_{el} is completely converted to mechanical rotating power on the pump shaft and thermal energy from dissipation in the motor.

B 6.4 Calculation of pump efficiency from measured data

The combined efficiency of pump, motor, transformer and speed controller (variable voltage inverter) can be determined from hydraulic power and electric power of the pump P_{el} :

$$\eta_{\text{is}}\eta_{\text{mot}} = \frac{P_{\text{hydr}}}{P_{\text{el}}} = \frac{\dot{V}\Delta p}{\eta_{\text{tr}}\eta_{\text{sc}}P_{\text{tr}}}. \quad (\text{B.71})$$

The pump transformer is fed by $U_Y/U_{\Delta} = 230/400 \text{ V}$ three-phase electric power. The three currents have been recorded. The real power of the transformer is calculated following Dubbel (2001) as:

$$P_{\text{tr}} = U_Y(I_1 + I_2 + I_3) \cos \varphi = \frac{U_{\Delta}}{\sqrt{3}}(I_1 + I_2 + I_3) \cos \varphi. \quad (\text{B.72})$$

⁵⁸ Calculated with REFPROP for water or with the geofluid model via numeric differentiation.

The phase difference φ is given by the manual as the power factor $\cos \varphi = 0.96$ at full speed. Part load behaviour is not described; therefore the full speed value is used.

Using these assumptions, assuming nominal Voltage, applying eq. B.72 on the data from the circulation test described in 6.4 and averaging the result for $t > 60$ h yields a combined efficiency of $\eta_{is}\eta_{mot} = 50.6\%$.

Table 12: Pump efficiency calculation from hydraulic and electric data, averaged for $t > 50$ h from circulation test (6.4). Power factor is $\varphi = 0.96$, Voltage is $U = 230/400$ V

Δp_{ESP} bar	\dot{V} m ³ /h	P_{hydr} W	I_{mot} A	P_{el} W	η_{is} -
116	15.7	50580	448.6	99048	51%

The transformer efficiency is usually very high. The efficiency of the speed controller is specified as $\eta_{sc} > 0.96$ (Electrospeed GCS Operator's Manual P/N 900350, 2001). If both efficiencies are approximated with $\eta_{tr} = \eta_{sc} = 1$ and the motor efficiency is assumed to be $\eta_{mot} = 0.9$, the pump efficiency is determined as $\eta_{is} = 56.3\%$. This value is much lower than the nominal efficiency of $\eta_{is} = 70...77\%$ (Centrilift, 2013) because the pump was operated outside of the design operation range.

B 6.5 Estimation of losses and temperature increase by losses

The losses related to the production pump are estimated based on a technical data sheet of the ESP installed in GrSk (printout of pump simulation software (Centrilift, 2013)).

Pump and engine losses

According to the data sheet the pump efficiency is $\eta_{is} = 70...77\%$ in the operation range of volume flow. The engine efficiency is assumed to be $\eta_{mot} = 90\%$. The efficiency during the circulation test was determined as $\eta_{is} = 56.3\%$.

If a pump head of 1000 m and a specific heat capacity of 3300 kJ/(kg·K) (see 5.2.4.5) are assumed, the temperature increase of the fluid by dissipation in the engine and the pump is estimated to be 1.75 K for $\eta_{is} = 70\%$ and 2.9 K for $\eta_{is} = 56.3\%$:

$$\Delta T_{loss} = \frac{\dot{Q}_{loss}}{\dot{m}c_p} = \frac{P_{el}(1 - \eta_{is}\eta_{mot})}{\dot{m}c_p} = \frac{P_{hyd}}{\eta_{is}\eta_{mot}} \frac{(1 - \eta_{is}\eta_{mot})}{\dot{m}c_p} = \frac{\dot{m}g\Delta z}{\eta_{is}\eta_{mot}} \frac{(1 - \eta_{is}\eta_{mot})}{\dot{m}c_p} \quad (B.73)$$

$$\Delta T_{loss} = \frac{9.81 \text{ m/s}^2 \cdot 1000 \text{ m} \cdot (1 - 0.9 \cdot 0.7)}{3300 \text{ J/(kgK)}} \approx 1.75 \text{ K} \quad (B.74)$$

This value is added to the temperature increase by isentropic pressure increase calculated in B 6.2.

Cable losses

The data sheet provides the following nominal electrical parameters:

Wellhead kVA	479.7 kVA
Wellhead Voltage	3025.6 V
Voltage Drop	105.7 V

In nominal operation the voltage of 3025.6 V drops by 105.7 V. which means that the same fraction (i.e. 3 %) of the electrical power fed in at the wellhead is converted to heat distributed over the length of the cable. Compared to the pump loss, the electric loss is small. It is therefore not considered separately in the model. It can, of course, be included in the pump losses.

B 7. Calculation of the enthalpy of the liquid phase using solution heat

The enthalpy of a solution of salt can be calculated from the enthalpies of the solvent and the solid solutes plus the enthalpies of solution, dilution and mixing.

$$h = \sum_{n_{\text{salt}}} X^i h_s^i + X_{\text{H}_2\text{O}} (h_{\text{H}_2\text{O}} + \Delta \tilde{h}_{\text{sol}} b_i) + \Delta h_{\text{dil}} + \Delta h_{\text{mix}} . \quad (\text{B.75})$$

The molalities b_i are given in mol/kg with respect to the mass fraction of water. The dilution enthalpy is the amount of heat released or absorbed due to a change of salinity by adding water. The mixing enthalpy is the amount of heat released/absorbed due to the mixing of substances.

Absolute enthalpy values are somewhat arbitrary, so usually only enthalpy differences are of interest. In this model the process of solvation is not considered, so the solution enthalpy cancels out in differences.

The change of concentration is limited, as only a little mass fraction of the water is removed from the liquid phase by evaporation. Therefore, enthalpy of dilution and mixing are considered constant and will likewise cancel out in the difference.

$$\Delta h = h^2 - h^1 = \sum_{n_{\text{salt}}} X^i \Delta h_s^i + X_{\text{H}_2\text{O}} \Delta h_{\text{H}_2\text{O}} . \quad (\text{B.76})$$

The enthalpy of water and thus its difference can be calculated directly using the IAPWS97 formulation (Wagner et al., 2000) provided by the MSL. The salt enthalpy difference is linearized, i.e. $c_p = \text{const}$ and $v = \text{const}$ (Müller, 2001):

$$\Delta h_{\text{salt}}(p, T) = \left. \frac{\partial h_{\text{salt}}}{\partial p} \right|_T \Delta p + \left. \frac{\partial h_{\text{salt}}}{\partial T} \right|_p \Delta T = v \Delta p + c_p \Delta T . \quad (\text{B.77})$$

Although, as stated above, only enthalpy differences are needed, they are calculated in the model from absolute enthalpies. Hence, the function of total enthalpy of the multi-salt solution is:

$$h = \sum_{n_{\text{salt}}} X^i (v^i \Delta p + c_p^i \Delta T) + X_{\text{H}_2\text{O}} (h_{\text{H}_2\text{O}}^2 - h_{\text{H}_2\text{O}}^1) . \quad (\text{B.78})$$

B 8. Surface fit for solution heat capacity ratios

Apparent molar heat capacities can be found in the literature (White et al., 1987a,b) for solutions of CaCl_2 and KCl . They list measurement results for a range of temperature and molality. Pressure is always the same, except for one pair of temperature and molality, where pressure is varied, revealing a negligible influence. Also given are the respective ratios of the heat capacities of solution and pure water. This quantity is more convenient for a surface fit of the data, as its graph is smoother.

The data of the heat capacity ratios has been rearranged and condensed by averaging over similar molalities and temperatures. Eventually, ignoring the pressure influence, a second/third degree polynomial function of two variables has been fit to the data using the MATLAB Curve Fitting Toolbox:

$$\frac{c_p}{c_p^{\text{H}_2\text{O}}} = a_0 + a_1 \hat{b} + a_2 \hat{T} + a_3 \hat{b}^2 + a_4 \hat{b} \hat{T} + a_5 \hat{T}^2 + a_6 \hat{b}^2 \hat{T} + a_7 \hat{b} \hat{T}^2 + a_8 \hat{T}^3 . \quad (\text{B.79})$$

Temperature and molality have been centred and scaled:

$$\hat{b} = \frac{b - \text{mean}(b)}{\text{std}(b)} , \quad \hat{T} = \frac{T - \text{mean}(T)}{\text{std}(T)} . \quad (\text{B.80})$$

The coefficients and the quality of the fit obtained are listed here in Table 13:

Table 13: Coefficients and goodness of fit of MATLAB 2D 2nd/3rd degree polynomial fit of heat capacity data

	KCl	CaCl₂
a_0	0.8966	0.8729
a_1	-0.08691	-0.1118
a_2	-0.03493	-0.01051
a_3	0.01326	0.0244
a_4	-0.03115	-0.01634
a_5	-0.0365	-0.01823
a_6	0.01272	0.008315
a_7	-0.01054	-0.01568
a_8	-0.0132	-0.01057
mean(b)	1.188	0.9803
std(b)	1.103	1.047
mean(T)	475.1	437.7
std(T)	103.5	104.5
R^2	0.9795	0.9964
average relative difference	1.1 %	0.46 %
maximum relative difference	6 %	2.3 %

C Error estimations

C 1. Error in pressure calculation due to upstream scheme for velocity

In eq. 5.53 an upstream velocity scheme is applied, that is, the average density in one element is assumed to have the inflow value. In this section the error induced in the friction head is estimated. The relative difference between friction heads calculated for linear density change (eq. B.37) and upstream scheme (eq. 5.53) is:

$$e_{\text{rel}}^{\text{fric}} = \left| \frac{\Delta p_{\text{fric}}^{\text{lin}} - \Delta p_{\text{fric}}^{\text{con}}}{\Delta p_{\text{fric}}^{\text{con}}} \right| = \left| \frac{\frac{(w_1 + w_2)^2 (\rho_1 + \rho_2)}{16d}}{\frac{w_1^2 \rho_1}{2d}} - 1 \right| \stackrel{!}{<} e_{\text{max}} \quad (\text{C.81})$$

$$e_{\text{rel}}^{\text{fric}} = \left| \frac{1}{8} \left(1 + \frac{w_2}{w_1}\right)^2 \left(1 + \frac{\rho_2}{\rho_1}\right) - 1 \right| \stackrel{!}{<} e_{\text{max}} \quad (\text{C.82})$$

Using the continuity equation 3.3 and a first order Taylor approximation converts the error term to:

$$e_{\text{rel}}^{\text{fric}} = \left| \frac{1}{8} \left(1 + \frac{w_2}{w_1}\right)^2 \left(1 + \frac{w_1}{w_2}\right) - 1 \right| \approx \frac{1}{2} \cdot \left| \frac{w_2}{w_1} - 1 \right| . \quad (\text{C.83})$$

The limiting condition for the ratio for velocities therefore is:

$$\left| \frac{w_2}{w_1} - 1 \right| \stackrel{!}{<} 2e_{\text{max}} . \quad (\text{C.84})$$

Hence, for example, for an error below $e_{\text{max}} = 1\%$, velocity change must stay within $\pm 2\%$.

C 2. Error in pressure calculation due to upstream scheme for density

In analogy to C 1, the relative difference between static pressure heads in eq. B.37 and eq. 5.53 is:

$$e_{\text{rel}}^{\text{stat}} = \left| \frac{\Delta p_{\text{stat}}^{\text{con}} - \Delta p_{\text{stat}}^{\text{lin}}}{\Delta p_{\text{stat}}^{\text{lin}}} \right| = \left| \frac{g\rho_1}{\frac{1}{2}g(\rho_1 + \rho_2)} - 1 \right| = \left| \frac{2}{1 + \frac{\rho_2}{\rho_1}} - 1 \right| \stackrel{!}{<} e_{\text{max}} \quad (\text{C.85})$$

A Taylor expansion simplifies the expression to

$$e_{\text{rel}}^{\text{stat}} \approx \frac{1}{2} \left| 1 - \frac{\rho_2}{\rho_1} \right| \stackrel{!}{<} e_{\text{max}}, \quad (\text{C.86})$$

which can be rewritten as

$$\left| \frac{\rho_2}{\rho_1} - 1 \right| \stackrel{!}{<} 2e_{\text{max}} . \quad (\text{C.87})$$

Hence, for the error to stay below e_{max} , the density change must stay within $\pm 2e_{\text{max}}$. Applying eq. 3.3 and another first order Taylor approximation shows that condition C.87 is consistent with C.84:

$$\left| \frac{\rho_2}{\rho_1} - 1 \right| = \left| \frac{w_1}{w_2} - 1 \right| \approx \left| \left(\frac{w_2}{w_1} - 1 \right) (-1) \right| = \left| \frac{w_2}{w_1} - 1 \right| \stackrel{!}{<} 2e_{\text{max}} . \quad (\text{C.88})$$

C 3. Error in pressure calculation by neglecting kinetic head

Setting kinetic head from eq. B.35 into relation to static head gives a limiting condition for the relative density gradient. The relative pressure calculation error by neglecting kinetic head is:

$$e_{\text{rel}}^{\text{kin}} = \frac{\Delta(\rho w^2)}{\rho_m \sin \varphi g \Delta s} = \frac{\Delta \left(\frac{\dot{m}^2}{\rho} / A^2 \right)}{\rho \sin \varphi g \Delta s} = \frac{\dot{m}^2 / A^2 \Delta \rho^{-1}}{\rho \sin \varphi g \Delta s} = \frac{\dot{m}^2}{A^2 g \sin \varphi \rho^3 \Delta s} \stackrel{!}{<} e_{\text{max}} \quad (\text{C.89})$$

$$\frac{\Delta \rho / \rho}{\Delta s} \stackrel{!}{<} \frac{A^2 g \sin \varphi \rho^2}{\dot{m}^2} e_{\text{max}} . \quad (\text{C.90})$$

For example, with $\rho = 1000 \text{ kg/m}^3$, $\dot{m} = 10 \text{ kg/s}$, $\varphi = 90^\circ$ and $A = 0.01 \text{ m}^2$ and a maximum error of 1 % one obtains the condition:

$$\frac{\Delta\rho/\rho}{\Delta s} \stackrel{!}{<} 10 \text{ m}^{-1} \cdot 0.01 = 0.1 \text{ m}^{-1} . \quad (\text{C.91})$$

The gradient of relative density change may be as high as 10 %/m in this example before kinetic head becomes significant. That is, the kinetic head is negligible, as long as density changes only little.

According to condition C.87 the density change is below 2 % for a pressure error of 1 %. Combining this with eq. C.88 C.91 yields a condition for the element length Δs :

$$\frac{\rho_2}{\rho_1} - 1 \stackrel{!}{<} 0.02 \stackrel{!}{<} 0.1 \text{ m}^{-1} \cdot \Delta s \quad (\text{C.92})$$

$$0.2 \stackrel{!}{<} \Delta s \quad (\text{C.93})$$

If the density change is below 2 % over the element length of more than 0.2 m, the error made by neglecting kinetic head and applying the upstream scheme is below 1 %.

C 4. Error in pressure calculation by neglecting slip in GrSk scenario

The effect of slip on the static pressure head is estimated by comparing the static density to the homogenous density which equals the static density without slip.

In a slip flow, one distinguishes between gas mass/volume fraction x/ε (in given volume) and gas mass/volume flow fraction $\dot{x}/\dot{\varepsilon}$ (in given volume flow), which are equal in homogenous flow without slip. Equally two different fluid densities appear in the following equations: the homogenous density ρ , which is the same as in the homogenous two-phase flow model and the static density $\hat{\rho}$, which is relevant for the static pressure head.

$$x = \frac{m''}{m}, \quad \dot{x} = \frac{\dot{m}''}{\dot{m}} \quad (\text{10.94})$$

$$\varepsilon = \frac{V''}{V}, \quad \dot{\varepsilon} = \frac{\dot{V}''}{\dot{V}} \quad (\text{10.95})$$

$$\rho = \rho'' \dot{\varepsilon} + \rho'(1 - \dot{\varepsilon}), \quad \hat{\rho} = \rho'' \varepsilon + \rho'(1 - \varepsilon) \quad (\text{10.96})$$

Slip is the velocity difference of gas and liquid phase. It is quantified by the slip factor, defined as the ratio of the mean flow velocities of the phases:

$$S = \frac{w''}{w'} \quad (\text{10.97})$$

The quantities above are related via the slip factor is as follows: (see A 3 or (Kraume, 2003: 450))

$$\dot{\varepsilon} = \frac{\varepsilon}{\frac{1-\varepsilon}{S} + \varepsilon} \Leftrightarrow \varepsilon = \frac{\dot{\varepsilon}}{-S\dot{\varepsilon} + \dot{\varepsilon} + S} \quad (\text{10.98})$$

$$\dot{x} = \frac{\rho''}{\rho} \frac{\varepsilon}{\frac{1-\varepsilon}{S} + \varepsilon} \Leftrightarrow x = \frac{\dot{x}}{-S\dot{x} + \dot{x} + S} \frac{\rho''}{\rho} \quad (\text{10.99})$$

The quantity calculated by the VLE model is the gas mass flow fraction \dot{x} (see B 3).

Slip increases with gas fraction. The highest gas fraction in the production well of the GrSk scenario is expected to occur at the wellhead, the point of minimum pressure. There the diameter of the production string is $d = 100.5 \text{ m}$ (Table 3). The production rate is assumed to be $25 \text{ m}^3/\text{h}$ and the wellhead pressure 10 bar. The fluid has a gas-liquid ratio of 1:1 at standard conditions (0°C , 1.01325 bar) (see 4.2), so

according to the ideal gas law at the wellhead it transforms to 1:10 ($\dot{\varepsilon} = 1/11$ %). The liquid density at the wellhead is set to 1100 kg/m^3 and the gas density is set to 10 kg/m^3 .

The homogenous fluid density consequently is (eq. 3.1):

$$\rho_h = 1100 \text{ kg/m}^3 \cdot \frac{9}{10} + 10 \text{ kg/m}^3 \cdot \frac{1}{11} = 1001 \text{ kg/m}^3 \quad (\text{C.100})$$

The slip factor can be estimated using the following formula by Ahmad (Kraume, 2003: 455) based on the density ratio, mass flow and liquid viscosity of $\eta' = 5 \cdot 10^{-4} \text{ Pa}\cdot\text{s}$:

$$S := \frac{w''}{w'} = \left(\frac{\rho'}{\rho''}\right)^{0.205} \left(\frac{\dot{m} \cdot d}{\eta'}\right)^{-0.016} = 2.3 \quad (\text{C.101})$$

With a slip factor of 2.3 the gas phase occupies proportionally less area of the cross-section. Hence, the volume flow fraction of 1:10 is turned into a gas-liquid volume ratio of 1:23 ($\varepsilon \approx 3.9$ %), resulting in an increased density:

$$\rho_S = 1100 \text{ kg/m}^3 \cdot \frac{22}{23} + 10 \text{ kg/m}^3 \cdot \frac{1}{23} = 1057 \text{ kg/m}^3 \quad (\text{C.102})$$

Alternatively the slip factor can be estimated from the bubble rise velocity, as for low gas fractions bubbly flow (single bubbles in a continuous liquid phase) can be expected. The bubble rise velocity can be estimated with an equation (Kraume, 2003: 578) assuming a surface tension of 0.06 N/m (pure water at 125°C (Wagner et al., 2000), slightly increased by salt).

$$w_B := w'' - w' = 1.24 \cdot \sqrt[4]{\frac{\rho'' - \rho'}{\rho'^2} g \cdot \sigma'} = 0.2 \text{ m/s} \quad (\text{C.103})$$

It can then be converted to the slip factor by (see A 4).

$$w_B = 0.2 \text{ m/s} \xrightarrow{\text{eq. A.11}} S = 1 + \frac{w_B A}{\dot{V}} = 1.11 \quad (\text{C.104})$$

A slip factor of 1.11 results in a static gas void fraction of $\varepsilon = 1/11.1 \approx 8.3$ % and a density of

$$\rho_S = 10 \text{ kg/m}^3 \cdot 0.083 + 1100 \text{ kg/m}^3 \cdot (1 - 0.083) = 1010 \text{ kg/m}^3 \quad (\text{C.105})$$

This calculation indicates that the no-slip assumption at the wellhead causes an error in the density and consequently in the pressure head of $(\rho_h - \rho_S)/\rho_S = -5.3$ % for $S = 2.3$ or -0.9 % for $S = 1.11$. The error in the pressure calculation cumulates over the length of the well. However, the considerable maximum error calculated here only occurs in the topmost part of the well, where pressure is low enough for a gas phase.

To gauge the effect of slip in the GrSk scenario, a constant slip factor is introduced into the density calculation (eq. 5.25) by dividing the calculated gas fraction by the slip factor $S = 2.3$:

$$\rho = \left(\frac{1 - x/S}{\rho'} + \frac{x/S}{\rho''} \right)^{-1} \quad (\text{C.106})$$

A calculation of the circulation test (6.5) with constant wellhead pressure using the thus modified model shows an increase of the pump head by 1.85 bar (1.6 %) This results in a proportionally increased pump load and loss. The wellhead temperature and the degassing point are, however, virtually unaffected.

C 5. Estimation of thermal error induced by neglecting slip in GrSk scenario

Slip increases the pump work load necessary to generate the pressure head for a constant mass flow from inlet at z_1 to outlet at z_2 , while the transported fluid gains the same amount of potential energy via the geodetic height. The difference can be assigned to the inner friction loss, which is to be estimated with the following calculations.

The energy balance of an adiabatic pipe flow with constant fluid density (from eq. 3.4) is:

$$0 = \dot{m} \left(w_2 - w_1 + (p_2 - p_1)v + g(z_2 - z_1) + \frac{w_2^2 - w_1^2}{2} \right) \quad (\text{C.107})$$

Kinetic head disappears because of the assumption of constant density, which implies constant velocity. Wall friction is not considered, because only the effect of inner friction is to be shown. Hence, pressure difference equals static head, which is calculated with the static density $\hat{\rho}$

$$(p_2 - p_1) = -\hat{\rho}g(z_2 - z_1), \quad (\text{C.108})$$

whereas enthalpy flow is calculated with the homogenous density ρ . We get

$$w_2 - w_1 = \hat{\rho}g(z_2 - z_1) \frac{1}{\rho} - g(z_2 - z_1) \quad (\text{C.109})$$

$$\frac{\partial w}{\partial z} = g \left(\frac{\hat{\rho}}{\rho} - 1 \right) \quad (\text{C.110})$$

$$\frac{\partial w}{\partial T} \frac{\partial T}{\partial z} = \frac{g}{\rho} (\hat{\rho} - \rho). \quad (\text{C.111})$$

With the definition of the fluid densities (eq. 10.96) and the specific heat capacity:

$$c_p \frac{\partial T}{\partial z} = \left((\rho'' \varepsilon + \rho' (1 - \varepsilon)) - (\rho'' \dot{\varepsilon} + \rho' (1 - \dot{\varepsilon})) \right) \frac{g}{\rho} \quad (\text{C.112})$$

$$c_p \frac{\partial T}{\partial z} = \left((\rho'' - \rho') \varepsilon + \rho' - ((\rho'' - \rho') \dot{\varepsilon} + \rho') \right) \frac{g}{\rho} \quad (\text{C.113})$$

$$\frac{\partial T}{\partial z} = \frac{\rho'' - \rho'}{((\rho'' - \rho') \dot{\varepsilon} + \rho')} (\varepsilon - \dot{\varepsilon}) \frac{g}{c_p} \quad (\text{C.114})$$

$$\frac{\partial T}{\partial z} = \frac{g}{c_p} \left(\frac{\dot{\varepsilon}}{-S \dot{\varepsilon} + \dot{\varepsilon} + S} - \dot{\varepsilon} \right) / \left(\dot{\varepsilon} + \frac{\rho'}{\rho'' - \rho'} \right) \quad (\text{C.115})$$

$$\frac{\partial T}{\partial z} = \frac{g}{c_p} \dot{\varepsilon} \left(\frac{1}{S(1 - \dot{\varepsilon}) + \dot{\varepsilon}} - 1 \right) / \left(\dot{\varepsilon} + \left(\frac{\rho''}{\rho'} - 1 \right)^{-1} \right) \quad (\text{C.116})$$

For the example in C 4 the slip dissipates around 1.2 W/m. Assuming $c_p = 3.3 \text{ J}/(\text{kg} \cdot \text{K})$ it causes a negligible temperature increase of:

$$\frac{\partial T}{\partial z} = 1.8 \cdot 10^{-5} \text{ K} \quad (\text{C.117})$$

D Numerics

D 1. Finite difference formulation

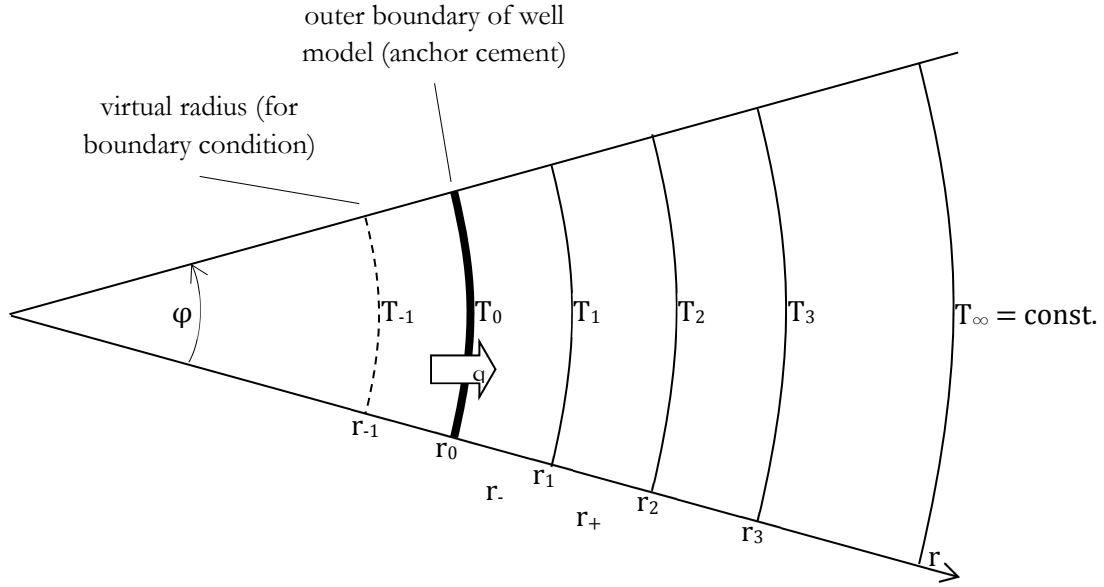


Fig. 46: Radial symmetric discretization of formation

D 1.1 Finite differences method on equidistant grid:

Discretization, n points (1... n) + additional point (index 0) at inner boundary to implement boundary condition.

Eq. 3.35 discretized in r for n point:

$$\frac{\rho c}{\lambda} \frac{\partial T_i}{\partial t} = \frac{1}{2(\Delta r)^2 r_i} \left((2r_i + \Delta r)(T_{i+1} - T_i) - (2r_i - \Delta r)(T_i - T_{i-1}) \right), \quad i = 1 \dots n - 1. \quad (\text{D.118})$$

Second order discretization of Neumann boundary condition for T_0 :

$$-\dot{q}_{\text{if}} = \lambda \frac{T_2 - T_0}{r_2 - r_0} \xrightarrow{\text{yields}} T_0 = T_2 + \frac{\dot{q}_{\text{if}}}{k} 2\Delta r. \quad (\text{D.119})$$

D 1.2 Finite differences method on non-equidistant grid

Due to the decrease of the temperature gradient at larger radii an increase of the element size is obvious. The formation is discretized in segments with exponentially growing radii as described in 5.5.4. One-dimensional transient radial heat conduction without heat generation is described by eq. 3.35:

$$\frac{\rho c}{\lambda} \frac{\partial T}{\partial t} = \frac{1}{r} \frac{\partial}{\partial r} \left(r \frac{\partial T}{\partial r} \right) = \frac{1}{r} \frac{\partial T}{\partial r} + \frac{\partial^2 T}{\partial r^2}$$

It is discretized in r for n points as a non-equidistant grid using the central differential quotients (Rung et al., 2002):

$$\frac{\partial f}{\partial r} = \frac{f_{i+1} - (1 - a_{i-1})f_i - a_{i-1}f_{i-1}}{a_{i-1}(1 + a_{i-1})(r_i - r_{i-1})} \quad \text{where } a_{i-1} = \frac{r_{i+1} - r_i}{r_i - r_{i-1}} \quad (\text{D.120})$$

$$\frac{\partial^2 f}{\partial r^2} = \frac{f_{i+1} - (1 + a_{i-1})f_i + a_{i-1}f_{i-1}}{\frac{1}{2}a_{i-1}(1 + a_{i-1})(r_i - r_{i-1})^2} \quad (\text{D.121})$$

Thus, the discretized heat equation for one-dimensional radial heat conduction is written as:

$$\frac{\rho c}{\lambda} \frac{\partial T_i}{\partial t} = \frac{1}{r_i} \frac{T_{i+1} - (1 - a_{i-1}^2) T_i - a_{i-1}^2 T_{i-1}}{a_{i-1}(1 + a_{i-1})(r_i - r_{i-1})} + \frac{T_{i+1} - (1 + a_{i-1}) T_i + a_{i-1} T_{i-1}}{\frac{1}{2} a_{i-1}(1 + a_{i-1})(r_i - r_{i-1})^2}, \quad i = 1 \dots n - 1 \quad (\text{D.122})$$

Determine T_0 using the Neumann boundary condition:

$$-\dot{q}_{if} = \lambda \frac{T_2 - (1 - a_0^2) T_1 - a_0^2 T_0}{a_0(1 + a_0)(r_1 - r_0)} \xrightarrow{\text{yields}} T_0 = \frac{\dot{q}_{if}}{\lambda} \left(\frac{1}{a_0} + 1 \right) (r_1 - r_0) + \frac{T_2 - T_1}{a_0^2} + T_1 \quad (\text{D.123})$$

$$\frac{1}{a_0^2} \left(\frac{\dot{q}_{if}}{\lambda} a_0(1 + a_0)(r_1 - r_0) + T_2 - (1 - a_0^2) T_1 \right) = T_0 \quad (\text{D.124})$$

$$\frac{\dot{q}_{if}}{\lambda} \left(\frac{1}{a_0} + 1 \right) (r_1 - r_0) + \frac{T_2}{a_0^2} - \left(\frac{1}{a_0^2} - 1 \right) T_1 = T_0 \quad (\text{D.125})$$

$$T_0 = \frac{\dot{q}_{if}}{\lambda} \left(\frac{1}{a_0} + 1 \right) (r_1 - r_0) + \frac{T_2 - T_1}{a_0^2} + T_1 \quad (\text{D.126})$$

The ratio of two subsequent radii must not exceed 3 (see D 1).

D 1.3 Finite differences method on non-equidistant grid with temperature dependent thermal conductivity

Eq. 3.35 with temperature dependent thermal conductivity is written as:

$$\rho c \frac{\partial T}{\partial t} = \frac{1}{r} \frac{\partial}{\partial r} \left(\lambda(T) r \frac{\partial T}{\partial r} \right) \quad (\text{D.127})$$

$$\rho c \frac{\partial T}{\partial t} = \lambda(T) \left(\frac{1}{r} \frac{\partial T}{\partial r} + \frac{\partial^2 T}{\partial r^2} \right) + \frac{\partial \lambda(T)}{\partial r} \frac{\partial T}{\partial r} \quad (\text{D.128})$$

$$\rho c \frac{\partial T}{\partial t} = \lambda(T) \frac{\partial^2 T}{\partial r^2} + \left(\frac{\lambda(T)}{r} + \frac{\partial \lambda(T)}{\partial r} \right) \frac{\partial T}{\partial r} \quad (\text{D.129})$$

The additional term in the factor in front of the first derivative is also discretized according to eq. D.120

$$\frac{\partial \lambda(T)}{\partial r} = \frac{\lambda_{i+1} - (1 - a_{i-1}^2) \lambda_i - a_{i-1}^2 \lambda_{i-1}}{a_{i-1}(1 + a_{i-1})(r_i - r_{i-1})} \quad (\text{D.130})$$

and inserted into eq. D.122. The boundary condition remains unchanged as given in eq. D.126.

D 1.4 Convergence of radial heat flow equation in the finite difference method

Consider radial symmetric one-dimensional heat flow at r_i :

$$\frac{\rho c_p}{\lambda} \frac{\partial T}{\partial t} = \frac{1}{r} \frac{\partial}{\partial r} \left(r \frac{\partial T}{\partial r} \right) = \frac{1}{r} \frac{\partial T}{\partial r} + \frac{\partial^2 T}{\partial r^2}. \quad (\text{D.131})$$

The discretized heat flow equation as given in D 1.2 (eq. D.122):

$$\frac{\rho c_p}{\lambda} \frac{\partial T_i}{\partial t} = \frac{1}{r_i} \frac{T_{i+1} - (1 - a_i^2) T_i - a_i^2 T_{i-1}}{a_i(1 + a_i)(r_i - r_{i-1})} + \frac{T_{i+1} - (1 + a_i) T_i + a_i T_{i-1}}{\frac{1}{2} a_i(1 + a_i)(r_i - r_{i-1})^2} \text{ with } a_i = \frac{(r_{i+1} - r_i)}{(r_i - r_{i-1})}. \quad (\text{D.132})$$

The (initial) conditions are:

$$T_{i-1} > T_i = T_{i+1} = \vartheta, \quad r_{i+1} > r_i > r_{i-1} \quad (\text{D.133})$$

The physically expected behaviour is heat flow from the warmer point at r_{i-1} to r_i and thus an increase of T_i :

$$\frac{\rho c_p}{\lambda} \frac{\partial T_i}{\partial t} = \frac{1}{r_i} \frac{\vartheta - (1 - a_i^2) \vartheta - a_i^2 T_{i-1}}{a_i(1 + a_i)(r_i - r_{i-1})} + \frac{\vartheta - (1 + a_i) \vartheta + a_i T_{i-1}}{\frac{1}{2} a_i(1 + a_i)(r_i - r_{i-1})^2} \stackrel{!}{>} 0 \quad (\text{D.134})$$

$$\frac{a_i^2(\vartheta - T_{i-1})}{r_i} + \frac{a_i(-\vartheta + T_{i-1})}{\frac{1}{2}(r_i - r_{i-1})} \stackrel{!}{>} 0 \quad (\text{D.135})$$

$$\frac{(r_{i+1} - r_i)}{(r_i - r_{i-1})} \frac{\vartheta - T_{i-1}}{r_i} - \frac{\vartheta - T_{i-1}}{\frac{1}{2}(r_i - r_{i-1})} \stackrel{!}{>} 0 \quad (\text{D.136})$$

$$(\vartheta - T_{i-1}) \left(\frac{r_{i+1} - r_i}{r_i} - 2 \right) \stackrel{!}{>} 0 \quad (\text{D.137})$$

$$(r_{i+1} - r_i) - 2r_i \stackrel{!}{>} 0 \quad (\text{D.138})$$

$$\frac{r_{i+1}}{r_i} \stackrel{!}{<} 3 \quad (\text{D.139})$$

Hence, in order for the discretisation to yield physically reasonable results it has to comply with the above condition.

D 2. VLE Algorithm

D 2.1 Stop criterion

The iterative VLE algorithm presented in 5.2.2.3 stops when all elements of the correction vector $\Delta \tilde{n}''[k]$ are below a certain threshold, called residual. The threshold determines how precisely the pressure equilibrium (5.14) is fulfilled. One way to select such a threshold when no analytical reference solution is available is to reduce the threshold until further reduction shows no significant effect (improvement). Doing this for the GrSk fluid at two different temperatures (Fig. 47) indicates that a threshold of $\text{tol} = 10^{-3}$ guarantees an error (with respect to the calculation with $\text{tol} = 10^{-5}$) below 1 %.

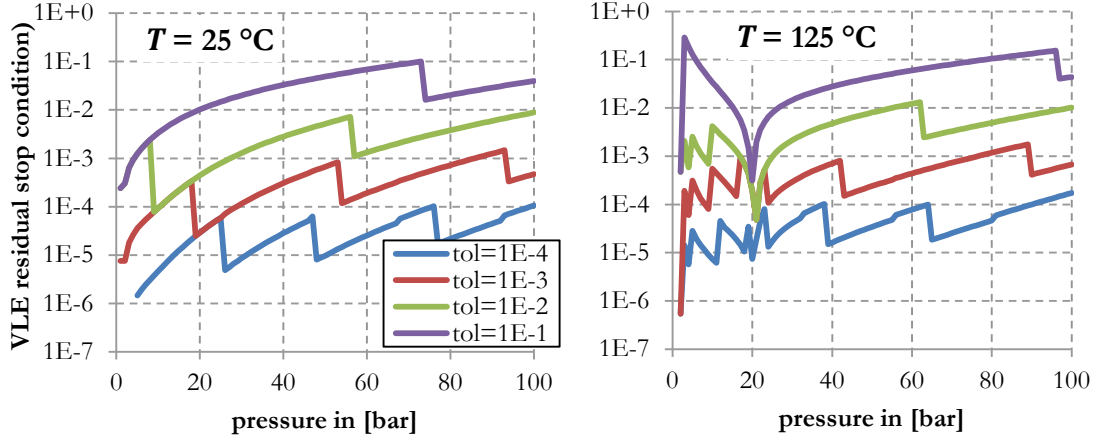


Fig. 47: Relative difference of calculated gas volume fraction (reference calculation with $\text{tol} = 10^{-5}$) vs. absolute pressure for different residuals, standard fluid composition, $T = \{25, 125\}$ °C

Reducing the residual obviously increases the necessary number of iterations (Fig. 48) and thus computation time (Table 14).

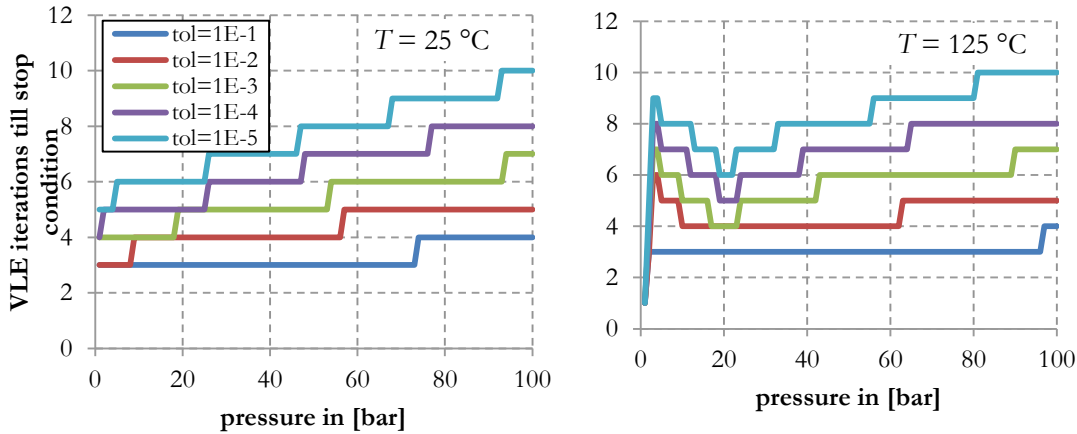


Fig. 48: Number of iterations of VLE algorithm depending on residual (stop criterion)

threshold	10 ⁻⁵	10 ⁻⁴	10 ⁻³	10 ⁻²	10 ⁻¹
calculation time in [s]	0.54	0.49	0.45	0.41	0.36

Table 14: Influence of tolerance on calculation time (500 data points, p = 1...100 bar at 125 °C)

D 2.2 Initialization

The iterative VLE algorithm (presented in 5.2.2.3) starts with the initialization vector, specifying an initial distribution of gases and water between both phases. When moving along the pipe it would be obvious to use the gas distribution values calculated for the current element as start values for the next element instead of using fixed values. Unfortunately, the syntax limitations of MODELICA do not allow that without breaking compatibility with the media package. The speed gain is, however, minimal if implemented anyway.

Fig. 49 shows that the calculated gas volume fraction virtually does not vary ($\Delta\epsilon = 4 \cdot 10^{-7}$) when the initial values for the VLE algorithm are varied synchronously or separately between 0.01 and 0.99. Only when the start value for water is varied separately and the start vector is set close to [0.5, 0.5, 0.5, 1] the calculated gas void fraction fluctuates significantly and reaches 1.

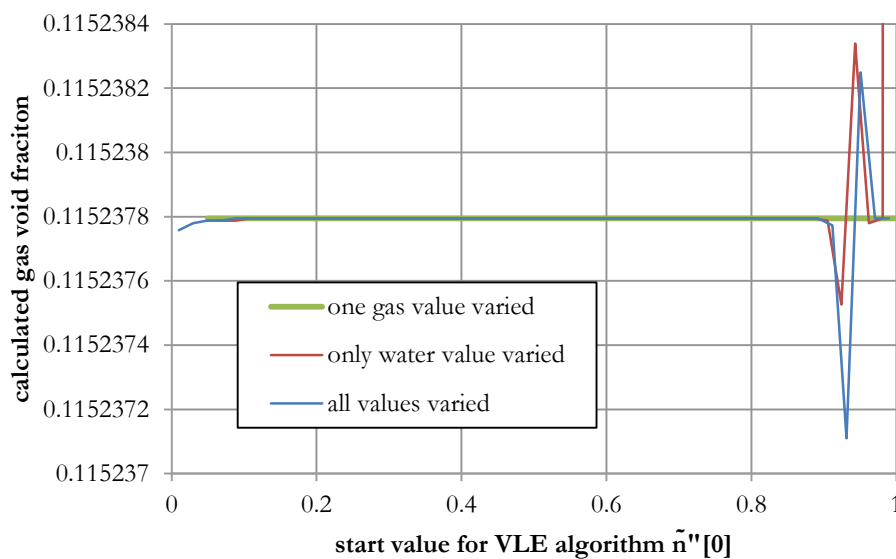


Fig. 49: Gas volume fraction calculated for GrSk fluid @ 125°C, 10 bar and with a tolerance of $5 \cdot 10^{-5}$ and a varying initialization vector $n_g_start = [1,1,1,1] \cdot \{0.01...0.99\}$

As a next step, this start value variation was repeated for different residuals (stop criterion of the VLE algorithm). Fig. 50 shows that the variance $\Delta\varepsilon$ of the calculated gas fraction by synchronous variation of the initial vector increases with the residual.

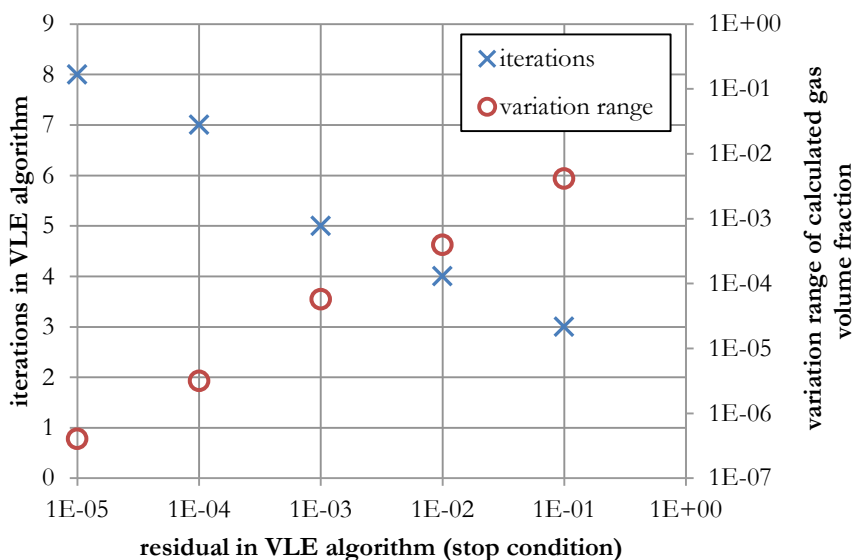


Fig. 50: Sensitivity of calculated gas volume fraction on residual as stop criterion of VLE algorithm (initial values are varied synchronously between 0.01 and 0.99)

These results are similar for other p-T conditions, with the general tendency to more iterations and slightly increasing variation range at lower gas fractions.

D 2.3 Inversion T(p,h)

Using the enthalpy calculation described in 5.2.4 temperature can be determined from given pressure by numerically inverting the enthalpy function by means of regula falsi. This is implemented in the function T(p,h). With the stop criteria set to temperature interval smaller than 0.01 °C and relative enthalpy difference less than 10⁻⁵, it typically takes 14 iterations to find the correct temperature.

Fig. 51 shows the calculated temperature and gas fraction v. specific enthalpy as a smooth curve.

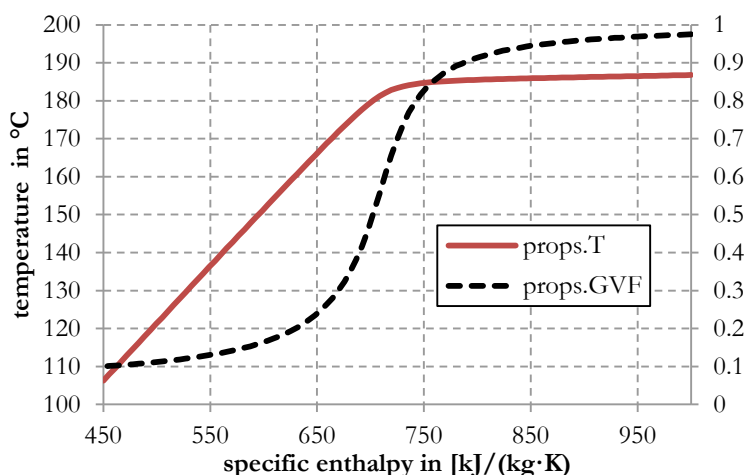


Fig. 51: Gas volume fraction vs. specific enthalpy, p = 2 bar, calculation time = 0.98 s for 100 data points

D 3. Axial pipe discretization

The number of axial pipe elements is a compromise between computational effort and precision. On the one hand, it directly scales the number of equations in the equations system generated from the model.

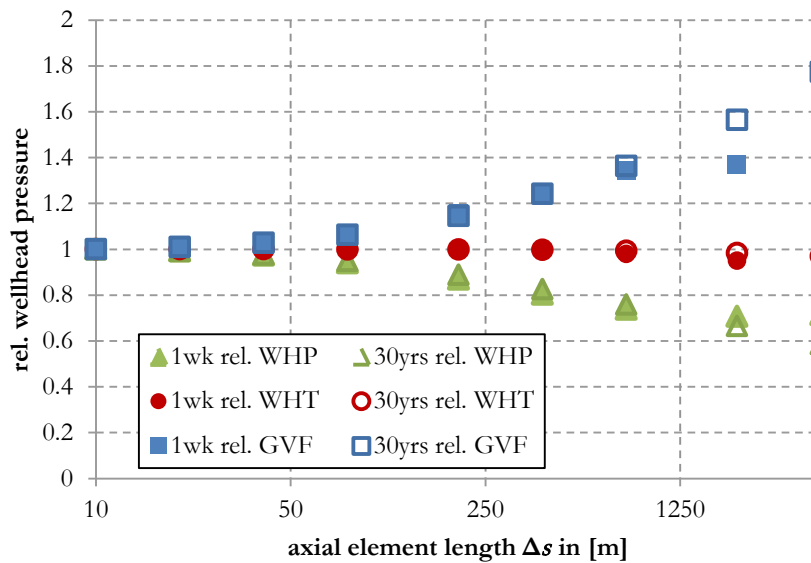
On the other hand, the balance equation with the upstream scheme (5.4.2), applied to overly long elements leads to discretization errors, because flow parameters are kept constant at their upstream value although they are actually changing. An additional discretization error is caused by the loss of details of the borehole washout and of the stratigraphy due to averaging.

Axial well element size was determined with a study of the sensitivity of the temperature drop and the pressure drop in a simplified well model. The simplified well model consists of a single vertical section of 4000 m length, with diameters $\{0.1, 0.11, 0.12, 0.14, 0.15\}$ m, formation layer L04 (see Table 1). 10 kg/s of the GrSk fluid enter the well at the bottom with 145 °C and 450 bar. Starting with one element, the axial mesh is gradually refined until 400 elements ($\Delta s = 10$ m) are reached. Pressure, temperature and gas fraction at the wellhead after 1 week / 30 years were evaluated. The element size is limited by the memory consumption⁵⁹.

Fig. 52 shows how the wellhead parameters converge when the axial well discretization is refined. The parameters are plotted relative to the ‘correct’ values, i.e. the values calculated with the finest discretization⁶⁰.

While the wellhead temperature does not change significantly below $\Delta s = 400$ m, wellhead pressure and gas fraction require much smaller elements. The difference between the finest ($\Delta s = 10$ m) and the second-finest ($\Delta s = 20$ m) discretization is below 1 % for p_{wh} and ϵ_{wh} after both 1 week and 30 years.

Hence, the well and formation are discretized with an axial element size of approx. $\Delta s \approx 25$ m.



D 4. Radial Heat Flow

D 4.1 Element size in discretization of formation model

This section studies and discusses the influence of the radial element size in the formation on the simulation result. The choice of mesh size and discretization scheme for the wellbore model is based on the following results.

The following parameters have been used for the mesh size studies:

Table 15: Formation model parameters

heat conductivity λ	1 W/(m·K)
inner radius r_0	0.1 m / 1 m
outer radius r_n	128 m, 256 m
inner boundary condition	$\dot{q} = 1 \text{ W/m}^2$
outer boundary condition	$T_\infty = 0 \text{ K}$

Heat propagation velocity

The influence of cell size on propagation velocity has been tested by calculating the formation heat flow with the parameters given above (inner radius $r_0 = 1 \text{ m}$) and determining the time when the temperature at $R = 0.5 \text{ m}$ and 1 m changes by 0.01 K .

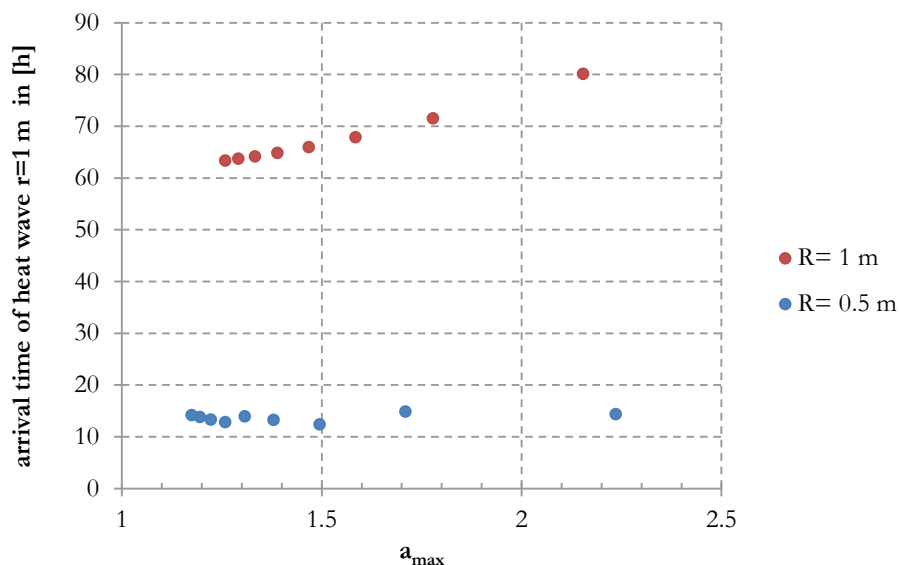


Fig. 53: time for heat wave to reach $r = 1 \text{ m}$ vs. element size

While the data for $R = 1 \text{ m}$ (or $R = 0.2 \text{ m}$) suggests that a coarser mesh delays the arrival of the heat front, the arrival for $R = 2 \text{ m}$ (or $R = 0.5 \text{ m}$) do not show a monotonous relation to mesh size. In any case, arrival times for $a_{\max} < 1.4$ do not vary much.

Final temperature

The influence of discretisation element size on the final inner boundary temperature is examined for stationary one-dimensional radial heat flow by comparing with the analytical solution (eq. 3.22). The parameters given above are used. The inner radius has been set to 1 m .

The element size of the mesh grows exponentially according to the maximum element growth factor a_{\max} as described in 5.5.4

The heat flow equation is solved using eq. 5.83 and 5.86 with $\partial T/\partial t = 0$ (i.e. final state of transient solution) and compared to the analytical solution eq. 5.73.

The discretization error e is calculated as:

$$e_i = \frac{T_t(r_i) - T_s(r_i)}{T_s(r_1) - T_s(r_n)} \tag{D.140}$$

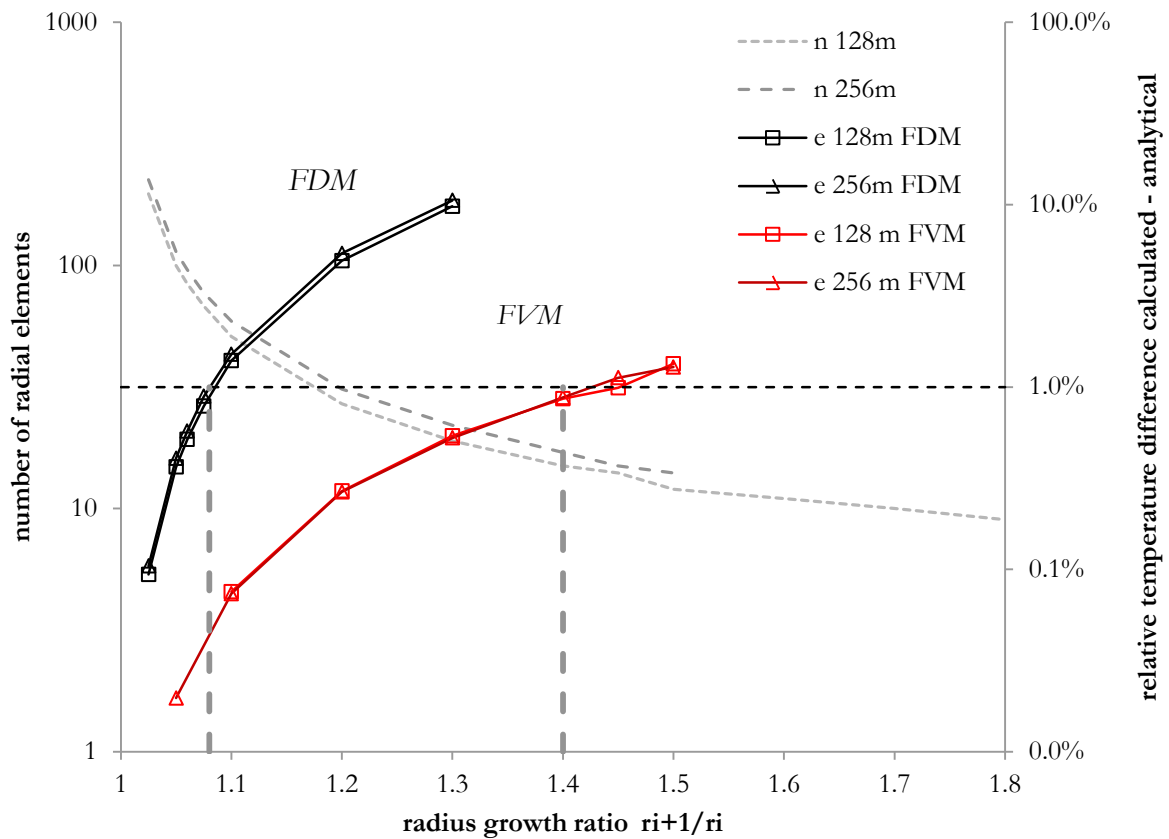


Fig. 54: number of elements and discretisation error vs. element size

Fig. 54 and Table 16 show the expected decrease of the discretisation error with increasing fineness of the mesh. In order to obtain an error of the temperature at the inner boundary below 1 % using the FDM, a_{\max} has to be set to 1.06, resulting in $n = 84$ or 96 elements, respectively. Using FVM a_{\max} can be set as high as 1.4, meaning only 15/17 elements are needed.

Table 16: Comparison FDM - FVM discretisation error vs. element size for different mesh ranges

a_{\max}	$r_{\infty} = 128 \text{ m}$			$r_{\infty} = 256 \text{ m}$		
	n	FDM	FVM	n	FDM	FVM
1.025	197	0.17%		225	0.19%	
1.05	100	0.65%		114	0.73%	0.02%
1.06	84	0.91%		96	1.03%	
1.075	68	1.39%		77	1.59%	
1.1	51	2.46%	0.08%	59	2.70%	0.07%
1.2	27	8.52%	0.27%	31	9.48%	0.27%
1.3	19	16.62%	0.54%	22	18.10%	0.53%
1.4	15		0.86%	17		0.88%
1.45	14		0.99%	15		1.12%
1.5	12		1.34%	14		1.29%
1.6	11		1.59%	12		1.74%
1.7	10		1.92%	11		2.07%
1.8	9		2.35%	10		2.49%

D 4.2 Radial extension of formation model

$$\dot{Q} = -2\pi\Delta s \frac{\lambda}{\ln(R/r)} (T(R) - T(r)) \quad (3.22)$$

What is the radial extension that should be covered by the model? As equation 3.22 shows, in the stationary case the radial temperature difference is inversely proportional to the logarithm of the ratio of r_{∞}/r_0 , i.e. it directly depends on the choice of r_{∞} . That is plausible, because in an infinite domain temperature will never reach a stationary state, but continue to grow at a decreasing rate.

For a transient simulation with a finite simulation time, on the other hand, r_{∞} can be set to a finite value without influencing the calculation result. The outer boundary has to be far enough from the heat source, so that the temperature at that distance would stay constant anyway. In other words the outer boundary has to be out of range of the influence of the heat source, so that the heat wave does not reach the boundary within simulation time.

The penetration depth of a diffusion process can be estimated for the linear case (Kraume, 2003). As heat conduction is can be understood as a diffusion process, it can be easily adapted:

$$r(t) = \sqrt{\pi \frac{\lambda}{\rho c_p} t} = \sqrt{\pi \alpha t} \quad (D.141)$$

In Table 17 2nd column the equations D.141 and D.142 have been evaluated for halite (layer L05) which has the highest diffusivity in GrSk scenario (see Table 1): $\alpha = 2.32 \cdot 10^{-6} \text{ m}^2/\text{s}$. In order to obtain the values for the radial heat equation, equation D.142 has been numerically inverted and evaluated for different q' (for code see E 3).

Table 17: Propagation range of heat front in formation

time	linear	radial ($q' = 50 \text{ W/m}$)		
		$\Delta T < 0.01 \text{ K}$	$\Delta T < 0.1 \text{ K}$	$\Delta T < 1 \text{ K}$
1 week	2.1 m	4.2 m	2.8 m	1.1 m
1 year	15.1 m	30.2 m	20.4 m	8.1 m
30 years	82.7 m	165.3 m	111.6 m	44.3 m

Likewise Fig. 55 shows the propagation of the heat front by radial heat conduction for different heat fluxes. Table 17 and Fig. 55 provide the minimum radial extent the heat flow model should have.

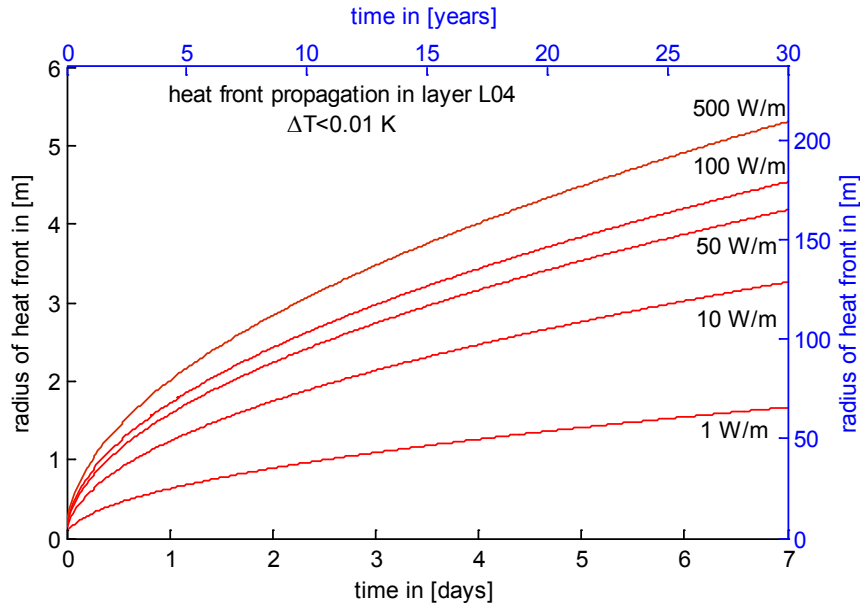


Fig. 55: heat front propagation in layer L04 (highest diffusivity) for different constant heat fluxes over 7 days and 30 years. The heat front is defined as the radius where temperature change surpasses 0.01 K.

D 4.3 Transient solution vs. analytical

Carslaw and Jaeger (1959) provide an analytical solution for the formation temperature around an infinite line source of a constant heat flux in an infinite domain:

$$\Delta T = T_{\infty} - T(r, t) = -\frac{q'}{4\pi\lambda} Ei\left(\frac{-r^2}{4at}\right) = \frac{q'}{4\pi\lambda} \int_{r^2/(4at)}^{\infty} \frac{e^{-u}}{u} du \quad (\text{D.142})$$

where q' is the heat flux per unit length flowing into the well, λ and a are the thermal conductivity and the thermal diffusivity of the formation, respectively. The thermal diffusivity has the unit $[\text{m}^2/\text{s}]$ and is defined as:

$$a = \frac{\lambda}{c_p \cdot \rho} \quad (\text{D.143})$$

The exponential integral Ei can be approximated by

$$Ei(-x) \approx 0.577 + \ln x - x, \quad (\text{D.144})$$

so that eq. D.142 can be written as

$$T(r, t) - T_{\infty} = \frac{q'}{4\pi\lambda} Ei\left(\frac{-r^2}{4at}\right) \approx \frac{q'}{4\pi\lambda} \left(0.577 + \ln\left(\frac{r^2}{4at}\right)\right). \quad (\text{D.145})$$

Eq. D.145 is evaluated numerically and compared to the result of the calculation described in 5.5 applying a constant of $q' = 1 \text{ W/m}$ and an initial homogenous temperature of $T_0 = 0 \text{ K}$. The thermal formation parameters were chosen as $\rho = 2000 \text{ kg/m}^3$, $\lambda = 2 \text{ W/(m}\cdot\text{K)}$, $c_p = 1.5 \text{ kJ/(kg}\cdot\text{K)}$. The calculated domain extends to $r_\infty = 10 \text{ m}$ and the radius growth ratio α_{\max} was set to 1.2 or 1.5 respectively.

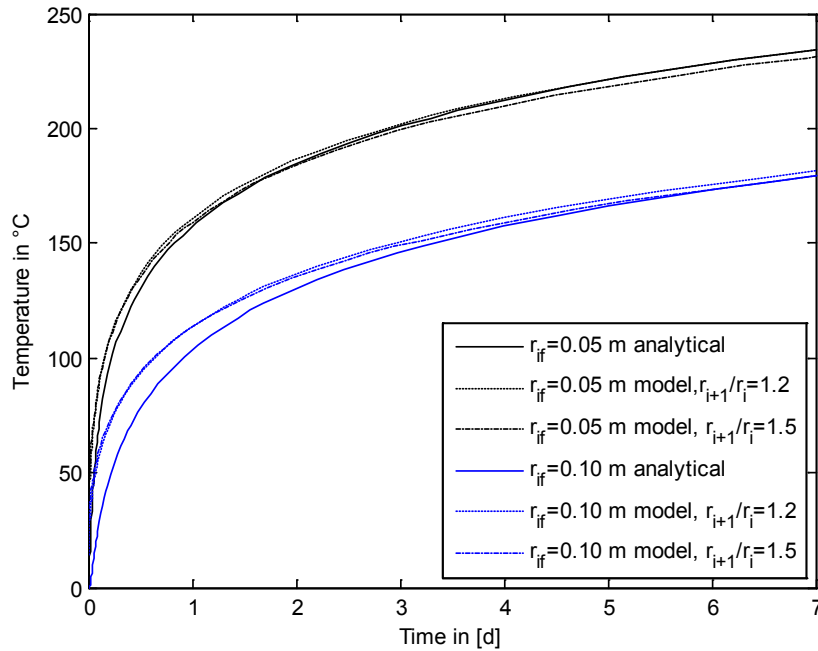


Fig. 56: Temperature at the interface well – formation, comparison analytical ILS solution vs. model with 2 different interface radii ($T = 0 \text{ }^\circ\text{C}$, $q' = 1 \text{ kW}$, $r_\infty = 10 \text{ m}$, $\rho = 2000 \text{ kg/m}^3$, $\lambda = 2 \text{ W/(m}\cdot\text{K)}$, $c_p = 1.5 \text{ kJ/(kg}\cdot\text{K)}$)

As the analytical solution assumes an infinite line source, best agreement is expected if the cylindrical heat source, i.e. the radius of the interface well-formation r_{if} , is small. And indeed, for $r_{\text{if}} = 0.01 \text{ m}$ there is no visible difference in the plot (which has therefore been omitted), for $r_{\text{if}} = 0.05 \text{ m}$ the accordance is very good (Fig. 56) and it decreases for $r_{\text{if}} = 0.1 \text{ m}$. The influence of the discretization fineness, i.e. the difference between the dashed and dash-dotted line, is small but increases later in the simulation. Note that, for greater t , the discretisation error may cancel out the error due to a greater r_{if} , as is the case for $r_{\text{if}} = 0.1 \text{ m}$ and α_{\max} , where the curve meets the analytical solution at $t = 6$ days.

The interface temperature is crucial for the calculation of the heat flow from the pipe to the formation. So, temperatures within the formation are not of primary interest. Nevertheless, Fig. 57 shows good accordance also at $r = 1 \text{ m}$.

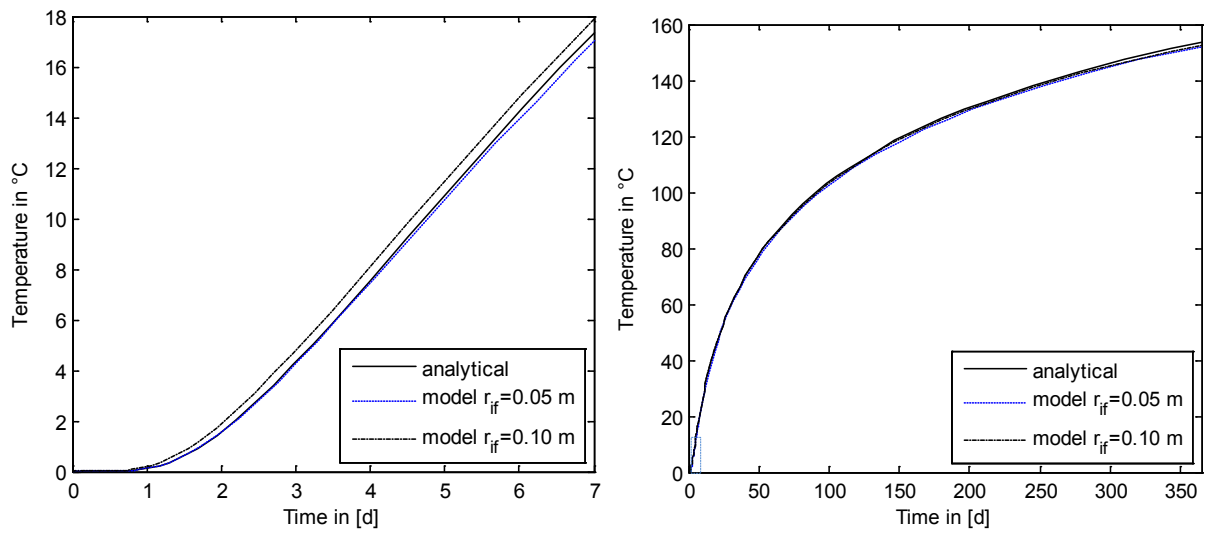


Fig. 57: Temperature at $r = 1$ m, comparison of analytical ILS solution vs. model with two different interface radii for 1 week and 1 year, radius growth ratio 1.2.

E Programming environment

E 1. Modelling using MODELICA

E 2. Implementation Details

E 2.1 Models, inverse functions

As described in 5.1.4, the idea of MODELICA is to define a model merely by its physical relations without specifying the input and output variables and let the solver do the transformations that necessary for solution. That allows for versatile models, such as a fluid property model accepting p and h , as well as T and d as state variables or on another level a pipe model where state variables can be defined for inlet or for the outlet alternatively.

Following this concept in the case of the fluid property model presented in 5.2, at first the equations for the phase equilibrium were implemented completely in the BaseProperties model. That worked fine for a given p and T , because solubility and phase specific enthalpy functions are p - T -dependent. With p and h given, however, numerical inversion tends to run into undefined ranges of T . Attempts to limit T using the min/max attribute were unsuccessful, as the problem was solved by the start value solver and those attributes apply guesses for the start values of a time dependent problem. Attempts to avoid undefined values by introducing max/min functions in the equations lead to inconsistent equations systems and impaired readability. While this model works for separate property calculations, it is more likely to fail when deployed in the well model.

Hence, as explained in 5.2.5, in order to gain more control about the numerical inversion, the VLE calculation was moved to a function `setState_pTX`, which is explicit in p - T and returns specific enthalpy, density, composition of the fluid and both phases as well as the gas fraction. It is called by the function $h(p,T)$, which extracts and returns only the specific enthalpy. Its inverse $T(p,h,X)$ was defined as an algorithm that numerically inverts $h(p,T,X)$.

Thus, the property model can be solved for p , h and for p,T as input parameters without any automatic (and error-prone) iteration by DYMOLA. Unfortunately, the definition of inverse functions is limited to scalar functions and cannot be applied directly to `setState_pTX`. Hence, the VLE has to be called at least twice, once by the invertible scalar function $h(p,T,X)$ and then again directly as `setState_pTX` in order to obtain the other variables. This one unnecessary calculation of the VLE offers considerable optimization potential for calls with p,T as input. It is, however, rather insignificant when p,h are the input variables, as the VLE calculation has already been called repeatedly by $T(p,h,X)$ during the numerical inversion and one more call does not add much more computational load.

E 2.2 Analytic differentials

During the solution of the ODE problem, DYMOLA uses derivatives of quantities that are defined in the equation system. If they cannot be derived analytically, they have to be calculated numerically each time they are required. In order to avoid the additional computational effort and accelerate calculation, derivatives of functions can be defined explicitly in separate functions. This has not been done for the brine properties model.

The complete implementation for media models can be tested with benchmark models in the MSL.

E 2.3 Brine property model

The implementation of geofluid property model is based on the Modelica.Media Library which is part of the MSL. It had to be extended to support two-phase multi-component fluids. For that purpose the existing templates `PartialMixtureMedium` and `PartialTwoPhaseMedium` were merged. The

resulting **PartialMixtureTwoPhaseMedium** contains the templates for additional property functions for two-phase mixtures. It is the base for **PartialBrine_ngas_Newton**, a template for aqueous solutions of salts and non-condensable gases, which contains, among others, the VLE algorithm. **Brine_5salts_TwoPhase_3gas** finally is the specific implementation of the GrSk Brine with its three salts and three gases, containing the respective correlations for density, enthalpy, solubility etc.

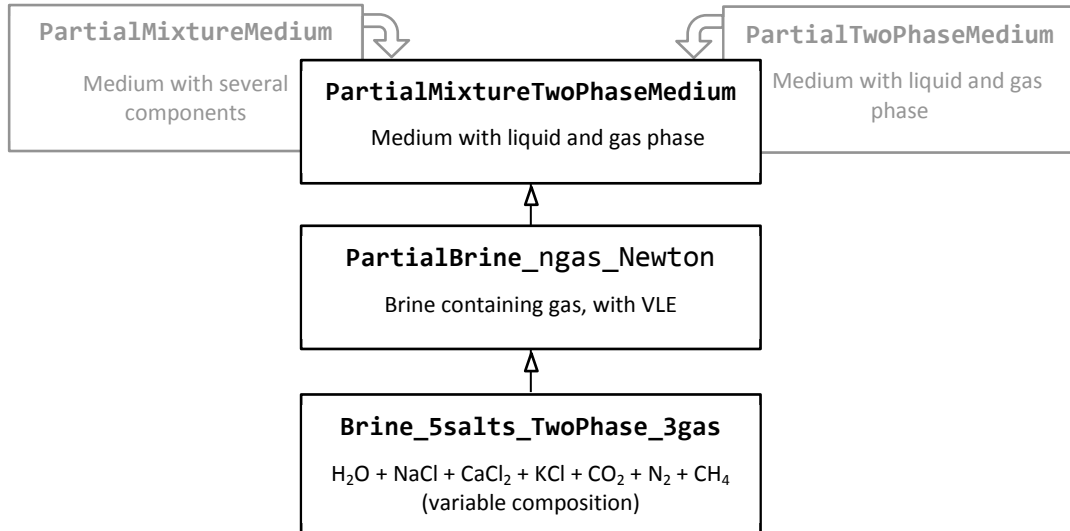


Fig. 58: Class diagram brine property model

E 2.4 Well section model

The components (black arrows) and classes (white arrows) of the well section model including heat flow and pressure drop are shown in Fig. 59.

The well section model uses the stream connector **Modelica.Fluid.Interfaces.FluidPort** from the MSL.

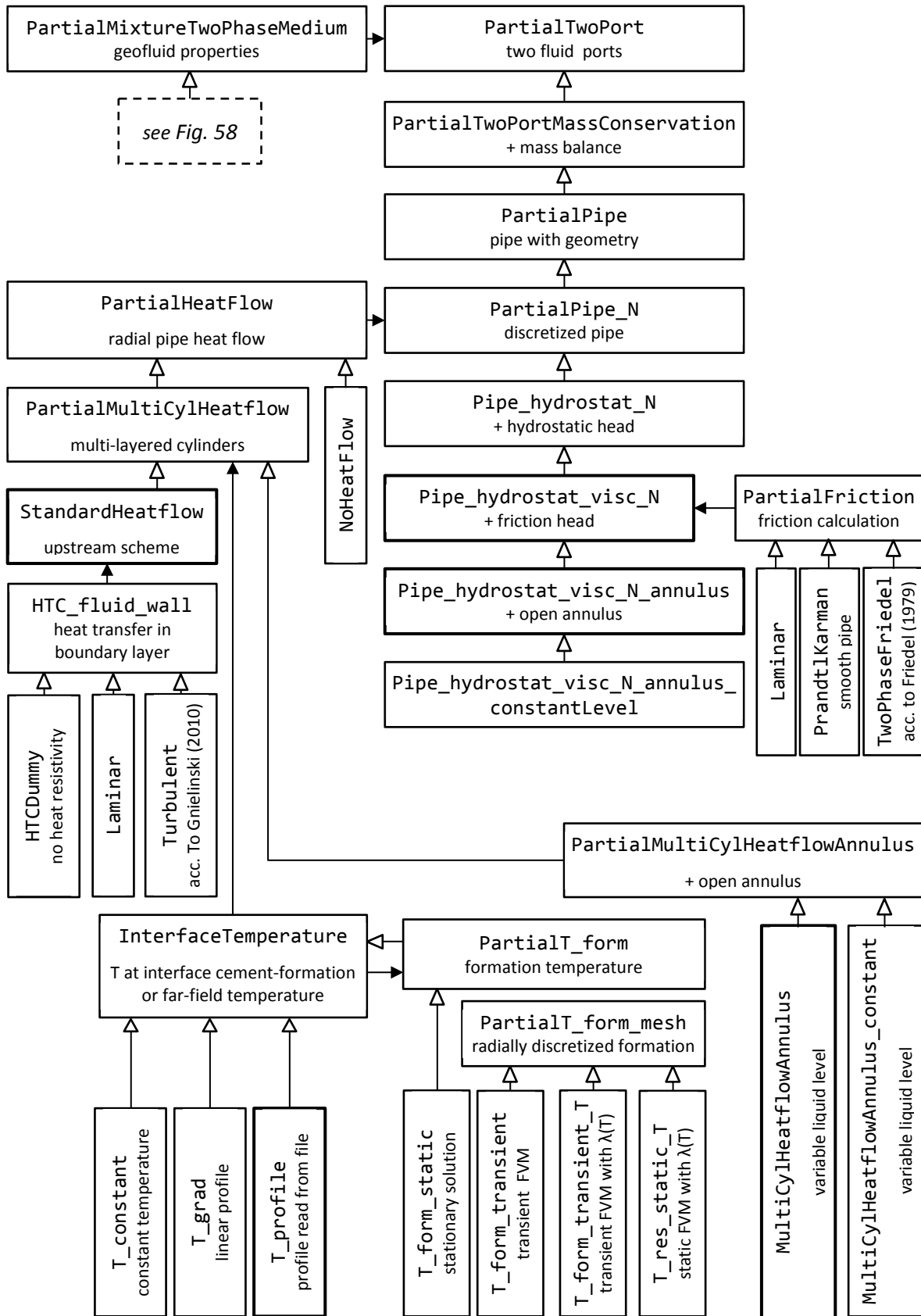


Fig. 59: Class and components in the well section model

E 3. MATLAB Script - Heat wave propagation

This script plots the heat front propagation vs. time. It was used to produce the results discussed in D 4.2.

```
% r_inf(t) Heat wave propagation
T_inf=8;
r_0=.05;
lambda= 4.5;
cp=746;
rho=2600;
alpha = lambda/(cp*rho);
q_prime=50; %W/m
t_30=30*365*24*3600;
T_eps=.01 %threshold for temperature change
T_r=@(r,t)T_eps-q_prime/(4*pi*lambda)*expint(r.^2./(4*alpha*t))
%Carslaw&Jaeger1959
r_inf_fun=@(t)abs(fzero(@(r)T_r(r,t),1));
ezplot(r_inf_fun,1,30*365*24*3600) %plot for 30 years
```

F List of figures

Fig. 1: Schematic view of a geothermal power plant including geofluid loop and cooling water loop (Frick et al., 2013).....	1
Fig. 2: Schematic view of the geothermal production site in Gross Schoenebeck with well, degasser and heat exchanger, arrows indicating fluid flow and heat flow, dashed box shows model boundary.....	2
Fig. 3: Simplified (stratified) two-phase flow with slip upward in an inclined pipe.....	8
Fig. 4: balance volume (production well), homogenous flow.....	14
Fig. 5: Vapour-liquid equilibrium in a closed system for 3 gases + water.....	16
Fig. 6: Nitrogen solubility in different NaCl solutions as provided by Mao and Duan (2006).....	21
Fig. 7: well heat flow (above pump) superposes natural heat flow.....	21
Fig. 8: Formation temperature profile: measurement, completed and linear.....	28
Fig. 9: Wellbore schema for a) production wellbore and b) injection wellbore in Gross Schoenebeck. The indicated diameters are outer diameters of casing/ liner/ tubing or drilled diameter.	30
Fig. 10: Washout (relative borehole volume increase) in production well plotted vs. true vertical depth. Profile from calliper measurements (blue), average values per well-segment (red) and overall well average (green).	31
Fig. 11: Graphical representation of the model of GrSk brine circuit.....	36
Fig. 12: Gas compressibility factor of test mixture of N ₂ /CH ₄ /CO ₂ with 80/15/5 Vol. %.....	47
Fig. 13: Thermo-hydraulic wellbore model (one section).....	53
Fig. 14: Heat flow in the well completion (with open annulus).....	57
Fig. 15: Radial symmetric discretization of formation for Finite Volume Method.....	62
Fig. 16: Comparison of calculated densities with measured data (discrete values are shown with continuous lines).....	66
Fig. 17: Measured data (crosses) and difference of calculated to measured density in [%].....	67
Fig. 18: gas phase composition as a function of composition of dissolved gas in oversaturated water at 25 atm, 25 °C.....	69
Fig. 19: gas phase composition as a function of composition of dissolved gas in oversaturated 5-molar NaCl-solution at 25 °C, 25 atm.....	69
Fig. 20: gas phase composition as a function of composition of dissolved gas in oversaturated 1-molar NaCl-solution at 150 °C, 25 atm (Harting) compared to 29.9 bar (geofluid model).....	70
Fig. 21: gas phase composition as a function of composition of dissolved gas in oversaturated 5-molar NaCl-solution at 150 °C, 25 atm (Harting) compared to 29.4 bar (geofluid model).....	70
Fig. 22: gas phase composition as a function of composition of dissolved gas in oversaturated pure water at 150 °C, 450 atm (Harting) compared to 461 bar (geofluid model).....	71
Fig. 23: gas phase composition as a function of composition of dissolved gas in oversaturated 5-molar NaCl-solution at 150°C, 450 atm (Harting) compared to 460 bar (geofluid model).....	71
Fig. 24: Density profile calculated from pressure gradient and from p-T profile using geofluid model.....	73
Fig. 25: Comparison of measured ($p_{pi,meas}$) and calculated ($p_{pi,calc}$) pump inlet pressure during probe measurement at $s = 4350$ m, X's mark absolute value and difference of calculation for last moment of measurement with fitted gas content.....	74
Fig. 26: Production rate (inversed), friction pressure loss (Δp_{dyn}) and calculation error ($\Delta p_{calc-meas}$) during probe measurement at $s = 4350$ m.....	75
Fig. 27: Comparison of simulated wellbore temperature with analytical solution (Ramey, 1962): a) Wellbore temperature over 30 years. b) Fluid temperature profile after 90 days. (Francke et al., 2013).....	76
Fig. 28: Production rate \dot{V} and produced fluid volume after degasser.....	77

Fig. 29: Pump inlet temperature (T_{pi}) and wellhead temperature T_{wh} , comparison of measured and calculated values during 7 days pump test.....	78
Fig. 30: Simulated temperature profiles of fluid (T_{fluid}), interface well-formation (T_{if}), annulus ($T_{annulus}$) and far-field formation (T_{∞}) as well as profile of heat flux density at the end of the pump test.....	81
Fig. 31: Simulated profiles of gas volume fractions of total gas phase, N_2 , CO_2 , CH_4 and water vapour at the end of the pump test.....	82
Fig. 32: Simulated profiles of mass percentage of gas in gas phase (at 100 % gas is fully degassed) for N_2 , CO_2 , CH_4 at the end of the pump test.....	82
Fig. 33: Density profile in wellbore and open annulus at the end of the circulation test.....	83
Fig. 34: (a) Temperature, (b) radial heat flow, (c) potential vertical heat flow and (d) artificial contribution in formation at end of pump test. The values have been calculated with a radially refined mesh (growth ratio of 1.1).....	84
Fig. 35: Calculated pressure at wellhead (right p-axis), bottomhole and reservoir of injection well (both left p-axis) during circulation test.....	85
Fig. 36: Calculated temperature at wellhead and bottom of injection well, injection rate during circulation test.....	86
Fig. 37: Profiles of temperature and heat flux of the injection well at the end of the circulation test.....	86
Fig. 38: Formation temperature in the vicinity of the injection well at the end of the circulation test.....	87
Fig. 39: Prognosis of wellhead temperature for 30 years for different volume flow rates.....	88
Fig. 40: Relative exergy output (ratio of exergy flows at wellhead and from reservoir) for different production rates.....	89
Fig. 41: a) Annulus liquid level and b) Wellhead temperature for constant and dynamic liquid level in annulus.....	93
Fig. 42: a) Heat flow and b) Temperature at interface well-formation for constant and dynamic liquid level in annulus.....	94
Fig. 43: Pump inlet temperature (T_{pi}) and wellhead temperature T_{wh} , comparison of measured and calculated values during 7 days pump test. Pump efficiency set to 56.3 %, as calculated from electrical measurements.....	94
Fig. 44: Force equilibrium in static pipe flow.....	IV
Fig. 45: Thought experiment to make VLE solution use for slip flow plausible.....	VIII
Fig. 46: Radial symmetric discretization of formation.....	XIX
Fig. 47: Relative difference of calculated gas volume fraction (reference calculation with $tol = 10^{-5}$) vs. absolute pressure for different residuals, standard fluid composition, $T = \{25,125\}$ °C.....	XXI
Fig. 48: Number of iterations of VLE algorithm depending on residual (stop criterion).....	XXII
Fig. 49: Gas volume fraction calculated for GrSk fluid @ 125°C, 10 bar and with a tolerance of $5 \cdot 10^{-5}$ and a varying initialization vector $n_g_start = [1,1,1,1] \cdot \{0.01...0.99\}$	XXII
Fig. 50: Sensitivity of calculated gas volume fraction on residual as stop criterion of VLE algorithm (initial values are varied synchronously between 0.01 and 0.99).....	XXIII
Fig. 51: Gas volume fraction vs. specific enthalpy, $p = 2$ bar, calculation time = 0.98 s for 100 data points.....	XXIII
Fig. 52: Convergence of pressure and gas fraction at wellhead for axial mesh refinement,.....	XXIV
Fig. 53: time for heat wave to reach $r = 1$ m vs. element size.....	XXV
Fig. 54: number of elements and discretisation error vs. element size.....	XXVI
Fig. 55: heat front propagation in layer L04 (highest diffusivity) for different constant heat fluxes over 7 days and 30 years. The heat front is defined as the radius where temperature change surpasses 0.01 K.....	XXVIII
Fig. 56: Temperature at the interface well – formation, comparison analytical ILS solution vs. model with 2 different interface radii ($T = 0$ °C, $q' = 1$ kW, $r_{\infty} = 10$ m, $\rho = 2000$ kg/m ³ , $\lambda = 2$ W/(m·K), $c_p = 1.5$ kJ/(kg·K)).....	XXIX
Fig. 57: Temperature at $r = 1$ m, comparison of analytical ILS solution vs. model with two different interface radii for 1 week and 1 year, radius growth ratio 1.2.....	XXX

Fig. 58: Class diagram brine property model.....XXXII

Fig. 59: Class and components in the well section model XXXIII

G List of tables

<i>Table 1: Stratigraphy of GrSk site - thermal parameters. Layer definition (Ollinger et al., 2010) and thermal conductivity λ under normal temperature, pressure and saturated conditions (Norden et al., 2008). Thermal capacity c_p by (Norden et al., 2012) and density (Norden et al., 2008).....</i>	<i>27</i>
<i>Table 2: GrSk Brine composition 2/2012 – calculated in B 5.....</i>	<i>29</i>
<i>Table 3: Well geometry GrSk4 (production well). Depths are given for the lower end of the respective well section. Ollinger layer specifies the assigned lithology as defined in Table 1. Cementation density is given for inner and outer cement layers.....</i>	<i>32</i>
<i>Table 4: Well geometry GrSk3 (injection well). Depths are given for the lower end of the respective well section. Ollinger layer specifies the assigned lithology as defined in Table 1.....</i>	<i>33</i>
<i>Table 5: Validity ranges and fitting parameters for apparent molar heat capacity (eq. 5.43) and apparent molar enthalpy (eq. 5.44)...</i>	<i>50</i>
<i>Table 6: Viscosity model validation results.....</i>	<i>68</i>
<i>Table 7: GrSk Brine composition in 9/2011 - Analysis by VKTA, uncertainty 10 %.....</i>	<i>72</i>
<i>Table 8: Probe measurements: Location, time, duration, mass flow rate from the reservoir, difference of measured and calculated pump inlet pressures, friction pressure loss and fitted variation of gas mass content.....</i>	<i>73</i>
<i>Table 9: Brine properties compared to water properties for selected states.....</i>	<i>80</i>
<i>Table 10: Sensitivity on simulated temperatures on removal of model features, the average has been calculated between 24 h after the beginning and the end of the circulation test.....</i>	<i>90</i>
<i>Table 11: Brine composition Gross Schoenebeck.....</i>	<i>IX</i>
<i>Table 12: Pump efficiency calculation from hydraulic and electric data, averaged for $t > 50$ h from circulation test (6.4). Power factor is $\varphi = 0.96$, Voltage is $U = 230/400$ V.....</i>	<i>XII</i>
<i>Table 13: Coefficients and goodness of fit of MATLAB 2D 2nd/3rd degree polynomial fit of heat capacity data.....</i>	<i>XIV</i>
<i>Table 14: Influence of tolerance on calculation time (500 data points, $p = 1 \dots 100$ bar at 125 °C).....</i>	<i>XXII</i>
<i>Table 15: Formation model parameters.....</i>	<i>XXV</i>
<i>Table 16: Comparison FDM - FVM discretisation error vs. element size for different mesh ranges.....</i>	<i>XXVII</i>
<i>Table 17: Propagation range of heat front in formation.....</i>	<i>XXVIII</i>

H References

- Ahmad, S. (1970) 'Axial Distribution of Bulk Temperature and Void Fraction in a Heated Channel With Inlet Subcooling', *Journal of Heat Transfer*, vol. 92, no. 4, p. 595, DOI: 10.1115/1.3449729.
- Antics, M. (1995) 'Modelling two phase flow in low temperature geothermal wells', Proceedings of world geothermal congress, Florence, Italy.
- Aunzo, Z., Bjornsson, G. and Bodvarsson, G. (1991) *Wellbore models GWELL, GWNACL, and HOLA user's guide*, Berkeley, USA, <http://escholarship.org/uc/item/6wt2d5b7.pdf> [30 Nov 2013].
- Ayala, M. (2010) *Coupled geothermal reservoir-wellbore simulation with a case study for the Námafjall field, N-Iceland*, (Master's thesis) edition, University of Island, <http://hdl.handle.net/1946/4616> [30 Nov 2013].
- Baehr, H. (1998) 'Thermodynamische Fundamentalgleichungen und charakteristische Funktionen', vol. 64, no. 1-2, pp. 35-43, <http://dx.doi.org/10.1007/pl00010764>.
- Baehr, H. (2003) *Thermodynamik: Grundlagen und technische Anwendungen*, Springer Berlin.
- Baehr, H. and Stephan, K. (2004) *Wärme- und Stoffübertragung*, Springer.
- Barnea, D., Shoham, O. and Taitel, Y. (1982) 'Flow pattern transition for vertical downward two phase flow', *Chemical Engineering Science*, vol. 37, no. 5, Jan, pp. 741-744, DOI: 10.1016/0009-2509(82)85034-3.
- Bhat, A., Swenson, D. and Gosavi, S. (2005) 'Coupling the HOLA wellbore simulator with TOUGH2', Proceedings of the 20th workshop on geothermal reservoir engineering. Stanford University, Stanford, California.
- Blöcher, G.a.M.I.a.M.H.a.Z.G. (2008) 'Modelling of pore pressure response due to hydraulic stimulation treatments at the geothermal research doublet EGRSK3/90 and GTGRSK4/05 in summer 2007', 33rd Workshop on Geothermal Reservoir Engineering, Stanford, USA.
- Blöcher, G., Kranz, S., Zimmermann, G., Frick, S., Hassanzadegan, A., Hassanzadegan, A., Moeck, I., Brandt, W., Saadat, A. and Huenges, E. (2010) 'Conceptual Model for Coupling Geothermal Power Plants with Deep Reservoirs', Proceedings World Geothermal Congress 2010, Bali, Indonesia 2010.
- Blöcher, G., Reinsch, T., Henningses, J. and Zimmermann, G. (2013) 'Opening of a Gel/Proppant Fracture during Production', no. Abstract Volume 2013, p. 43, <http://edoc.gfz-potsdam.de/gfz/20722> [30 Nov 2013].
- Blöcher, G., Zimmermann, G., Moeck, I., Brandt, W., Hassanzadegan, A. and Magri, F. (2010) '3D numerical modeling of hydrothermal processes during the lifetime of a deep geothermal reservoir', *Geofluids*, vol. 10, no. 3, Aug, pp. 406-421, DOI: 10.1111/j.1468-8123.2010.00284.x.
- Bridgman, P. (1914) 'A Complete Collection of Thermodynamic Formulas', *Physical Review*, vol. 3, no. 4, Apr, pp. 273-281, DOI: 10.1103/physrev.3.273.
- Carslaw (1948) *Conduction of heat in solids*, Clarendon Press, <http://www.worldcat.org/oclc/21383520> [30 Nov 2013].
- Casas, W., Pröll, K. and Schmitz, G. (2005) 'Modeling of Desiccant Assisted Air Conditioning Systems', 4th International Modelica Conference, Hamburg University of Technology, 487-496.
- Çengel, Y. (2002) *Heat Transfer: A Practical Approach*, Mcgraw-Hill.
- Centrilift (2013) *AutographPC®*, 15 Feb, [Online], <http://www.bakerhughes.com/news-and-media/resources/brochures/autographpc-software> [30 Nov 2013].
- Claesson, J. and Eskilson, P. (1988) 'Conductive heat extraction to a deep borehole: Thermal analyses and dimensioning rules', *Energy*, vol. 13, no. 6, Jun, pp. 509-527, DOI: 10.1016/0360-5442(88)90005-9.

- Dassault Systèmes AB (2013) *DYMOLA*, [Online], <http://www.3ds.com/products/catia/portfolio/dymola> [30 Nov 2013].
- DiPippo, R. (2012) *Geothermal Power Plants, Third Edition: Principles, Applications, Case Studies and Environmental Impact, Third Edition*, Butterworth-Heinemann.
- Driesner, T. (2007) 'The system H₂O–NaCl. Part II: correlations for molar volume, enthalpy, and isobaric heat capacity from 0 to 1000 °C, 1 to 5000 bar, and 0 to 1 XNaCl', *Geochimica et Cosmochimica*.
- Duan, Z. and Mao, S. (2006) 'A thermodynamic model for calculating methane solubility, density and gas phase composition of methane-bearing aqueous fluids from 273 to 523K and from 1 to 2000bar', *Geochimica et Cosmochimica Acta*, vol. 70, no. 13, Jul, pp. 3369-3386, DOI: 10.1016/j.gca.2006.03.018.
- Duan, Z., Sun, R., Zhu, C. and Chou, I. (2006) 'An improved model for the calculation of CO₂ solubility in aqueous solutions containing Na⁺, K⁺, Ca²⁺, Mg²⁺, Cl⁻, and SO₄²⁻', *Marine Chemistry*, vol. 98, no. 2-4, Feb, pp. 131-139, DOI: 10.1016/j.marchem.2005.09.001.
- Dubbel (2001) *Dubbel - Taschenbuch Für Den Maschinenbau (20., Neubearb. U. Erw. Aufl.)*, Springer.
- Dukler, A., Wicks, M. and Cleveland, R. (1964) 'Frictional pressure drop in two-phase flow: B. An approach through similarity analysis', *AIChE J.*, vol. 10, no. 1, Jan, pp. 44-51, DOI: 10.1002/aic.690100118.
- Electrospeed GCS Operator's Manual P/N 900350* (2001), Claremore, OK, USA.
- Elmi, D. and Axelsson, G. (2009) 'Application of a Transient Wellbore Simulator to Wells HE-06 and HE-20 in the Hellisheidi geothermal system, SW-Iceland'.
- Elmqvist, H., Tummescheit, H. and Otter, M. (2003) 'Object-Oriented Modeling of Thermo-Fluid Systems', 3rd International Modelica Conference, Linköpings Universitet, Linköping, Sweden, 269-286.
- Feldbusch, E., Regenspurg, S., Banks, J., Milsch, H. and Saadat, A. (2013) 'Alteration of fluid properties during the initial operation of a geothermal plant - results from in-situ measurements in Gross Schoenebeck', *Environmental Earth Sciences*, no. SI:Geoenergy.
- Francke, H. (2008) *Energetische Optimierung der kombinierten Strom- und Wärmebereitstellung aus Geothermie*, (Diploma thesis) edition, Berlin.
- Francke, H., Kraume, M. and Saadat, A. (2013) 'Thermal-hydraulic measurements and modelling of the brine circuit in a geothermal well', *Environmental Earth Sciences*, no. SI:Geoenergy, Jul, pp. 1-15, DOI: 10.1007/s12665-013-2612-8.
- Francke, H. and Thorade, M. (2010) 'Density and viscosity of brine: An overview from a process engineers perspective', *Chemie der Erde - Geochemistry*, vol. 70, Aug, pp. 23-32, DOI: 10.1016/j.chemer.2010.05.015.
- Frick, S., Kranz, S. and Saadat, A. (2013) 'Designing the Cooling of Low Temperature Power Plants', Minsk, Belarus.
- Friedel, L. (1978) 'Druckabfall bei der Strömung von Gas/Dampf-Flüssigkeits-Gemischen in Rohren', *Chemie Ingenieur Technik*, vol. 50, no. 3, pp. 167-180, DOI: 10.1002/cite.330500304.
- Fuchs, S. and Kather, A. (2013) 'Zwei-Phasen-Strömung im Thermalwassersystem von Geothermiekraftwerken', *bbr - das Fachmagazin für Leitungsbau, Brunnenbau und Geothermie*, no. 5, pp. 40-47, <http://www.bbr-online.de/archiv/05-2013/#c1210> [30 Nov 2013].
- Gnielinski, V. (1995) 'Ein neues Berechnungsverfahren für die Wärmeübertragung im Übergangsbereich zwischen laminarer und turbulenter Rohrströmung', *Forschung im Ingenieurwesen*, vol. 61, no. 9, pp. 240-248, DOI: 10.1007/BF02607964.

- Gnielinski, V. (2010) 'Heat Transfer in Pipe Flow', in *VDI Heat Atlas*, VDI, DOI: 10.1007/978-3-540-77877-6.
- Guðmundsdóttir, H. (2012) *A Coupled Wellbore-Reservoir Simulator utilizing Measured Wellhead Conditions*, (Master's thesis) edition, <http://hdl.handle.net/1946/13219> [30 Nov 2013].
- Harting, P., May, F. and Schütze, H. (1981) *Tabellen und Diagramme zur Löslichkeit von Methan-Stickstoff-Gemischen in wässrigen Natriumchloridlösung*, Leipzig: Akademie der Wissenschaften der DDR, Zentralinst. für Isotopen- u. Strahlenforschung.
- Hasan, A. and Kabir, C. (1994) 'Aspects of Wellbore Heat Transfer During Two-Phase Flow (includes associated papers 30226 and 30970)', *SPE Production & Facilities*, vol. 9, no. 3, Aug, DOI: 10.2118/22948-pa.
- Hasan, A. and Kabir, C. (2010) 'Modeling two-phase fluid and heat flows in geothermal wells', *Journal of Petroleum Science and Engineering*, vol. 71, no. 1-2, Mar, pp. 77-86, DOI: 10.1016/j.petrol.2010.01.008.
- Hennings, J. (2012) 'Durchführung Fluidprobenahme Gt GrSk 4/05 März 2012 und vorläufige Auswertung Bohrlochmessdaten', *GFZ Potsdam*, Mar.
- Hennings, J., Brandt, W., Erbas, K., Moeck, I., Saadat, A., Reinsch, T. and Zimmermann, G. (2012) 'Downhole monitoring during hydraulic experiments at the in-situ geothermal lab Gross Schönebeck', *Proceedings 37th Workshop on Geothermal Reservoir Engineering*, Stanford, USA, 51-56.
- Herwig, H. (2007) 'Die irreführende Verwendung der thermodynamischen Größe Enthalpie – ein didaktischer Sündenfall', *Forschung im Ingenieurwesen*, vol. 71, no. 2, Jun, pp. 107-112, DOI: 10.1007/s10010-007-0049-5.
- Hewitt, G. and Roberts, D. (1969) 'Studies of two-phase flow patterns by simultaneous X-ray and flash photography', *Atomic Energy Research Establishment Harwell*, <http://www.dtic.mil/cgi-bin/GetTRDoc?AD=ADA953138> [30 Nov 2013].
- Hoffert, U. and Milsch, H. (2013a) 'Thermophysical properties of synthetic geothermal brines', Rostock, Germany.
- Hoffert, U. and Milsch, H. (2013b) 'Thermophysical properties of synthetic geothermal brines', London, UK.
- Huenges, E. (2011) 'Forschungsplattform Groß Schönebeck: Technologieentwicklung für eine effiziente Wärme- und Strombereitstellung aus tiefer Erdwärme', *System Erde*, vol. 1, pp. 32-43, DOI: 10.2312/GFZ.syserde.01.02.3.
- Huenges, E. and Seibt, A. (2004) 'Zusammensetzung des Reservoir-Fluids', pp. 25-27, <http://bib.gfz-potsdam.de/pub/str0416/0416.pdf> [30 Nov 2013].
- Ingersoll, L. and Plass, H. (1948) 'Theory of the ground heat pipe heat source for the heatpump', *Transactions of the American Society of Heating and Ventilating Engineers*.
- Ishii, M. and Hibiki, T. (2006) *Thermo-Fluid Dynamics of Two-Phase Flow*, Boston, MA: Springer US, DOI: 10.1007/978-0-387-29187-1.
- Jansen, J.D. and Currie, P.K. (2003) *Modelling and Optimisation of Oil and Gas Production Systems (Lecture Notes)*, Delft: TU Delft.
- Kraume, M. (2003) *Transportvorgänge in der Verfahrenstechnik: Grundlagen und apparative Umsetzungen (VDI-Buch / Chemische Technik / Verfahrenstechnik) (German Edition)*, Springer.
- Laliberté, M. and Cooper, E. (2004) 'Model for Calculating the Density of Aqueous Electrolyte Solutions', *J. Chem. Eng. Data*, vol. 49, no. 5, pp. 1141-1151, DOI: 10.1021/je0498659.

- Lemmon, E., Huber, M. and McLinden, M. (2010) *NIST Standard Reference Database 23: Reference Fluid Thermodynamic and Transport Properties - REFPROP. 9.0.*, Gaithersburg, <http://nist.gov/srd/nist23.cfm> [30 Nov 2013].
- Livescu, S., Durlofsky, L., Aziz, K. and Ginestra, J. (2010) 'A fully-coupled thermal multiphase wellbore flow model for use in reservoir simulation', *Journal of Petroleum Science and Engineering*, vol. 71, no. 3-4, Apr, pp. 138-146, DOI: 10.1016/j.petrol.2009.11.022.
- Lockhart, R. and Martinelli, R. (1949) 'Proposed correlation of data for isothermal two-phase, two-component flow in pipes', *Chem. Eng. Prog.*, vol. 45, no. 1, pp. 39-48.
- Loose, P. (2007) *Erdwärmennutzung: Versorgungstechnische Planung und Berechnung*, Heidelberg: C.F. Müller.
- Mao, S. and Duan, Z. (2006) *A thermodynamic model for calculating nitrogen solubility, gas phase composition and density of the H₂O-N₂-NaCl system*, Oct, [Online], DOI: 10.1016/j.fluid.2006.07.020.
- Mao, S. and Duan, Z. (2008) 'The P,V,T,x properties of binary aqueous chloride solutions up to T=573 K and 100 MPa', *The Journal of Chemical Thermodynamics*, vol. 40, no. 7, pp. 1046-1063, DOI: 10.1016/j.jct.2008.03.005.
- Mao, S. and Duan, Z. (2009) 'The Viscosity of Aqueous Alkali-Chloride Solutions up to 623 K, 1,000 bar, and High Ionic Strength', *International Journal of Thermophysics*, vol. 30, no. 5, Oct, pp. 1510-1523, DOI: 10.1007/s10765-009-0646-7.
- McBride, B., Zehe, M. and Gordon, S. (2002) *NASA Glenn Coefficients for Calculating Thermodynamic Properties of Individual Species*, http://ntrs.nasa.gov/archive/nasa/casi.ntrs.nasa.gov/20020085330_2002141071.pdf [30 Nov 2013].
- Miller, C. (1980) *WELBORE user's manual*, Berkeley, USA: Lawrence Berkeley Laboratory.
- Milsch, H., Giese, R., Poser, M., Kranz, S., Feldbusch, E. and Regenspurg, S. (2013) 'Technical paper: FluMo—a mobile fluid—chemical monitoring unit for geothermal plants', pp. 1-5, DOI: 10.1007/s12665-013-2408-x.
- Müller, I. (2001) *Grundzüge der Thermodynamik 3. Auflage*, Berlin: Springer.
- Naumann, D. (2000) *Salinare Tiefenwässer in Norddeutschland Dissertation*, Potsdam: GFZ Potsdam.
- Nelson, E. (1986) 'Improved cement slurry designed for thermal EOR wells', *Oil and Gas Journal*, no. 84, pp. 39-44.
- Norden, B., Förster, A. and Balling, N. (2008) 'Heat flow and lithospheric thermal regime in the Northeast German Basin', *Tectonophysics*, vol. 460, no. 1-4, pp. 215-229, DOI: 10.1016/j.tecto.2008.08.022.
- Norden, B., Förster, A., Behrends, K., Krause, K., Stecken, L. and Meyer, R. (2012) 'Geological 3-D model of the larger Altensalzwedel area, Germany, for temperature prognosis and reservoir simulation', *Environmental Earth Sciences*, vol. 67, no. 2, pp. 511-526, DOI: 10.1007/s12665-012-1709-9.
- Ollinger, D., Baujard, C., Kohl, T. and Moeck, I. (2010) 'Distribution of thermal conductivities in the Groß Schönebeck (Germany) test site based on 3D inversion of deep borehole data', *Geothermics*, vol. 39, no. 1, pp. 46-58, DOI: 10.1016/j.geothermics.2009.11.004.
- PAAR, A. (2008) *Manual Anton Paar Density Meter DPRn 427HT (LATEX) HastelloyC276*.
- Paglianti, A., Andreussi, P. and Barelli, A. (1995) 'Reinjection of noncondensable gases in geothermal wells', in *Proceedings of the World Geothermal Congress, 1995*, Florence, Italy.
- Philippe, M., Bernier, M. and Marchio, D. (2009) 'Validity ranges of three analytical solutions to heat transfer in the vicinity of single boreholes', *Geothermics*, vol. 38, no. 4, Dec, pp. 407-413, DOI: 10.1016/j.geothermics.2009.07.002.

- Pourafshary, P., Varavei, A., Sepehrnoori, K. and Podio, A. (2009) 'A compositional wellbore/reservoir simulator to model multiphase flow and temperature distribution', *Journal of Petroleum Science and Engineering*, Mar, DOI: 10.1016/j.petrol.2009.02.012.
- Prandtl, L. (1925) 'Bericht über Untersuchungen zur ausgebildeten Turbulenz', *Z. Angew. Math. Mech*, vol. 5, p. 139.
- Press, F. and Siever, R. (1995) *Allgemeine Geologie*, München: Spektrum Akademischer Verlag.
- Quoilin, S., Desideri, A., Bell, I., Weonski, J. and Lemort, V. (2013) 'Robust and computationally efficient dynamic simulation of ORC systems: The Thermocycle Modelica library.', <http://www.thermocycle.net> [30 Nov 2013].
- Ramey (1962) 'Wellbore Heat Transmission', *Journal of Petroleum Technology*, vol. 14, no. 4, DOI: 10.2118/96-PA.
- Regenspurg, S., Wiersberg, T., Brandt, W., Huenges, E., Saadat, A., Schmidt, K. and Zimmermann, G. (2010) 'Geochemical properties of saline geothermal fluids from the in-situ geothermal laboratory Groß Schönebeck (Germany)', *Chemie der Erde - Geochemistry*, vol. 70, no. Supplement 3, pp. 3-12, DOI: 10.1016/j.chemer.2010.05.002.
- Richert, F., R and Schlo (2003) 'Vergleich von Modelica und Matlab anhand der Modellbildung eines Dieselmotors (Comparison of Modelica and Matlab by means of the Model of a Diesel Engine)', *at?Automatisierungstechnik/Methoden und Anwendungen der Steuerungs-, Regelungs- und Informationstechnik*, vol. 51, no. 6/2003, pp. 247-254.
- Rung, T., Xue, L., Yan, J., Schatz, M. and Thiel, F. (2002) *Numerische Methoden der Thermo- und Fluidodynamik*, Berlin.
- Saeid, S., Al-Khoury, R. and Barends, F. (2013) 'An efficient computational model for deep low-enthalpy geothermal systems', *Computers & Geosciences*, vol. 51, Feb, pp. 400-409, DOI: 10.1016/j.cageo.2012.08.019.
- Sanahuja, A. and Gómez-Estévez, J. (1986) 'Determination of the enthalpies of solution at infinite dilution of KCl and NaCl in water at 303.15, 308.15, and 313.15 K', *The Journal of Chemical Thermodynamics*, vol. 18, no. 7, Jul, pp. 623-628, DOI: 10.1016/0021-9614(86)90063-7.
- Sander, R. (1999) *Compilation of Henry's Law constants for inorganic and organic species of potential importance in environmental chemistry*, Rolf Sander, <http://www.henrys-law.org>.
- Scheffer, Schachtschabel, Blume, H.-P., Brümmer, G., Schwertmann, U., Horn, R., Kögel-Knabner, I., Stahr, K. and Wilke (2009) *Lehrbuch der Bodenkunde*, Spektrum Akademischer Verlag.
- Schlumberger (2008) *Schlumberger - Y-Tool and Bypass System*, [Online], http://www.slb.com/~media/Files/artificial_lift/product_sheets/dual_esp_ps.pdf [2 Nov 2013].
- Schön, J. (2004) *Physical Properties of Rocks, Volume 8: Fundamentals and Principles of Petrophysics (Handbook of Petroleum Exploration and Production)*, Pergamon.
- Sinke, G., Mossner, E. and Curnutt, J. (1985) 'Enthalpies of solution and solubilities of calcium chloride and its lower hydrates', *The Journal of Chemical Thermodynamics*, vol. 17, no. 9, Sep, pp. 893-899, DOI: 10.1016/0021-9614(85)90083-7.
- Smith, J., Ness, H.V. and Abbott, M. (2001) *Introduction to Chemical Engineering Thermodynamics (The McGraw-Hill Chemical Engineering Series)*, McGraw-Hill Science/Engineering/Math.
- Sokolichin, A., Becker, S. and Eigenberger, G. (2004) *Mathematische Modellbildung und numerische Simulation von Gas-Flüssigkeits-Blasenströmungen*, Stuttgart: Fakultät Konstruktions-, Produktions- und Fahrzeugtechnik, Universität Stuttgart, DOI: 10.1002/cite.330660411.

- Somerton, W. (1992) *Thermal Properties and Temperature-Related Behavior of Rock/Fluid Systems*, Elsevier Science.
- Thorade, M. (2014) *Entropiebasierte Bewertungskriterien für den Wärmeübergang in Kraftwerksprozessen*, (Doctoral Thesis) edition, Hamburg: Technische Universität Hamburg-Harburg.
- Viswanath, D., Ghosh, T., Prasad, D., Dutt, N. and Rani, K. (2006) *Viscosity of Liquids*, Springer.
- Wagner, W., Cooper, J., Dittmann, A., Kijima, J., Kretzschmar, H., Kruse, A., Mareš, R., Oguchi, K., Sato, H., Stöcker, I., Šifner, O., Takaishi, Y., Tanishita, I., Trübenbach, J. and Th (2000) 'The IAPWS Industrial Formulation 1997 for the Thermodynamic Properties of Water and Steam', *Journal of Engineering for Gas Turbines and Power*, vol. 122, no. 1, pp. 150-184, DOI: 10.1115/1.483186.
- Wellenhofer, A. and Muschelknautz, S. (2010) 'Pressure Drop in Tubes, Valves, and Fittings', in *VDI Heat Atlas*, VDI, DOI: 10.1007/978-3-540-77877-6.
- White, D., Doberstein, A., Gates, J., Tillett, D. and Wood, R. (1987a) 'Heat capacity of aqueous CaCl₂ from 306 to 603 K at 17.5 MPa', *The Journal of Chemical Thermodynamics*, vol. 19, no. 3, mar, pp. 251-259, DOI: 10.1016/0021-9614(87)90132-7.
- White, D., Ryan, M., Armstrong, M.C., Gates, J. and Wood, R. (1987b) 'Heat capacities of aqueous KCl from 325 to 600 K at 17.9 MPa', *The Journal of Chemical Thermodynamics*, vol. 19, no. 10, oct, pp. 1023-1030, DOI: 10.1016/0021-9614(87)90012-7.
- Wiersberg, T., Seibt, A. and Zimmer, M. (2004) 'Gas-geochemische Untersuchungen an Formationsfluiden des Rotliegend der Bohrung Groß Schönebeck 3/90', *Geothermie Report 04-1*, DOI: 10.2312/GFZ.b103-04036.
- wikipedia.org* (2013), 8 Oct, [Online], <http://en.wikipedia.org/wiki/Seawater>.
- Willhite, P. (1967) 'Over-all Heat Transfer Coefficients in Steam And Hot Water Injection Wells', *Journal of Petroleum Technology*, vol. Volume 19, Number 5, no. 5, May, DOI: 10.2118/1449-PA.
- Yusufova, V., Pepinov, R., Nikolaev, V. and Guseinov, G. (1975) 'Thermal conductivity of aqueous solutions of NaCl', *Journal of Engineering Physics and Thermophysics*, vol. 29, no. 4, pp. 1225-1229, DOI: 10.1007/BF00867119.
- Zhang, H.-L., Chen, G.-H. and Han, S.-J. (1997) 'Viscosity and Density of H₂O + NaCl + CaCl₂ and H₂O + KCl + CaCl₂ at 298.15 K', *Journal of Engineering Physics and Thermophysics*, vol. 42, no. 3, May, pp. 526-530, DOI: 10.1021/je9602733.